

SOME PROBLEMS WITH SEISMIC REFLECTION TECHNIQUES

by

Gregory John Blackburn, B.Sc.(Hons.)

Submitted in partial fulfilment of the
requirements for the degree of
Doctor of Philosophy.

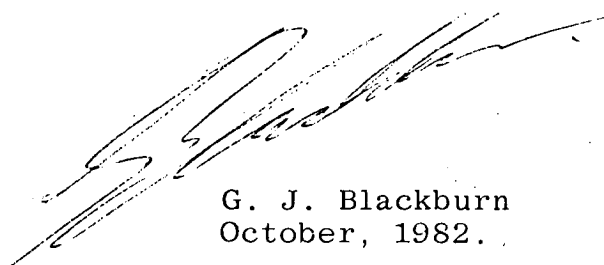
UNIVERSITY OF TASMANIA

Hobart

1982

(conferred on March 1983)

This thesis contains no material which has been accepted for the award of any other degree or diploma in any university, and, to the best of my knowledge and belief, the thesis contains no copy or paraphrase of material previously published or written by another person, except where due reference is made in the text of the thesis.

A handwritten signature in dark ink, appearing to read 'G. J. Blackburn', is written over the printed name and date.

G. J. Blackburn
October, 1982.

CONTENTS

	page
Figures	ii
Abstract	ix
Acknowledgements	x
Chapter 1 INTRODUCTION	1.1
Chapter 2 ERRORS IN VELOCITY CONVERSION FOR SIMPLE GEOLOGICAL STRUCTURES	2.1
Chapter 3 STATIC CORRECTION IN IRREGULAR OR STEEPLY DIPPING WATER-BOTTOM ENVIRONMENTS	3.1
Chapter 4 SEISMIC VELOCITY AND MIGRATION DETERMINATION	4.1
Chapter 5 REFLECTIVITY, TRANSMISSIVITY AND MODE CONVERSION FOR THIN LAYERS	5.1
Chapter 6 CONCLUSIONS	6.1
REFERENCES	R.1
Appendix 1 RAY TRACING SYSTEM - TWO DIMENSIONS	A1.1
Appendix 2 RAY TRACING USING FERMAT'S PRINCIPLE	A2.1
Appendix 3 THOMPSON-HASKELL METHOD	A3.1
Appendix 4 COMPUTER PROGRAM LISTING (MICROFILM)	A4.1

LIST OF FIGURES

	page
Fig. 2.1 Idealised view of a reflection profile.	2.6
2.2 Schematic geological section depicting areas for velocity analysis.	2.6
2.3 Schematic geological section showing actual raypaths and hypothetical raypaths for a vertical CRP.	2.10
2.4 Schematic geological section containing a high velocity inhomogeneity.	2.10
2.5 Schematic T^2-X^2 plots for a reflector whose arrival time due to migration or raypath distortion problems is earlier than for the homogeneous case (A) or where the arrival time is later than expected (B).	2.11
2.6 Wedge model with corresponding error-factor plot.	2.15
2.7 Unconformity model with corresponding zero-offset raypaths and error-factor plots.	2.17
2.8 Selected gather locations along the unconformity model for surface 6 and their corresponding time-difference plots.	2.18
2.9 Unconformity variation-factor and gather plots at selected gather locations.	2.19
2.10 Timing and depth errors for the unconformity model.	2.24
2.11 High velocity patch reef model with corresponding zero-offset raypaths and error-factor plots.	2.25
2.12 Selected gather locations along the reef model for surface 8.	2.26
2.13 Patch reef time-difference plots for surface 8.	2.26
2.14 Patch reef variation-factor plots.	2.28
2.15 Patch reef variation-factor plots.	2.28
2.16 High velocity fill channel model with corresponding zero-offset raypaths and error-factor plots.	2.31
2.17 Gathers and time-difference plots for selected locations along the surface of the high velocity fill channel model for surface 5.	2.32
2.18 Gathers at E, and time-difference plots for the high velocity fill channel base.	2.35
2.19 Selected gather locations for the high velocity channel fill model along surface 8.	2.35
2.20 High velocity fill channel time-difference plots for surface 8.	2.36
2.21 High velocity fill channel variation-factor plots.	2.36
2.22 Low velocity fill channel model with corresponding zero-offset raypaths and error-factor plots.	2.38
2.23 Selected gathers and time-difference plots for surface 5 for the low velocity fill channel model.	2.39
2.24 Selected gathers and time-difference plots for surface 7 for the low velocity fill channel model.	2.39

List of Figures cont.

	page
Fig. 2.25 Low velocity fill channel model variation-factor and gather plots at selected gather locations for surface 7.	2.42
2.26 Synclinal model with corresponding zero-offset raypaths and error-factor plots.	2.43
2.27 Selected gather locations for surface 6 and their corresponding time-difference plots for the synclinal model.	2.44
2.28 Syncline model variation-factor plots at selected gather locations.	2.44
2.29 Anticline model with corresponding zero-offset raypaths and error-factor plots.	2.46
2.30 Selected gather locations for surface 7 for the anticline model.	2.47
2.31 Selected gather locations for surface 6 and their corresponding time-difference plot for the anticline model.	2.48
2.32 Anticline model variation-factor and gather plots at selected gather locations.	2.49
2.33 Prograding delta model with corresponding zero-offset raypaths and error factor plots.	2.51
2.34 Selected gather locations for surface 4 and their corresponding time-difference plots for the prograding delta model.	2.52
2.35 Selected gather locations for surface 6 and their corresponding time-difference plots for the prograding delta model.	2.55
2.36 Selected gather locations for surface 10 and their corresponding time-difference plots for the prograding delta model.	2.56
2.37 Prograding delta model variation-factor curves at selected gather locations for surface 6.	2.57
2.38 Prograding delta model variation-factor and gather plots at selected gather locations for surface 10.	2.58
2.39 Timing and depth errors for the prograding delta model.	2.61
3.40 Shelf margin model and corresponding error-factor plot.	2.62
2.41 Seismic stratigraphic interpretation for line 1.	2.66
2.42 Seismic stratigraphic interpretation for line 2.	2.67
2.43 Seismic stratigraphic interpretation for line 6.	2.68
2.44 Seismic stratigraphic interpretation for line 7.	2.69
2.45 Location and depth structure maps for horizons 1 to 7.	2.70
2.46 Synthetic seismogram and velocity and density logs for drillhole 5.	2.71
2.47 Time-depth curves, interval and average velocity plots for drillhole 5.	2.72
2.48 Isochrons for the seismic stratigraphic sequences.	2.73
2.49 Two-dimensional sections along lines 1 to 5.	2.74

List of Figures cont.

	page
Fig. 2.50	Interpreted stacking velocities and calculated stacking velocities for seven horizons on line 6. 2.75
3.1	Earth model illustrating raypaths to two horizons. 3.4
3.2	The relationships along source coordinate s , geophone receiver coordinate g , offset coordinate $f = g-s$, and mid-point coordinate $g = (g+s)/2$ (after Claerbout, 1976). 3.4
3.3	Geometry of a wavefront approaching receivers (after Shah, 1973). 3.8
3.4	Earth model illustrating the shot replacement and receiver replacement length. 3.8
3.5	Model of a deep water canyon overlying a series of horizontal layers. 3.11
3.6	Canyon model gather plots together with wavefront shot and geophone statics for three surfaces at four locations. 3.12
3.7	Velocity profiles for the canyon model. 3.13
3.8	Seismic section together with its corresponding model for and irregular water-bottom layer overlying a series of sub-horizontal layers. 3.15
3.9	Velocity profiles for the irregular water-bottom model. 3.16
3.10	Irregular water-bottom model gathered plots together with wavefront static curves for three surfaces at four locations. 3.18
4.1	Schematic geological section showing actual raypaths and hypothetical raypaths for a vertical CRP. 4.2
4.2	Schematic geological section containing a high velocity inhomogeneity. 4.3
4.3	Plane dipping layer model. 4.5
4.4	Hypothetical curved reflector model. 4.8
4.5	Synthetic CDP gathers and their stacking velocity distribution. 4.9
4.6	Near, middle and far traces for the synthetic gathers generated at location A. 4.10
4.7	Near, middle and far traces for the synthetic gathers generated at location B. 4.11
4.8	The seismic problem. Given a time trace, can reflection events A, B and C be placed in their correct spatial position? 4.12
4.9	Three-dimensional plane dipping model. 4.16
4.10	Relationship between the perpendicular to a plane and the profile line to the dip of the interface (θ) and the directional angle. 4.17
4.11	Ratio of the stacking velocity to the overburden velocity for varying directional and dip angles. 4.19

List of Figures cont.

	page
Fig. 4.12 Raypath geometry for a diffracting point.	4.22
4.13 Irregular water bottom layer model and its velocity profile.	4.25
4.14 Selected traces for the gather at location A.	4.26
4.15 The relationship among source coordinate S , geophone receiver coordinate g , offset coordinate $l = g - s$, and midpoint coordinate $y = (g + s)/2$.	4.28
4.16 Geometry of a wavefront approaching receivers.	4.30
5.1 Destruction of the frequency content of the far trace wavelets due to NMO correction of a CDP gather.	5.4
5.2 Uncorrected CDP gather illustrating that amplitude variations are frequency as well as offset dependent.	5.5
5.3 Interference effects in frequency domain due to two reflectors having the same polarity and opposite polarity.	5.6
5.4 Sequence composed of a number of thin layers.	5.6
5.5 Typical synthetic seismogram exhibiting no interference effects (after Dunkin & Levin, 1973).	5.10
5.6 NMO corrected gather.	5.11
5.7 Raypath geometries for a thin layer.	5.13
5.8 Models of thinly laminated media and their corresponding layer parameters.	5.13
5.9 Reflection coefficients for direct normal incidence waves for three layered media (after Paige, 1973).	5.14
5.10 Amplitude reflectivities for models 1, 3, 4, 6, 7 and 8.	5.18
5.11 Phase reflectivities for models 1, 3, 4, 5, 6, 7 and 8.	5.19
5.12 Amplitude variations for both the total and direct waves for models 1, 4, 7 and 8.	5.21
5.13 Intrabed multiple raypaths.	5.21
5.14 Frequency-thickness amplitude reflectivity variations for various incident angles - model 1.	5.25
5.15 Frequency-thickness phase reflectivity variations for an incident angle of 1 degree - model 1.	5.27
5.16 Zero-phase and non-zero-phase wavelets (after Anstey, 1977).	5.30
5.17 Compressional velocity ranges for various geological rock types.	5.32
5.18 Amplitude and phase reflectivities for varying bed velocities.	5.33
5.19 Amplitude reflectivities for direct and total waves for varying bed velocity ratios.	5.35
5.20 Typical density ranges for various geological rock types.	5.35
5.21 Velocity-density relationships for common sedimentary rocks (after Gardner et al., 1974).	5.36

List of Figures cont.

	page
Fig. 4.15 Ricker wavelet with a dominant frequency of 30 hz and its frequency spectrum.	4.20
4.16 High velocity channel fill together with stacking and rms velocity curves and stacked sections for surface 8.	4.22
4.17 Selected gather locations for the high velocity channel fill model and their corresponding relative amplitudes for horizon 8.	4.23
5.1 Destruction of the frequency content of the far trace wavelets due to NMO correction of a CDP gather.	5.4
5.2 Uncorrected CDP gather illustrating that amplitude variations are frequency as well as offset dependent.	5.5
5.3 Interference effects in frequency domain due to two reflectors having the same polarity and opposite polarity.	5.6
5.4 Sequence composed of a number of thin layers.	5.6
5.5 Typical synthetic seismogram exhibiting no interference effects (after Dunkin & Levin, 1973).	5.10
5.6 NMO corrected gather.	5.11
5.7 Raypath geometries for a thin layer.	5.13
5.8 Models of thinly laminated media and their corresponding layer parameters.	5.13
5.9 Reflection coefficients for direct normal incidence waves for three layered media (after Paige, 1973).	5.14
5.10 Amplitude reflectivities for models 1, 3, 4, 6, 7 and 8.	5.18
5.11 Phase reflectivities for models 1, 3, 4, 5, 6, 7 and 8.	5.19
5.12 Amplitude variations for both the total and direct waves for models 1, 4, 7 and 8.	5.21
5.13 Intrabed multiple raypaths.	5.21
5.14 Frequency-thickness amplitude reflectivity variations for various incident angles - model 1.	5.25
5.15 Frequency-thickness phase reflectivity variations for an incident angle of 1 degree - model 1.	5.27
5.16 Zero-phase and non-zero-phase wavelets (after Anstey, 1977).	5.30
5.17 Compressional velocity ranges for various geological rock types.	5.32
5.18 Amplitude and phase reflectivities for varying bed velocities.	5.33
5.19 Amplitude reflectivities for direct and total waves for varying bed velocity ratios.	5.35
5.20 Typical density ranges for various geological rock types.	5.35
5.21 Velocity-density relationships for common sedimentary rocks (after Gardner et al., 1974).	5.36

List of Figures cont.

	page
Fig. 5.22 Amplitude reflectivities for varying density contrasts for models 1, 4, 7 and 8.	5.38
5.23 Phase reflectivities for varying density contrasts for models 1, 4, 7 and 8.	5.39
5.24 Amplitude variations for both the total and direct waves due to varying bed density ratios for models 1, 4, 7 and 8.	5.41
5.25 Amplitude variations for both the total and direct waves due to varying bed density ratios for models 1, 4, 7 and 8.	5.41
5.26 Amplitude and phase reflectivities for various thickness-bed velocity combinations using the model 1 type parameters.	5.42
5.27 Comparison of conventional and broadband seismic data.	5.44
5.28 Phase spectrum for model 1.	5.46
5.29 Synthetic seismograms for various phase shifted pulses.	5.47
5.30 Coherence measurements used in NMO velocity determination.	5.51
5.31 Cyclic buildup due to reflection from a single interface.	5.54
5.32 Onset time variations due to absorption (after Anstey, 1977).	5.54
5.33 Reflection process for two interfaces illustrating their interference effect.	5.55
5.34 Synthetic seismogram showing complex interference effects and consequent onset time delay problems.	5.56
5.35 Time pulses for various incident angles showing the difficulties in trace correlation due to amplitude and phase variations.	5.56
5.36 Intrabed and interbed multiples.	5.58
5.37 Log characteristics of a braided stream sequence.	5.59
5.38 Log characteristics of a beach-shoreface sequence.	5.59
5.39 Braided stream and beach-shoreface models.	5.60
5.40 Amplitude and phase spectra for the braided stream and shoreface models.	5.61
5.41 Acoustic properties of the brine, oil and gas models.	5.64
5.42 Amplitude reflectivities for PP waves due to brine, oil and gas saturated sands of varying thickness.	5.65
5.43 Phase reflectivities for PP waves due to brine, oil and gas saturated sands of varying thicknesses.	5.66
5.44 Comparison of wave trace shapes for the oil, gas and brine saturated sand models at different incident angles.	5.67
5.45 Comparison of wave trace shapes for oil and gas saturated sands of varying thicknesses.	5.69
5.46 Time traces for Ricker wavelets having dominant frequencies of 20, 40, 60, 80 and 100 hz and thicknesses of 15, 35 and 55 m.	5.70

List of Figures cont.

	page
Fig. 5.47 Frequency thickness amplitude and phase reflectivity variations for normally incident plane waves.	5.71
5.48 Time traces for Ricker wavelets having dominant frequencies of 20, 40, 60, 80 and 100 hz and velocity contrasts of 0.8, 1.0 and 1.2 (corresponds to bed velocities of 2536, 3170 and 3804 m/sec).	5.73
5.49 Normal incident amplitude and phase reflectivities for varying velocity contrasts.	5.74
5.50 Amplitude reflectivities for mode-converted PS waves due to brine, oil and gas saturated sands of varying thicknesses.	5.75
5.51 Phase reflectivities for mode-converted PS waves due to brine, oil and gas saturated sands of varying thicknesses.	5.76
5.52 Four density and sonic logs over a 120 m interval representing varying gross oil columns and their incident angle dependent amplitude reflectivity spectra.	5.78
5.53 Density and velocity models for 120m intervals and their acoustic impedance logs.	5.79
5.54 Normal incident reflectivities for models 1 to 4.	5.80
5.55 Fourier frequency components at 5 hz intervals for the model 1 shaped spectrum using the approximate minimum phase (A) and zero-phase (B) spectra.	5.82
5.56 Cepstra (a) and complex cepstra (b) for models 1 to 4.	5.84
5.57 Comparison of the complex cepstrum and impedance log for model 3.	5.85
5.58 Reflection and refraction of an incident plane compressional wave at a boundary.	5. 91
5.59 PS:PP amplitude ratios for models 1, 4, 7 and 8.	5. 93
5.60 Transmissivity for models 1, 4, 7 and 8.	5. 94
A2.1 Two-dimensional geological model with curved boundaries.	A2.2
A2.2 Flow diagram for computer program FERMAT.	A2.8
A2.3 Flow diagram for function routine SIMUL.	A2.9
A2.4 Three-dimensional geological model with curved boundaries.	A2.10
A3.1 Transition zone between two homogeneous half-spaces.	A3.2

ABSTRACT

Non-zero offset raypath tracing of primary P waves over a suite of geologically complex two-dimensional models illustrates that large errors occur in the conversion of stacking velocities to vertical velocities. Consequently (1) stacking velocities may not be consistent for seismic lines shot over the same area for different field configurations, (2) stacking velocities can vary greatly for a given spread length and different shot offsets, (3) rapid lateral changes in stacking velocities due to geological factors may disguise velocity information from horizons overlain by irregularities, (4) the customary assumption that stacking velocities approximate root mean square velocities is not valid in areas of geological complexity, (5) fictitious time shifts and consequent timing and velocity errors are introduced when conventional replacement statics are used, and (6) statics are time variant and surface inconsistent so that appropriate corrections should be made according to layer depth.

Simple mathematical expressions are derived for velocity and depth migration determination in both steeply dipping and complicated overburden environments.

Model studies show that the amplitude, frequency and wavelet characteristics of a reflector are dependent on both the reflector and overlying formations and may preclude definition of the reflecting surface. The use of CDP methods is detrimental in preserving these essential parameters. Interference due to thin layers results in reflectivities, transmissivities and mode conversion that depend on the layering properties, frequency and angle of the incident plane wave. Increased resolution of thin beds can be obtained by using the converted PS or SS waves.

ACKNOWLEDGEMENTS

The project was supervised by Dr. John E. Shirley and Dr. Roger J. G. Lewis to whom I am indebted for guidance and assistance. I would also like to thank John and his wife, Jill, for their friendship and hospitality. Discussions with Dr. W. D. Parkinson, Dr. D. E. Leaman and Mr. K. Spence have proved a source of inspiration. I am deeply indebted to Mr. E. Stanford, Geophysical Manager of Esso Australia Ltd., who released velocity data, seismic sections and well information over one of their prospects. West Australian Petroleum Pty. Ltd. are also thanked for providing seismic sections.

To Dr. R. G. Richardson for his discussions, inspiration and friendship, and to Ms. J. Pongratz for her thesis production assistance I express my deepest and most sincere thanks.

The study was financed by a University of Tasmania Post-graduate Research Award.

Finally, I would like to thank my family, without whose support this project would not have been possible.

Chapter 1
INTRODUCTION

	page
I. INTRODUCTION	1.1
II. AIMS	1.2

I. INTRODUCTION

This investigation of seismic wave propagation through geologically complex regions began at a time when CDP based wave equation migration was gaining popularity amongst exploration geophysicists and problems with migration in complex regions were becoming apparent. Migrated reflection events which appeared on a seismic section rarely corresponded to their true position in space. In areas of moderate dip (up to 10°) the seismic section approximated the structure with sufficient accuracy to be acceptable. For example the distortion of anticlinal limbs in simply-folded sections was acceptable because the important crestal positions are horizontal and were thus correctly positioned.

Coherent seismic events could be transformed to approximate the true section by manual migration techniques such as using raypath charts (Dobrin, 1976, p.240) or by collapsing diffraction curves (Hagedoorn, 1954). Rapid advancement in migration techniques began with the introduction of solutions to the wave equation to implement the migration process. Claerbout, in a series of papers (Claerbout, 1970, 1971; Claerbout & Johnson, 1971; Claerbout & Doherty, 1972), outlined a procedure for propagating a wave field using finite difference approximations to the wave equation to position the source of the reflected and diffracted seismic events. Later researchers have extended the limits and increased the speed of Claerbout's process (e.g. Alford *et al.*, 1974). Lowenthal *et al.* (1976) have described the limits and errors of the method.

Velocity information in an undrilled region is determined from stacking velocities or by inversion techniques (e.g. Seislog). Dix (1955) developed graphical techniques for determining interval and rms velocities. The process has since been automated by performing hyperbolic searches for the maximum semblance of coherent events for CDP gathered traces (Taner & Koehler, 1969). When used to convert the time section to a depth section these resulting stacking velocities yield depths which are too large. Al-Chalabi (1973) found that stacking velocities were accurate to better than 1 percent when the spread length/depth ratio did not exceed unity. He also noted (Al-Chalabi, 1974) that the difference between stacking velocities and rms velocities increased with increasing offset.

II. AIMS

Determination of a true depth picture and implementation of the wave equation migration procedure requires an accurate knowledge of the velocity variations within the earth. Thus this thesis was directed at the crucial velocity determination procedures and consideration of the implications of any deviations from accepted theory.

The aims of this thesis are:

- (i) to study the effect of non-horizontal anisotropic velocity layering on the conversion of stacking velocities to vertical velocities by ray tracing;
- (ii) to study the effect of field configuration induced errors on stacking velocities;

- (iii) to investigate alternatives to the conventional replacement statics techniques. These techniques introduce possible time shifts, timing and velocity errors for long spreads or in regions of irregular near surface geology. Residual statics may also be time variant and surface inconsistent;
- (iv) to use modelling techniques to determine the dependence of the amplitude, frequency and wavelet characteristics of an arrival on the section complexities and geological conditions at the reflector;
- (v) to study the nature of reflections from thin layers and develop possible techniques for the extraction of the characteristics of these layers from the time traces; and
- (vi) to derive mathematical expressions for calculating velocity distributions and for performing depth migration in complex geological situations.

Initially it was hoped to apply some of the techniques developed to conventional field data but approaches to the Australian companies or subsidiaries of Broken Hill Proprietary Co. Ltd., Delhi International Oil Corporation, Esso Australia Ltd., Shell Development Pty. Ltd., Utah Development Company, West Australian Petroleum Pty. Limited, and Woodside Petroleum Development Pty. Ltd. to obtain CDP gathered field tapes were unsuccessful. However field situations on sections supplied by Esso Australia Ltd. and West Australian Petroleum Pty. Limited were used to guide the formulation of models.

Chapter 2

ERRORS IN VELOCITY CONVERSION FOR SIMPLE GEOLOGICAL STRUCTURES

	page
I. INTRODUCTION	2.1
II. SPREAD DESIGN PHILOSOPHY	2.5
III. VELOCITY MEASUREMENTS AND SOME GEOLOGICAL CONSTRAINTS	2.7
IV. GEOLOGICAL MODELS AND VELOCITY DETERMINATIONS	2.8
1. Stratigraphic Wedge	2.14
2. Unconformity	2.16
3. Patch Reef	2.23
4. Buried Channels	2.30
(a) High velocity channel fill	2.30
(b) Low velocity channel fill	2.37
5. Syncline	2.40
6. Anticline	2.45
7. Prograding Delta	2.50
8. Shelf Margin	2.59
V. MIGRATION VELOCITY ESTIMATES	2.59
VI. STACKING VELOCITIES DETERMINED FROM THREE-DIMENSIONAL MODELS	2.60
VII. CONCLUSIONS	2.76

I. INTRODUCTION

Interpretation of seismic reflections and their conversion to depth remains a key problem in seismic exploration - especially in geologically complex areas. The difficulty of correctly interpreting geological structures on time sections was illustrated by May & Hron (1978). Existing velocity estimation techniques based on layered media assumptions (Schneider & Backus, 1968; Taner & Koehler, 1969) are downgraded as the reflectors become curved or discontinuous (Taner *et al.*, 1970; Miller, 1974).

The need for accurate velocity information and discrimination between primary and multiple reflections has prompted the use of the common depth point (CDP) method, often with large shot-geophone offsets. Large offsets result in improved accuracy in the normal moveout (NMO) corrections, due to the large moveout, with resultant improved velocity determination.

Levin (1971) showed that the NMO velocity obtained for a dipping interface overlain by a uniform medium, is always greater than the true medium velocity and is

$$v_{\text{NMO}} = \frac{\bar{v}}{\cos \phi} \quad \dots(1)$$

where ϕ is the dip of the reflector

\bar{v} is the true velocity.

For layered models with reflectors of arbitrary dip and curvature equation (1) often provides the only correction needed to obtain true velocities from NMO velocities, provided the seismic data allows computation of the dip.

In the presence of near-surface anomalies or where lateral velocity anomalies at depth have dimensions of the order of a CDP gather, large errors may occur in moveout based velocity estimates. As the spread is moved across such an anomaly differential traveltimes variations are introduced at varying offsets within the CDP set, producing residual moveout errors.

Stacking velocities derived from the NMO correction of CDP gathers need have no physical relationship to the true velocity distribution below the gather location. They are merely a variable defining the hyperbola which best fits the reflection alignment. For uniform horizontal layers and small offsets the stacking velocity approximates the rms velocity (Dix, 1955).

Shah & Levin (1973) examined the nature of the time-distance curves and velocities determined for models with sub-surface beds separated by plane-horizontal interfaces and noted that the NMO velocity increased monotonically as the spread length increased.

The arrival time (T_x) for various offsets (X) can be given by an infinite series of the form

$$T_x^2 = C_1 + C_2X^2 + C_3X^4 + C_4X^6 \quad \dots(2)$$

(Taner & Koehler, 1969)

where the coefficients C_1 , C_2 , C_3 , depend on layer thicknesses and interval velocities.

Brown (1969), using horizontally layered earth models, noted that even for long offsets the straight ray computation (two term truncation of the series expansion in equation 2) provided sufficient accuracy for calculating rms velocities for seismic exploration purposes. Most existing stacking

velocity techniques are based on this truncation. The stacking velocity equals the rms velocity only where the earth is homogeneous and the higher order terms in the series are zero. Shah & Levin (1973) and Al-Chalabi (1973, 1974) studied the effect on moveout velocities if further terms are included in the expansion. Shah & Levin generated horizontally layered sub-surfaces and noted that errors were less than 2 percent when a three-term expansion for T_x^2 was used.

After studying over 1000 model cases with randomly generated velocities, Al-Chalabi (1973) found that when the spread length/depth ratio did not exceed unity all results were accurate to better than 0.5 percent. When the spread length/depth ratio increased to two none of the two-term truncation results were accurate to better than 3 percent. Al-Chalabi also showed that in 97 percent of these cases, a three-term truncation was sufficient to improve the accuracy to better than 1 percent.

Al-Chalabi (1974) noted that the difference between the stacking velocity and rms velocity increased with increasing offset and decreased with increasing depth.

Levin (1979) noted that the P wave moveout velocity found from surface seismic data can deviate from the vertical P wave velocity to a value approaching the horizontal P wave velocity, the actual value depending on the elastic parameters and the spread length used for velocity determination. Levin studied wave propagation in transversely isotropic solids and concluded that:

- 1) as long as the amount of anisotropy is less than 15 percent T^2-X^2 plots are straight lines that yield moveout velocities lying between the velocities for primary (P) wave travel in the horizontal and vertical directions;
- 2) for small anisotropy and short spreads the P wave velocity found from a T^2-X^2 plot is the P wave velocity in the vertical direction; and
- 3) for large P wave anisotropy and greatly different values for Poisson's ratio, T^2-X^2 data do not define a straight line.

In complex areas migration techniques have been used to take into account the deviation in raypaths (Gardner *et al.*, 1974; Schneider, 1971; French, 1974). Velocity interpretation based on migrated data (Claerbout & Doherty, 1972; Sattlegger & Stiller, 1974; Schultz & Claerbout, 1978) has also helped reduce complications. In addition, Doherty & Claerbout (1976) showed that when data is migrated prior to velocity analysis, reflectors of arbitrary curvature can be treated as horizontal layers in velocity estimation procedures. They used finite difference approximations to the wave equation to derive a structure-independent velocity estimator for such models.

The difficulties of correctly interpreting geological structures on time sections (May & Hron, 1978) and the potential errors in existing velocity techniques for curved or discontinuous reflectors (Miller, 1974) illustrate that problems may occur in complex geological areas. Consequently an analysis has been made of the precise contribution of these features on fairly "normal" interpretations and the impact on interpretation reliability.

II. SPREAD DESIGN PHILOSOPHY

The following requirements need to be satisfied in designing the field layout for CDP data collection:

- 1) attenuate multiples,
- 2) improve the signal-to-noise ratio,
- 3) avoid strong coherent noise,
- 4) retain vital shallow reflections, and
- 5) obtain reliable velocity information.

The seismic system is limited by the dynamic range of the recording instruments and consequently the overall requirement is to record target reflections, however contaminated, within this range.

Figure 2.1 represents an idealised reflection profile. The straight line segments V_1 to V_4 correspond to refractions from surface layers. P_1 to P_4 are reflections from depth while M_1 is a multiple of the reflection P_2 .

Attenuation of multiple reflections is accomplished by the use of long spreads so that there is a large difference in residual moveout between the multiple and primary events (a on Figure 2.1). Strong coherent noise can be avoided by an appropriate choice of offset (b on Figure 2.1). This will indirectly improve the signal-to-noise ratio. The signal-to-noise ratio can also be increased by increasing the CDP fold. To record the shallow reflections it is imperative that the offset between the shot and nearest geophone be small (c in Figure 2.1). It must be noted that at early times stretching distortions due to NMO correction may be such that only a few traces may be stacked.

To obtain reliable velocity information long spreads are necessary, especially in high velocity regions. In such

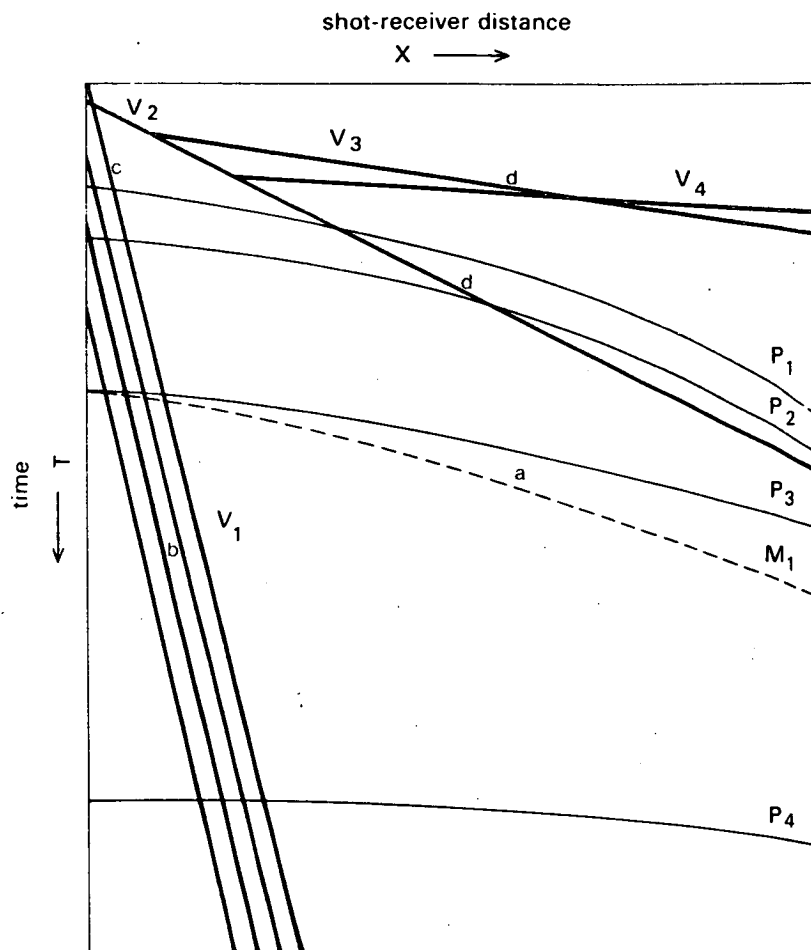


Fig. 2.1 Idealised view of a reflection profile. The straight line segments V_1 to V_4 represent refractions from surface layers, P_1 to P_4 are reflections from depth, while M_1 is a multiple of reflection P_2 .

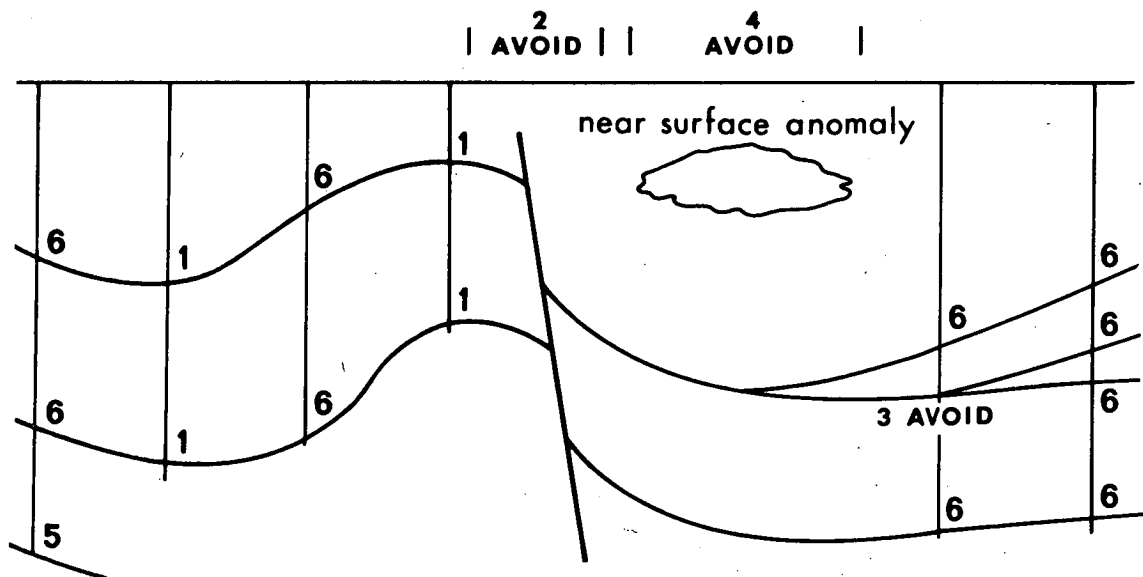


Fig. 2.2 Schematic geological section depicting areas for velocity analysis (regions 1, 5 and 6). Areas 2, 3 and 4 should be avoided.

areas and at long distances strong, straight line coherent noise occurs (d on Figure 2.1) so that the outer traces may have to be muted.

III. VELOCITY MEASUREMENTS AND SOME GEOLOGICAL CONSTRAINTS

If stacking velocities are to approximate rms velocities, very careful selection of the velocity gather location is required. Hence -

- 1) Analyses are positioned at the crests and troughs of folds where conditions approximate uniform horizontal layering (1 on Figure 2.2). Velocity determinations on the flanks (6 on Figure 2.2) yield velocity distributions which are unrealistically high (Levin, 1971);
- 2) Gather locations at levels where raypaths have passed through faulted or otherwise disturbed zones (area 2 on Figure 2.2) are to be avoided. Within this constraint an analysis each side of the fault should be made;
- 3) Analysis at levels where there is obvious interference, for example pinchouts (area 3 on Figure 2.2), is to be avoided;
- 4) Locations where raypaths pass through an obvious near-surface anomaly (area 4 on Figure 2.2) should also be avoided;
- 5) Velocity determinations over areas where fragmentary reflections are visible at depth (5 on Figure 2.2) may have to be used if they provide the only velocity information at depth; and
- 6) Other locations should be selected with discretion.

The determination of velocity is critically sensitive to overburden complications. The following points (Anstey, 1977), are generally considered to be true:

- a) a local velocity anomaly results in a static variation in stacking velocity for horizons below the anomaly,

- b) the largest variations of stacking velocity occur in zones below the ends of anomalies,
- c) the variations grow in magnitude and horizontal extent with depth below the anomaly,
- d) if dip develops at depth, without lateral change of interval velocity in any layer, then the "depth point" for the far traces of the gather move up dip, the NMO (ΔT) decreases accordingly and the stacking velocity increases from its "correct" value,
- e) if there is no dip, but a smooth lateral change of interval velocity in any layer, the far trace "depth point" on deeper layers moves in the direction of the lower velocity, ΔT decreases and the stacking velocity increases from its "correct" value,
- f) in the general case involving both dip and lateral velocity change, the final effect on stacking velocities is an amalgam of both effects, and
- g) whenever a more abrupt change of interval velocity occurs very large swings of stacking velocity occur.

IV. GEOLOGICAL MODELS AND VELOCITY DETERMINATIONS

The author has developed a two-dimensional ray tracing program (Appendix 1) that allows curved reflectors and lateral velocity variations. Using this program model studies have outlined variations in stacking velocity due to geological structure and spread configuration. Two potential geological causes for velocity variations are defined:

1. Errors in stacking velocity due to differences between true vertical time and zero offset time.

For the purposes of this thesis this is called *the migration problem*. Consider the case where the zero offset ray arrives earlier than the true vertical ray. All the non-zero offset rays will arrive earlier than those for the common reflection point (CRP) below the gather. Hence the stacking velocity as determined from a T^2-X^2 graph (taken as the square root of the reciprocal of the slope of a least squares straight line through points on the graph) will be greater than that for the case of a CRP below the gather (Figure 2.3).

2. Errors in stacking velocity due to static variations as a result of overburden complications.

Consider the case (B) shown in Figure 2.4. The outer traces pass through a lateral inhomogeneity, with higher velocity than the surrounding material. The time of arrival of the far traces is relatively early, so that the least squares best fit line differs from that for the homogeneous case [case (A)]. Thus in this situation the stacking velocity is larger than for the homogeneous case. This is called *the raypath distortion problem*.

Offset and spread length induced velocity variations result from migration and raypath distortion problems. Consider the case where raypath distortions produce earlier arrival times for the far traces than would be expected for a horizontal layered case [case (A) in Figure 2.5]. For the situation in which short and long spreads have the same shot-first receiver offset it is noted that the stacking velocity determined for the short spread is less than that for the long spread. Where the arrival times of the far traces

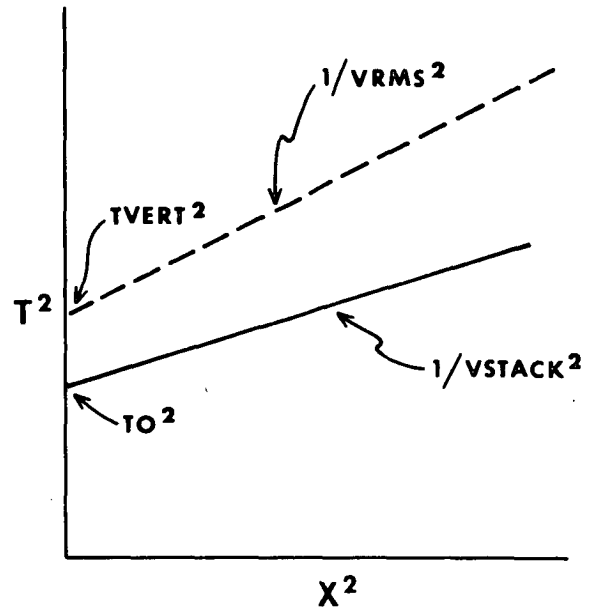
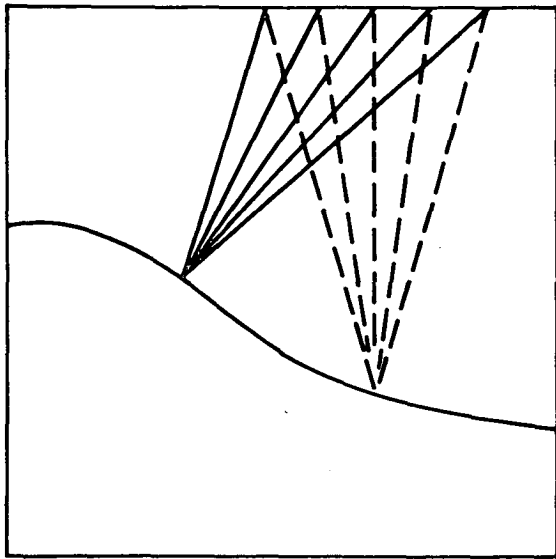


Fig. 2.3 Schematic geological section showing actual raypaths (solid lines) and hypothetical raypaths for a vertical CRP (dashed lines). Corresponding T^2 - X^2 plots show that the zero-offset time is less than the vertical traveltime while actual stacking velocities are greater than the root mean square velocities for that location. This is the migration problem.

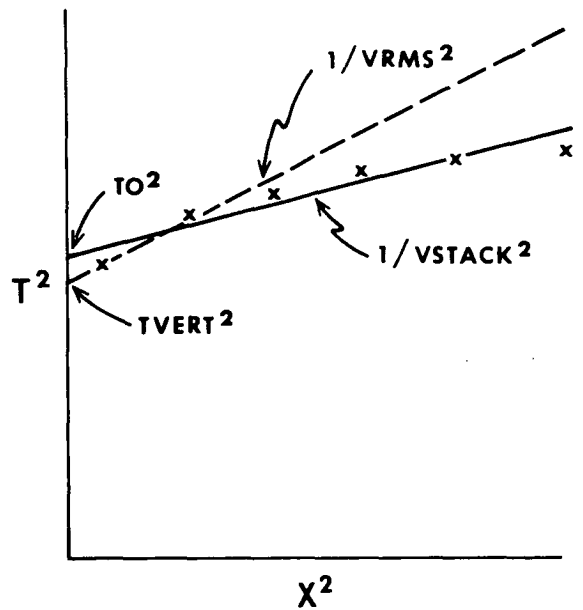
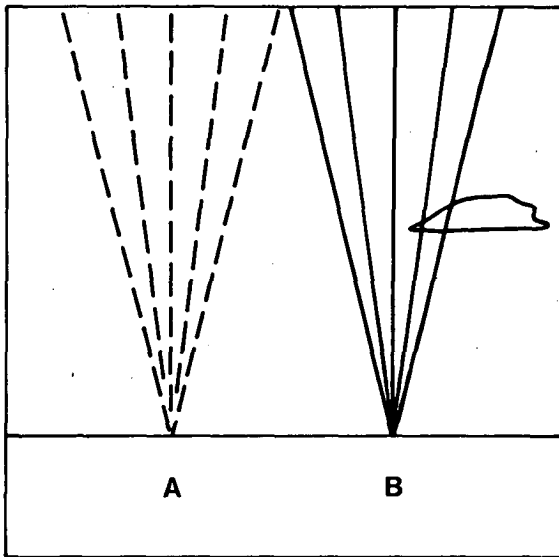


Fig. 2.4 Schematic geological section containing a high velocity inhomogeneity. Gathered plots and their corresponding T^2 - X^2 plots show that the stacking velocities and zero-offset time over the inhomogeneity (B) are greater than the corresponding homogeneous case (A). This is the raypath distortion problem.

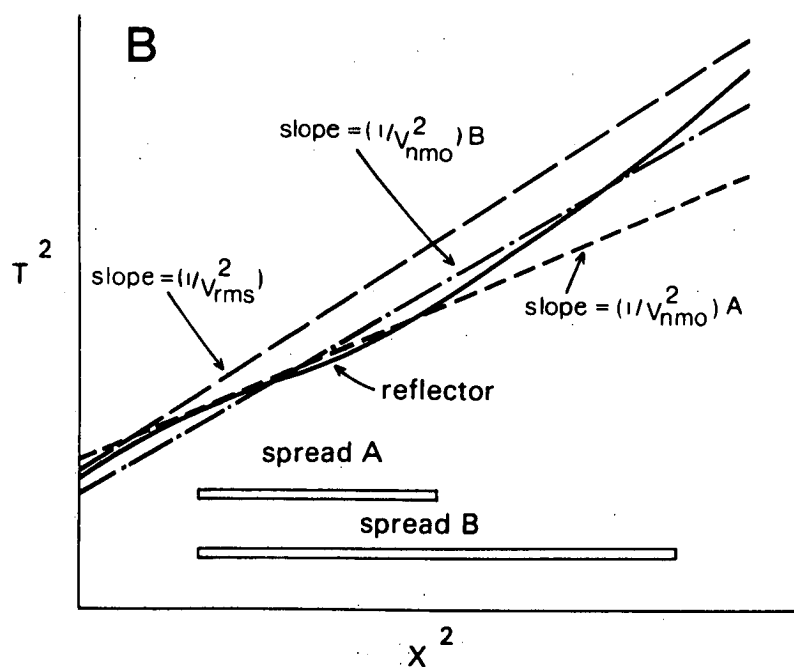
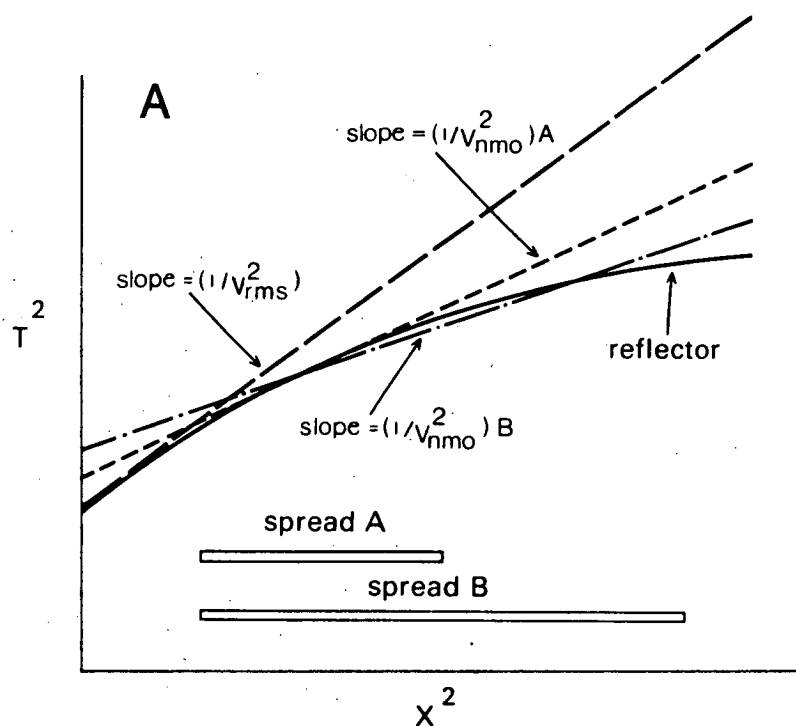


Fig. 2.5 Schematic T^2 - X^2 plots for a reflector whose arrival time due to migration or raypath distortion problems is earlier than for the homogeneous case (case A) or where the arrival time is later than expected (case B). Case A illustrates that the stacking velocity determined for the long spread B is greater than that for the short spread A. The converse is true for case B.

are later than expected [case (B) in Figure 2.5] the stacking velocity for the short spread will be greater than that for the longer spread.

Simplified models of typical geological situations are illustrated in this section. Each gather consists of 72 traces with a geophone separation of 46 m and a shot-first receiver offset of 46 m. The rays have been traced to within 1 m of the shot and receiver locations. The effect of geological structure on stacking velocities has been determined using a fixed gather consisting of 24 traces with a shot-first receiver offset of 92 m and a spread length of 2195 m. To emphasize the variations in stacking velocity an error factor approach has been used where the factor is defined as the difference between the stacking velocity derived from ray modelling and the average velocity at the gather location divided by the stacking velocity. The error factor is expressed as a percentage.

Two arbitrary spreads have been chosen to study the effect of spread length and offset on stacking velocity for the geological models.

The first consists of 24 traces, each having a geophone separation of 46 m. The shot-first receiver offset increases from 46 m to 1104 m in 46 m increments. The second spread consists of 48 traces (36 traces for some models) having the same receiver separation and offset variations as the first case. For convenience these are called short and long spreads. Stacking velocities for each of these spreads and for the range of offsets have been determined. In order to normalise the variation of stacking velocities with offset a variation factor is defined as the ratio of the difference between stacking velocity at a particular offset

derived from ray modelling and the rms velocity to the rms velocity expressed as a percentage. Changes in the variation factor with offset or spread size will thus highlight areas exhibiting offset induced velocity problems.

It is necessary to determine what causes the velocity variations. For uniform horizontal layers and small offsets the stacking velocity approximates the rms velocity. Thus an excellent gauge can be formed by calculating the difference between the traveltime of the ray traced to a geophone and the traveltime calculated from

$$T_x^2 = \frac{X^2}{V_{rms}^2} + T_{vert}^2 \quad \dots(3)$$

where X is the shot to geophone distance

V_{rms} is the rms velocity

T_{vert} is the vertical traveltime.

Migration type problems are manifest as time differences for zero offset ($X = 0$) while departures in time from this zero offset time difference result from raypath distortion. Diagrams based on these factors will be called time difference plots. A negative time difference on these plots indicates that the traced ray arrives earlier than the ray calculated using the rms velocity and vertical traveltime.

Migration problems are evident when large variation factors (and hence large deviations of the stacking velocities from rms velocities) occur for very small offsets, in particular for the small spread. Large changes in the variation function for small offsets at particular locations frequently reflect the differences between zero offset and true vertical times at these locations. Raypath distortions and migration problems are closely related and both problems

affect the accuracy of stacking velocity determination; especially when the geology is not composed of horizontal layers.

In the models, variation factors for both spreads have been plotted as a function of the shot-first receiver offset. Positive variation functions correspond to a stacking velocity, determined by ray tracing, greater than the rms velocity at the particular gather location. The value of the variation factor for a particular offset and spread shows the percentage error of the velocity determination for that location, while differences in the variation factors for the two spreads at the same offset highlight the effect of different spread lengths on velocity accuracy. An increasing variation-factor value with increasing offset implies a progressively increasing stacking velocity. The converse is also true.

1. STRATIGRAPHIC WEDGE

Figure 2.6 shows a sandstone wedge (P velocity 4270 m/sec) surrounded by a lower velocity shale (3350 m/sec) and the corresponding error factors for surfaces 5 and 6. Surface 5 can be divided into two distinct regions corresponding to the break in slope at the wedge apex. Applying equation (1) for surface 5 to the right of the wedge and assuming the region above the surface to be homogeneous so that surface 5 may be treated as a single dipping reflector, yields an apparent error factor of 0.15 percent. To the left of the wedge apex the apparent error factor is 1.19 percent. The error factor curve determined by ray tracing shows these trends, the jump near the wedge apex corresponding to the difference in these two levels. Because the horizons above this layer are dipping and the velocity is not vertically

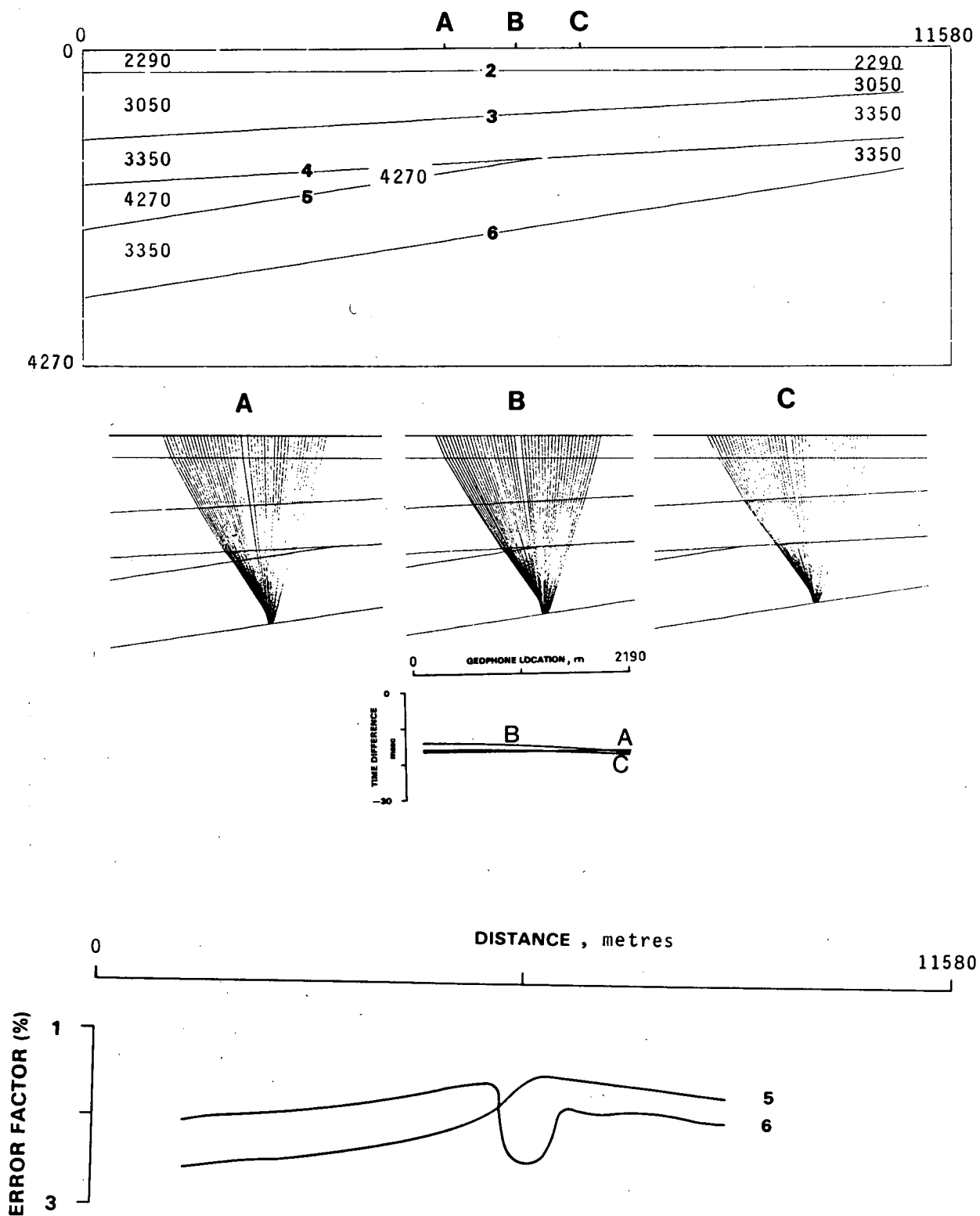


Fig. 2.6 Wedge model with corresponding error-factor plot. The gathers and associated time-difference plot are located about the apex of the wedge.

homogeneous there is an overall increase in the actual error factors.

Similarly, for surface 6, the apparent error factor is 1.20 percent. As there are no dip breaks along this surface the actual error factor curve tends to be level about a slightly higher base, with an anomalous zone around the wedge apex. CDP gathers and time difference plots for gathers at locations A (4880 m), B (5790 m) and C (6710 m) show an overall migration time lag of -15 milliseconds. Time difference plots for the gather at B show a time difference increasing with offset, corresponding to the far traces arriving earlier than would be expected in a horizontally layered situation. This is clearly seen for the gather plot where the far traces travel through a larger portion of the higher velocity wedge material and results in a somewhat larger stacking velocity and hence larger error factor. The gather at A, on the other hand, shows little time difference between near and far traces relative to the horizontal layered model. The gathered plot indicates that the time spent in the high velocity wedge by the far traces corresponds to that for the near traces. The gather at C is unaffected by the wedge.

2. UNCONFORMITY

Figure 2.7 shows a simple unconformity. Error-factor plots for surfaces 5, 6 and 7 indicate that severe velocity problems occur for surfaces below the termination of a layer along the unconformity. The effect becomes greater for deeper surfaces. Time-difference plots (Figure 2.8) for surface 6 illustrate the problem. Moving along the line from

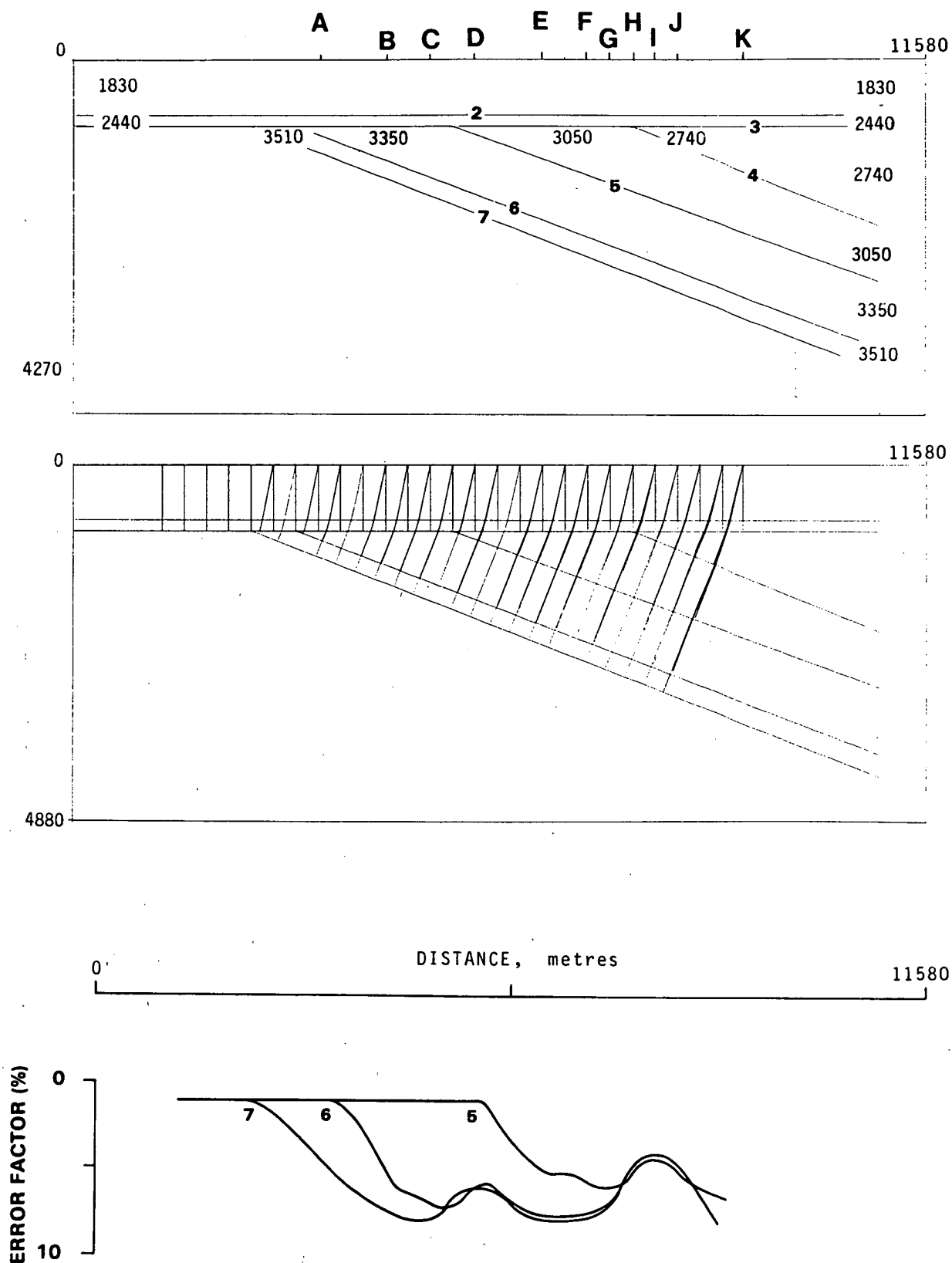


Fig. 2.7 Unconformity model with corresponding zero-offset raypaths and error-factor plot.

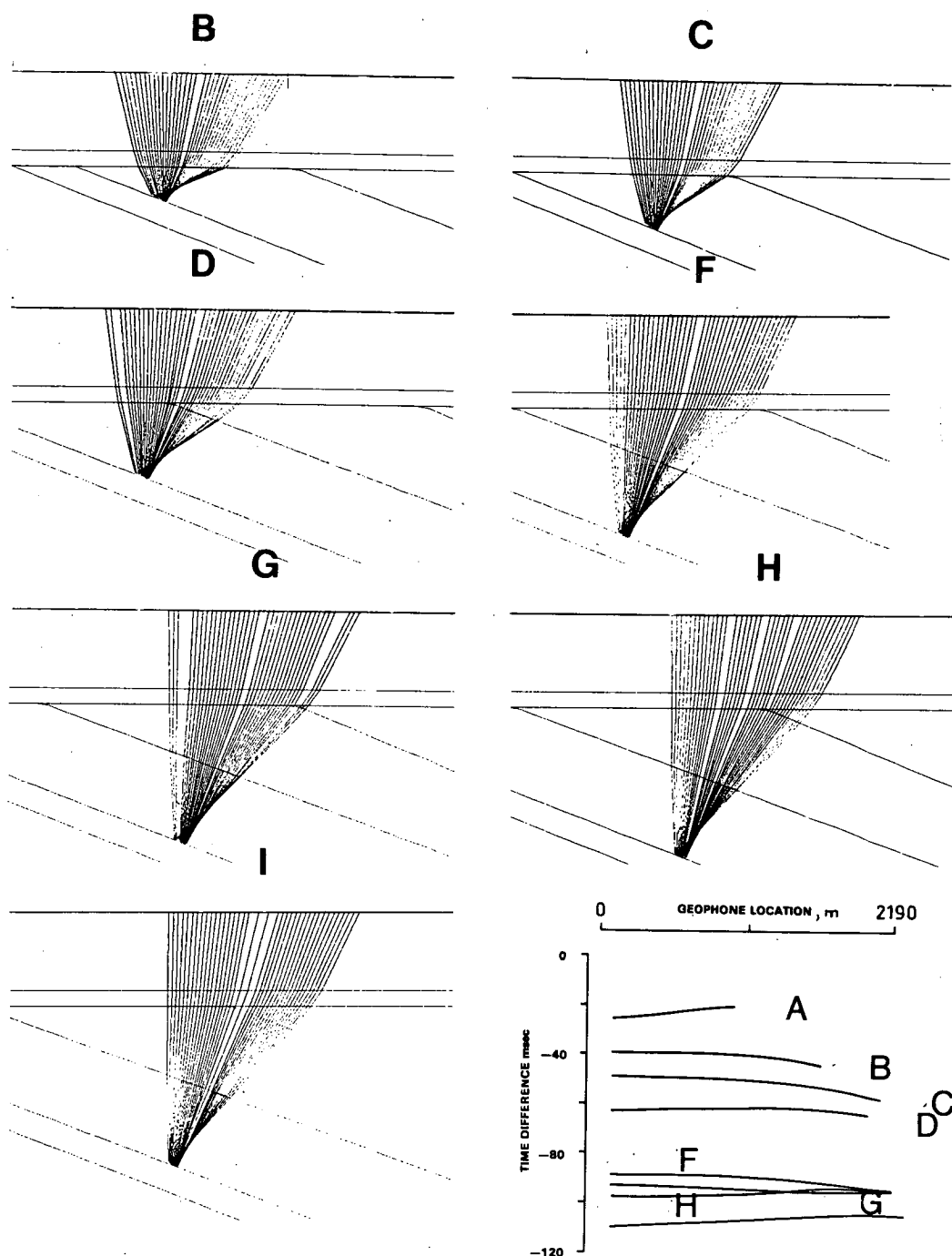


Fig. 2.8 Selected gather locations along the unconformity model for surface 6 and their corresponding time-difference plots.

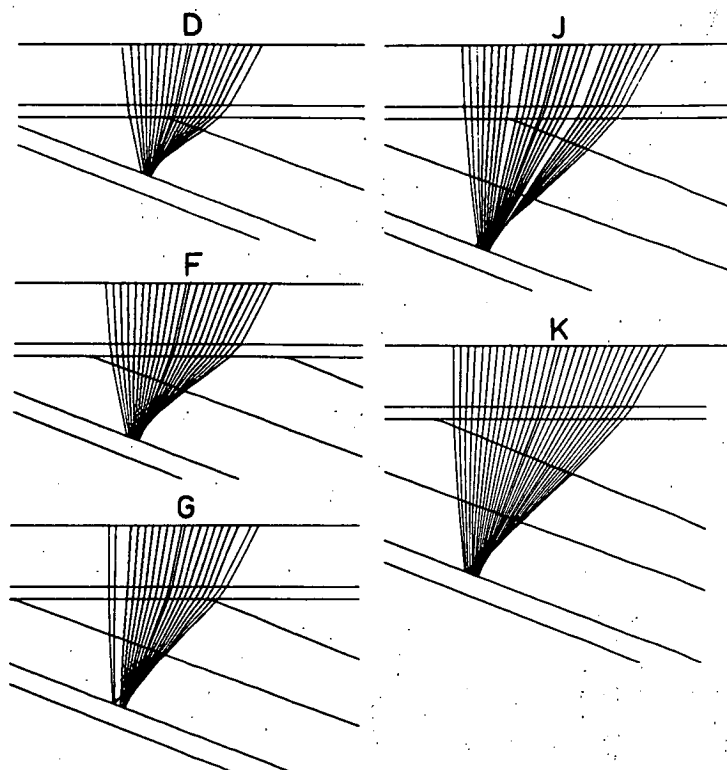
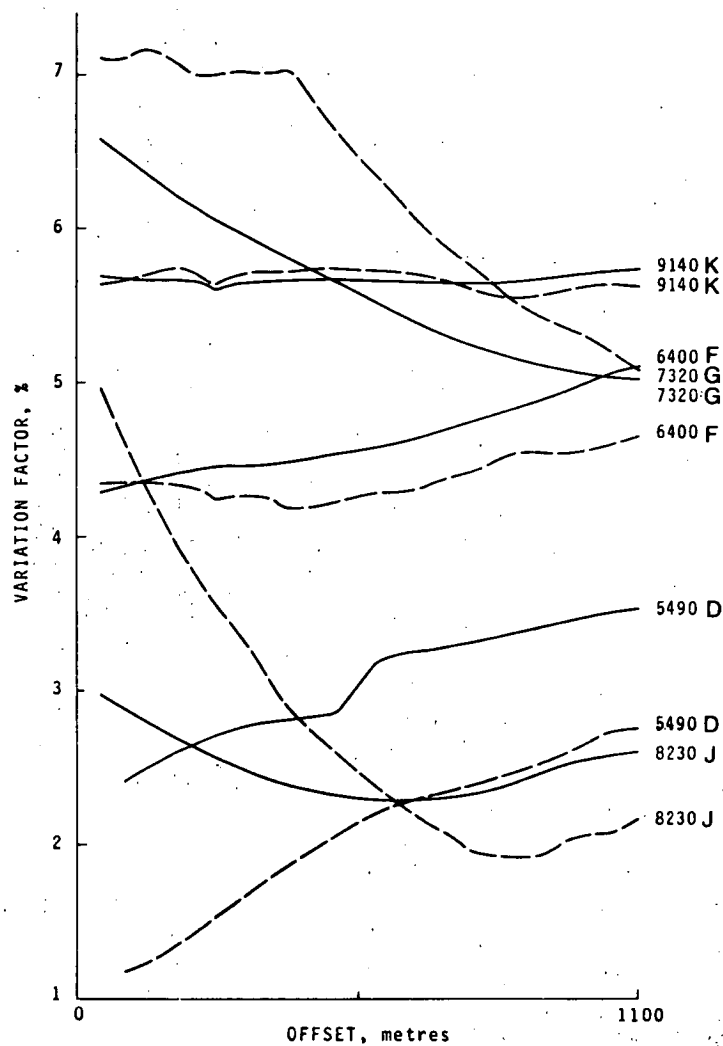


Fig. 2.9 Unconformity variation-factor and gather plots illustrating the percentage deviation of the stacking velocity from the rms velocity as a function of offset distance for a short spread (dashed lines) and a long spread (solid lines) at selected gather locations.

A (3350 m) to K (9140 m) the effect of time errors due to migration, as determined from zero-offset raypath plots, increases. They account for a 40 msec error in timing at B (4270 m) and a 110 msec error at I (7920 m). Superimposed on these errors are raypath distortions for the non-zero offset rays. The far traces for the gather at location A, for example, arrive later than would normally be expected with a consequent increase in stacking velocity and a smaller error factor for that gather. This is because the common reflector point has moved up dip, extending the path of the far traces in the material above the unconformity. The converse is true at C (4880 m) where the far traces arrive earlier than would normally be expected due to the larger path length for these traces in the high velocity dipping layer between surfaces 5 and 6. However, at location D (5490 m) the influence of the lower velocity layer between surfaces 4 and 5 retards the middle and far traces thereby decreasing the error factor. The effect of this low velocity wedge diminishes as the gather location is moved towards location F (7010 m). The far traces still arrive earlier than would normally be expected thereby retaining high error factors. Gathers at G (7320 m), H (7620 m) and I (7920 m) are affected by the additional low velocity wedge material between surfaces 3 and 4 which results in later arrival times as the traces cross over the wedge. Conversion to depth in such areas would be extremely difficult due to the large error in timing because of migration and the subsequent difficulty in conversion to true vertical velocities.

Field configuration induced errors are illustrated for selected gathers for surface 6 (Figure 2.9). For this model

the long spread has been reduced to 36 traces, partly corresponding to the far trace muting routinely applied in processing shallow reflections. The long spread has a shot-first receiver offset of 92 m and corresponds to the fixed spread configuration. Thus the variation factor values at each location should reflect the general trend of the error factor curve for the fixed spread. The difference in the numerical value results from the differing definitions of the two factors. Migration errors increase from locations A to K. This accounts for the progressively larger stacking velocities relative to the rms velocities and hence the increased positive variation factors with increasing horizontal distance. Inaccuracies in velocity conversion of up to 7 percent may result. Deviations from this generalisation are produced by the interplay of raypath distortion and migration problems.

The variation factors for the gather at D exhibit a 1 percent variation in velocity due to different spread lengths and the factors progressively increase with offset (1.5 percent change). This large variation is due mainly to the raypath distortions (Figure 2.9) associated with the wedge-shaped lower velocity layer between surfaces 4 and 5. The effect of this wedge diminishes for the gather at F and there is only a very slight increase of stacking velocities with offset distance. The 4.5 percent error derives mainly from migration errors. Due to the small raypath distortions variation factors for both long and short spreads are similar (Figure 2.9).

The gather for the short spread at G shows a 2 percent change in the variation factor corresponding to a progressively

decreasing stacking velocity. For small offsets the variation factor is constant but as the offset increases beyond 368 m it decreases due to the later arrival of the far traces through the low velocity wedge between surfaces 3 and 4. This delay, combined with the early arrival of the zero-offset time relative to the true vertical time, results in the 7 percent inaccuracy in velocity conversion. For the larger spread there is a more gradual decrease in the variation factor due to the smearing effect of the increased CDP fold.

The progressive decrease in stacking velocity with offset is pronounced for the gather at J where there is a 3 percent decrease in the variation factor due to offset changes for the short spread. This decrease results from the influence of the lower velocity wedge material between surfaces 3 and 4. The relatively early arrival of the far traces, where one leg of the path does not pass through this wedge material, accounts for the progressive increase in stacking velocity for large offsets. The 2 percent difference in velocities for small offsets indicates potential problems in the choice of spread length sizes over such geological situations.

The raypaths for the gather at K are not influenced by terminating wedges so that raypath distortions are minimal and errors result mainly from migration problems. Thus stacking velocities determined for both spreads and for all offsets are similar. However velocity conversion errors are still large (5.5 percent).

Depth determination errors depend on both timing and velocity accuracies. For this model there are migration induced errors of 35 to 135 msec between locations B and K

(Figure 2.10). These errors when translated into depth values using true vertical velocities result in underestimates of between 90 and 340 m. Similarly, depths are overestimated by 90 to 260 m when calculated using measured stacking velocities and true vertical times. The partial cancellation of the velocity and timing errors in this particular model reduces the error in depth estimates to a range of only 130 m. The maximum errors occur for gathers above the termination of dipping beds along the unconformity surface.

3. PATCH REEF

Figure 2.11 is an illustration of a high velocity reef model but it could also represent an inhomogeneity in the section. Zero-offset raypaths are also shown. The gathers at A (2440 m) and C (2740 m) receive rays from two locations on surface 5, resulting in two potential stacking velocities. Fixed spread error factors (Figure 2.11) for horizons below surface 5 show large oscillations and stacking velocities less than the true vertical velocities may be obtained.

Gathers (Figure 2.12) and time-difference plots (Figure 2.13) illustrate these variations. The gather at A (2440 m) represents a horizontally layered case. However at B (2590 m) the far traces of the gather travel through the outer portions of the reef and consequently arrive earlier than expected (Figure 2.13). By C more traces have transgressed this high velocity material. As a consequence of the outer rays passing through the reef, the common reflection point shifts significantly resulting in two distinct raypath "packets" and a large stacking velocity error.

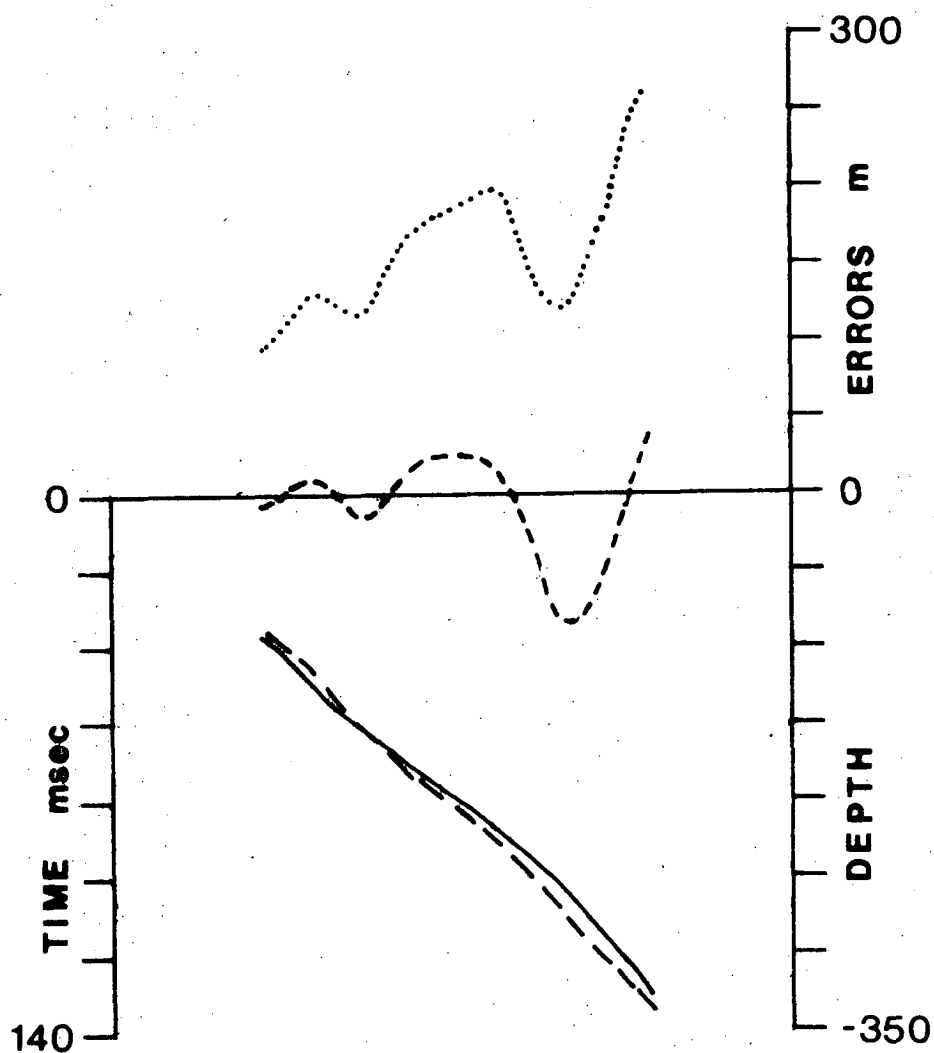
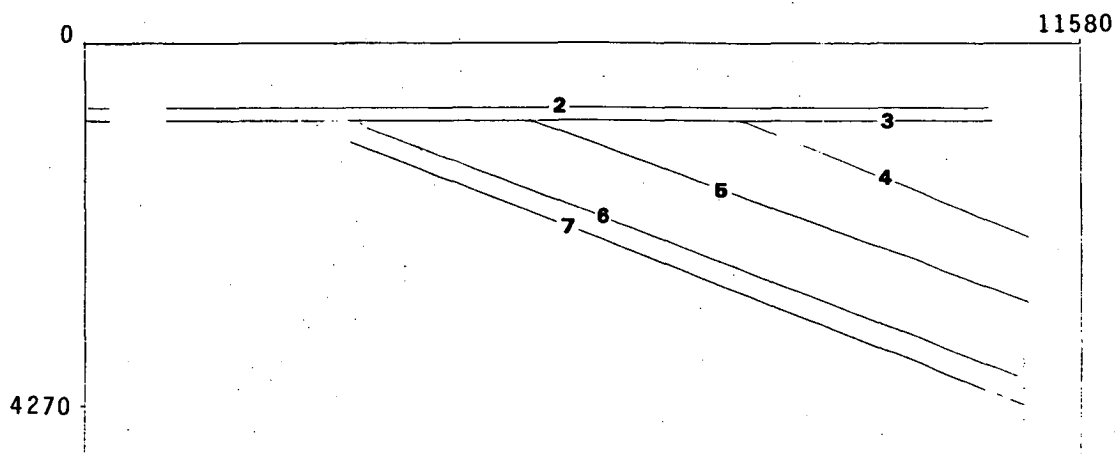


Fig. 2.10 Timing and depth errors for the unconformity model.

- migration time error
- - - migration depth error
- velocity induced depth error
- . - . - combined depth error using stacking velocities and zero-offset times.

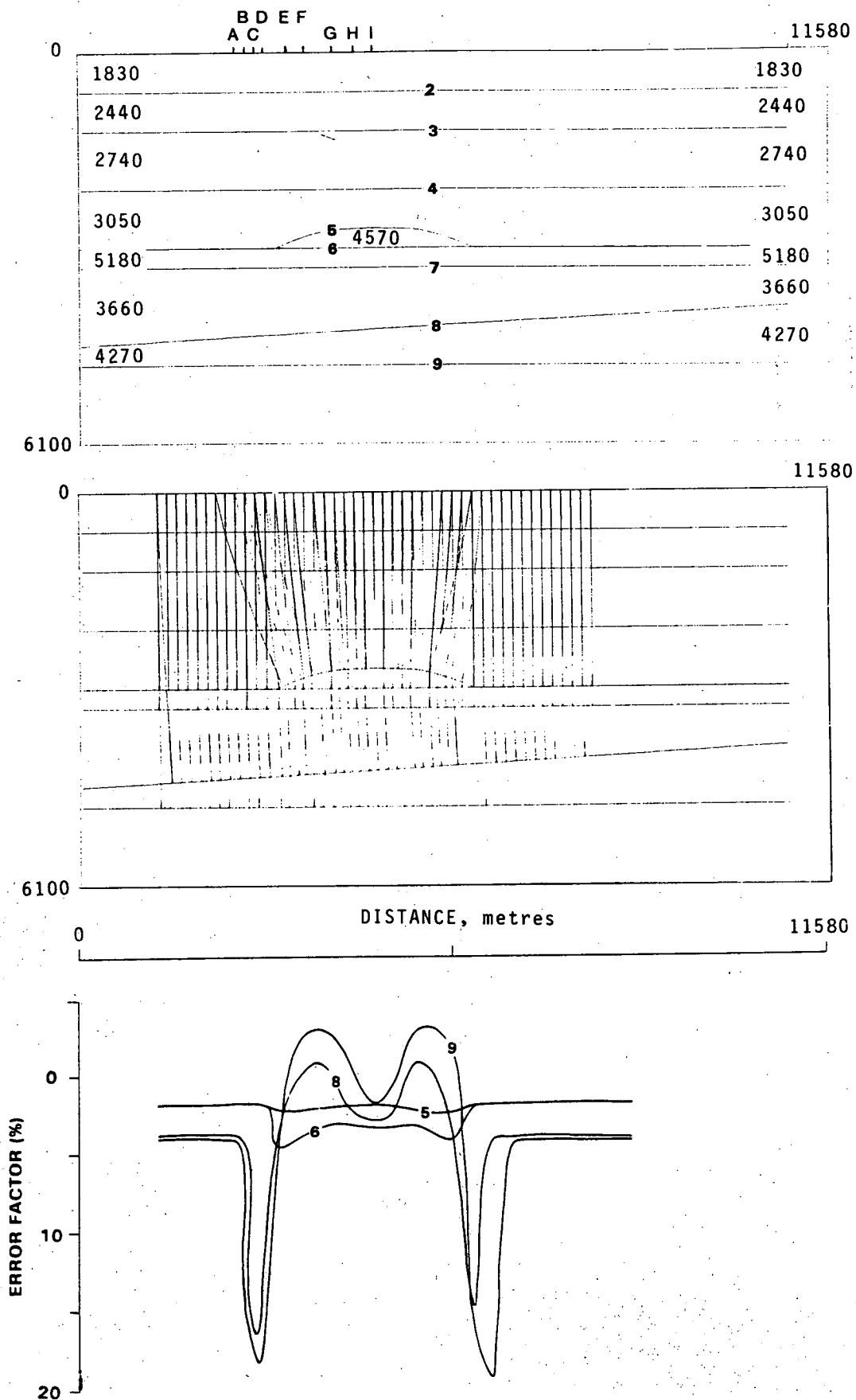


Fig. 2.11 High velocity patch reef model with corresponding zero-offset raypaths and error-factor plot.

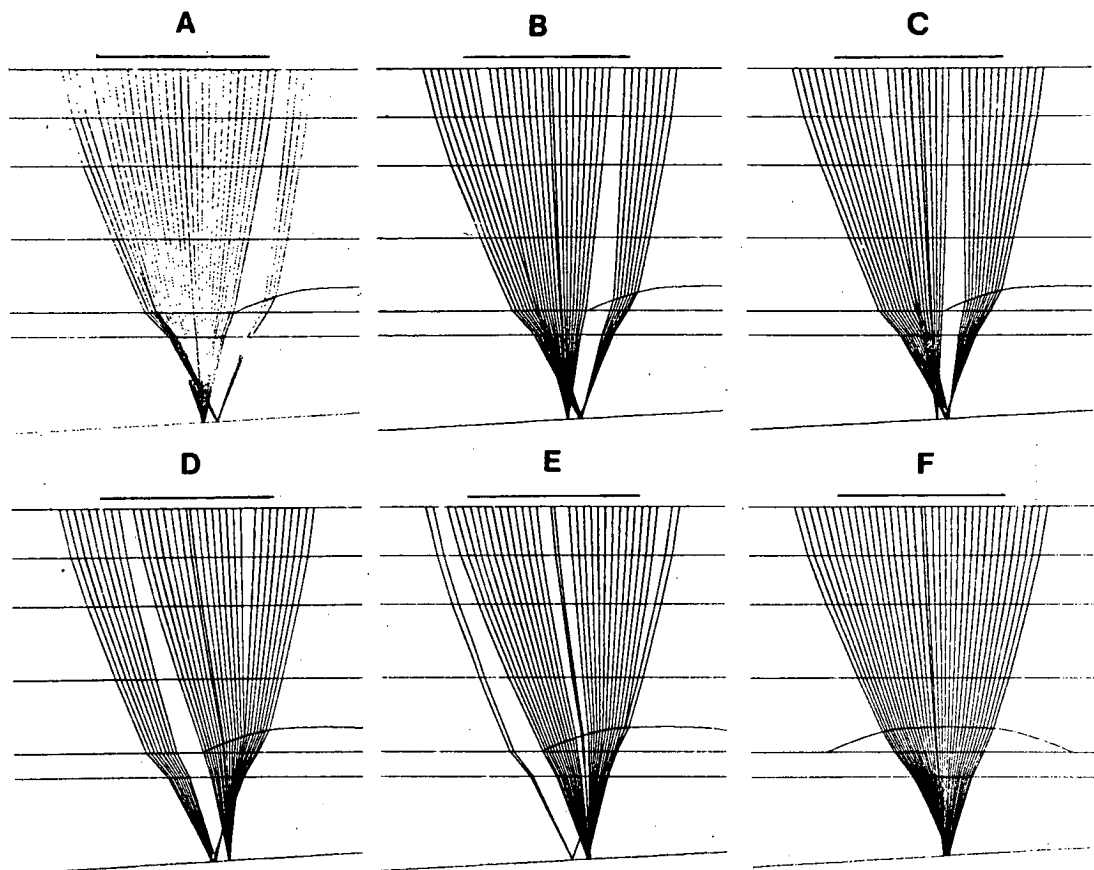


Fig. 2.12 Selected gather locations along the reef model for surface 8. Solid lines represent the fixed spread.

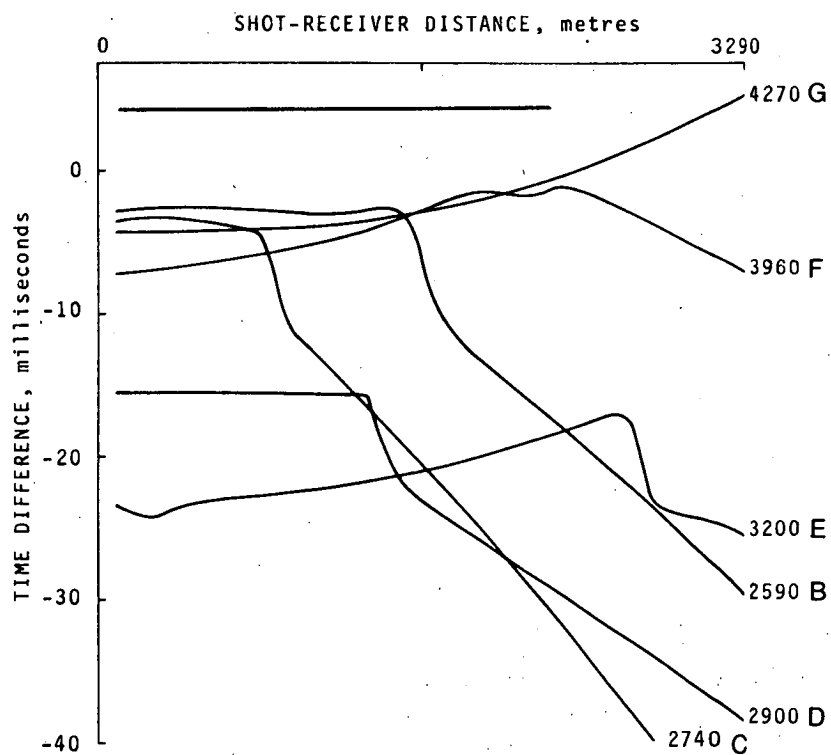


Fig. 2.13 Patch reef time-difference plots for surface 8. Solid line represents the fixed spread.

By E (3200 m) all traces pass through the reef, although there is a slight retardation of the far traces due to the shape of the reef edge. Raypath distortions tend to be minimal, but a time difference of -28 msec due to migration affects the stacking velocity slightly. At location F (3660 m) the far traces have been delayed considerably due to the sloping reef edge, decreasing the error factor. Migration errors are reduced to -13 msec. At location H (4270 m) migration errors are minimal and there is only a slight retardation of the far traces so that the error factor returns to the horizontally layered value.

Error factors exhibit larger variations as the depth increases (Figure 2.11) because small time fluctuations produced by inhomogeneities in the upper section have a more profound effect on the smaller NMO curves of the deep horizons.

Variation factor changes for surface 8 are illustrated in Figures 2.14 and 2.15.

For short spreads and small offsets the gather at B is still that of the horizontal case (Figure 2.12). However as the offset increases the far traces of this gather travel through the outer portions of the reef and consequently arrive earlier than expected. Thus stacking velocities increase significantly and variation factors of up to 15 percent result. Due to the very rapid increase in variation factors, velocity accuracies are strongly offset-dependent. The variation factor curve for the long spread (Figure 2.15) shows a 2 percent offset-dependent variation but there is a large (up to 10 percent) difference in velocities determined for the two spreads.

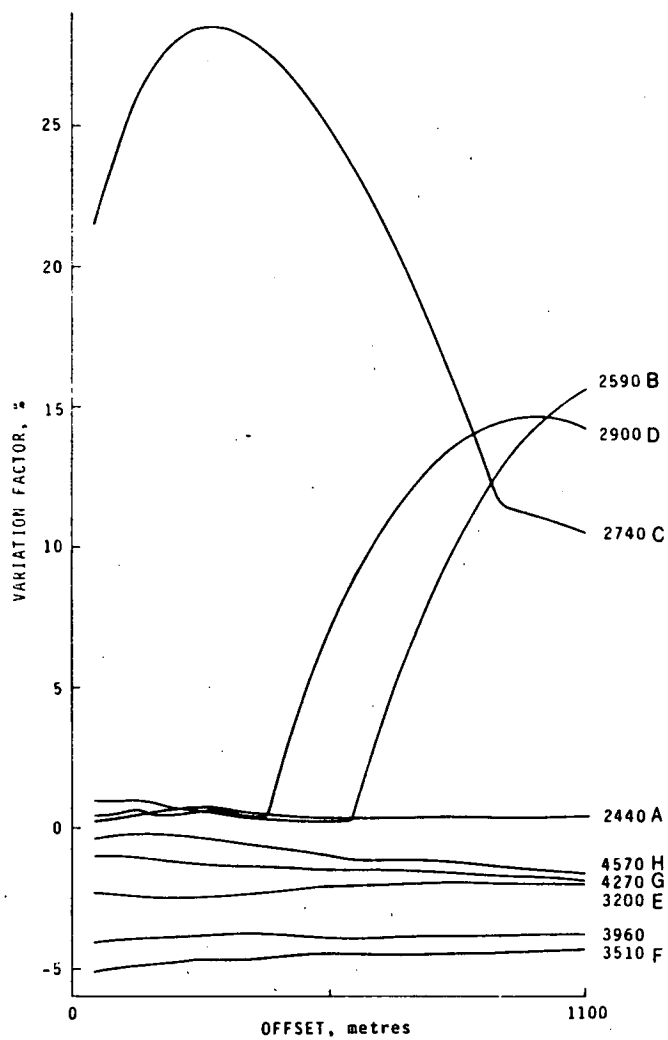


Fig. 2.14 Patch reef variation-factor plots illustrating the percentage deviation of the stacking velocity from the rms velocity as a function of offset distance for a short spread at selected gather locations.

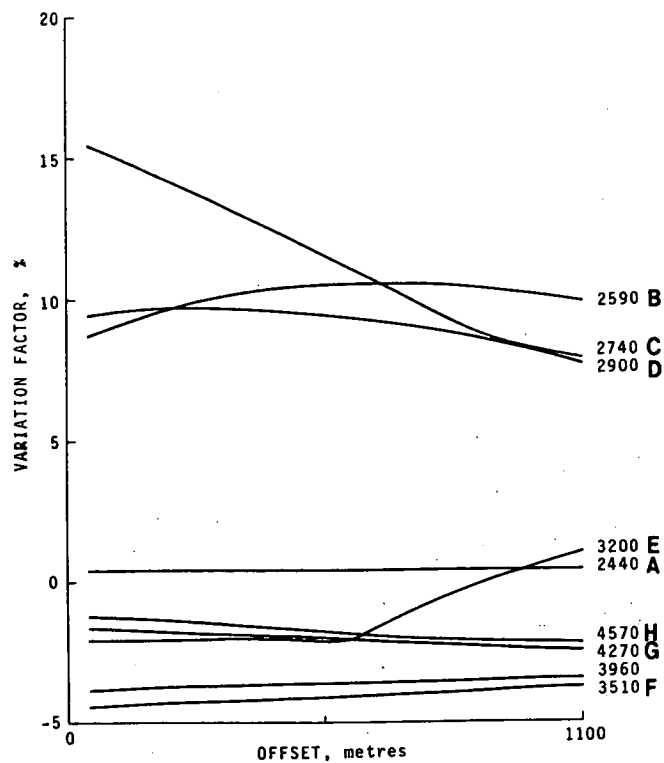


Fig. 2.15 Patch reef variation-factor plots illustrating the percentage deviation of the stacking velocity from the rms velocity as a function of offset distance for a long spread at selected gather locations.

At C more traces have transgressed the high velocity reef (Figure 2.12).

In considering the short spread it can be seen (Figure 2.14) that offset changes produce a 14 percent change in the variation factor. For small offsets there is an increase in the variation factor with offset but as the offset increases beyond 322 m the far traces consist of the earlier arriving reef traversing rays, so that stacking velocities decrease markedly as more of these reef "packet" rays are included. The variation factor is reduced when the traces consist exclusively of reef "packet" rays. The greater length of the long spread allows more reef rays to be included in the stacking process. Inaccuracies in velocity determination are still large, but these decrease with increased offset. The large difference in the variation factor for the same offsets illustrates the importance of choice of field geometry on the overall velocity accuracy.

By E migration errors are large (Figure 2.13). Because the time-difference plot becomes less negative with increasing shot-receiver distance, stacking velocities are smaller than rms velocities and variation factors are negative. The two spreads yield similar stacking velocities except for large offsets and for spread lengths where the effect of the much earlier arrival of the far traces becomes significant. Time difference plots for E and G also become less negative with increasing shot-receiver distance so that stacking velocities are less than rms velocities and the variation factors are negative. The migration problem for the gather at G is minimal. The small increase in variation factor for long offsets with the long spread is due to the sudden relatively

early arrival of the furthest traces at shot-receiver distances greater than 2380 m (Figure 2.13).

Variation factors for the gathers at H and I are also negative and decrease by approximately 1 percent with offset because the time-difference plots show progressively less negative values with increasing shot-receiver distance.

4. BURIED CHANNELS

(a) High velocity channel fill

Error factors for surface 5 (Figure 2.16) show a significant increase (10 percent) above the channel base. The asymmetry of the error-factor curves results from the different side dips of the channels. Time-difference plots (Figure 2.17) show that migration problems become significant on the channel sides [gathers at D (4270 m), G (5490 m) and H (6100 m)]. Raypaths for these gathers pass through a smaller section of the channel fill than would be expected if the CRP was vertically below the gather location, so stacking velocities are large and error factors increase across the channel. Inspection of the zero-offset raypath plot (Figure 2.16) for surface 5 with a gather at location E indicates three potential CRP's. Figure 2.18 illustrates gathers for the three CRP's for this location, while the time-difference plot shows that although there is little error in determining the vertical traveltimes, the far traces arrive much earlier (up to -20 msec across the gather) than the near traces and consequently have higher stacking velocities.

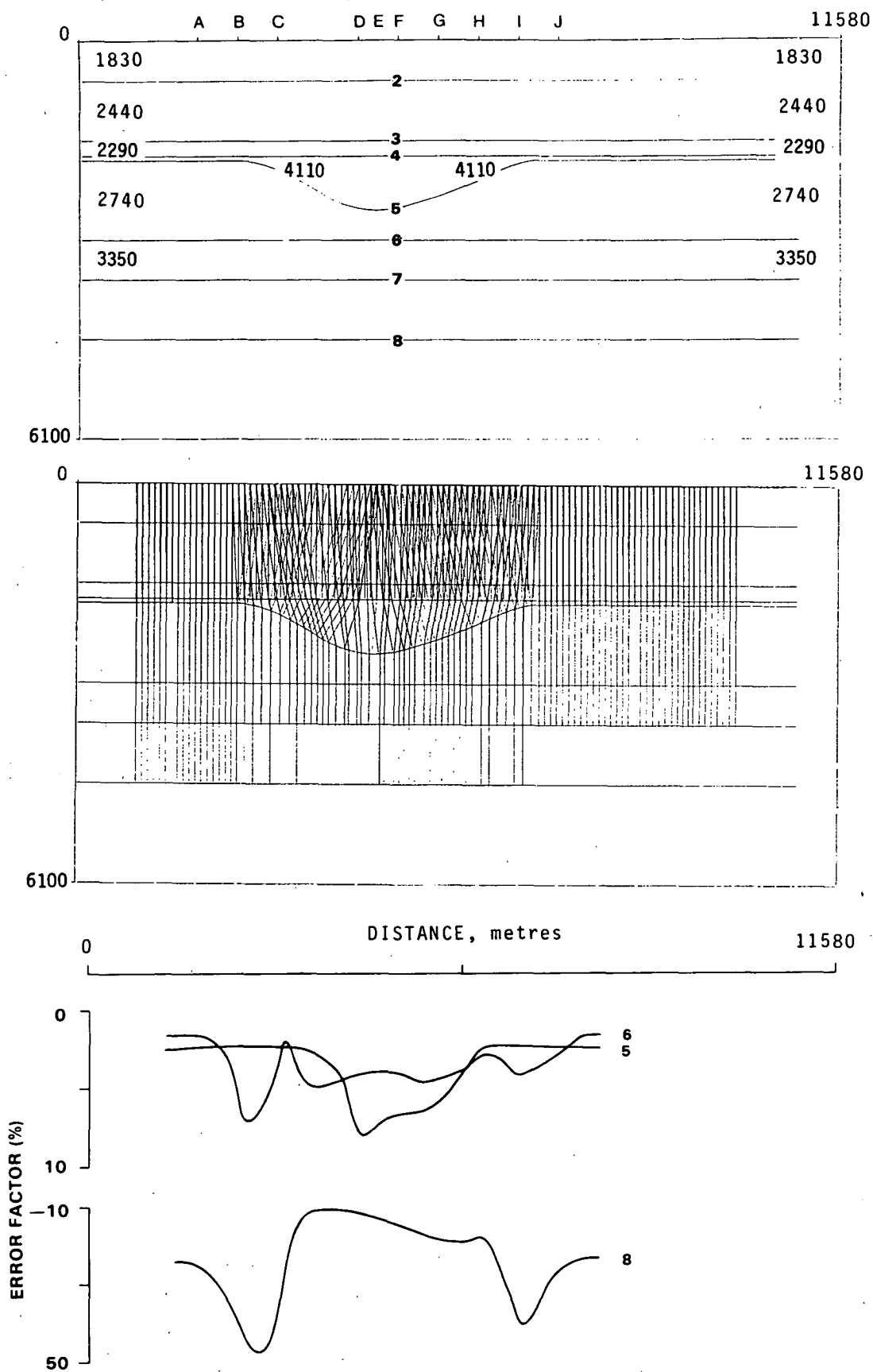


Fig. 2.16 High velocity fill channel model with corresponding zero-offset raypaths and error-factor plot.

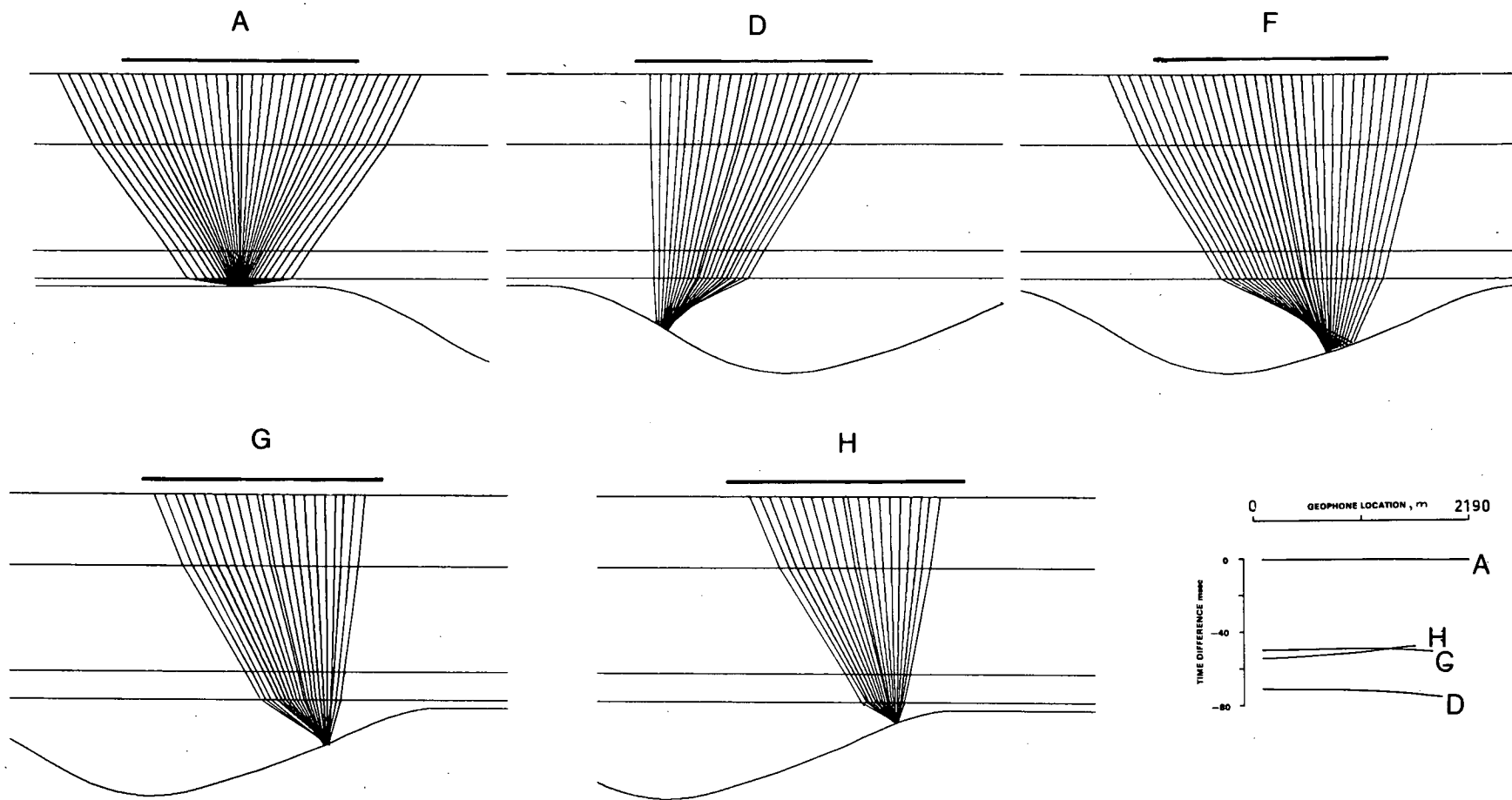


Fig. 2.17 Gathers and time-difference plots for selected locations along the surface of the high velocity fill channel model for surface 5. Solid lines represent the fixed spread.

Large oscillations of the error-factor curve for surface 8 are typical of the effect of raypath problems due to the channel fill. The gather at A (2440 m) (Figure 2.19) shows very little migration error, but the far traces arrive some 40 msec earlier than for the horizontal case (Figure 2.20). Shifts in the CRP are necessary to accommodate the distortions produced by the far traces passing through the channel edges. Error factors of the order of 45 percent result. At C (3050 m) migration problems for the zero-offset trace result in timing errors of -25 msec and the raypaths (Figure 2.19) occur as two distinct packets due to a large shift of the CRP. Again the far traces arrive sooner than expected, but the middle traces arrive later giving the gather a "banana bend" appearance.

The converse situation applies to the gather at location F (4880 m). The near traces, which travel through the base of the channel fill, arrive earlier than expected, while the far traces (Figure 2.19) which pass through the channel sides and hence a smaller section of the channel fill, arrive later than expected. Time differences of 20 msec occur between near and far traces (Figure 2.20) resulting in low stacking velocities and negative error factors. Migration errors are small for this gather.

Error factors for horizons below the channel exhibit larger variations as the depth increases because (a) shallower horizons have a smaller "cone" of rays passing through the channel, thereby minimizing discrepancies associated with ray-path differences of near and far traces, and (b) small fluctuations in arrival times produced by the channel fill

lead to more significant errors because of the small NMO associated with deeper horizons.

Large oscillations of the variation-factor curves (Figure 2.21) for surface 8 (Figure 2.16) depict the significant effect of the raypath problems due to the channel fill. The errors for the gather at A are relatively small but increase for large offsets and the long spread due to the earlier arrival of the far traces (Figures 2.19 and 2.20). Variation plots for the two spreads at location A show discrepancies of between 5 and 10 percent (Figure 2.21). The large inaccuracies result from the much earlier arrival of the traces as shot-receiver distance increases (Figure 2.20). Changes occur in variation factor of up to 14 percent for the short spread and 8 percent for the long spread due to increasing offset.

Time-difference plots and gather plots at D and F show that the near traces which travel near the base of the channel fill arrive earlier than expected while the far traces, because they pass through the channel sides and hence a smaller section of the channel fill, arrive later than expected. Consequently stacking velocities are lower than rms velocities and variation factors are negative. Migration errors tend to be minimal. There is little variation in stacking velocity with offset for both spreads.

Variation factors for gathers at I and J are similar to those on the opposite channel side, except for the effect of the slight steeper channel side. These gathers are characterised by large variation factors and large differences in velocity estimates with spread type and offset.

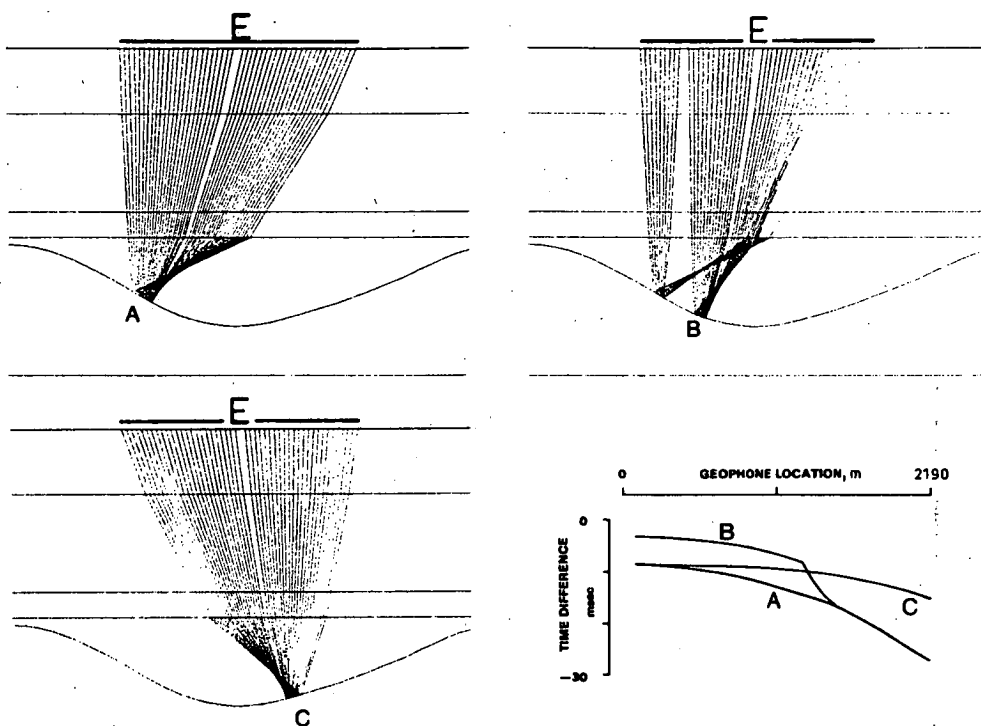


Fig. 2.18 Gathers at E (4570 m) for the high velocity fill channel base illustrating non-zero offset raypaths for CRP's at A, B and C. Time-difference plots are also given.

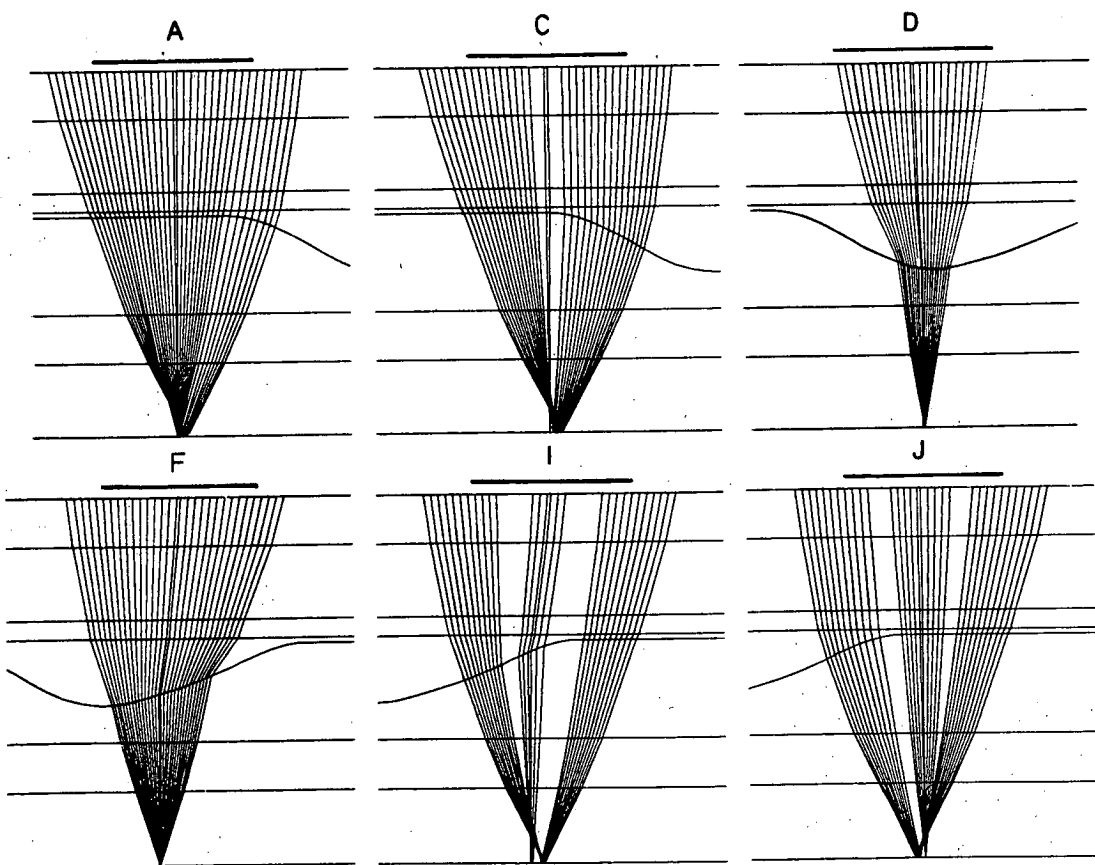


Fig. 2.19 Selected gather locations for the high velocity channel fill model along surface 8. Solid lines represent the fixed spread.

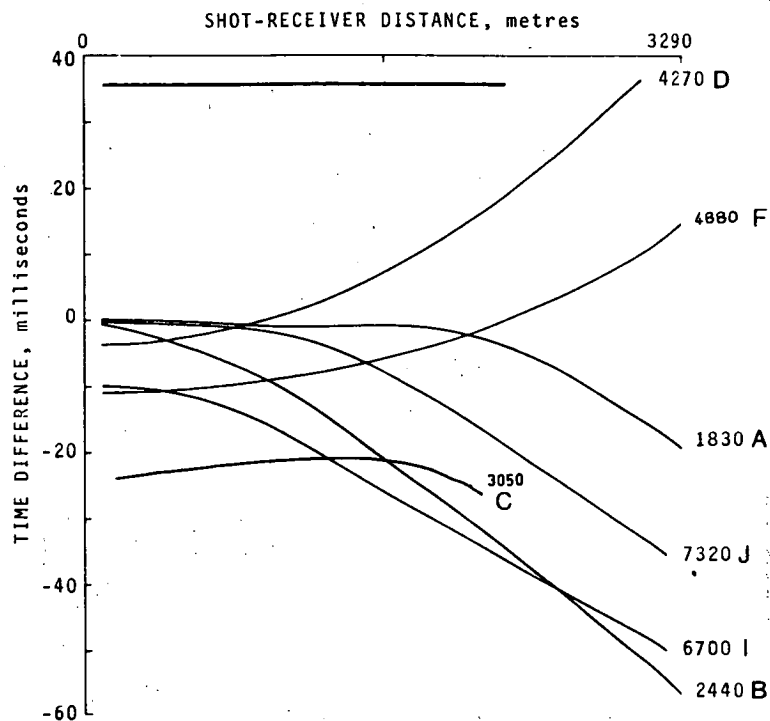


Fig. 2.20 High velocity fill channel time-difference plots for surface 8. Solid line represents the fixed spread.

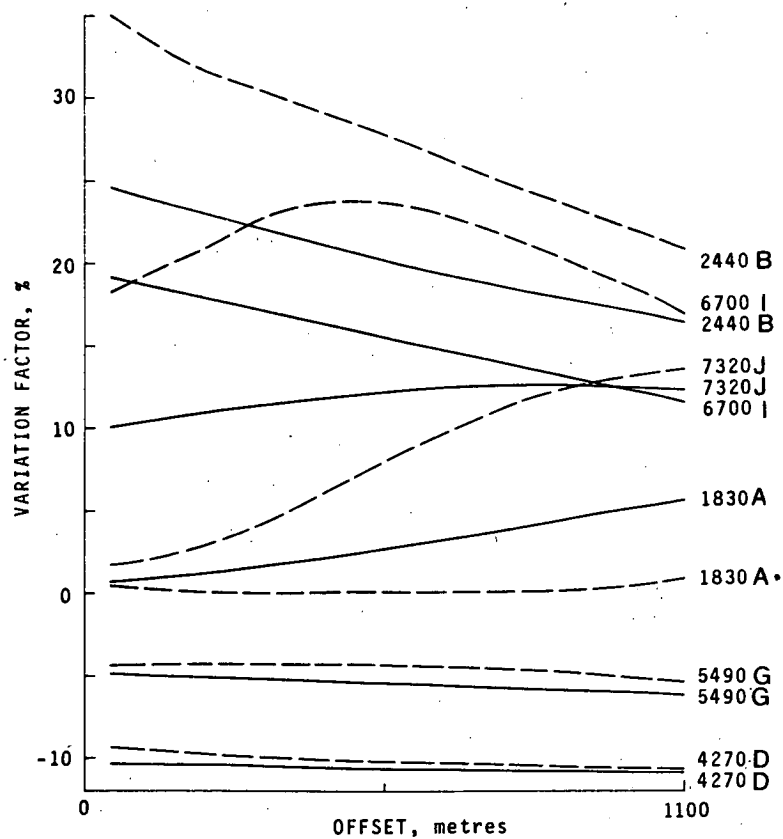


Fig. 2.21 High velocity fill channel variation-factor plots illustrating the percentage deviation of the stacking velocity from the rms velocity as a function of offset distance for a short spread (dashed lines) and a long spread (solid lines) at selected gather locations.

(b) Low velocity channel fill

The zero-offset raypath plots (Figure 2.22) for the buried low velocity channel fill show migration of the CRP for horizons below the channel to be opposite to that for the high velocity fill model.

Error factors for surface 5 indicate trends similar to the high velocity fill channel and show a 12 percent increase over the channel base.

For gathers above the channel sides sampling of a smaller portion of channel fill than would occur for a vertical CRP results in migration errors of up to 190 msec (Figure 2.23). Raypath plots for gathers (Figure 2.23) illustrate this trend. The gather at F (4880 m) demonstrates a curious effect. Here the far traces arrive much later than one would expect, thereby making the stacking velocity lower. Because the zero offset ray arrives 70 msec earlier than a vertical ray, velocity determination by least squares line fitting of a T^2-X^2 plot will result in an excessively large stacking velocity.

Error factor trends for horizons deeper than the channel base tend to mirror the curves for the high velocity channel fill case. Comparison of zero-offset raypaths (Figures 2.16 and 2.22) for deep horizons indicates that for a high velocity channel fill the rays are deviated towards the channel base whereas the converse is true for the low velocity fill model. Thus as a generalisation, the time of travel of the rays through the low velocity channel fill material will be much less than expected for a vertical CRP. The gather at C (3050 m) shows distinct "banana bending" (Figure 2.24). The near traces arrive later than expected after travelling through

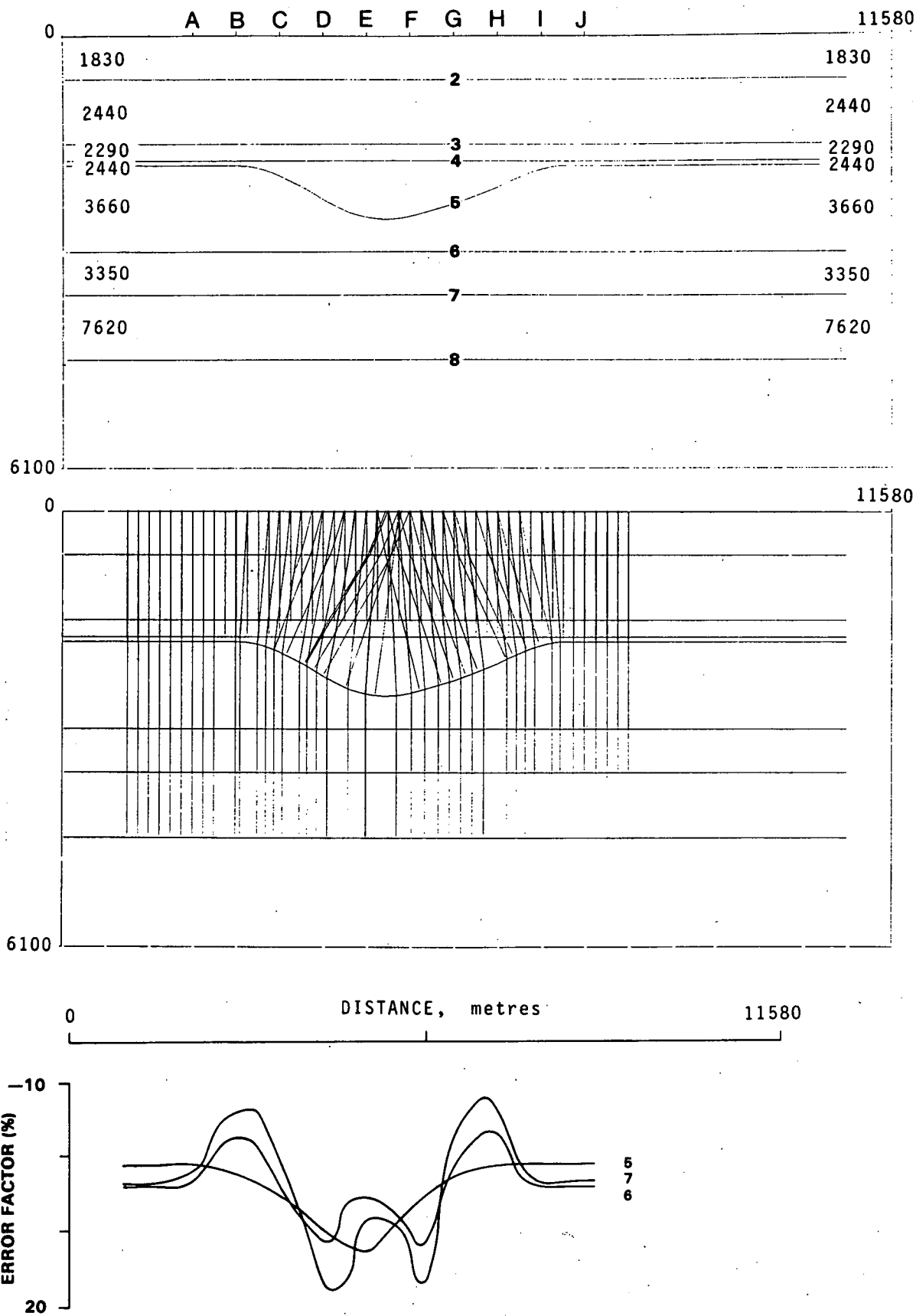


Fig. 2.22 Low velocity fill channel model with corresponding zero-offset raypaths and error-factor plot.

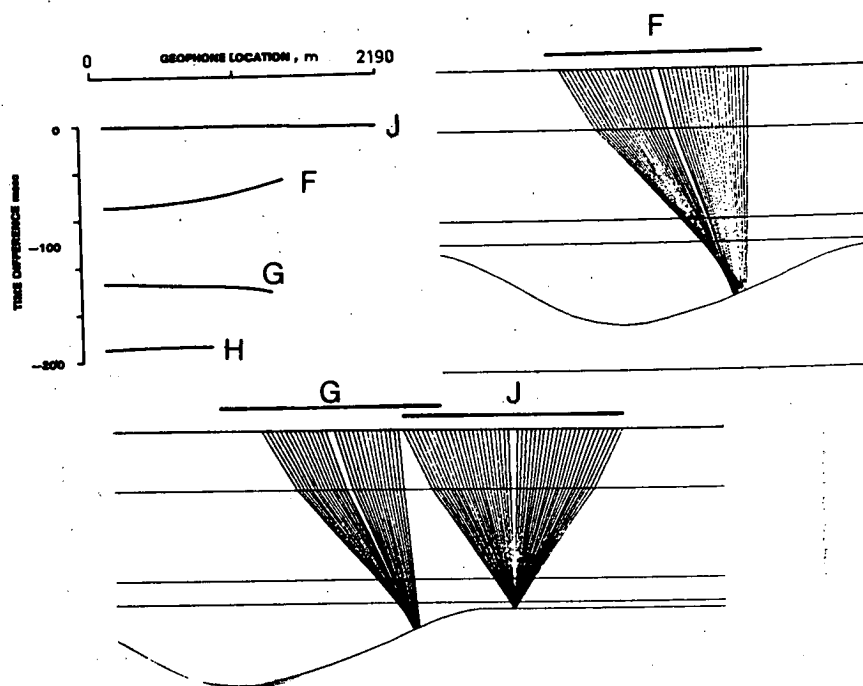


Fig. 2.23 Selected gathers and time-difference plots for surface 5 for the low velocity fill channel model. Solid lines represent the fixed spread.

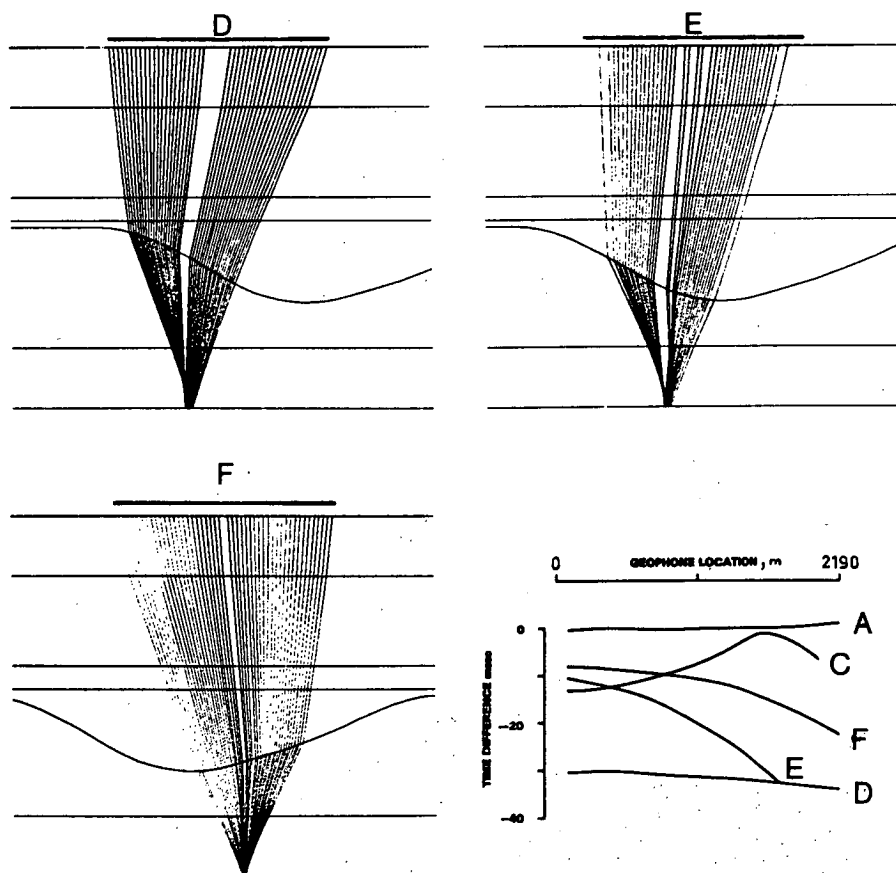


Fig. 2.24 Selected gathers and time-difference plots for surface 7 for the low velocity fill channel model. Solid lines represent the fixed spread.

more low velocity fill material, while the far traces show a relative time decrease from travelling through a larger proportion of the higher velocity underlying material. The main effect on the gather at D (3660 m) is a -30 msec difference between the zero offset and vertical traveltimes. Arrivals at the far traces are slightly earlier than for the horizontal case because the rays pass through more of the higher velocity underlying channel base material. The earlier arrival of the far traces is more pronounced at locations E (4270 m) and F (4880 m) where up to 20 msec difference occurs across the traces.

Offset and spread length variation factors for horizons deeper than the channel base tend to mirror (positive curves are now negative) the curves for the high velocity channel fill model. Variation-factor curves for surface 7 (Figure 2.25) are similar for both long and short spreads despite large overall inaccuracies in velocity determination over the channel.

These examples indicate that accurate velocity determination of horizons at depth in areas of buried channels is far from easy and probably rarely achieved in normal processing. When such models are contrasted with typical "simple" geological sections it may be readily appreciated that substantial errors are inevitable.

5. SYNCLINE

The error-factor curves for a model of a simple syncline (Figure 2.26) indicate an increase in true velocity determination errors with increasing depth and with decreasing distance from the centre of the syncline. These curves are

similar (in many respects) to those from the channel base in the previous channel-fill model. Zero-offset time plots illustrate the defocussing effect of synclines and the associated migration problems.

Error factors for surface 6 show large (5 percent) variations across the structure. Even the gather at A (1220 m), which is over an essentially horizontal section, shows variations due to the overburden geology (Figure 2.27). A slight but distinctive "banana bend" occurs; traces with an offset of 1550 m or less show an increase in traveltimes associated with a slightly slower return path on the synclinal base side. Beyond this distance a slight shift of CRP causes a relative decrease in traveltimes. As gathers move towards B (1980 m) the far traces arrive much earlier than in the horizontal case, resulting in higher stacking velocities and larger error factors. By D (3660 m) migration errors are large (-65 msec) and the far traces arrive earlier than would normally be expected for the horizontal case, further increasing the error factor. At F (4570 m) migration errors are reduced, but the far traces still arrive much earlier than expected and once again the error factors are large. The time-difference plots (Figure 2.27) show that migration errors are greatest on the slope of the syncline. The relatively early arrival of the far traces becomes more pronounced as the syncline is crossed, thereby increasing error factors.

The variation-factor plots (Figure 2.28) show a 12 percent range across the syncline. These plots indicate that the stacking velocity does not vary greatly with changing offset

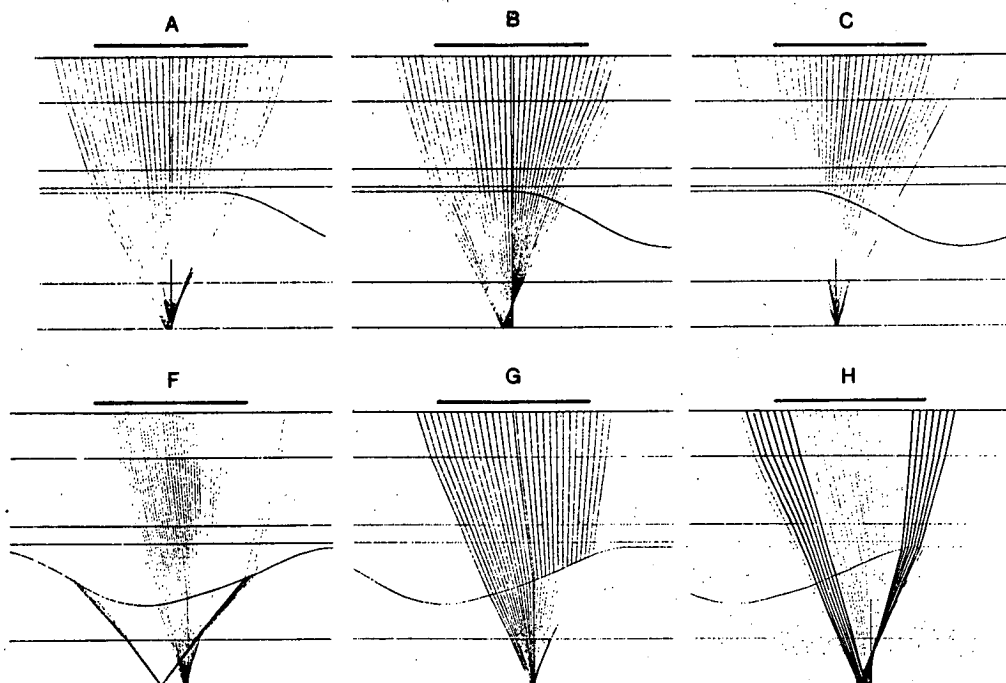
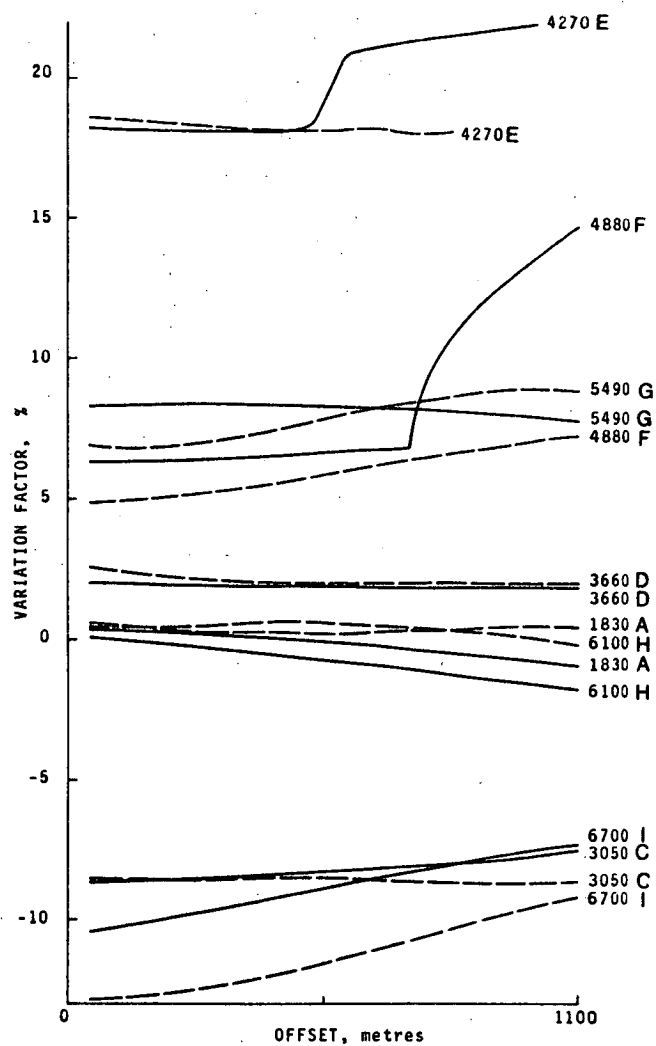


Fig. 2.25 Low velocity fill channel variation-factor and gather plots for a short spread (dashed lines) and a long spread (solid lines) at selected gather locations for surface 7.

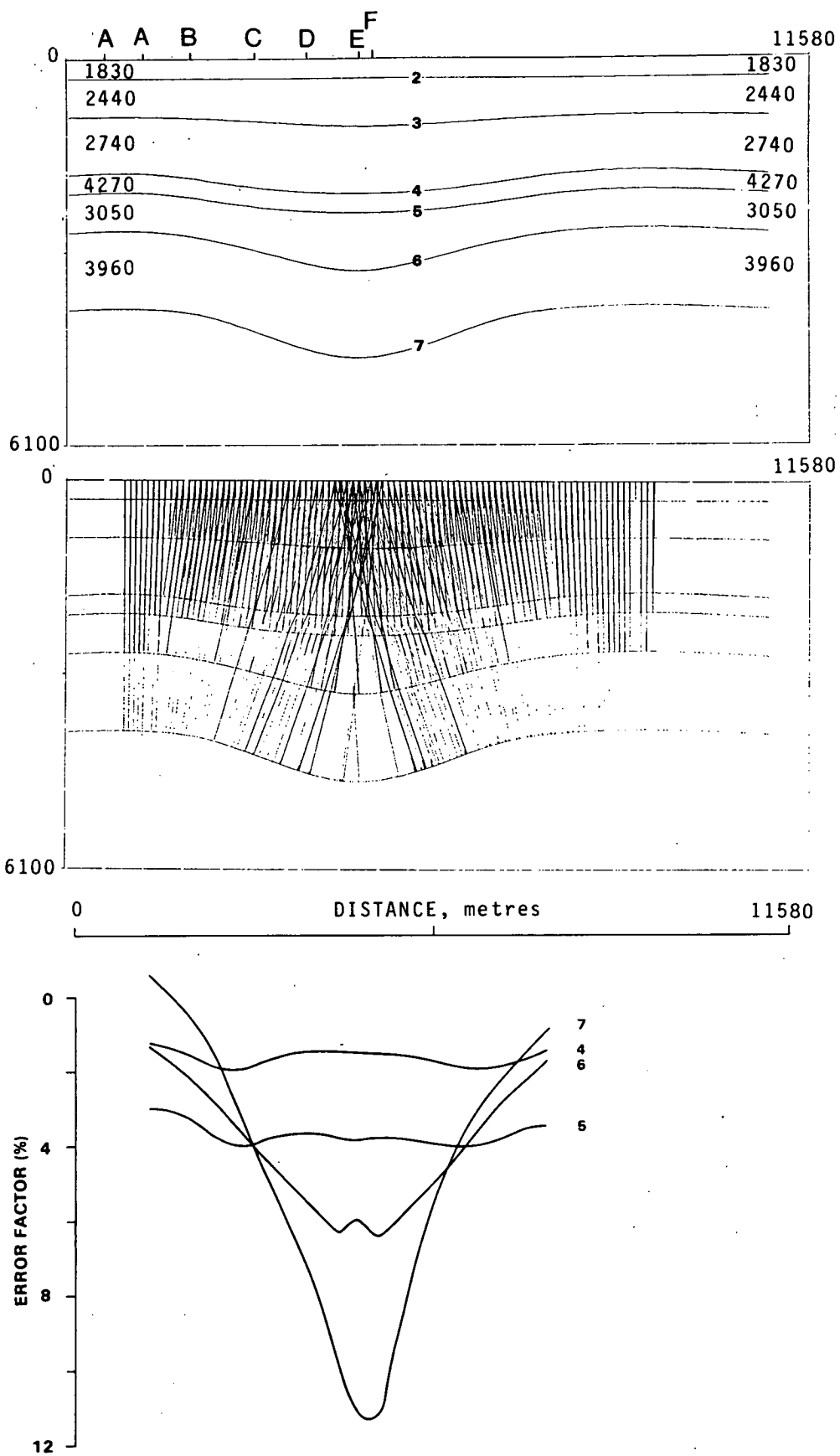


Fig. 2.26 Synclinal model with corresponding zero-offset raypaths and error-factor plot.

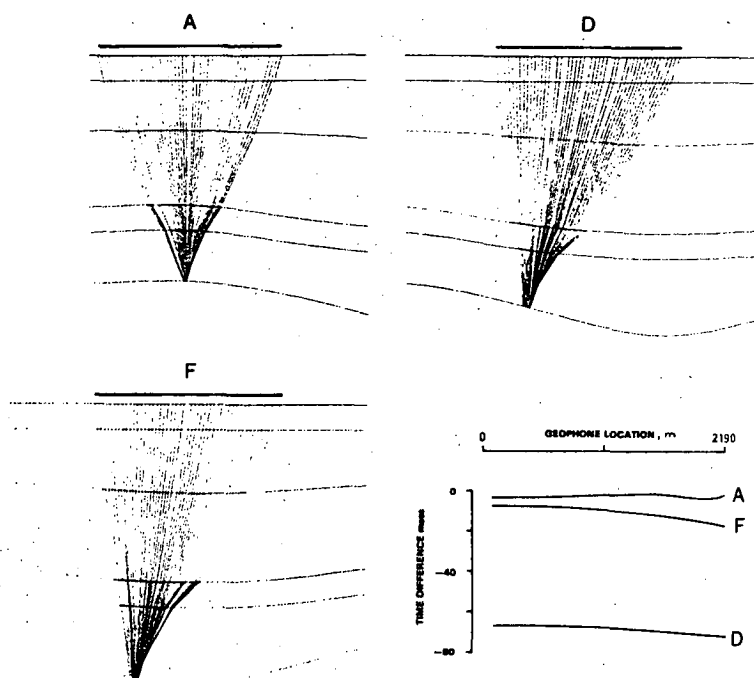


Fig. 2.27 Selected gather locations for surface 6 and their corresponding time-difference plots for the syncline model. Solid lines represent the fixed spread.

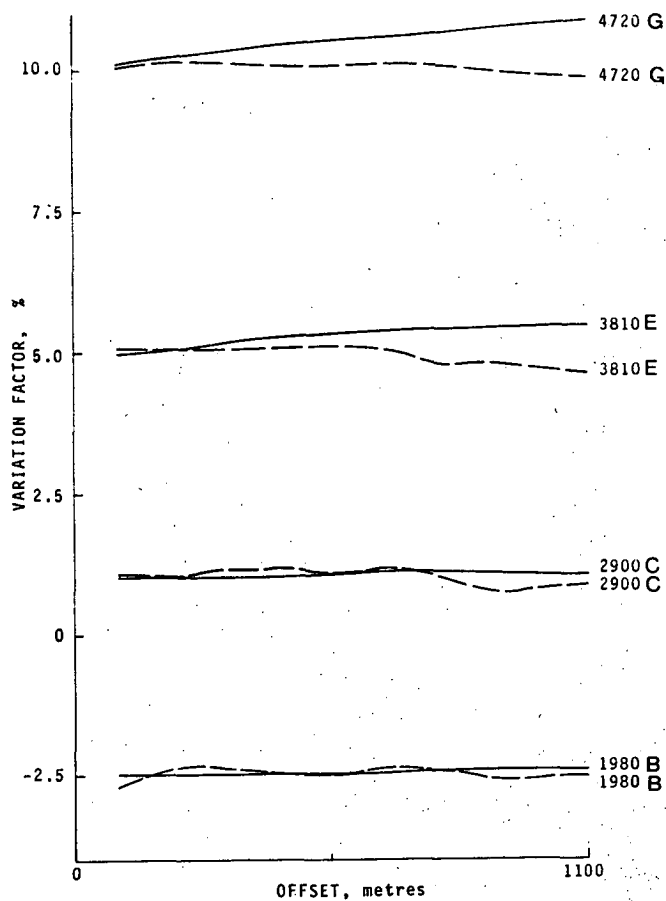


Fig. 2.28 Syncline model variation-factor plots illustrating the percentage deviation of the stacking velocity from the rms velocity as a function of offset distance for a short spread (dashed lines) and a long spread (solid lines) at selected gather locations.

or spread length but increases as the traverse crosses the syncline. The respective gathers are illustrated in Figure 2.28.

6. ANTICLINE

Error factors across a simple anticline show an almost sinusoidal variation across the structure (Figure 2.29). The variation is greatest for deeper reflectors. Zero-offset raypath plots indicate that most of the problem is due to migration error. Time-difference plots (Figure 2.30) for surface 7 show that while there is little migration error for a gather at A (1220 m), large errors (approximately -100 msec) occur on the flanks of the anticline at C (2130 m) and E (3050 m) and decrease towards the crest G (3660 m).

Few reflections can be obtained from surface 7 for gathers over the anticlinal crest. Gathered plots (Figure 2.30) also show that many gathers contain only sporadic reflection information, thereby making velocity processing methods indeterminate. The time-difference plots together with their respective raypath-gather plots (Figure 2.30) illustrate the raypath distortions due to the overburden geology. The far traces for the gather at A, for example, have energy arriving earlier than expected due to the quicker return path on the flank side of the anticline, whereas the far traces for gathers at E (3050 m) and G (3660 m) show a relative delay. Similar trends occur for surface 6 (Figure 2.31).

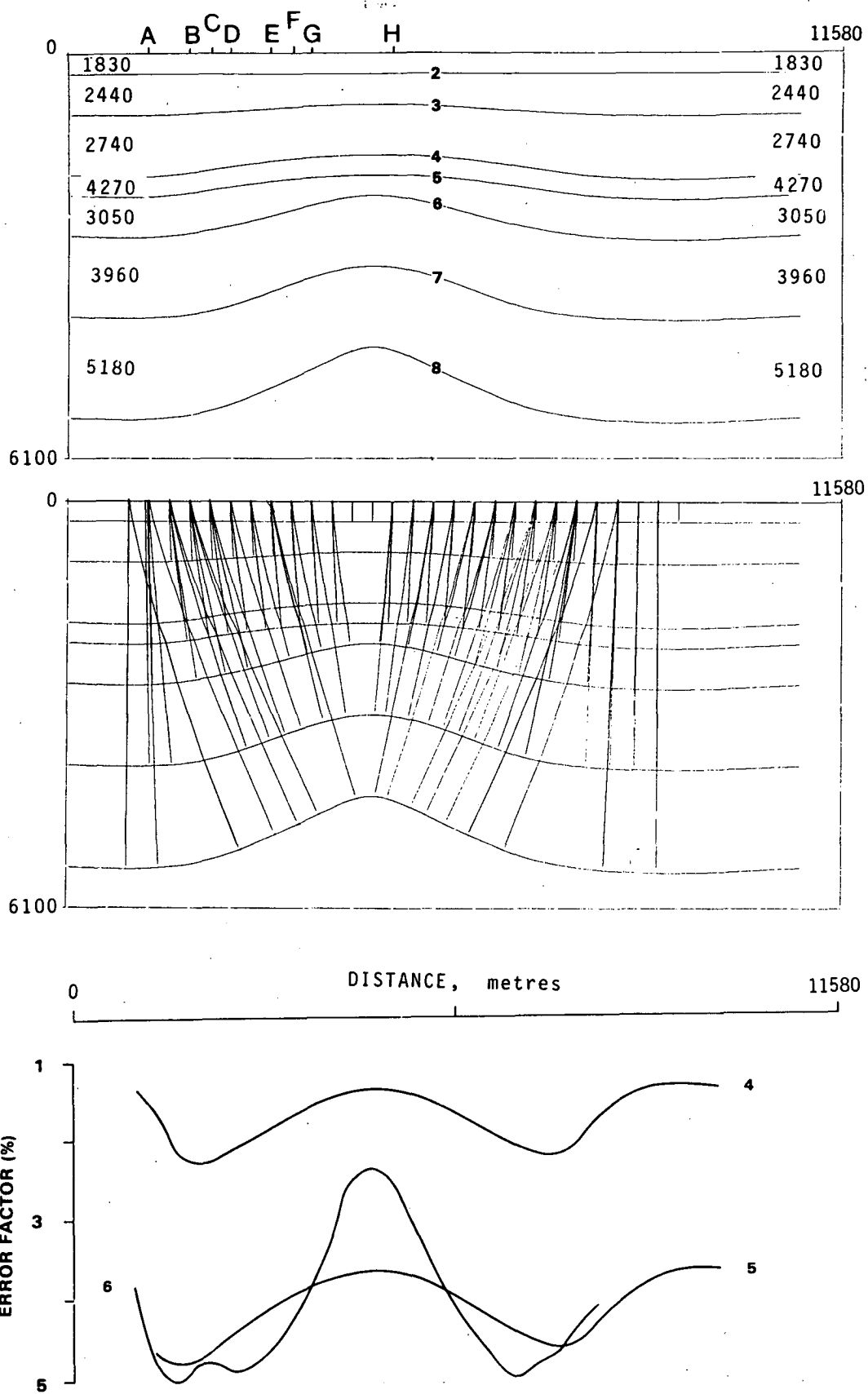


Fig. 2.29 Anticline model with corresponding zero-offset raypaths and error-factor plot.

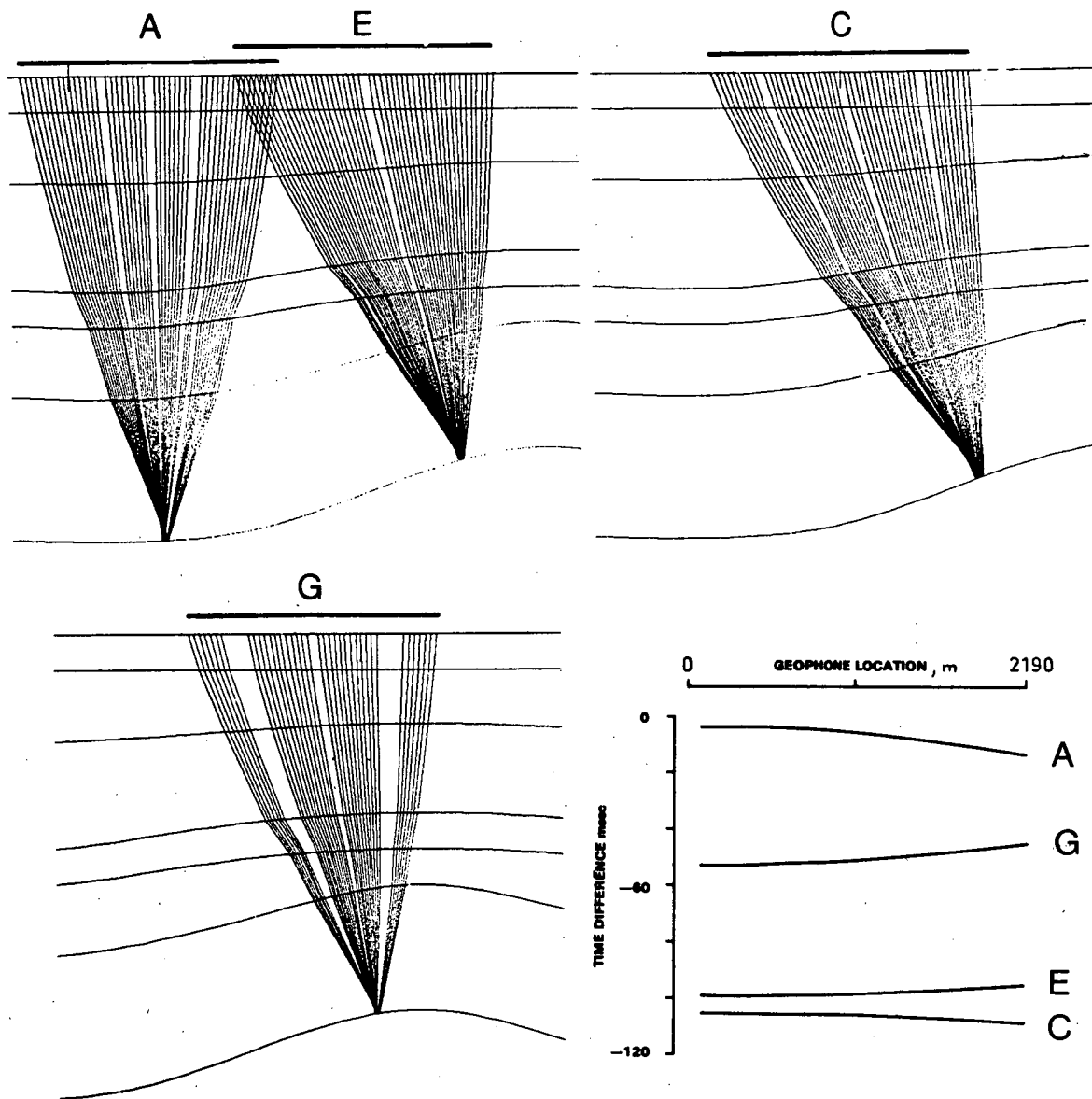


Fig. 2.30 Selected gather locations for surface 7 and their corresponding time-difference plot for the anticline model. Solid lines represent the fixed spread.

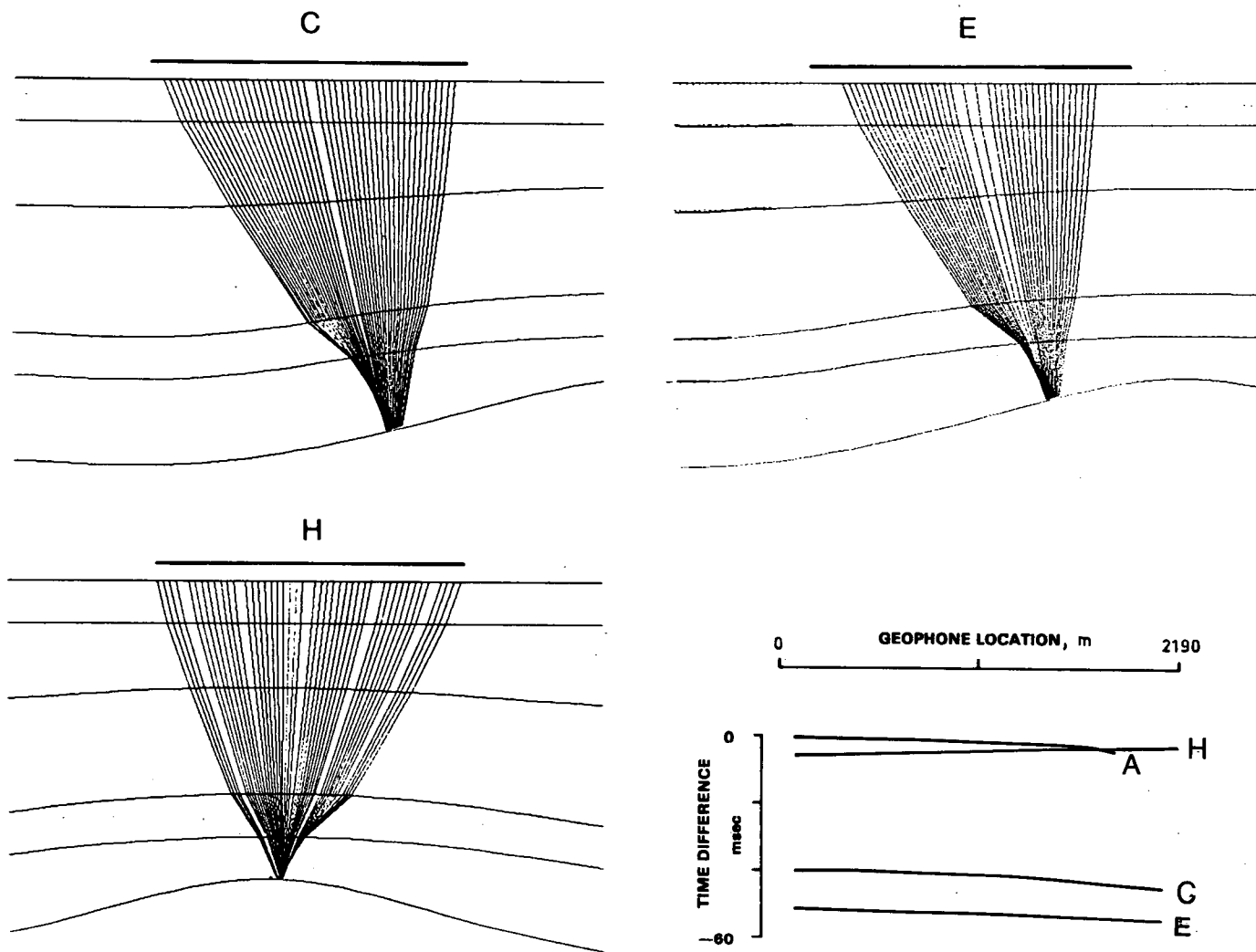


Fig. 2.31 Selected gather locations for surface 6 and their corresponding time-difference plot for the anticline model. Solid lines represent the fixed spread.

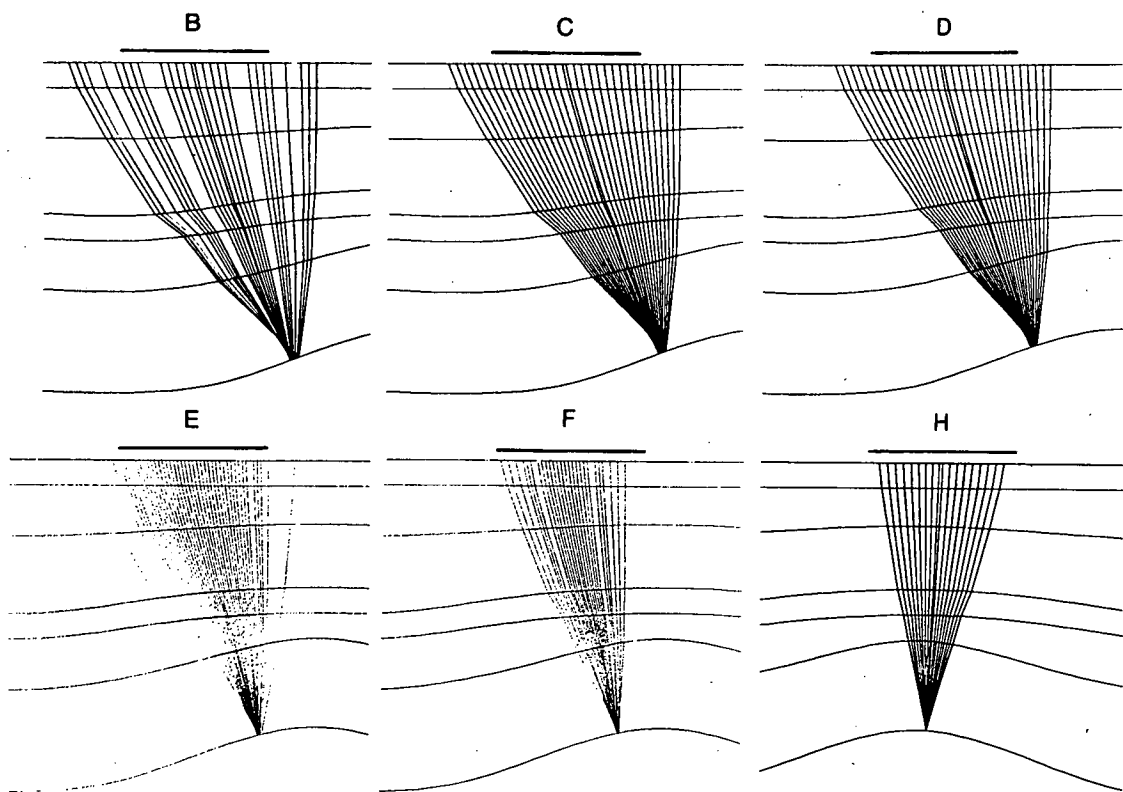
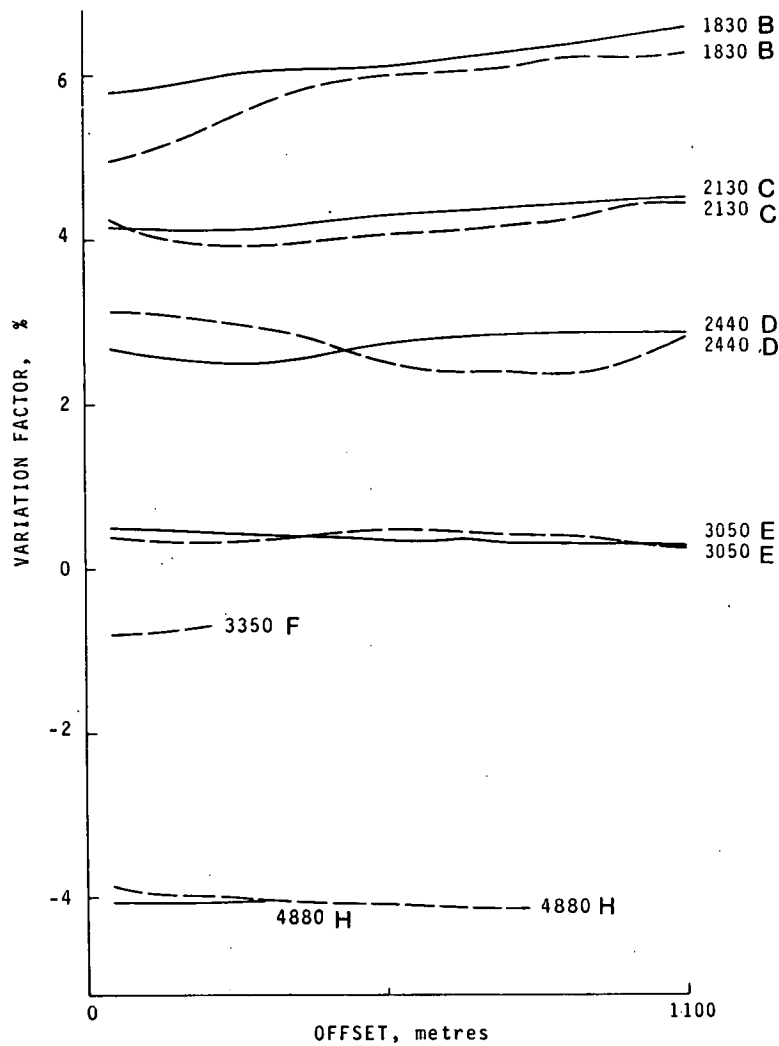


Fig. 2.32 Anticline model variation-factor and gather plots for a short spread (dashed lines) and a long spread (solid lines) at selected gather locations.

Variation factors for surface 7 (Figure 2.32) show a 10 percent change across the structure and exhibit only minor changes as offsets and spread lengths vary.

7. PROGRADING DELTA

While the horizons below the base of prograding show only minor raypath migration problems (Figure 2.33) reflections from individual prograding wedges originate at points removed from the gather location. Two distinct types of reflections are evident: (1) reflections from the tops of the prograding wedges, and (2) reflections from layers below the delta sequence. Error factors for the reflections from the tops of the prograding wedges are shown in Figure 2.33.

Surface 4 yields a smooth error factor curve having a 4 percent variation. The larger error factor near C (3050 m) (Figure 2.34) is due both to a large migration error and the relatively early arrival of the far traces. Gathers at A (1520 m) and F (4590 m) have reduced timing errors and the far traces are less advanced. By K (6710 m) migration errors are small, although the far traces traverse a higher velocity route than would normally be expected. Raypath geometries for these gathers (Figure 2.34) demonstrate these points.

Surfaces 5 and 6 have larger error-factor variations (6 percent) than surface 4. While these error factors have basically the same broad shape as those for surface 4 they increase sharply at 2740 m and 3960 m under the influence of the termination of the overlying prograding tongue. The location of the maximum error factor for

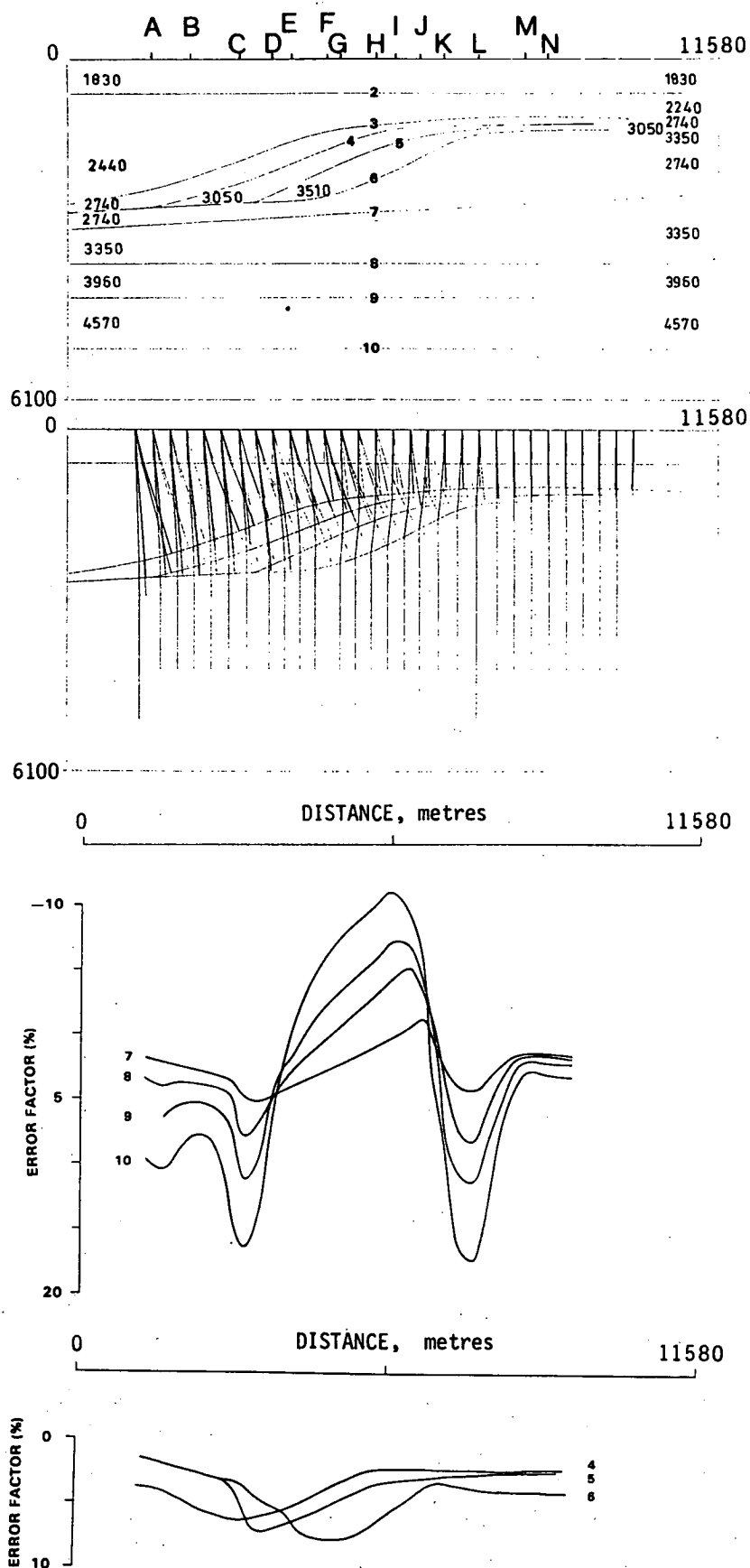


Fig. 2.33 Prograding delta model with corresponding zero-offset raypaths and error factor plot.

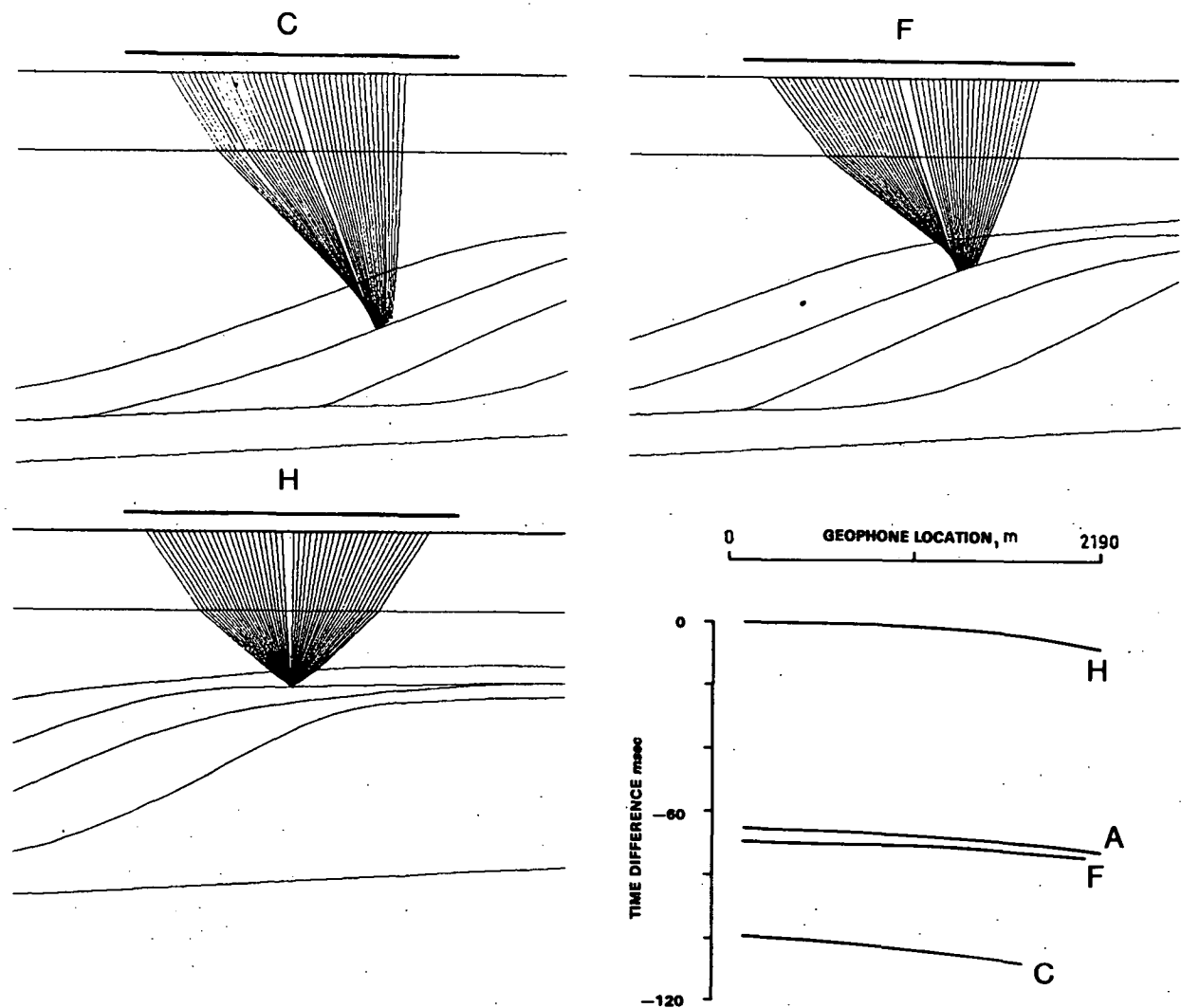


Fig. 2.34 Selected gather locations for surface 4 and their corresponding time-difference plots for the prograding delta model.

surfaces 4, 5 and 6 corresponds to the position of maximum migration error for each surface (Figure 2.33).

Time-difference plots for surface 6 are similar to those for surface 4 with the exception of the gather at K (6710 m) where the far traces arrive later than expected (Figure 2.35). This causes a relative decrease in error factor near this point.

Error factors for surfaces below the base of prograding have similar variations with the fluctuations becoming more extreme for deeper surfaces (surface 10 has fluctuations of over 25 percent). Time-difference plots (Figure 2.36) for various gathers show that the errors between zero-offset and true vertical times are minimal (less than -10 msec) and that the fluctuations in stacking velocities arise entirely from raypath distortions of the far traces.

The far traces for the gather at B (2130 m) arrive much earlier than expected (Figure 2.36). Large error factors for the gather at C (3050 m) are due to the much earlier arrivals at the far traces which traverse the higher velocity prograding wedge tongue (Figure 2.36). Gathers at G (4880 m) and I (5790 m) have "banana bend" characteristics due to the rays passing through different portions of the prograding wedges. The relatively early arrivals of far traces increases stacking velocities to such an extent that negative error factors result. At K (6710 m) the far traces arrive only marginally earlier than expected (Figure 2.36) and error factors are similar to those for horizontal layers. The far traces of the gather at L (7320 m) arrive early as part of the reflection path passes through the high velocity

prograding wedge (Figure 2.36) and the error factors increase significantly. By N (8530 m) stability is achieved and error factors approach those for horizontal layers.

Field configuration variations for surface 6 are small (Figure 2.37). The positive variation factors result from large migration errors. Variation factors for surfaces below the base of prograding have large ranges. Surface 10, for example, has a range of 22 percent (Figure 2.38). Travel-times for rays from the gather at C (2740 m) arrive relatively earlier than expected, especially for the far traces which traverse the high velocity prograding wedge tongue material between interfaces 5 and 6. This explains the high stacking velocities and the abrupt change in the variation factor for the short spread at an offset of 460 m. There is a large discrepancy in stacking velocities for the different spreads and offsets. By D (3660 m) the increase in travel-time for the trace on the downward path is counteracted by the relatively earlier time on the return path for all traces. Consequently errors are small but gradually increase with increasing offset. Variation factors for the different spreads at H (5490 m) are similar and show only minor variation with offset. However they exhibit large negative values due to the simultaneous relative delay on the near traces and earlier arrival of the far traces that traverse quicker paths through the prograding wedges on the tongue side of the gather. This effect still occurs for the gather at J (6400 m), but the relative time differences across the traces are smaller and the earlier arrival of the far traces becomes significant. There is a 3 percent difference in variation factor for the two spreads, and a 4 percent variation due to

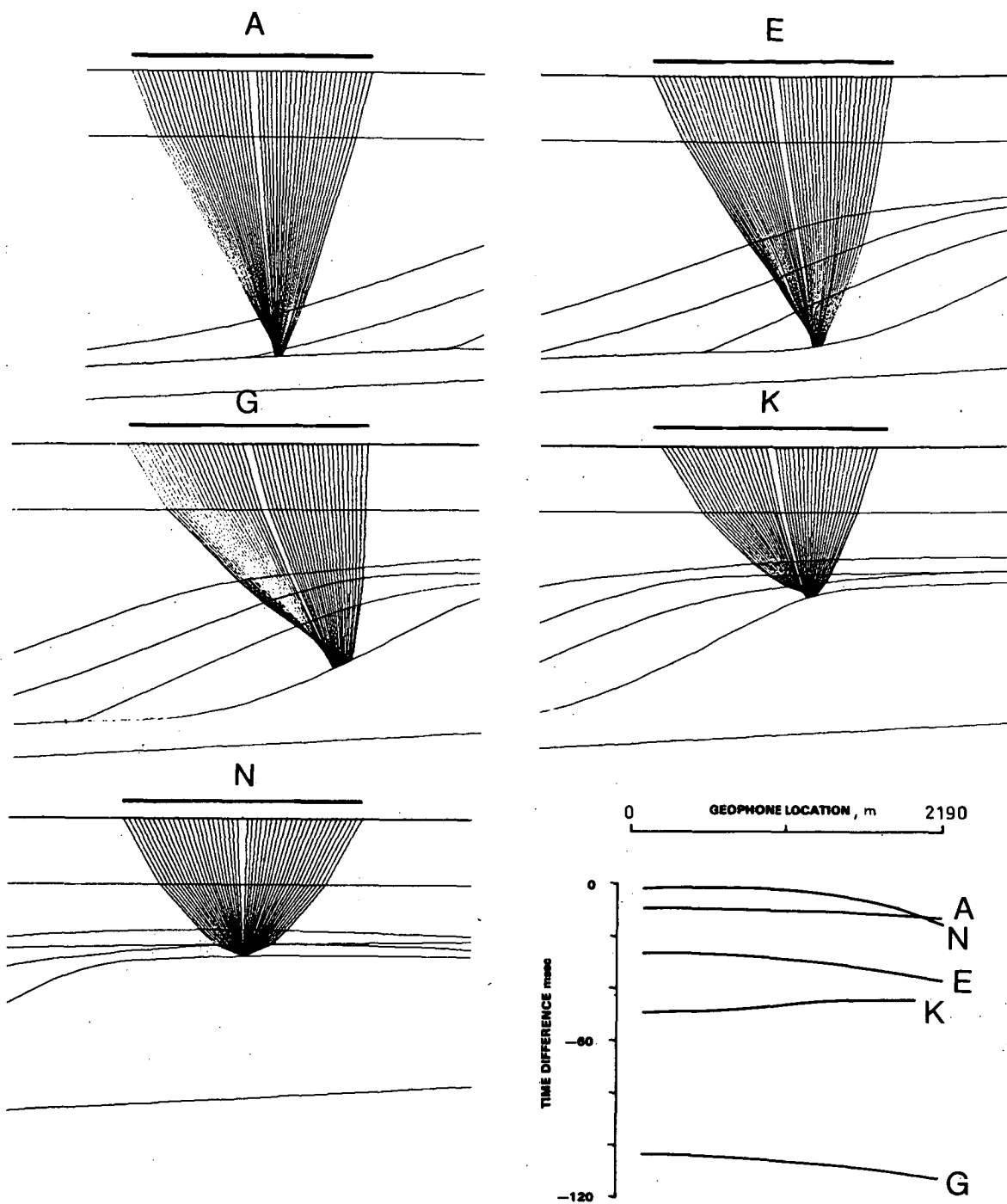


Fig. 2.35 Selected gather locations for surface 6 and their corresponding time-difference plots for the prograding delta model.

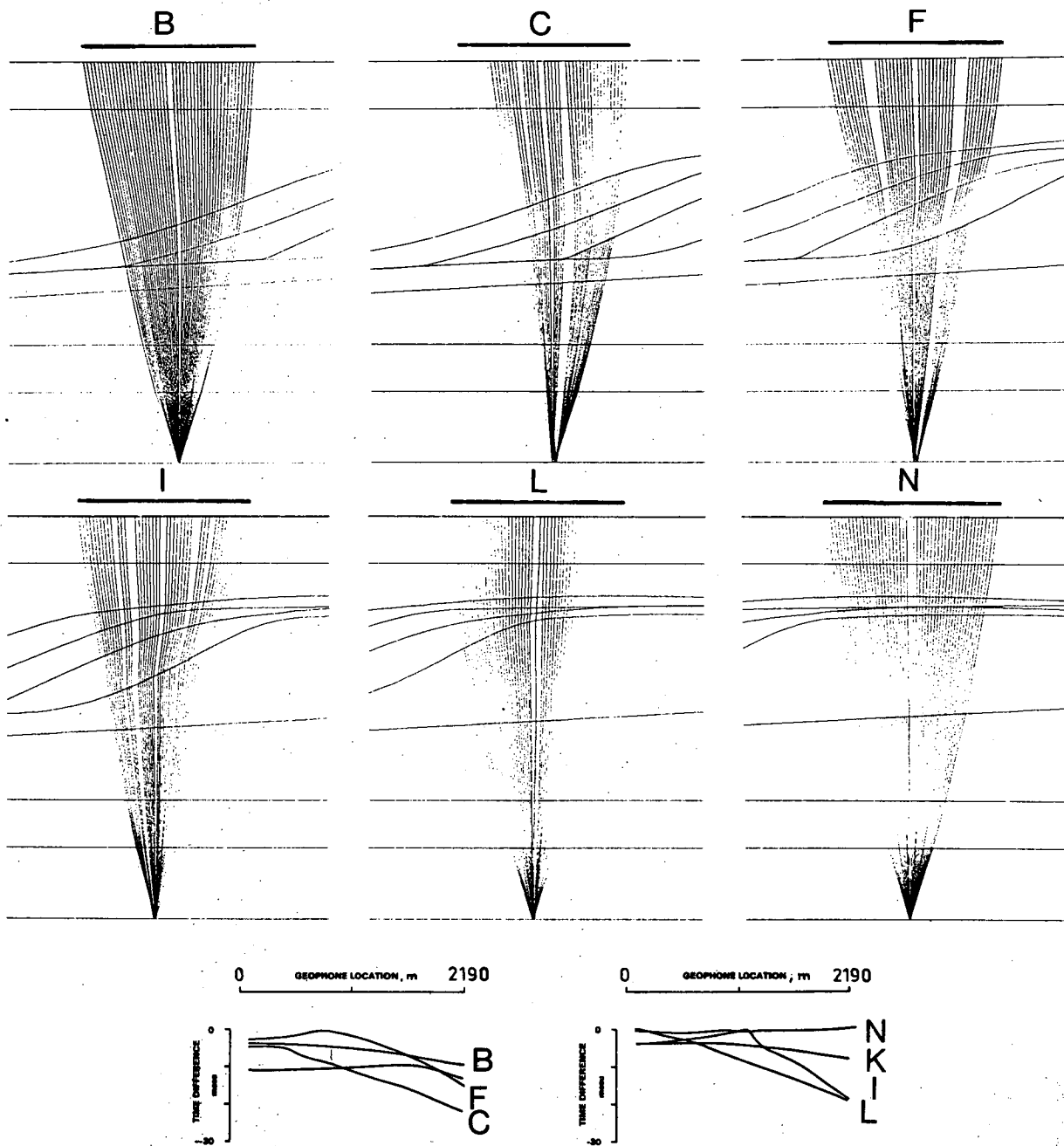


Fig. 2.36 Selected gather locations for surface 10 and their corresponding time-difference plots for the prograding delta model.

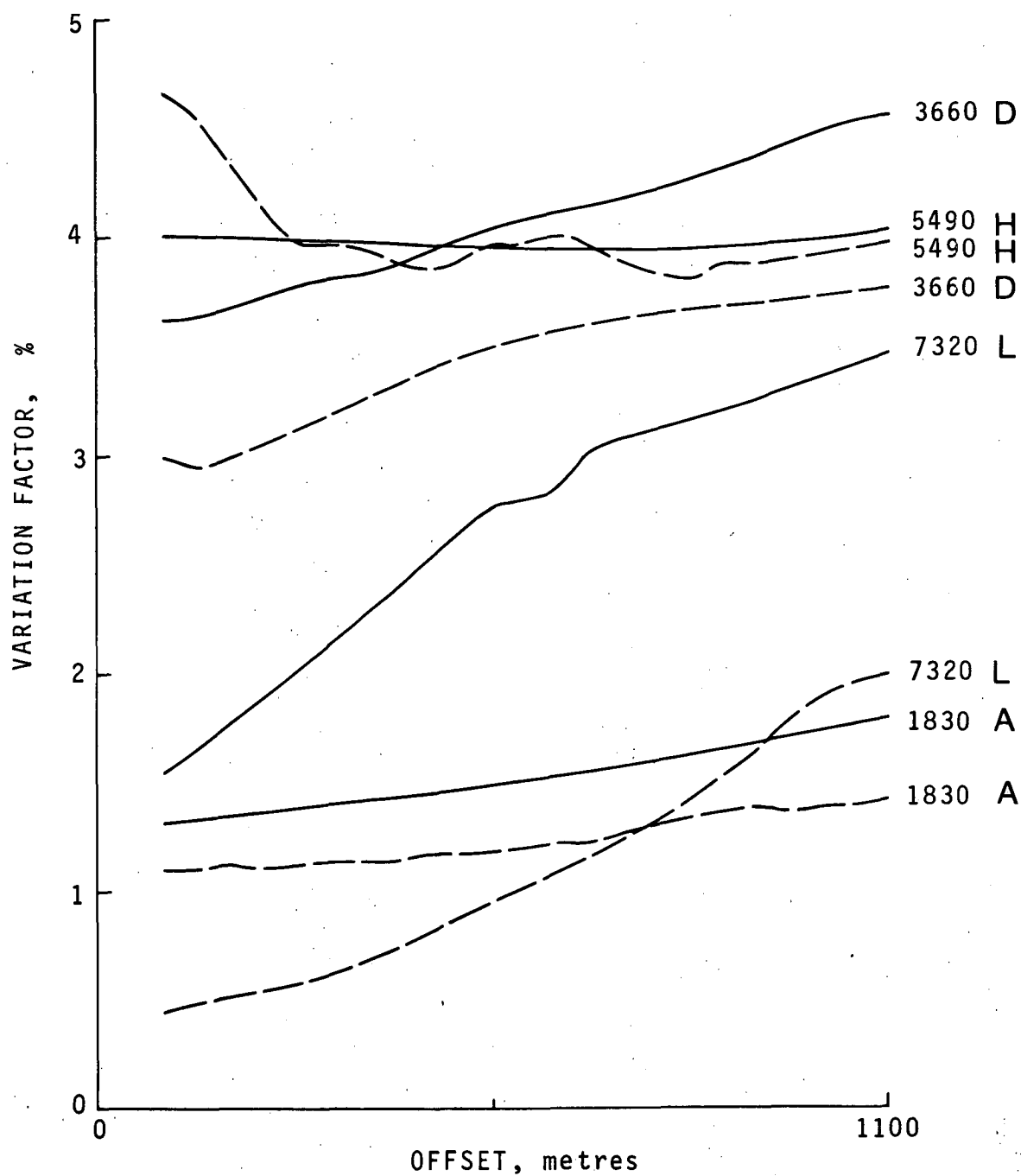


Fig. 2.37 Prograding delta model variation-factor curves for short (dashed lines) and long (solid lines) spreads at selected gather locations for surface 6.

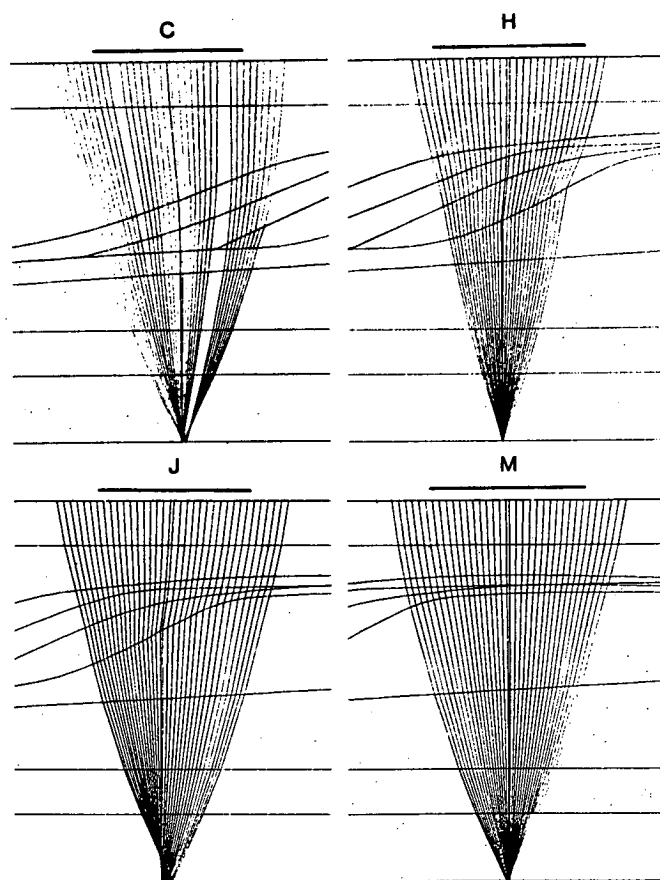
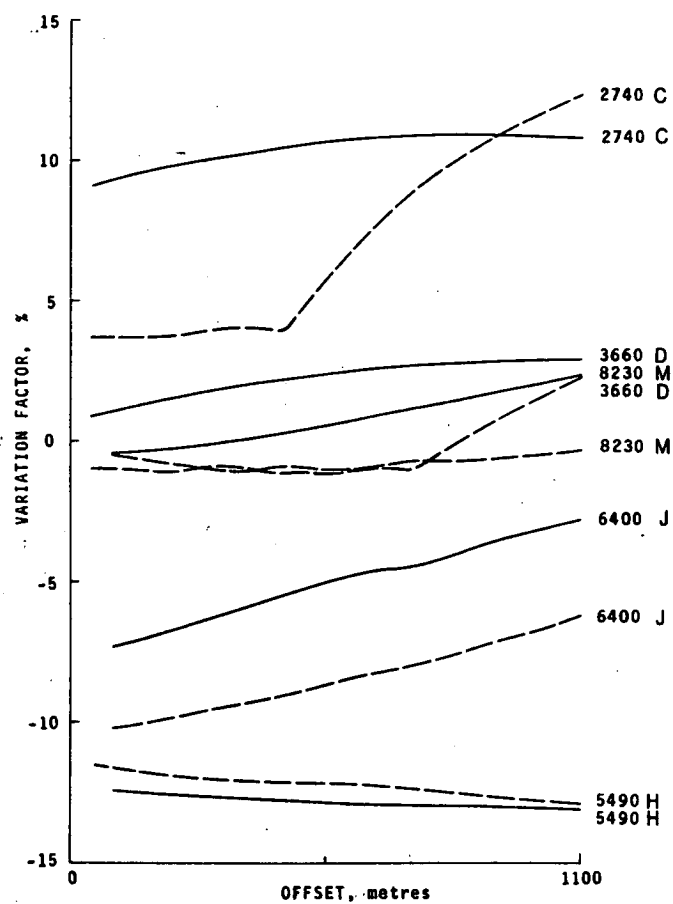


Fig. 2.38 Prograding delta model variation-factor and gather plots for a short spread (dashed lines) and a long spread (solid lines) at selected gather locations for surface 10.

offset changes. By M (8230 m) conditions have stabilised.

Migration induced depth estimates calculated using true vertical velocities are up to 300 m shallow for surface 6, while only minor depth errors (up to 30 m) occur for surface 10 (Figure 2.39). Alternatively, depths are overestimated by up to 200 m for surface 6 when calculated using measured stacking velocities and true vertical times. Corresponding errors for surface 10 range from an overestimate of 1000 m to an underestimate of 420 m (Figure 2.39).

8. SHELF MARGIN

A model of a carbonate shelf margin is illustrated in Figure 2.40. Laterally varying velocities are used. While the dips of the horizons are relatively small, large variations in error factor are observed for surfaces 8 and 9.

V. MIGRATION VELOCITY ESTIMATES

Doherty & Claerbout (1976) used finite difference formulations of the scalar wave equation to derive structure independent velocity estimates for earth models in which the velocity is horizontally layered but the reflectors have arbitrary dip and curvature. Migration and velocity techniques using the Kirchhoff summation method also apply only to such earth models. For a multilayered subsurface isovelocity layered model with curved interfaces, complete migration and hence accurate velocity determination can only be performed for the uppermost interface. Both methods therefore provide meaningful velocities for migration problem situations but are misleading where raypath distortion

problems occur. The models described above show that raypath distortion problems are significant and that velocities determined by techniques of migration before stack, which do not take into account lateral velocity changes, must be treated with caution.

VI. STACKING VELOCITIES DETERMINED FROM THREE-DIMENSIONAL MODELS

In two-dimensional modelling seismic rays which are recorded by geophones along a line profile are confined to a single plane. Displacement of depth points to the side of the profile line occurs for a three-dimensional inhomogeneous earth. Interpretation problems may result. Sideswiping, where arrivals from more than one structure are recorded simultaneously, may cause the seismic structure of an anticline to die out upward yet not affect its companion syncline.

Rather than use the two-dimensional ray tracing approach described earlier, the writer has treated the transmission of rays through three-dimensional models as a variational problem based on Fermat's Principle. Given the coordinates (x_s, y_s, z_s) and (x_g, y_g, z_g) of the source and detector respectively, and the equations of n three-dimensional interfaces:

$$A_i + B_i x + C_i y + D_i x^2 + E_i y^2 + F_i xy = 0$$

for $i = 1 \dots n$, in which $(A_i, B_i, C_i, D_i, E_i$ and $F_i, i = 1, n)$ are known and assuming layers of constant velocity, the resultant program uses the Newton-Raphson iterative procedure for non-linear equations to determine the origin coordinates and transit times. A brief description is given in Appendix 2.

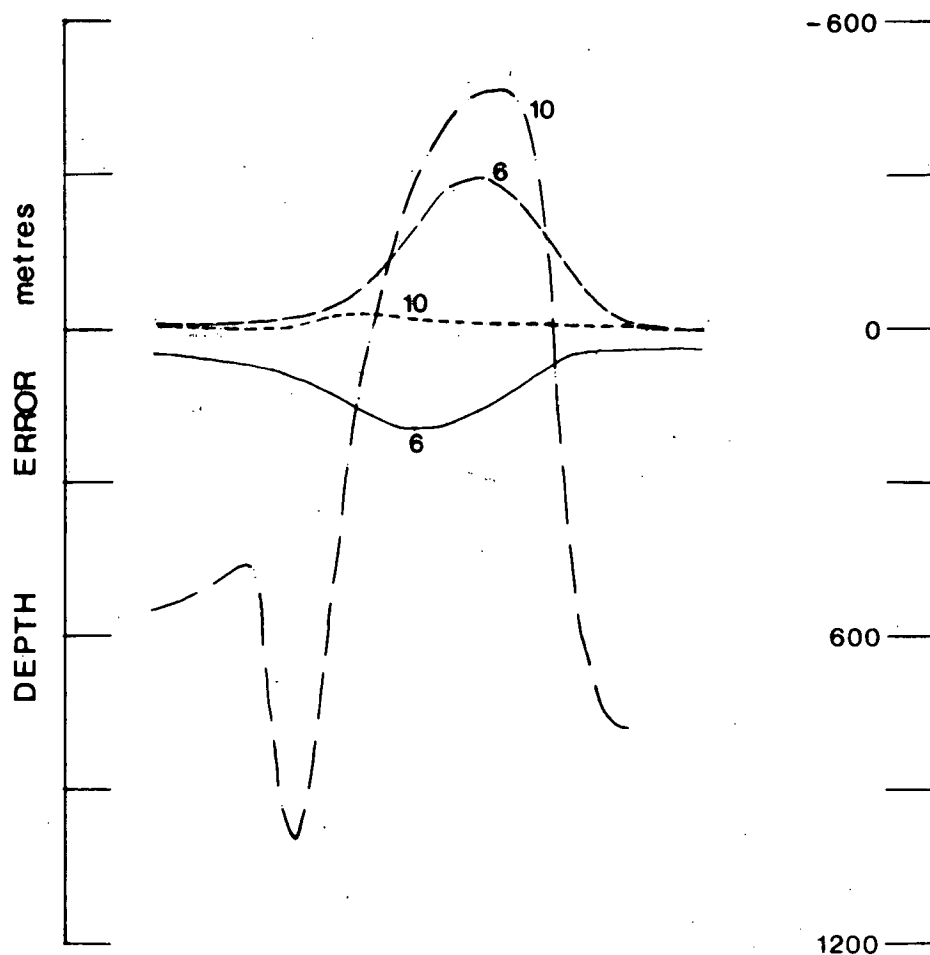
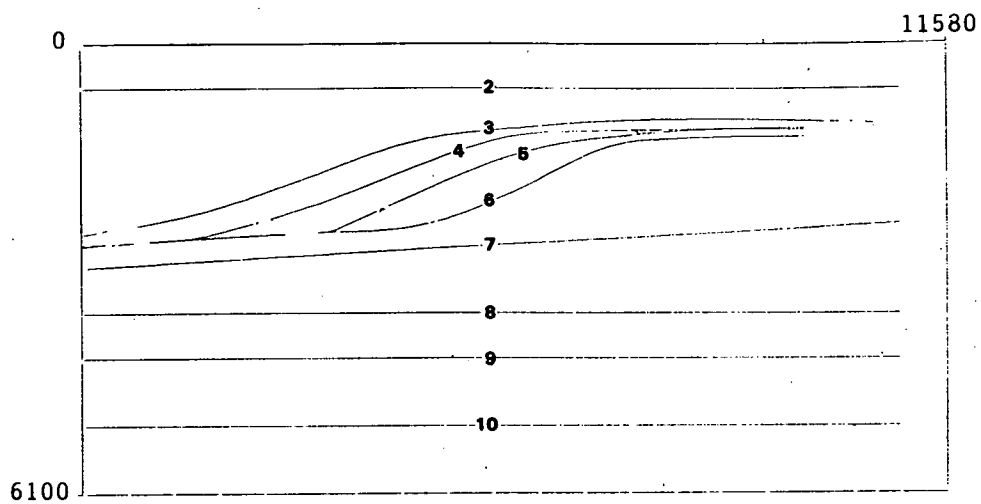


Fig. 2.39 Timing and depth errors for the prograding delta model.

- migration depth error (surface 6)
- migration depth error (surface 10)
- velocity induced depth error (surface 6)
- velocity induced depth error (surface 10)

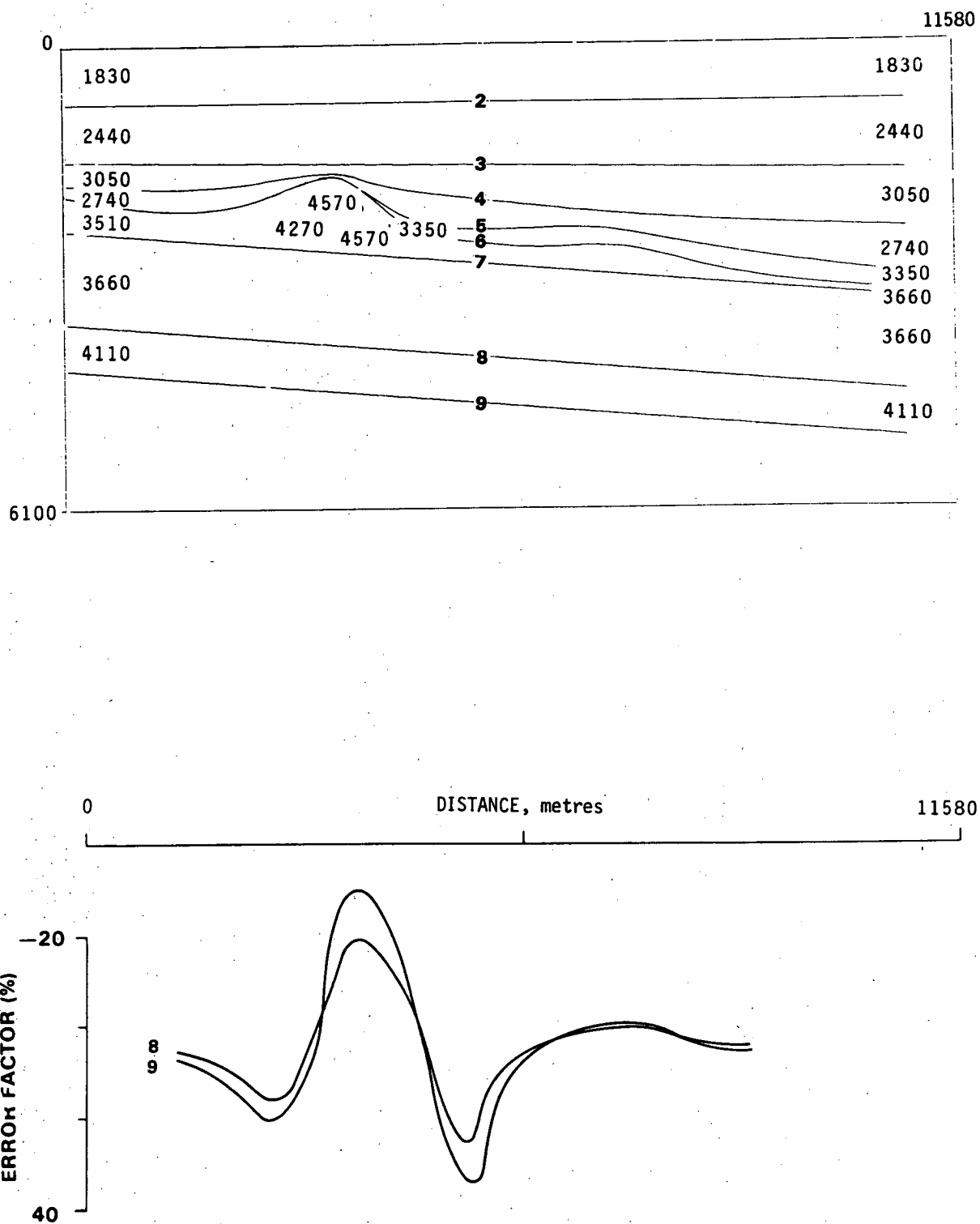


Fig. 2.40 Shelf margin model and corresponding error-factor plot.

Seismic stratigraphic interpretation of 18 seismic lines has defined 7 major seismic sequences. Figures 2.41 to 2.44 illustrate four typical time sections together with their interpreted sequence units. The line location is illustrated in Figure 2.45. Time structure maps to each horizon have been contoured while depth contours, obtained using vertical velocities generated from sonic log and check shot information at each of six well locations, are shown in Figure 2.45. Large lateral variations were apparent in the well data, but constant vertical velocities were obtained by averaging the six values.

Interval velocities and densities together with a synthetic seismogram, which was generated using the method of Rudman & Blakey (1976), for well 5 are illustrated in Figure 2.46. Average and interval velocities are given in Figure 2.47. Isochrons for each sequence are illustrated in Figure 2.48.

A detailed description of each sequence is given below:

Surface to Horizon 1 - Water depths for the region range from 75 to 114 m with an average of 85 m. This sequence consists of up to 1000 m of subhorizontal marine sediments, with interspersed channeling (e.g. eastern portion of line 2 around 0.5 to 0.6 seconds). The velocity of the sequence increases with depth (Figure 2.47).

Horizon 1 to Horizon 2 - Isochrons for this sequence (Figure 2.48) show two prograding tongues: one with a northerly source and the other of westward origin. The tongues terminate abruptly on an unconformity surface marked by horizon 2 (line 6). Reflectors are subparallel within the lobes (lines 2 and 6), however the western end of

line 2 and also line 7 which are offset from these masses have wavy reflectors which exhibit rapid lateral changes in reflection amplitude.

Horizon 2 to Horizon 3 - Horizon 3 is characterised by a channelled reflector (northern portion of lines 1 and 7 and the middle section of line 2) containing divergent reflector patterns which represent fill sediments. Interval velocities for this sequence are high (Figure 2.47) and this explains the large amplitude low frequency reflections. Isochrons (Figure 2.48) show a distinctive WNW-ESE trending channel in the northern part of the area. A distinctive ridge separates this channel from a northeasterly thickening sequence in the south.

Horizon 3 to Horizon 4 - Horizon 4 is a distinctive unconformity surface (southern portion of line 6 and eastern end of line 2) with channelling occurring at the northern end of line 7. The sequence consists of a series of complex channels (middle section of line 2). Reflectors may be parallel (eastern end of line 2) or prograding (middle northern end of line 1) and have interval velocities of 3800 m/sec (Figure 2.47). A WNW-ESE trending channel occurs in the central-northern portion of the region (Figure 2.45); the small time interval in the north is the result of channelling of horizon 3 in this area.

Horizon 4 to Horizon 5 - Horizon 5 represents a distinct velocity discontinuity (Figure 2.47) and corresponds to a broad channel which has a downcut into underlying anticlinally folded sediments. The channel axis overlies the anticlinal high (lines 6 and 7). It is this dominant channel trend that has controlled later channelling and

progradation. The isochrons (Figure 2.48) show a WNW-ESE trending channel in the central-northern area, and a large thickness of high velocity material in the central region. A gentle southward thickening of the sediments away from the channel axis occurs in the southern region. The distinctive reflection for horizon 5 on lines 1, 2 and 6 is due to the large velocity contrast, and to a less extent the large density contrast between the channel fill and the underlying sediments.

Horizon 5 to Horizon 6 - This sequence contains anticlinally folded low velocity sediments which thicken away from the fold axis. The folding becomes more open with decreasing depth indicating contemporaneity between the sedimentation and the folding (southern end of line 6). The isochrons show the channelling of horizon 5 into this sequence and further highlight the channel axis.

Horizon 6 to Horizon 7 - Horizon 7 represents an unconformity event which has been folded prior to deposition of the overlying sediments, as evidenced by onlap at the southern end of lines 6 and 7 and also the east and western ends of line 2. A westward thickening of the sequence occurs (Figure 2.48). There is a rapid increase in velocity at horizon 7.

Raypath models have been computed over the dotted portions of lines 1 to 5 (Figure 2.45). Figure 2.49 shows cross sections for these lines with the seven horizons and their interval velocities.

Stacking velocities for the seven horizons along line 6 have been interpreted from velocity analyses (G.S.I. scattergrams) (Figure 2.50). The large scatter in the velocities is illustrated for selected analyses (Figure 2.50) at R, S, T

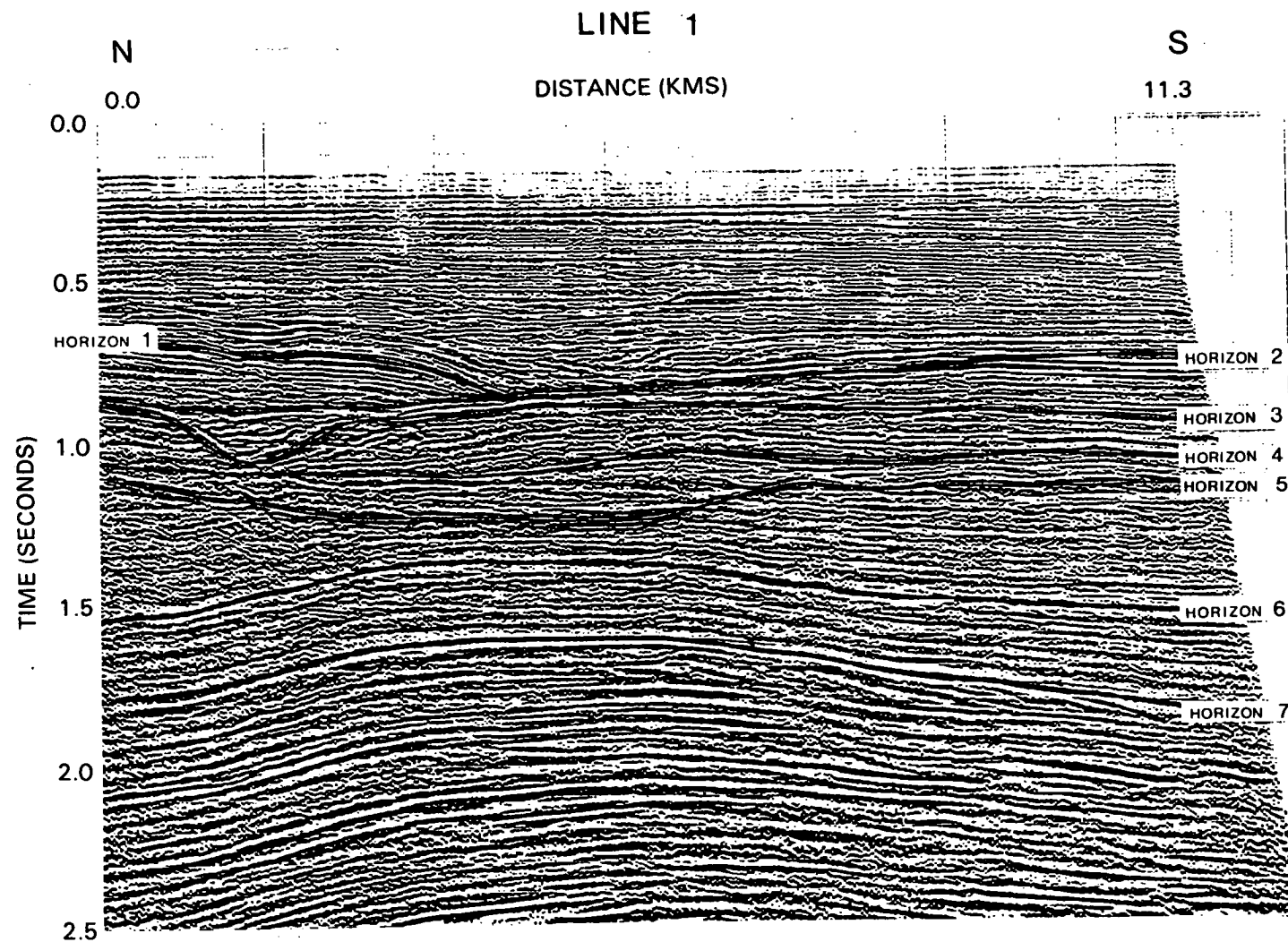


Fig. 2.41 Seismic stratigraphic interpretation for line 1.

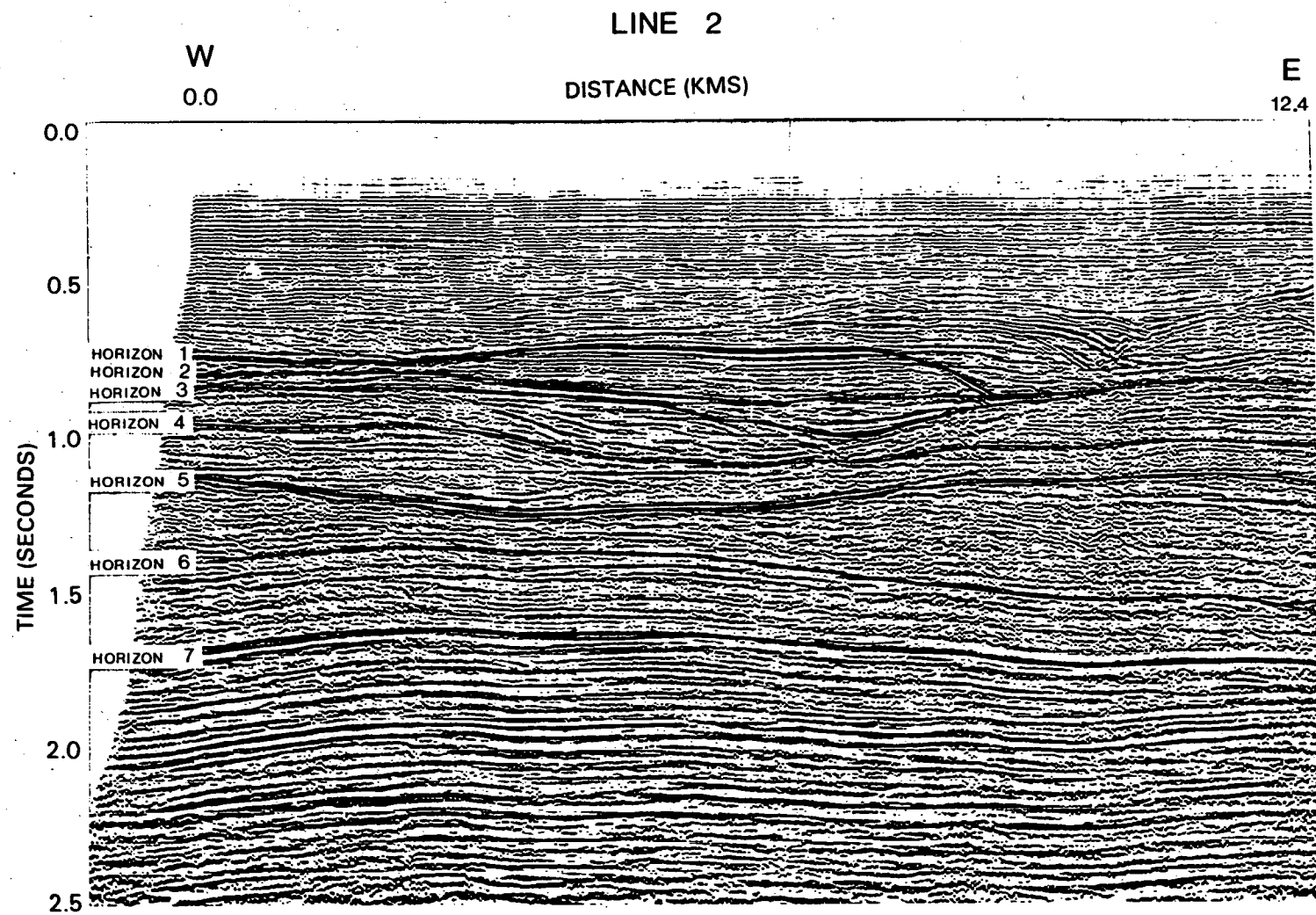


Fig. 2.42 Seismic stratigraphic interpretation for line 2.

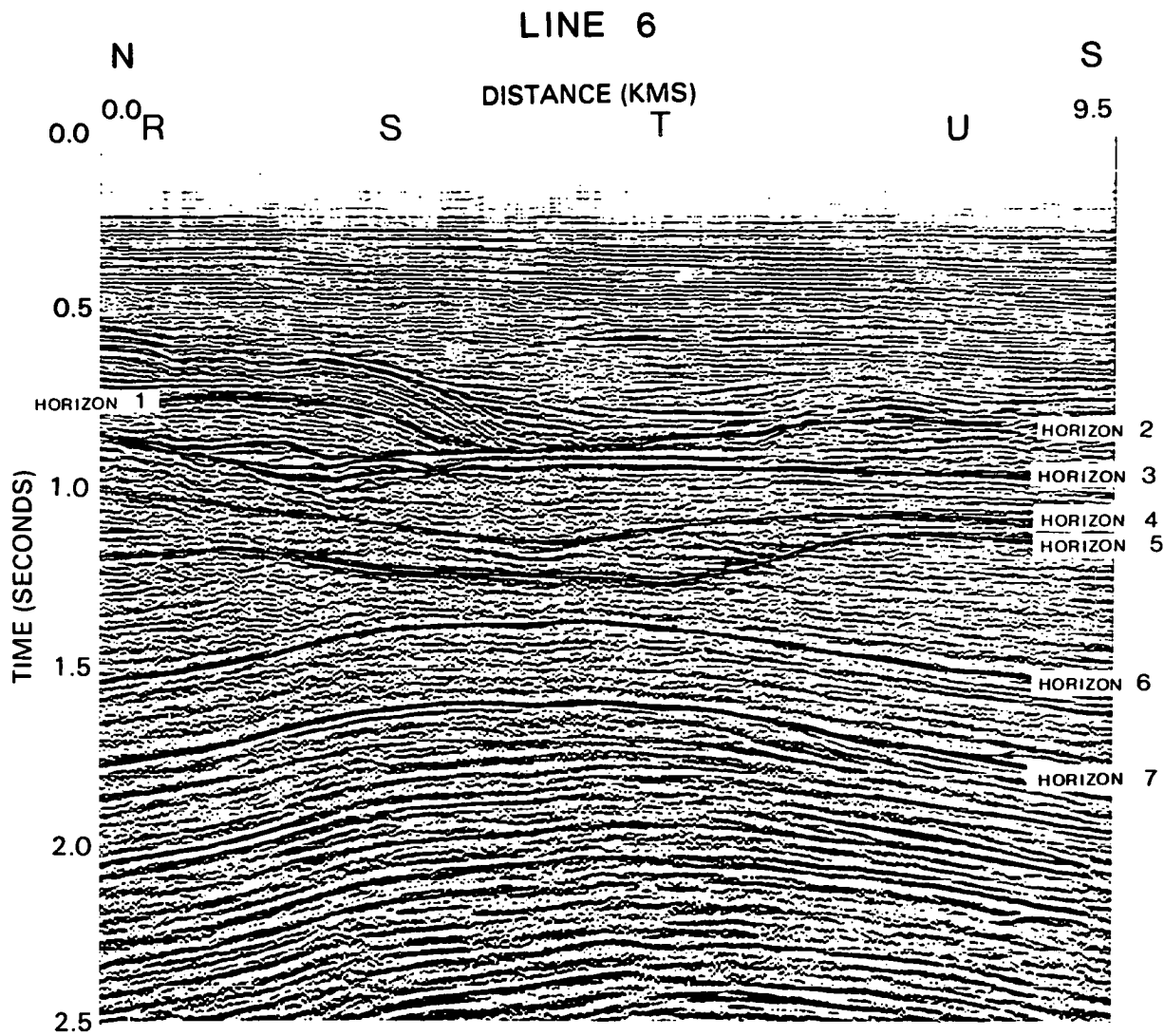


Fig. 2.43 Seismic stratigraphic interpretation for line 6.

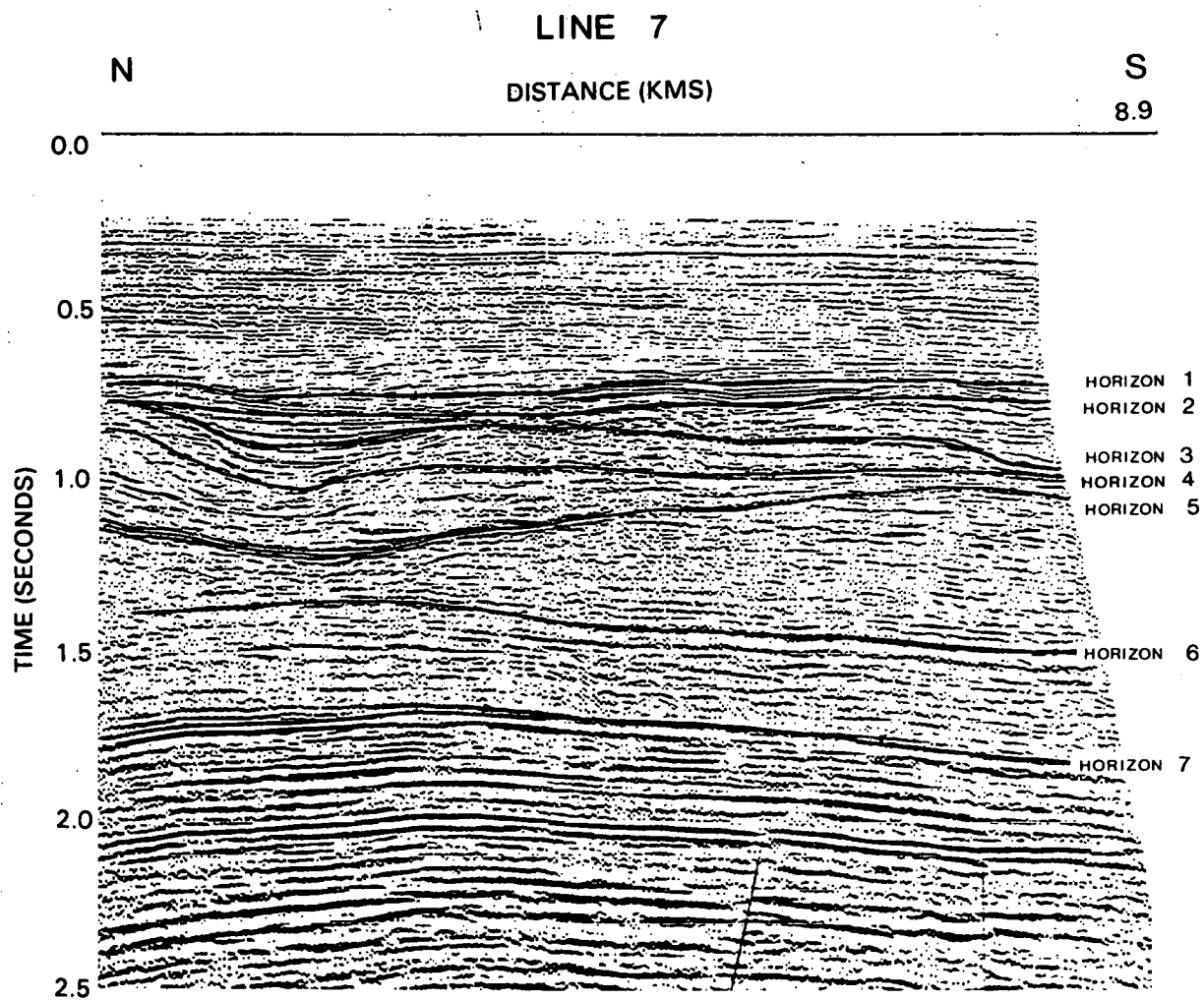


Fig. 2.44 Seismic stratigraphic interpretation for line 7.

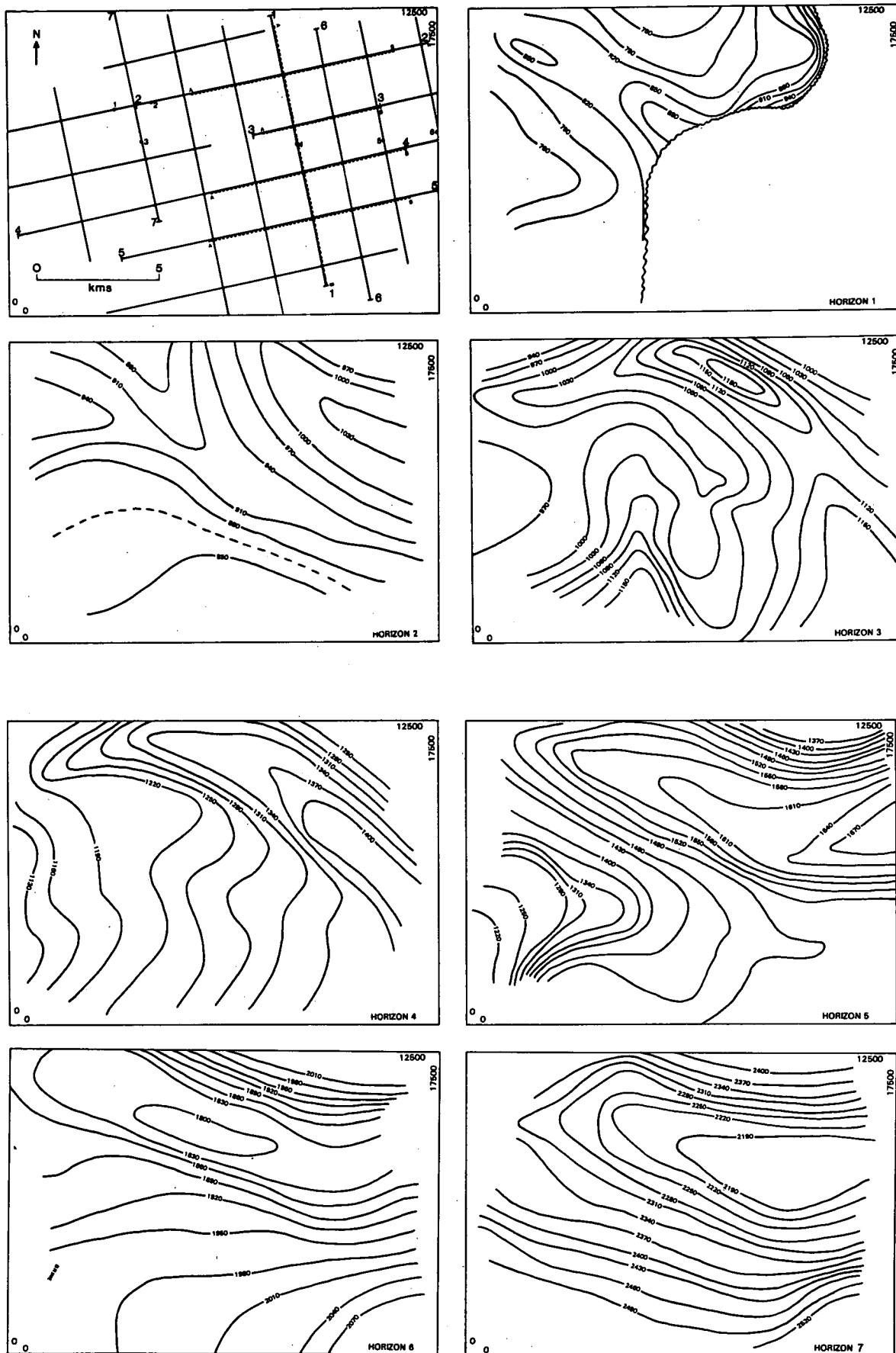
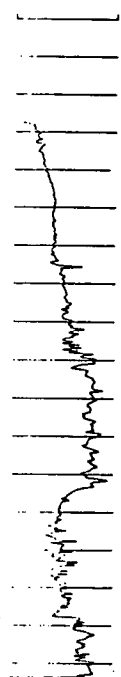


Fig. 2.45 Location and depth structure maps for horizons 1 to 7.

VELOCITY

km/sec

1.5 4.5



0.

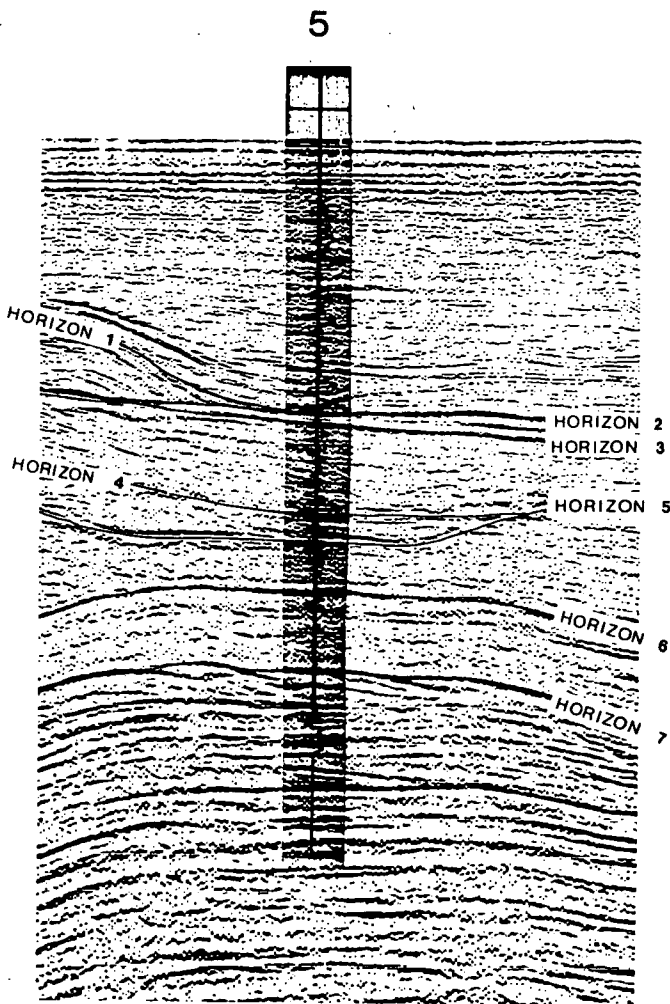
0.5

1.0

1.5

2.0

2.5



DENSITY

t/m³

2.0 3.0

0.

0.5

1.0

1.5

2.0

2.5



Fig. 2.46 Synthetic seismogram and velocity and density logs for drillhole 5.

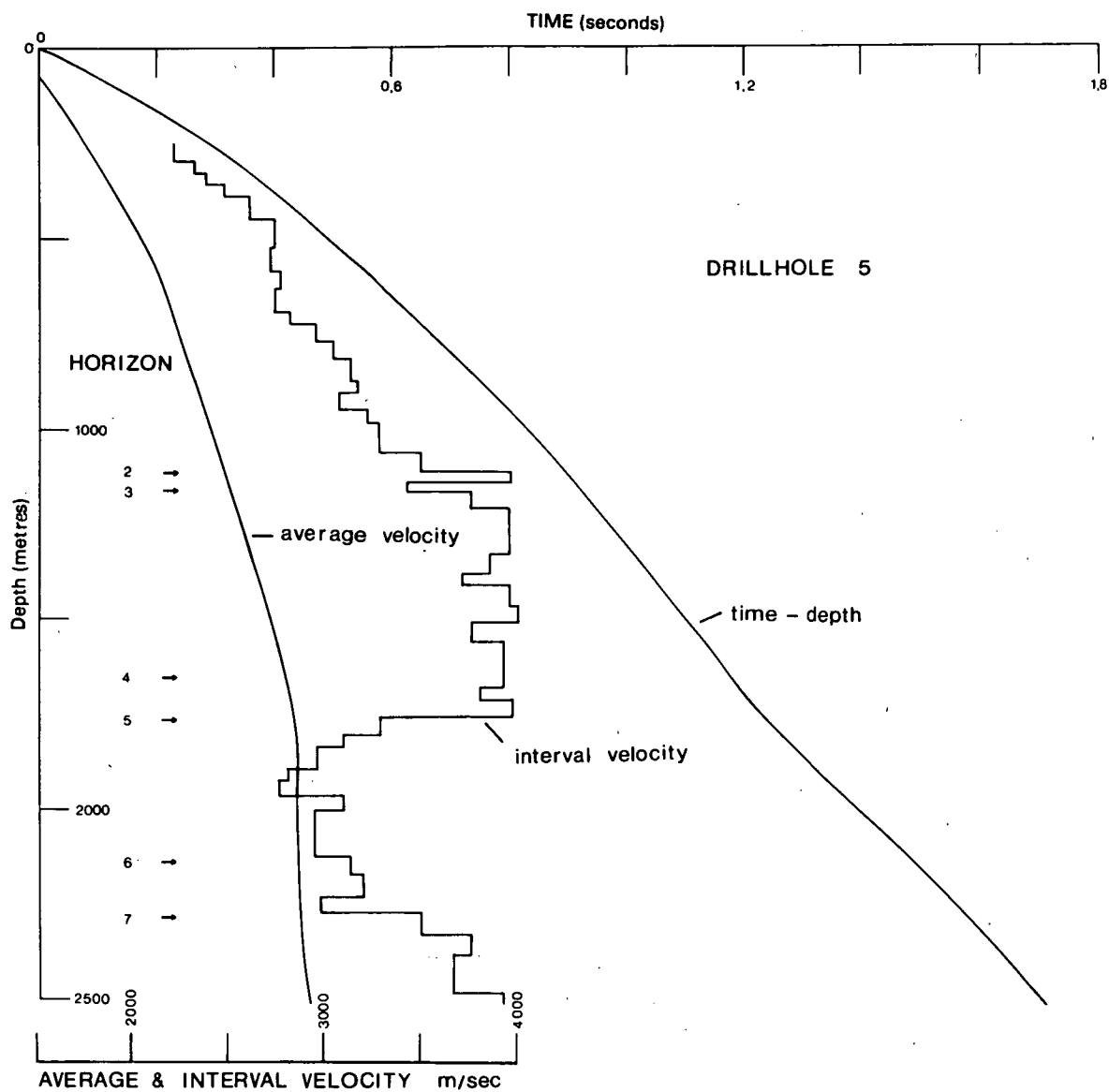


Fig. 2.47 Time-depth curves, interval and average velocity plots for drillhole 5.

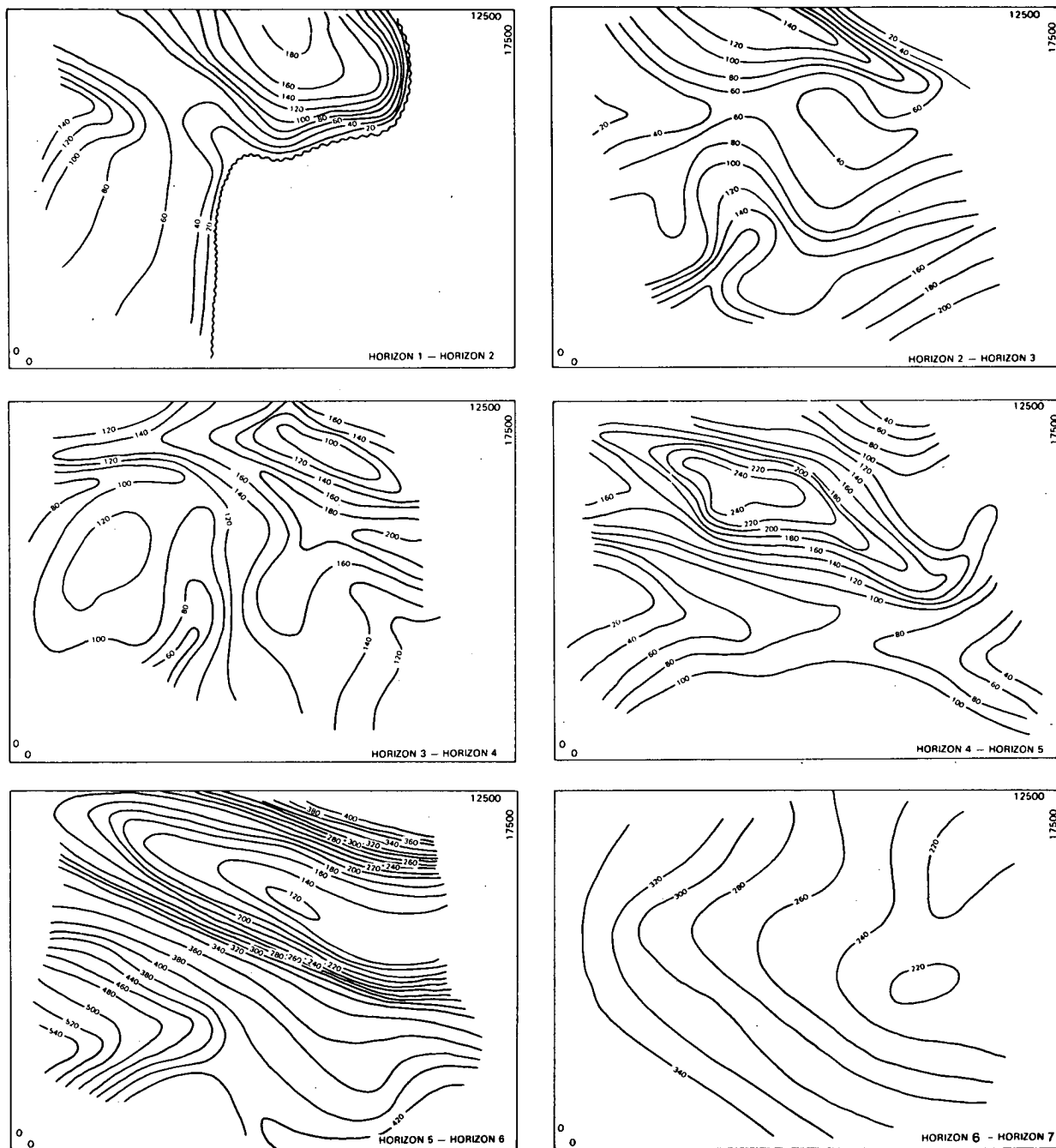


Fig. 2.48 Isochrons for the seismic stratigraphic sequences.

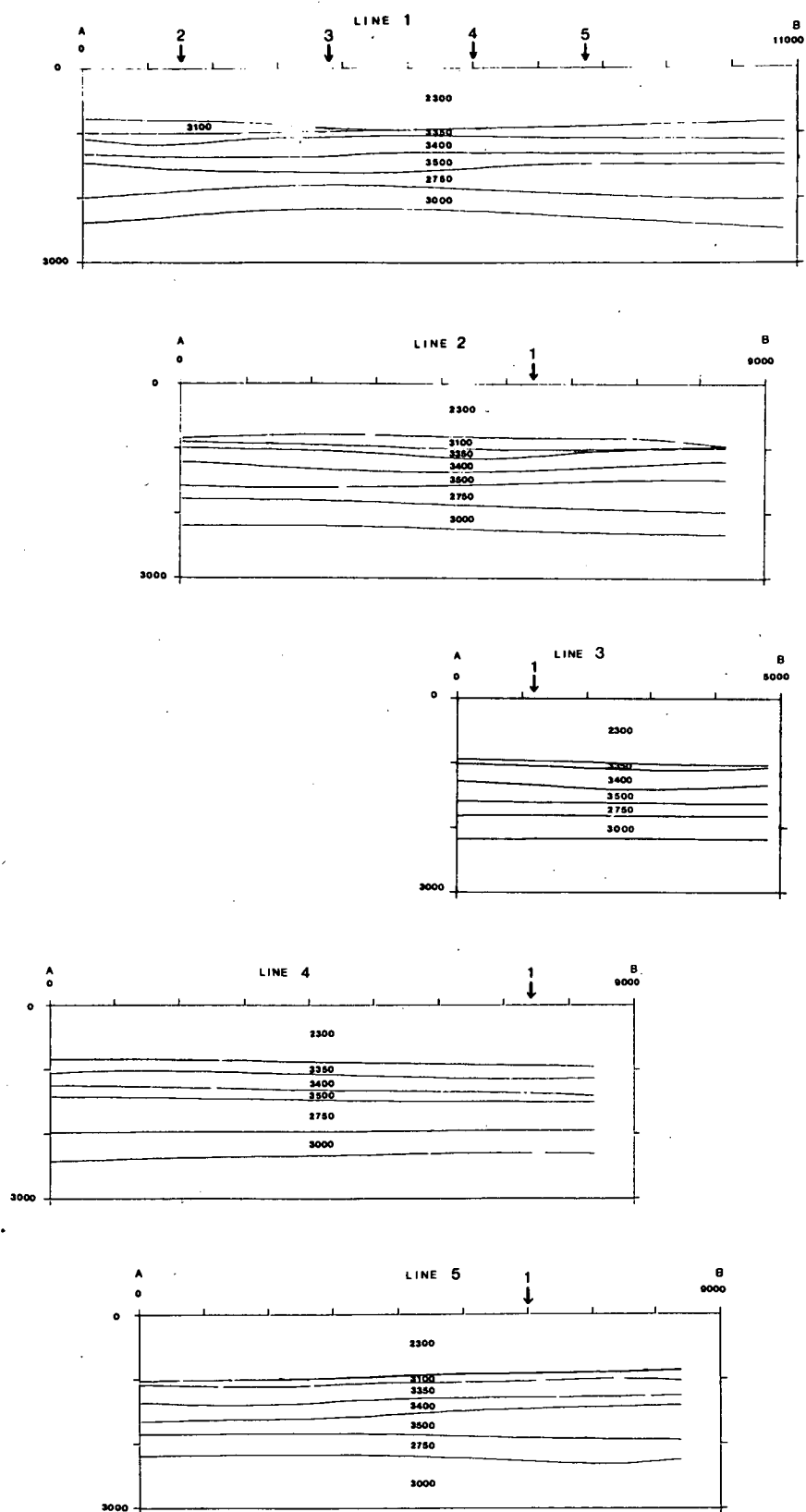


Fig. 2.49 Two-dimensional sections along lines 1 to 5.

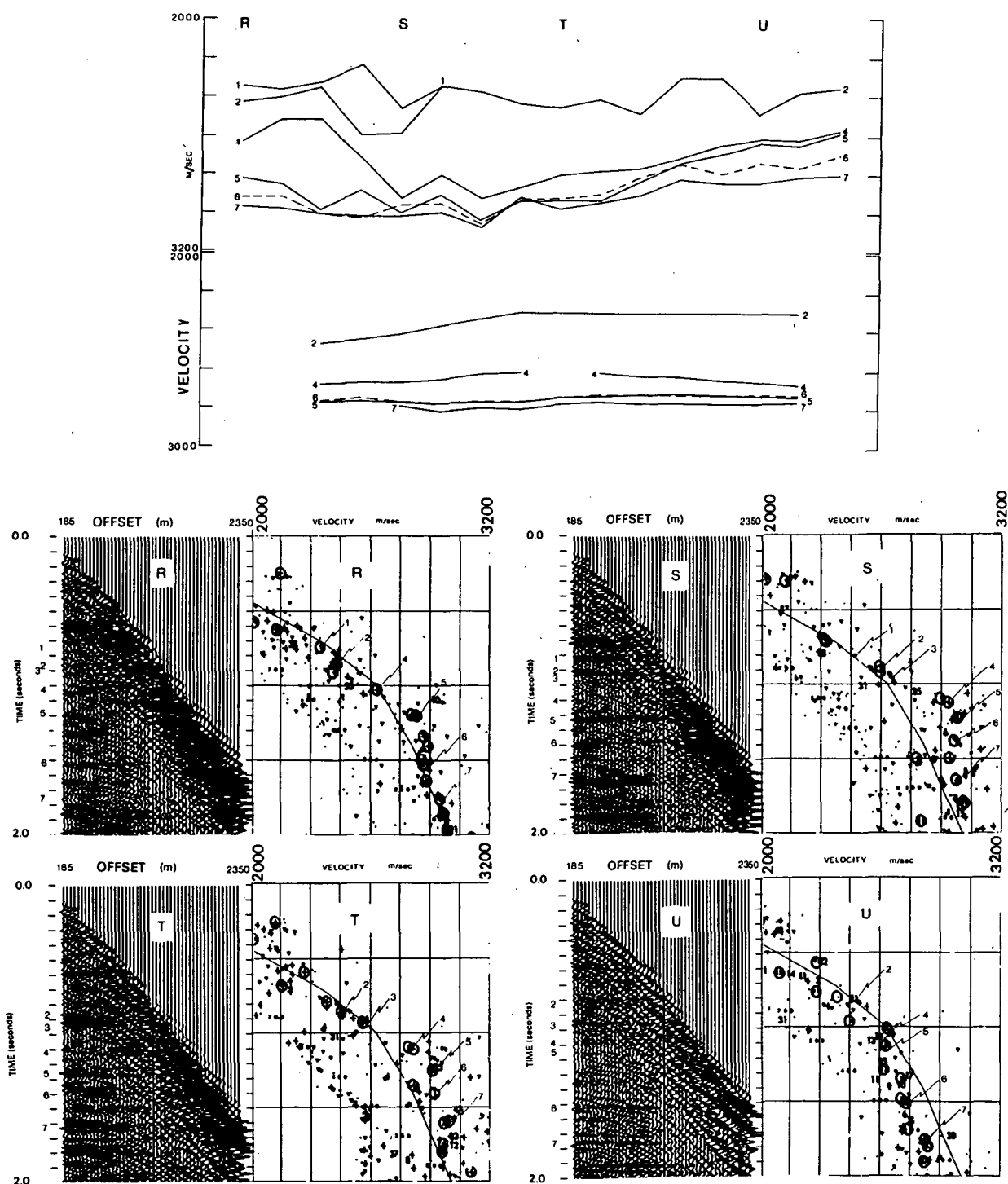


Fig. 2.50 Interpreted stacking velocities (top curves), and calculated stacking velocities for seven horizons on line 6. R, S, T and U represent typical velocity analyses along the line.

and U (Figure 2.43). Modelled velocities (Figure 2.50) suggest a smoother distribution. The large variance is due to the inability of the program to account for the laterally varying layer velocities and intrabed complexities. For this area raypath distortion problems are more significant than inconsistencies resulting from three-dimensional structures.

VII. CONCLUSIONS

The problems inherent in the conversion of stacking velocities to true vertical velocities have been studied by non-zero offset raypath tracing of primary P waves through a suite of varied geological sections. It has been shown that conversion errors can be caused by timing errors as a result of migration and raypath distortions.

Raypath modelling shows that:

1. The customary assumption that stacking velocities approximate root mean square velocities is invalid in areas of non-horizontal structures.
2. Essential velocity information from horizons overlain by geological irregularities is often difficult to recognise and is easily ignored or misidentified.
3. Standard fitting of hyperbolic curves to produce NMO traces is not valid in geologically difficult areas.
4. Stacking velocities need not be consistent for seismic lines shot over the same area using different field configurations.

5. Stacking velocities can vary greatly for the same spread length with different shot-first receiver offsets.
6. Three dimensional structures further increase conversion errors.

Velocity conversion errors of up to 50 percent and timing errors of up to 120 msec may occur for the simplest geological models. Depth errors involve the interplay of both velocity and timing errors and may be so significant as to impede the detection of subtle hydrocarbon traps.

The extension of these simple geological structures to the complex real earth further downgrades the accuracies of depth determination.

Chapter 3

STATIC CORRECTION IN IRREGULAR OR STEEPLY DIPPING WATER- BOTTOM ENVIRONMENTS

	page
I. INTRODUCTION	3.1
II. OBJECTION TO EXISTING REPLACEMENT STATIC CORRECTION TECHNIQUES	3.3
III. BASIC PHILOSOPHY	3.5
IV. MODELLING	3.10
1. Deep Water Canyon Model	3.10
2. Irregular Water-Bottom Model	3.14
V. CONCLUSIONS	3.17

I. INTRODUCTION

The distortions of apparent structure and stratigraphy in seismic sections, together with errors in seismic velocity determination caused by irregular geological subsurface interfaces, are well known (Miller, 1974; Wiggins *et al.*, 1976). Miller (1974) studied the effects of weathering on velocity, time estimates and stacking. Using a two-step static correction he first applied a replacement static to the CDP gathers and then a post-stack static correction to adjust reflection traveltimes to a mean depth on each stacked trace. Miller (*loc. cit.*) obtained reasonable stacked sections using rms velocity estimates from the NMO curves. The applied replacement static assumed that the rays passed directly downward to the interface from the source and directly upward to the receiver. Taner *et al.* (1974) considered this an acceptable assumption when a low velocity weathered layer overlays higher velocity sub-weathering layers as refraction causes waves to travel along paths which are close to vertical in the low velocity layer. Thus the variation of time delay along various paths remained reasonably small. It was noted that this assumption is doubtful when the near-surface layers producing the time anomalies have a higher velocity than the layers below.

Hileman *et al.* (1968), Taner *et al.* (1974), Wiggins *et al.* (1976) and Brooker *et al.* (1976) have used the redundancy inherent in CDP data to compute a statistical estimate of the static corrections. The static corrections used in these automatic static procedures are the time shifts necessary to best align the CDP traces before stacking such that

the primary reflections are enhanced for all record times. The time shifts are computed for all input traces using cross-correlation functions between CDP traces. The time shifts for each trace are composed of a shot static, a receiver static, any residual NMO present, and noise. Estimates of the shot and receiver static corrections are obtained by averaging different sets of the measured time shifts.

The automatic statics techniques are based on three major assumptions:

1. Near-surface effects introduce pure time delays which are surface consistent. Thus the same shot static applies to the shot at a particular location, independent of the various receiver locations. Similarly the receiver static is assumed to be the same for all shots received at a given location.
2. The corrections are time invariant.
3. The corrections are independent of frequency.

Brooker *et al.* (1976) stated that many automated static techniques are unable to extract statics whose spatial wavelengths are longer than a spread length. They illustrated a new procedure for broadband estimation of surface consistent statics.

II. OBJECTION TO EXISTING REPLACEMENT STATIC CORRECTION

TECHNIQUES

This chapter describes a technique suitable for determining shot and receiver statics for both the broad and narrow wavelength problems. The need for such a technique arose due to the following objections to existing schemes:

1. The use of replacement statics induces errors in regions where rays do not pass directly downward to the weathered interface from the source or directly upward at the receiver. The use of large offsets and long spreads dictates that this condition is rarely met. Furthermore in regions with steeply dipping and irregular weathered layers, raypath distortions may also dictate that the rays do not leave the shots or arrive at the receivers in a vertical sense. The use of replacement statics in such cases introduces fictitious time shifts and consequent timing and velocity errors.
2. The shot static is not the same for all receivers at a given location since the raypath through the weathered layer varies for different receiver locations. Similar problems apply to receiver statics.
3. Near-surface effects cannot be considered to be time-consistent because reflections from successively deeper horizons take a progressively more vertical travel path from source to receiver (Figure 3.1). For a smooth near-surface layer the variation in path has little effect on the traveltime because the time increment in the near-surface layer is almost constant. However when there are excessive and abrupt variations of weathering the path variations for deeper reflectors may change sufficiently to make a

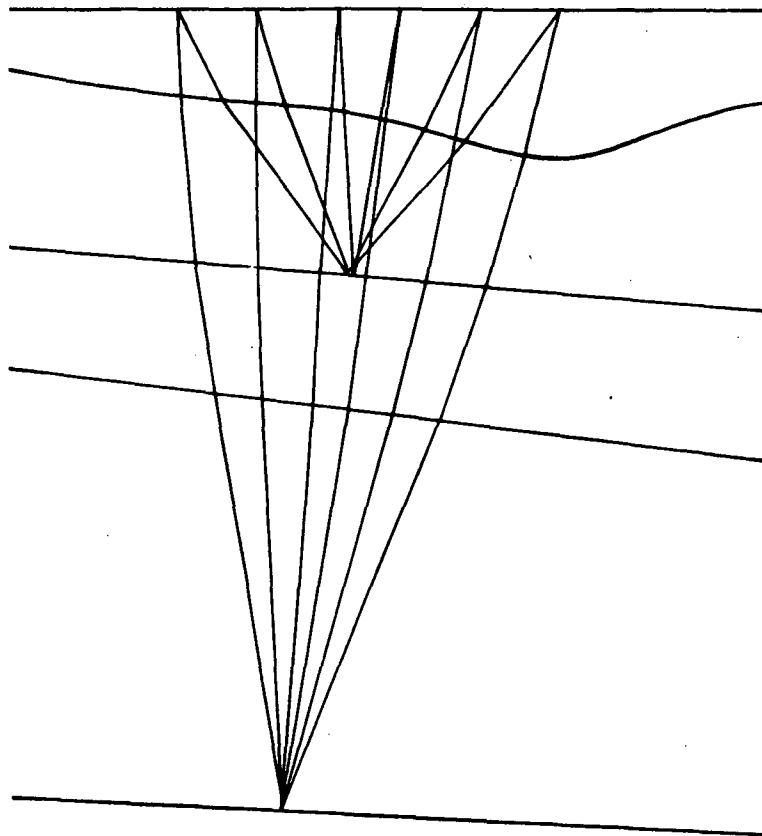


Fig. 3.1 Earth model illustrating raypaths to two horizons. Due to the different raypaths in the weathered layer for each shot or receiver location the static corrections cannot be considered time consistent.

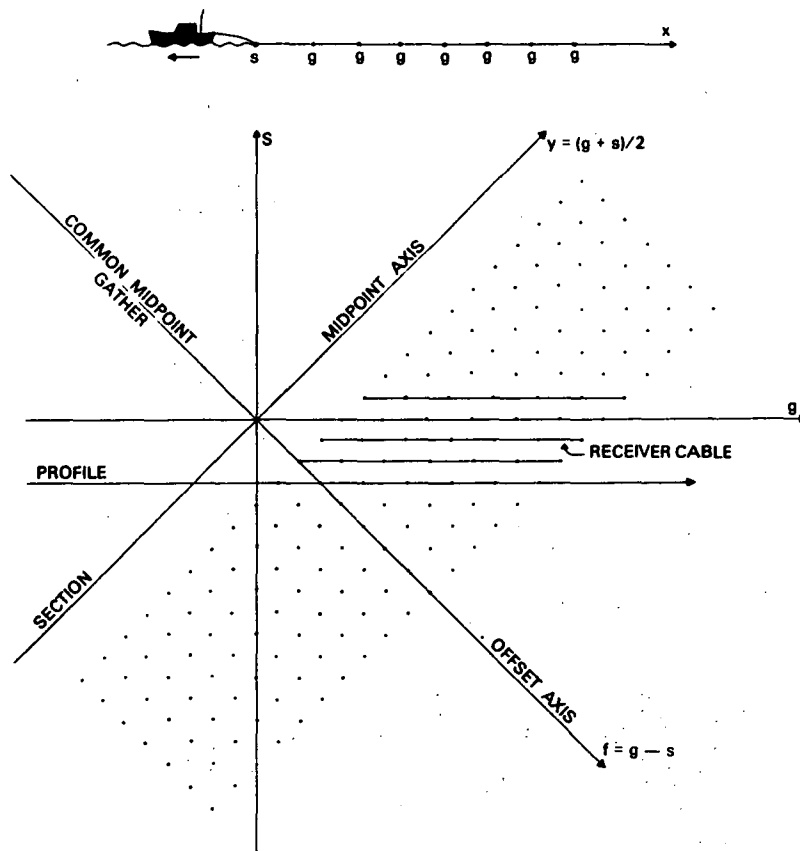


Fig. 3.2 The relationships along source coordinate s , geophone receiver coordinate g , offset coordinate $f = g - s$, and mid-point coordinate $y = (g + s)/2$ (after Claerbout, 1976).

replacement static correction applicable at only one time on the seismic trace. For multi-coverage work the time varying effect of replacement static corrections for any one family of CDP traces may be sufficient to cause reflections to be stacked out of phase.

4. To obtain a seismic section that represents the deeper horizons in their correct relative position without the influence of the shallower layers, automatic static determination techniques produce statics which are relative time shifts with respect to some datum plane. These relative shifts may not correspond to the absolute time measurement to the reflector.

These objections highlight the need to determine the raypath geometry through the near-surface layer for different reflectors in order to determine shot and receiver corrections. This chapter provides one such mechanism. The technique is especially useful for irregular water-bottom problems where the bottom profile may be accurately determined.

III. BASIC PHILOSOPHY

The method for determining shot and receiver wavefront statics consists of three important functions. The first two functions inter-relate to determine the raypath geometry through the near-surface layer while the third uses this information to determine the relative statics.

1. Determination of derivatives of the time surfaces for different reflectors.

In processing seismic data it is necessary to transform the data from a continuous profile coordinate system to give CDP data (Figure 3.2). The coordinates of the source (s) and detector (g) are measured, along the x axis which represents the ship's course. Also along the x axis are the shot to geophone offset coordinate, $f = g-s$, and the midpoint coordinate, $y = (g+s)/2$, between the shot and the geophone. Let the functions $t(s,g)$ and $t(x,y)$ represent continuous lines passing through the measured values of the reflection time (t) corresponding to any one reflector. Let $t_g = \partial t / \partial g$, $t_s = \partial t / \partial s$, $t_y = \partial t / \partial y$ and $t_f = \partial t / \partial f$ be derivatives of these time lines. t_g is the tangent to the time-distance curve (t versus g) seen on a profile corresponding to a fixed shotpoint (S_i). t_s is the tangent to the time-distance curve (t versus s) seen on a profile corresponding to a fixed receiver (g_i). t_y is the gradient along the seismic-section plane for a given offset while t_f is the gradient along a CRP gather for a particular midpoint coordinate.

The derivatives of the time surfaces in the two coordinate systems are

$$t_g = t_y/2 + t_f \quad \dots(1)$$

$$t_s = t_y/2 - t_f \quad \dots(2)$$

(Shah, 1973)

t_y and t_f are easily determined from CDP data so t_g and t_s are readily calculated.

2. Determination of the emergence angle from the source and incident angle at the detector.

Consider a fixed source and two of its rays emerging at two neighbouring receivers A and B (Figure 3.3) a distance Δg apart on the surface, after reflection from some interface. Further consider a two-dimensional model of the earth with a point source located in the same plane. Let the emergence angles (with the vertical) of the raypaths at A and B be β_g and $\beta_g + \Delta\beta_g$ and the traveltimes from the source to receivers A and B be t and $t + \Delta t$ respectively. AC is a tangent to the wavefront at A and if V_1 is the velocity of the material near the receivers, the infinitesimal distance BC is equal to $V_1 \Delta t$. Thus

$$\frac{V_1 \Delta t}{\Delta g} = \sin \beta_g \quad \dots(3)$$

In the limiting case as $\Delta g \rightarrow 0$ this equation becomes

$$V_1 t_g = \sin \beta_g \quad \dots(4)$$

By means of the law of reciprocity for shot and receivers, the emergence angle for rays from various shots to a fixed receiver can also be determined. If β_g is the departure angle from the shot, then

$$V_1 t_s = \sin \beta_s \quad \dots(5)$$

Using equations (4) and (5) it is possible to determine the incident angles at all receivers and emergence angles at all shots for data in CDP format.

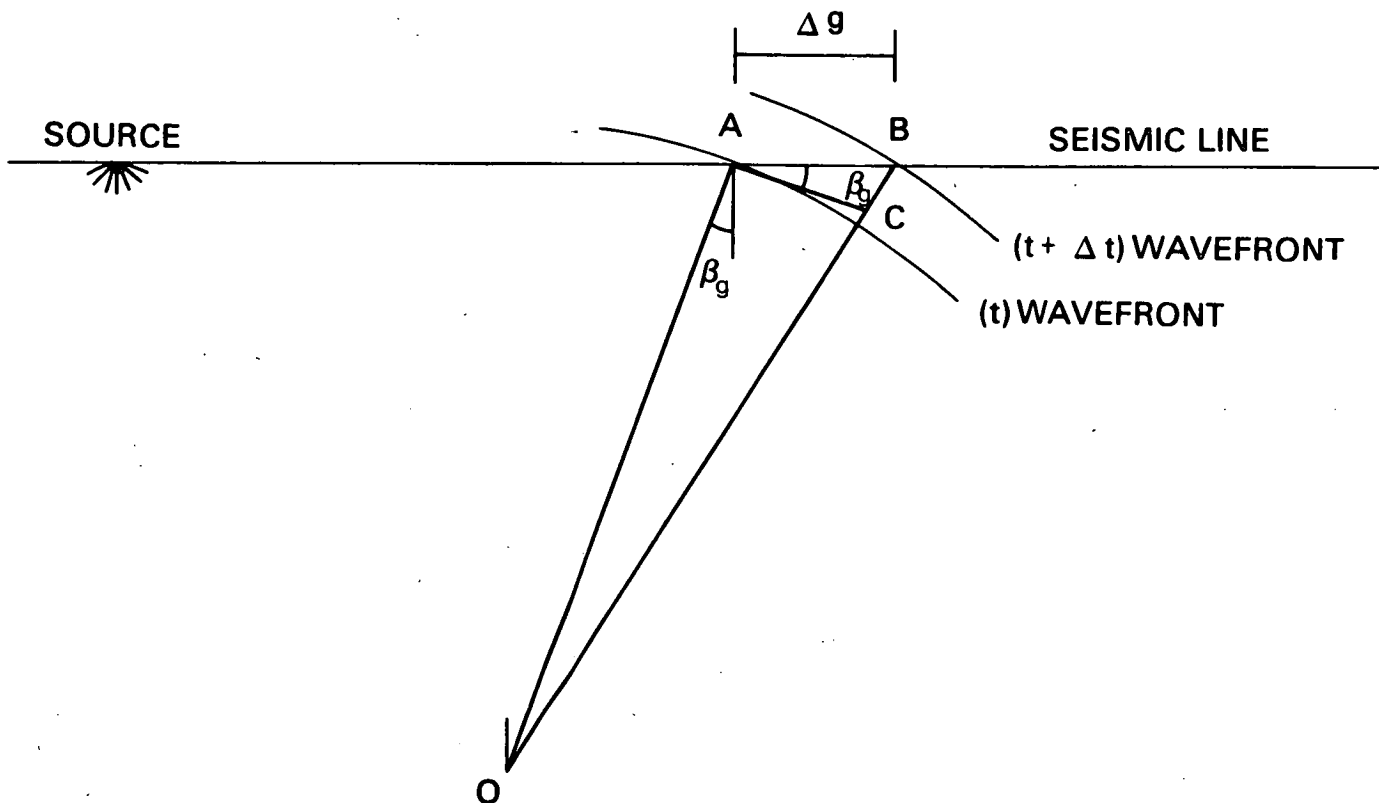


Fig. 3.3 Geometry of a wavefront approaching receivers (after Shah, 1975).

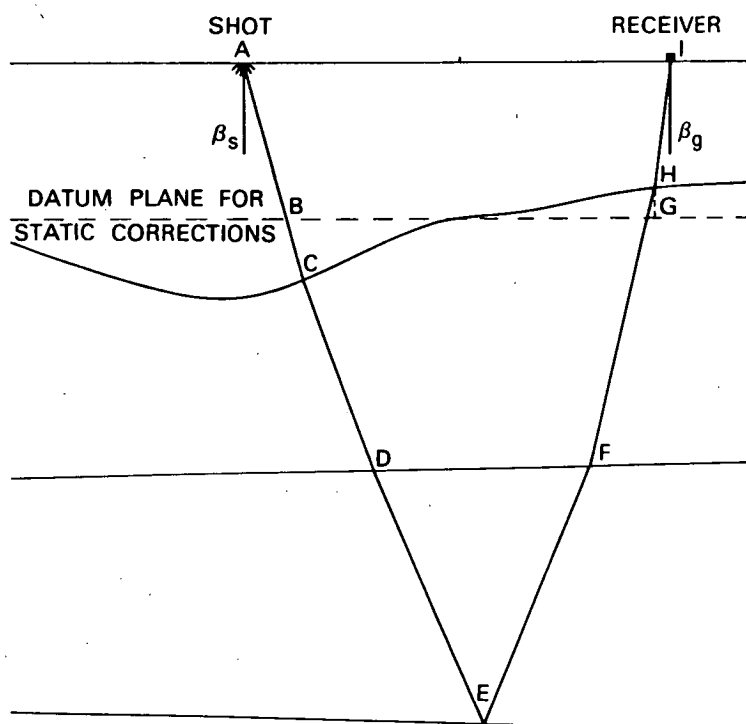


Fig. 3.4 Earth model illustrating the shot replacement, BC, and receiver replacement length, HG, used for determining wavefront static corrections relative to a datum plane defined as the depth below the surface to the near-surface layer at the centre of the given CDP gather.

3. Determination of static corrections using raypath geometry data.

Static corrections are merely time shifts for all raypaths to a floating reference plane, arbitrarily defined here to be the depth of the base of the near-surface layer at the centre of the given CDP gather (Figure 3.4). The near-surface layer depth profile is known. Thus the shot replacement length, BC, and receiver replacement length, HG, can be determined knowing β_s and β_g .

The shot static is defined as

$$\Delta t_s = \frac{BC}{V_1} - \frac{BC}{V_2} \quad \dots(6)$$

while the receiver static is defined by

$$\Delta t_g = \frac{HG}{V_1} - \frac{HG}{V_2} \quad \dots(7)$$

where Δt_s is the shot static correction to the n^{th} time trace in a CDP set.

Δt_g is the receiver static correction to the n^{th} time trace in a CDP set.

V_1 is the velocity of the near-surface layer.

V_2 is the velocity of the material immediately below the weathering layer.

The static corrections have a negative sign if the point of intersection of the ray with the near-surface layer is above the datum plane. The corrections can be applied to all traces in a CDP set. By selecting different reflectors the time dependency of the corrections can be determined.

IV. MODELLING

A test set of CDP seismic reflection data was generated using a ray tracing program and analysed with processing techniques currently used on actual field records. The superior quality and flexibility of the synthetic sections when compared to real data allowed the various sources of stacking, velocity and timing errors due to replacement static problems to be easily isolated.

Simplified models of two typically complex irregular water-bottom situations have been modelled.

1. DEEP WATER CANYON MODEL

Figure 3.5 represents a deep water canyon overlying a series of horizontal layers whose velocity increases with depth. One half of this model could represent a continental slope. Gathers consisting of 24 traces with a geophone separation of 92 m and a shot-first receiver offset of 92 m for surfaces 3, 5 and 7 have been traced (Figure 3.6) at selected locations along the surface. Raypath plots, together with the corresponding shot and receiver statics determined by the wavefront method have been plotted. The total static applied to a single trace is the summation of the shot and receiver statics. Two features emerge. Firstly, the traces deviate from a vertical path so that normal replacement static techniques are invalid. Secondly, the static corrections are time variant. The static corrections for the gather at 6065 m, for example, have a static difference of up to 45 msec for the far traces between

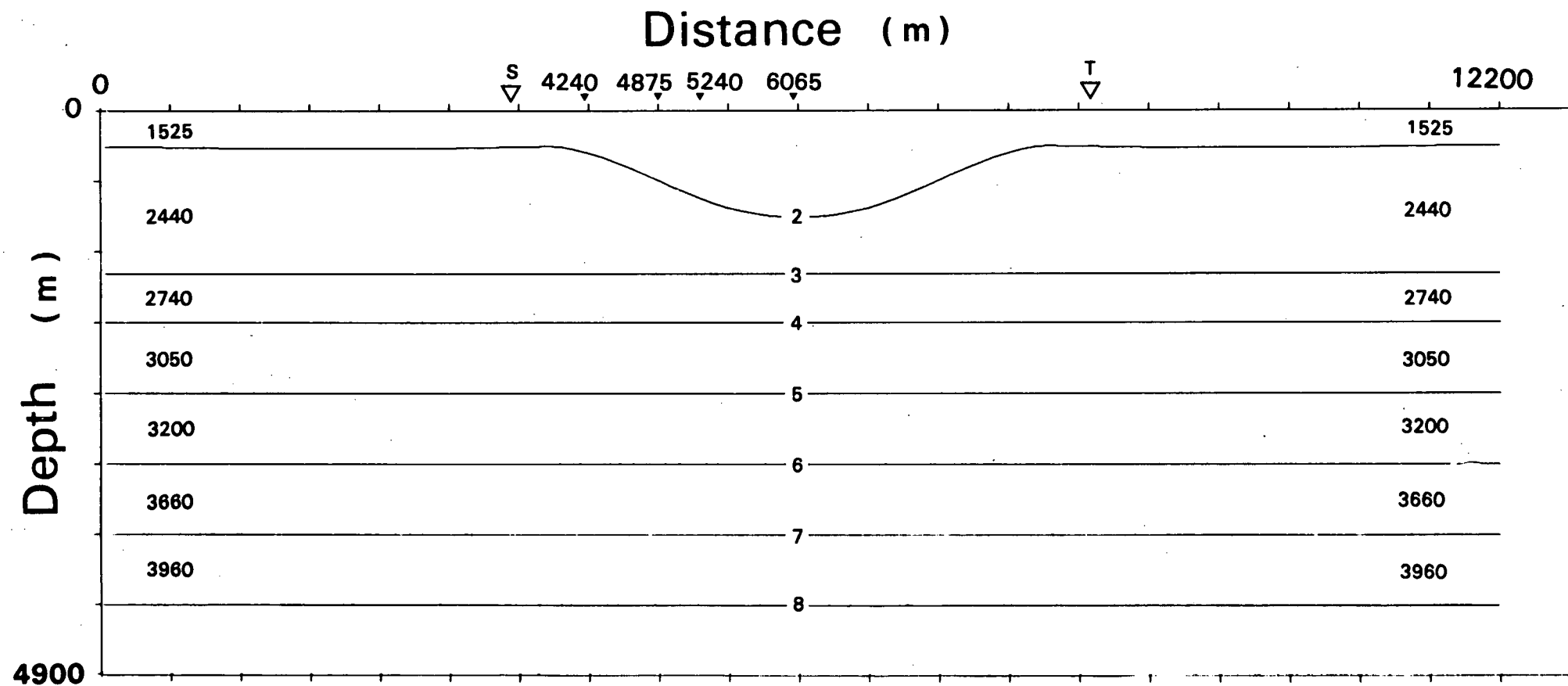


Fig. 3.5 Model of a deep water canyon overlying a series of horizontal layers, with velocity increasing with depth. S and T are the velocity profile extremities.

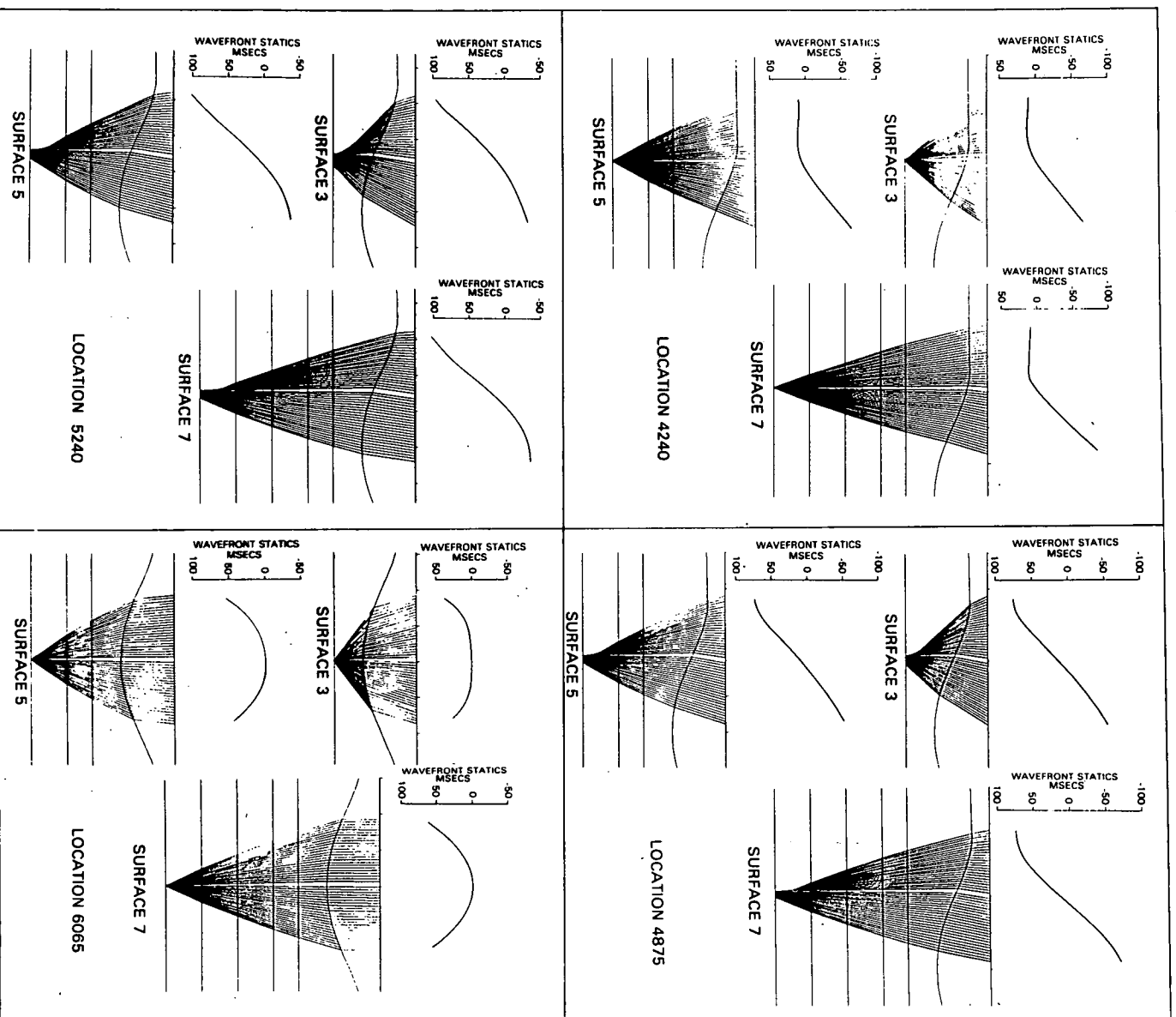


Fig. 3.6 Canyon model gathered plots together with wavefront shot and geophone statics for three surfaces at four locations.

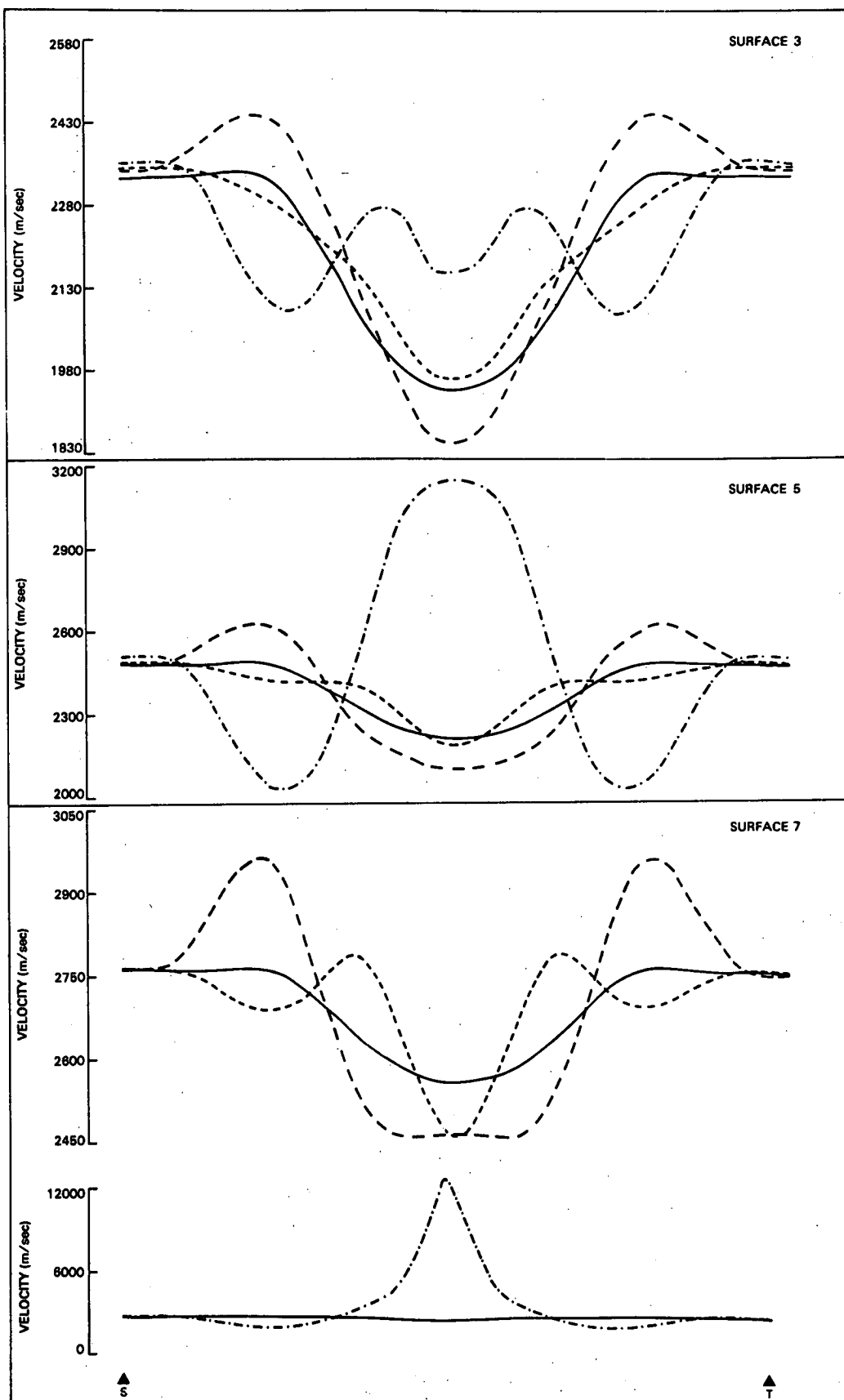


Fig. 3.7 Velocity profiles for the canyon model.

- rms velocity profiles
- stacking velocity profile as determined by ray tracing, without static corrections
- - - stacking velocity profile with normal replacement statics
- . - . - stacking velocity profile with wavefront statics.

surfaces 3 and 7, a static difference of 15 msec for traces of the gather at 4875 m. Static difference errors of 10 msec occur in the shot receiver statics for these traces corresponding to the middle traces of the gather at 5240 m. Figure 3.7 shows the rms velocity distribution, between S and T, across the canyon for surface 3. Superimposed on this curve are the stacking velocities derived prior to static correction, the stacking velocities obtained with normal replacement statics and those for wavefront replacement statics. The wavefront static most closely approximates the rms velocity curve. Similar trends (Figure 3.7) occur for surfaces 5 and 7, but the wavefront static corrected velocity curve for surface 7 oscillates about the rms curve. This is because refraction at the base of the first layer has been ignored and slight timing errors occur.

2. IRREGULAR WATER-BOTTOM MODEL

A seismic section and the corresponding model of an irregular water-bottom layer overlying a series of sub-horizontal layers are shown in Figure 3.8. The rms and stacking velocity curves between C and D, determined with and without wavefront replacement, together with actual velocity analysis picks at selected locations for surfaces 4, 7 and 10 show the reliability of the velocity determination using wavefront statics (Figure 3.9). The difference between the stacking velocity picks, which have no replacement statics applied, and those from ray tracing is due partially to the averaging of velocities about the gather point in normal processing, as well as imperfections in the model.

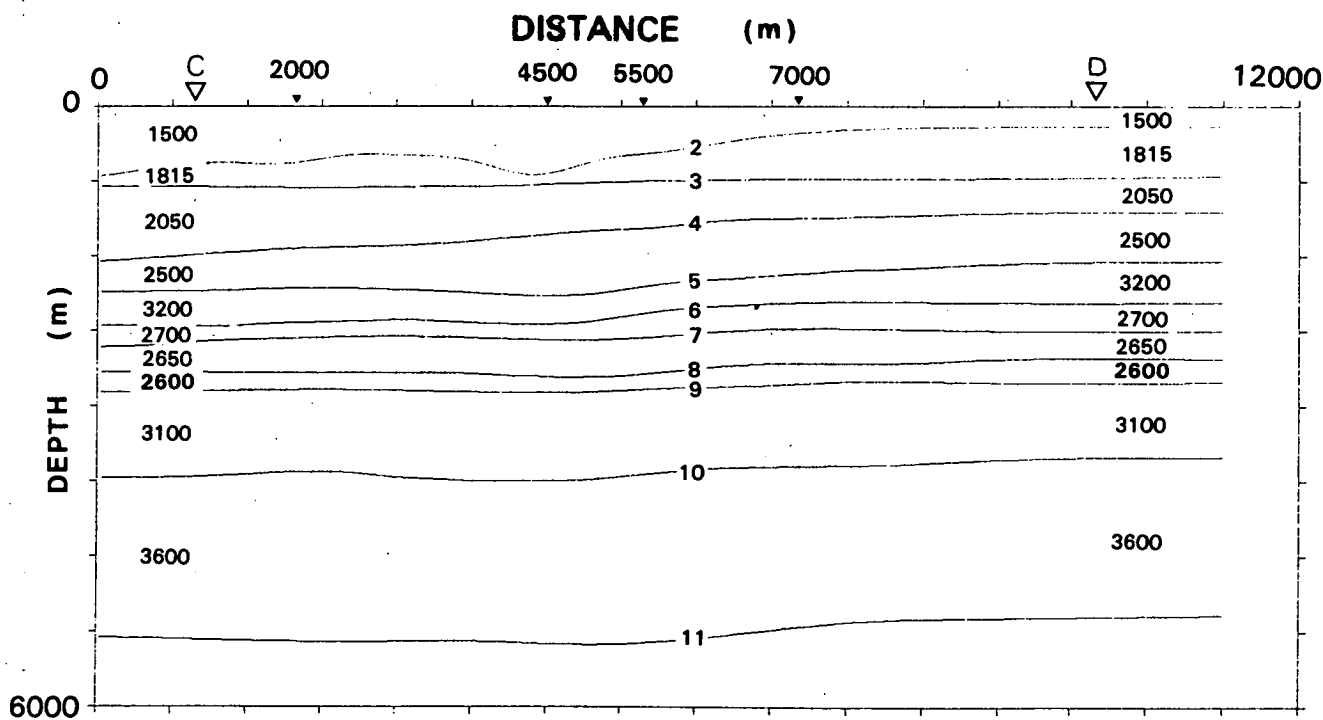
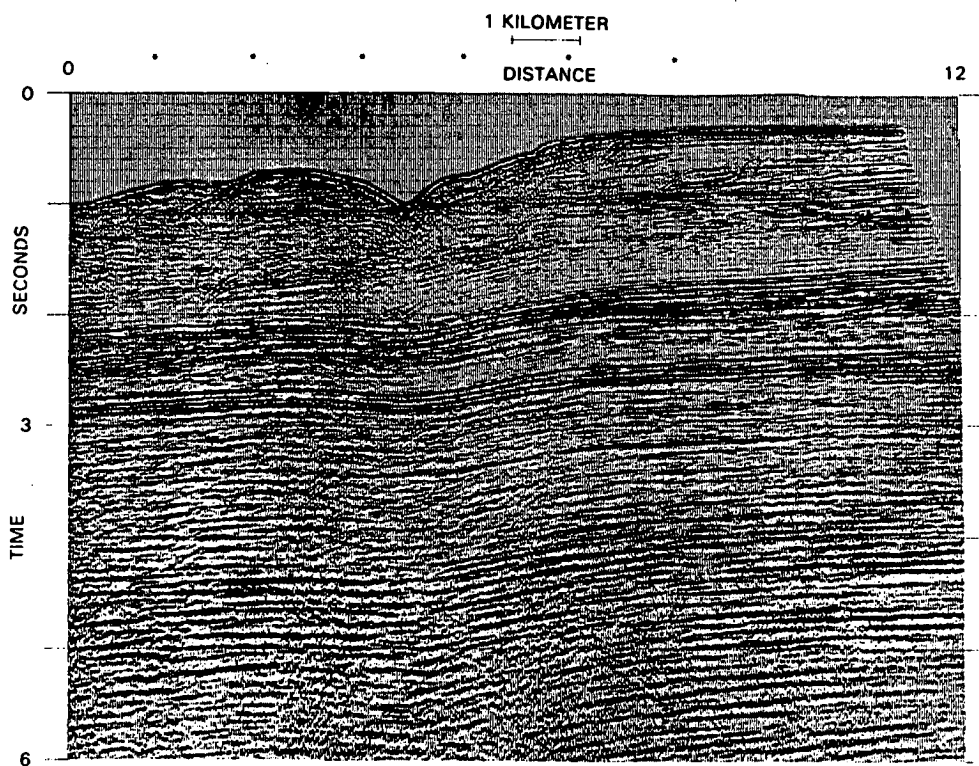


Fig. 3.8 Seismic section together with its corresponding model for an irregular water-bottom layer overlying a series of sub-horizontal layers. The asterisks indicate locations of velocity data.

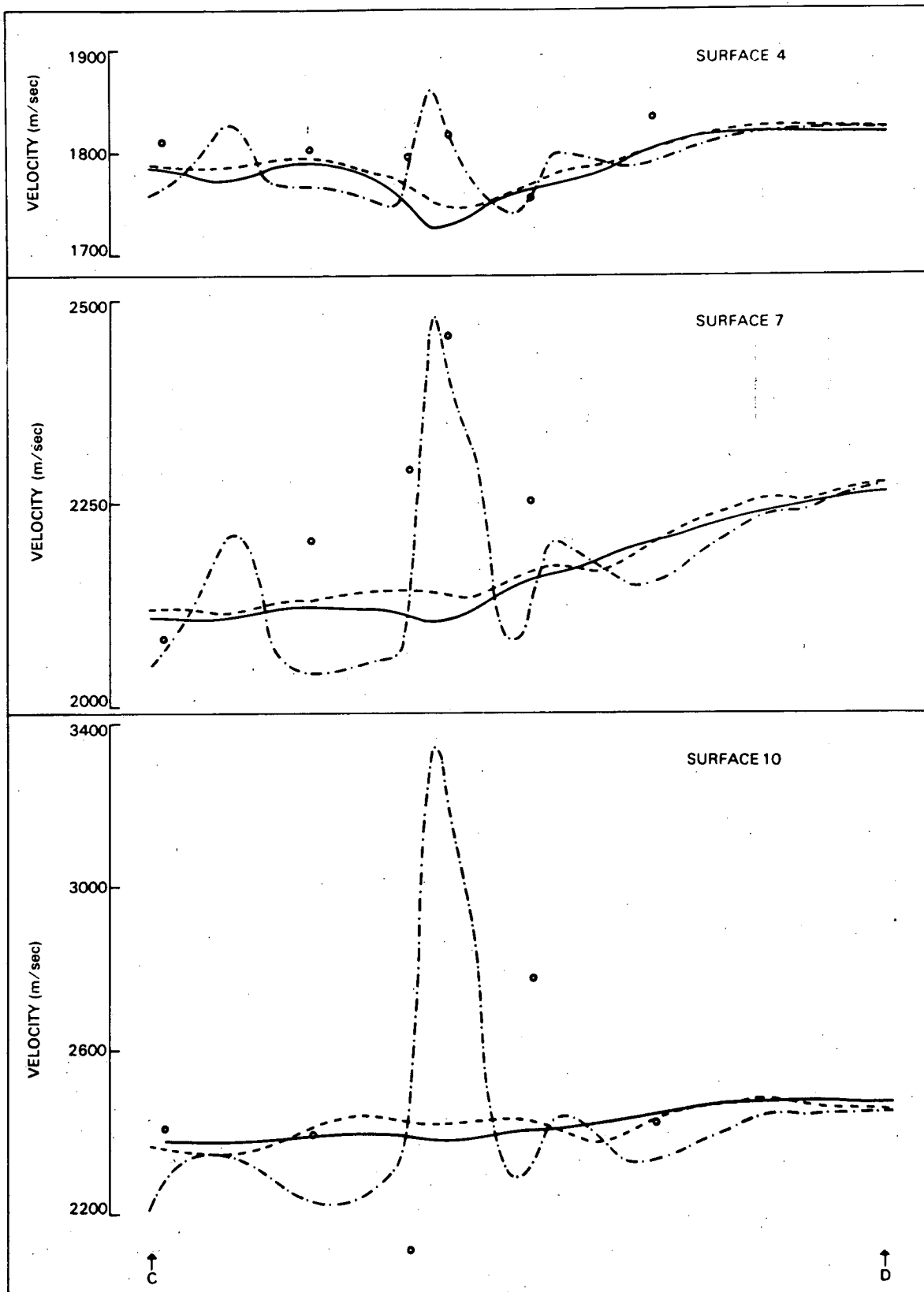


Fig. 3.9 Velocity profiles for the irregular water-bottom model.

- rms velocity profile
- · - · - stacking velocity profile, as determined by ray tracing without static corrections
- - - - stacking velocity profile with wavefront statics.

Raypath plots and the corresponding wavefront statics (Figure 3.10) for selected gathers show the departure of the waves from the vertical as assumed in ordinary replacement statics. The gathers at 4500 m and 5500 m clearly show the time variance of the static corrections.

V. CONCLUSIONS

Raypath modelling over complex water-bottom situations has indicated pitfalls in existing replacement static correction procedures. Raypaths for long seismic spreads, or in regions with irregular water bottoms, do not pass directly downward to the water bottom or directly upward at the receiver, and introduce fictitious time shifts and consequent timing and velocity errors when conventional replacement statics are used. With irregular or long wavelength water bottoms replacement statics cannot be considered time invariant and if correct stacking is to be performed appropriate static corrections should be made for various layers. Surface consistency in static corrections, whereby the same shot (receiver) static applies to the shot (receiver) at a particular location, independent of the various receiver (shot locations) is shown to be false in irregular water-bottom environments.

Wiggins *et al.* (1976) noted that static corrections, determined by automatic cross-correlation techniques, which have spatial wavelengths longer than a cable length are poorly determined. The wavefront technique is independent of the wavelength of the near-surface layer providing the

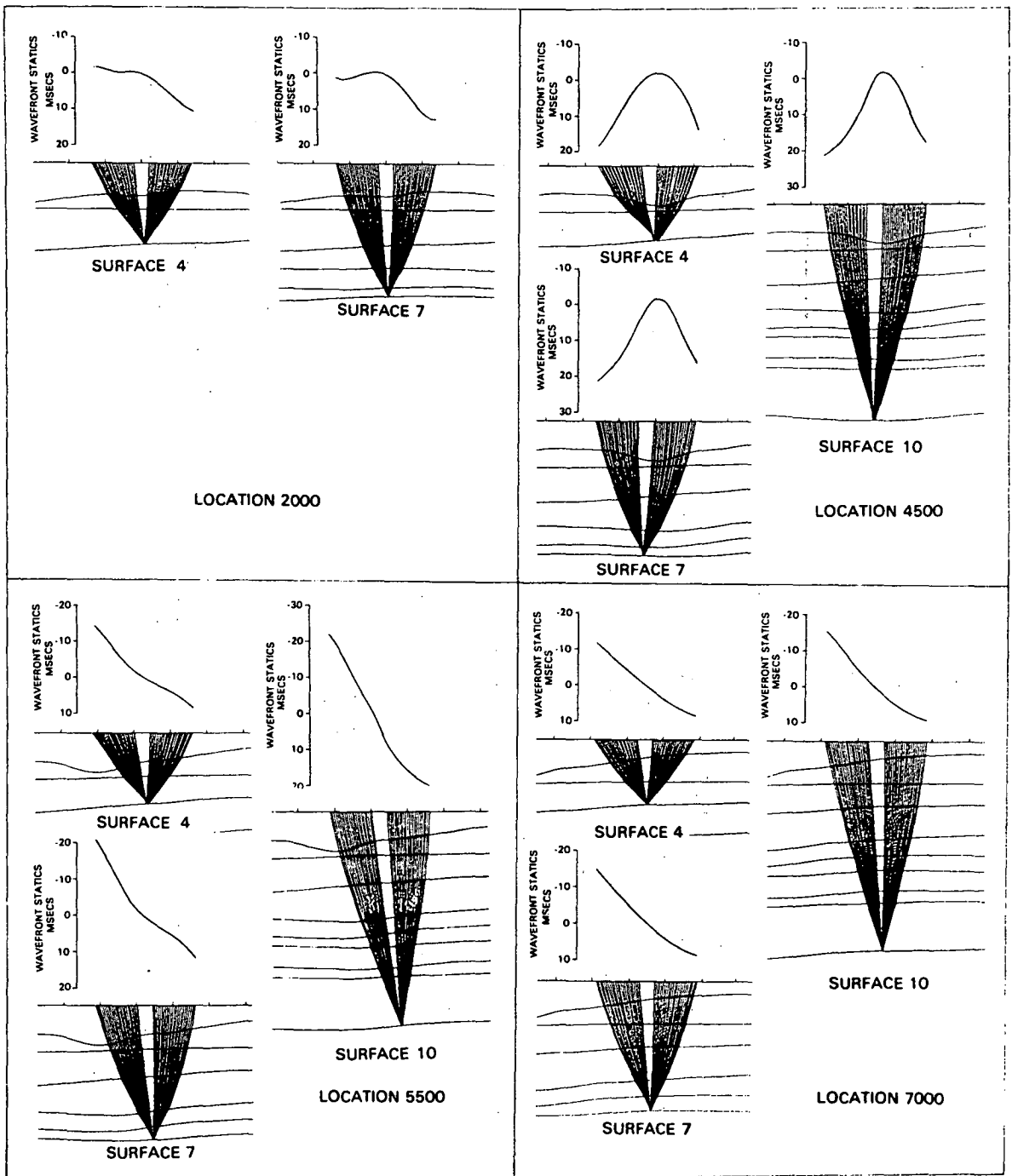


Fig. 3.10 Irregular water-bottom model gathered plots together with wavefront static curves for three surfaces at four locations.

layer can be defined. Use of the wavefront static method to account for three-dimensional variations in the near-surface layer is an obvious extension, and would enhance the effective use of the wavefront technique.

The method is not exclusive. Digicon with their sophisticated datum correction program REVEAL* (Sherwood *et al.*, 1976) correct seismic data, given an estimate of the near-surface velocity variations and the specification of the desired replacement medium. Their program computes times of raypaths through the assumed and the replacement media to hypothetical horizontal reflectors at depth. For each seismic trace a list of hypothetical reflection times on the actual input seismic trace and a corresponding list of times for the desired output are developed, so establishing a dynamic time correction to apply to each seismic trace, as opposed to a more simplistic static time shift. The difference between the two methods is that the wavefront method approximates the appropriate path of the ray through the near-surface region by noting the incident angle of the emerging rays, and as such can be used for horizons which dip in any direction at depth. No comparison of the two methods has been made and the wavefront method is presented as another alternative to a recognised problem.

While automatic cross-correlation techniques result in a final section having better spatial continuity and, to some extent, a more consistent velocity analysis after than before correction, the question still arises as to whether

* Trademark of Digicon Inc.

these velocities are consistent with real velocities. As the technique involves bringing primary events into alignment amongst CDP traces for some input velocity function generally determined prior to static corrections, inaccuracies in this initial choice of velocity function will result in an overall velocity inaccuracy after automatic statics even though the velocity spectra may be more consistent after such corrections. The wavefront static technique results in a better velocity determination which could be subsequently used in cross-correlation static techniques to yield a section having reflectors with greater continuity.

Chapter 4

SEISMIC VELOCITY AND MIGRATION DETERMINATION FOR COMPLEX GEOLOGICAL AREAS

	page
I. INTRODUCTION	4.1
II. THE MIGRATION PROBLEM	4.4
1. Two-Dimensional Plane Dipping Layer	4.4
2. Three-Dimensional Plane Dipping Layer	4.15
3. Diffractions	4.21
4. Multiples	4.23
III. THE RAYPATH DISTORTION PROBLEM	4.24
IV. CONCLUSIONS	4.32

I. INTRODUCTION

Existing velocity determination methods operate by fitting time-distance hyperbolas to reflection events. Taner & Koehler (1969) and Hubral & Krey (1980, pp.14-16) related the travel-time (T_s) from a shotpoint, through a number of uniform horizontal layers, to an interface and back to a receiver a distance X from the shotpoint by the infinite series

$$T_s^2 = C_1 + C_2 X^2 + C_3 X^4 + \dots + C_j X^{j-2} + \dots \quad \dots(1)$$

The coefficients C_j ($j = 1, 2, \dots, \infty$) are functions of the layer thickness and velocities. The first two coefficients are defined by

$$C_1 = T_0^2 \quad \dots(2)$$

and

$$C_2 = \frac{1}{V_{rms}^2} \quad \dots(3)$$

where T_0 is the two-way vertical travelttime and V_{rms} is the root mean square (rms) velocity.

Most current methods of obtaining stacking velocities are based on the two-term truncation of equation (1) so that the stacking velocity does not equal the true rms velocity except where the ground is homogeneous.

Blackburn (1980) in studying non-zero offset raypaths through a suite of varied geological models illustrated the order of magnitude of these errors which result from migration and raypath distortions due to complex overburden structures (Figures 4.1 and 4.2), while Hubral & Krey (1980) provided an algorithm based on normal incident wavefront curvatures, for recovering interval velocities from common depth point (CDP) surface measurements in such regions. Similar methods do not

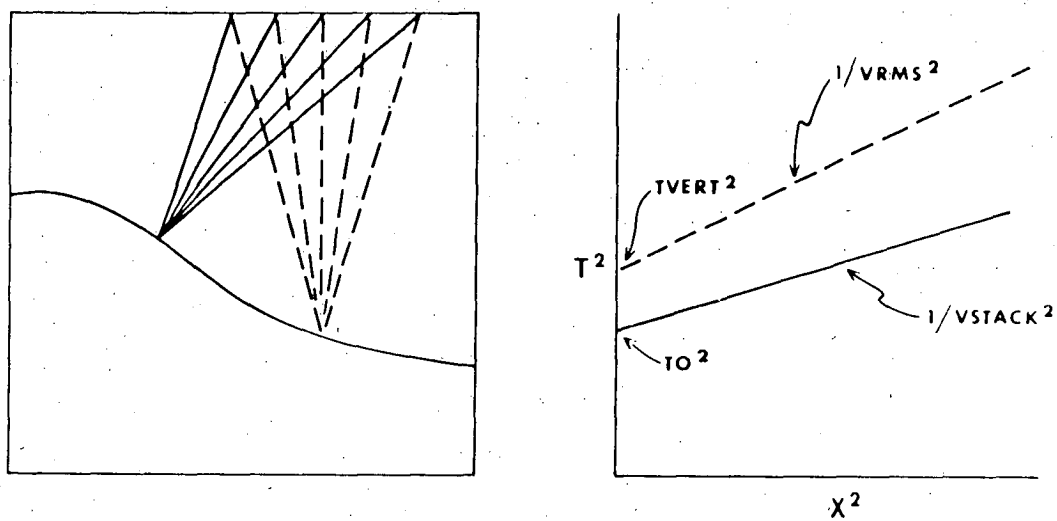


Fig. 4.1 Schematic geological section showing actual raypaths (solid lines) and hypothetical raypaths (dashed lines) for a vertical common reflector point. Corresponding $T^2 - X^2$ plots show that the zero offset time is smaller than the vertical travel-time while actual stacking velocities are greater than the rms velocities for that location. The CRP is removed from the vertical position. This is the migration problem.

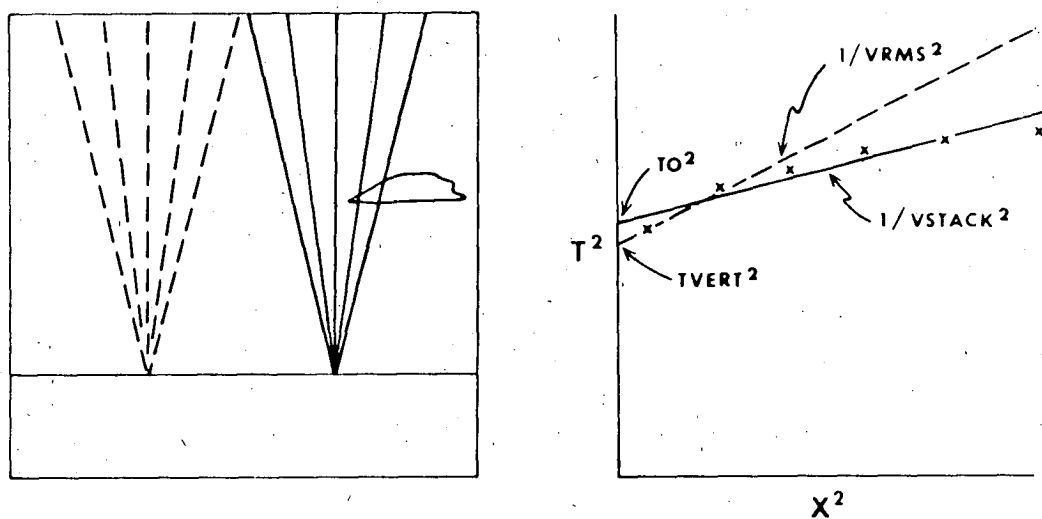


Fig. 4. 2 Schematic geological section containing a high velocity inhomogeneity. Gathered plots and their corresponding $T^2 - X^2$ plots show that the stacking velocities and zero offset time over the inhomogeneity are greater than the corresponding homogeneous case. The CRP for the inhomogeneous situation is smeared. This is the raypath distortion problem.

exist for non-zero offset raypaths. This chapter provides a method for determining velocities in complex media for general raypaths. Both the migration and raypath distortion problems are discussed.

II. THE MIGRATION PROBLEM

1. TWO-DIMENSIONAL PLANE DIPPING LAYER

Consider a plane dipping layer (Figure 4.3) which can be represented by the equation

$$Z = Z_0 + a \tan \theta \quad \dots(4)$$

where θ is the layer dip angle, Z_0 the depth below the origin (0) and the horizontal distance (a) is measured from the origin. The distance SG between the source S and receiver G is ℓ , while x denotes the abscissa of the midpoint of the baseline. The reflection point P (a , $Z_0 + a \tan \theta$) is located on the boundary and SP and PG correspond to the incident and reflected rays. PN is the normal from the reflection point P and α is the angle of reflection.

It can be shown that the travel time (t) is given by

$$t = \frac{1}{V} \left(\ell^2 \cos^2 \theta + 4(x \sin \theta + Z_0 \cos \theta)^2 \right)^{\frac{1}{2}} \quad \dots(5)$$

where V is the overlying velocity.

Simple construction shows that the bracketed term $(x \sin \theta + Z_0 \cos \theta)$ is the distance MQ along the normal from the midpoint of the profile. Equation (5) corresponds to the formula given by Levin (1971) for a common depth point (CDP) gather. Only for $\ell = 0$ is the curve t represented by a

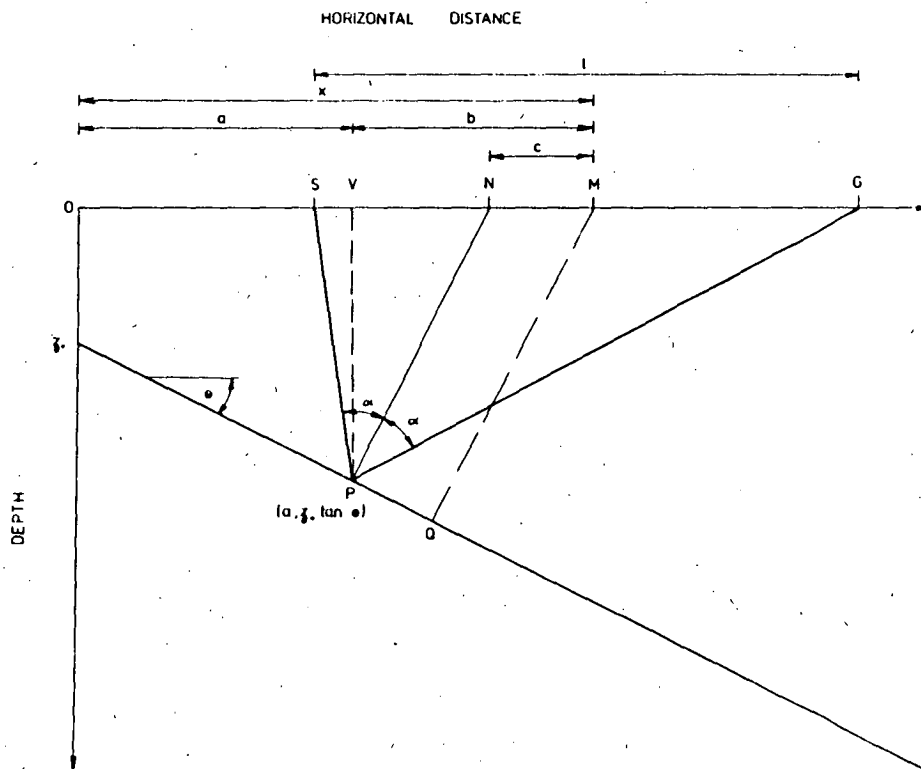


Fig 4. 3. Plane dipping layer model. The segment SPG represents a ray from source (S) to geophone (G) reflected from a plane dipping at an angle (θ), b and c are the horizontal displacements from the midpoint of the spread (M) to the reflector point and the surface intersection of the normal from the common reflector point (P).

straight line: the departure from a straight line increases with increasing shot-geophone separation and reflector dip. Intuitively the offset and time gradients should be related to the velocity and dip parameters.

The time gradient $dt/d\ell$ and dt/dx of the field have the form

$$A = \frac{dt}{d\ell} = \frac{\ell \cos^2 \theta}{V(\ell^2 \cos^2 \theta + 4(x \sin \theta + Z_0 \cos \theta)^2)^{\frac{1}{2}}} \quad \dots(6)$$

and

$$B = \frac{dt}{dx} = \frac{4(x \sin \theta + Z_0 \cos \theta) \sin \theta}{V(\ell^2 \cos^2 \theta + 4(x \sin \theta + Z_0 \cos \theta)^2)^{\frac{1}{2}}} \quad \dots(7)$$

Solving equations (5) to (7) and taking the origin about the midpoint M, it can be shown that

$$V = \left[\frac{4\ell(t - A\ell)}{4At(t - A\ell) + B^2\ell t} \right]^{\frac{1}{2}} \quad \dots(8)$$

$$Z_0 = \left[\frac{\ell(t - A\ell)}{4A} \right]^{\frac{1}{2}} \quad \dots(9)$$

$$\theta = \pm \arctan \left[\frac{B^2\ell}{(4A(t - A\ell))} \right]^{\frac{1}{2}} \quad \dots(10)$$

where the sign of the dip angle is dependent on the sign of B.

Furthermore the horizontal distance (b) (Figure 4.3) between the reflecting point (P) and the midpoint (M) is given by

$$b = \frac{B\ell t}{4A(t - A\ell) + B^2\ell} \quad \dots(11)$$

while the distance c from the midpoint to the surface expression of the normal from the reflecting point is

$$c = \frac{B\ell^2}{4(t - A\ell)} \quad \dots(12)$$

Both b and c are always offset from the midpoint of the shot receiver locations in the up-dip direction.

The depth of the reflecting point P , can be obtained from

$$Z = Z_0 + b \tan \theta \quad (13)$$

Thus complete depth migration and velocity determination can be obtained from the time gradients about the trace.

The use of these formulae are demonstrated for the hypothetical curved reflector model (Figure 4.4) having a constant overburden velocity of 2000 m/sec. While the formulae are for plane dipping layers, the curved surface approximates a plane for the reflection region required to obtain accurate time gradients. Synthetic CDP gathers consisting of 48 traces with geophone separation of 50 m and a shot-first receiver offset of 50 m have been raytraced (Figure 4.5) and their stacking velocities, which are taken to equal the square root of the reciprocal of the slope of a least squares straight line through points on the t^2 - X^2 graph derived from the gather information, are plotted (Figure 4.5). Raypaths for the zero offset, midpoint and end traces have been plotted for two gather locations (Figures 4.6 and 4.7).

Note the three common reflector points for each gather and the smearing of the CDP for reflections from synclinal limbs. Only the stacking velocities from gathers to the synclinal base reflector point give a realistic velocity. Errors between 23% and 42% result from the velocities obtained from the synclinal limb reflector points. This model represents the classical synclinal bow-tie problem. The seismic problem is pictorially shown in Figure 4.8 and the problem can be summarized thus —

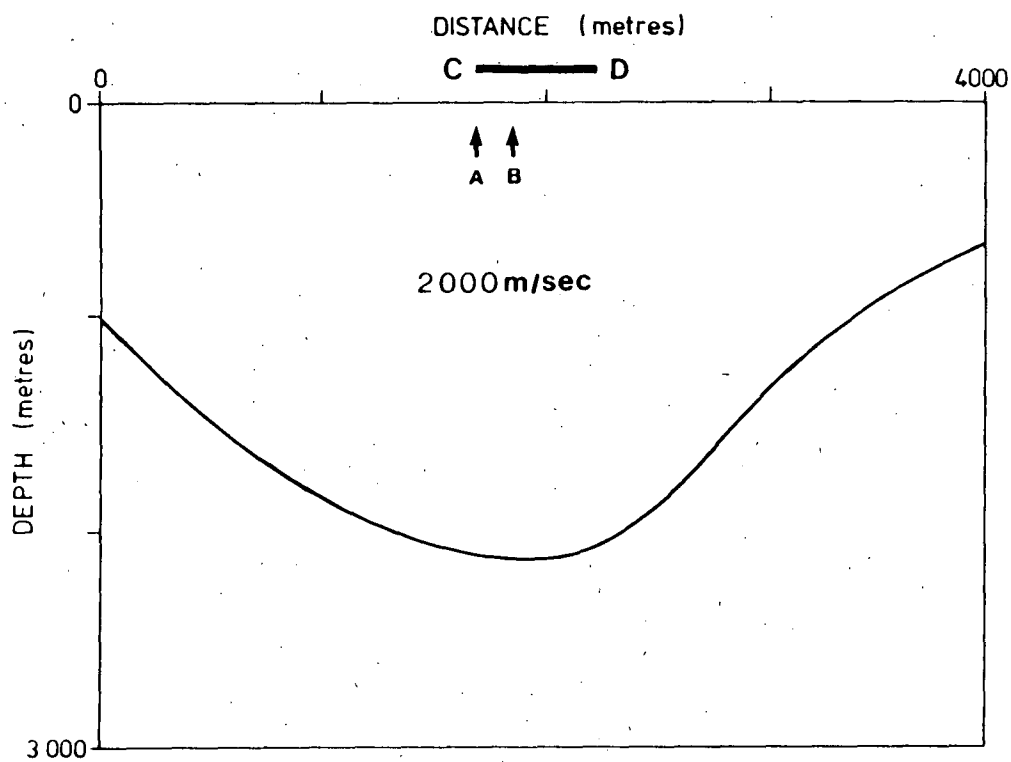


Fig. 4.4 Hypothetical curved reflector model. Synthetic gathers were generated every 50m in the region of the solid line (CD) (Figure 4.5) while gathers have been raytraced at locations A and B (Figure 4.6 and 4.7).

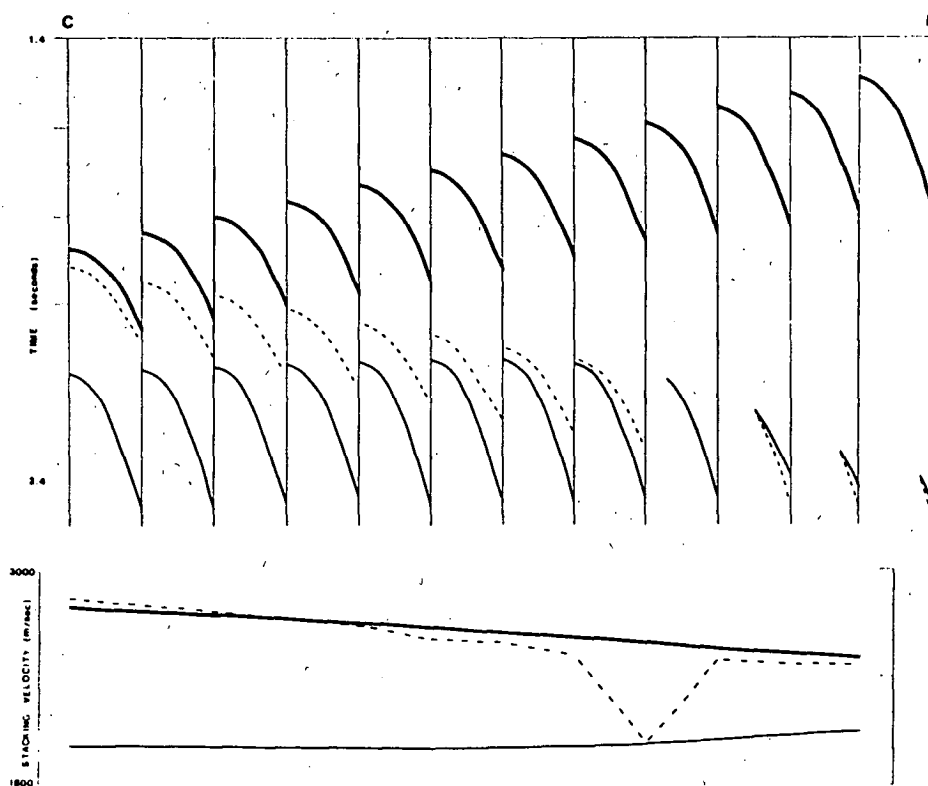


Fig. 4. 5 Synthetic CDP gathers and their stacking velocity distribution for the region C-D in Figure 4.4. Gather represented by the dashed lines are from the left synclinal limb, the medium continuous lines from the synclinal base while the solid continuous lines are from gathers whose common reflector points are on the right synclinal limb. Stacking velocities determined from gathers whose common reflector points are on the synclinal limbs are consistently greater than the true overburden velocity of 2000m/sec.

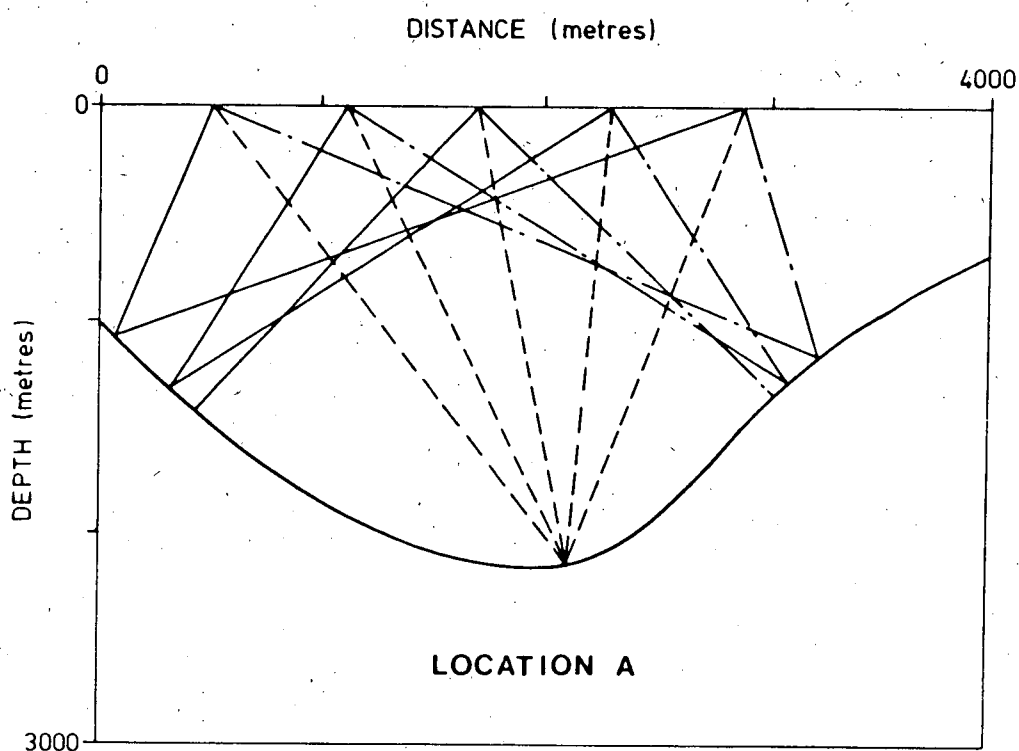


Fig. 4. 6 Near, middle and far traces for the synthetic gathers generated at location A (Figure 4.4). Note the three common reflector point positions and their smearing on the synclinal limbs.

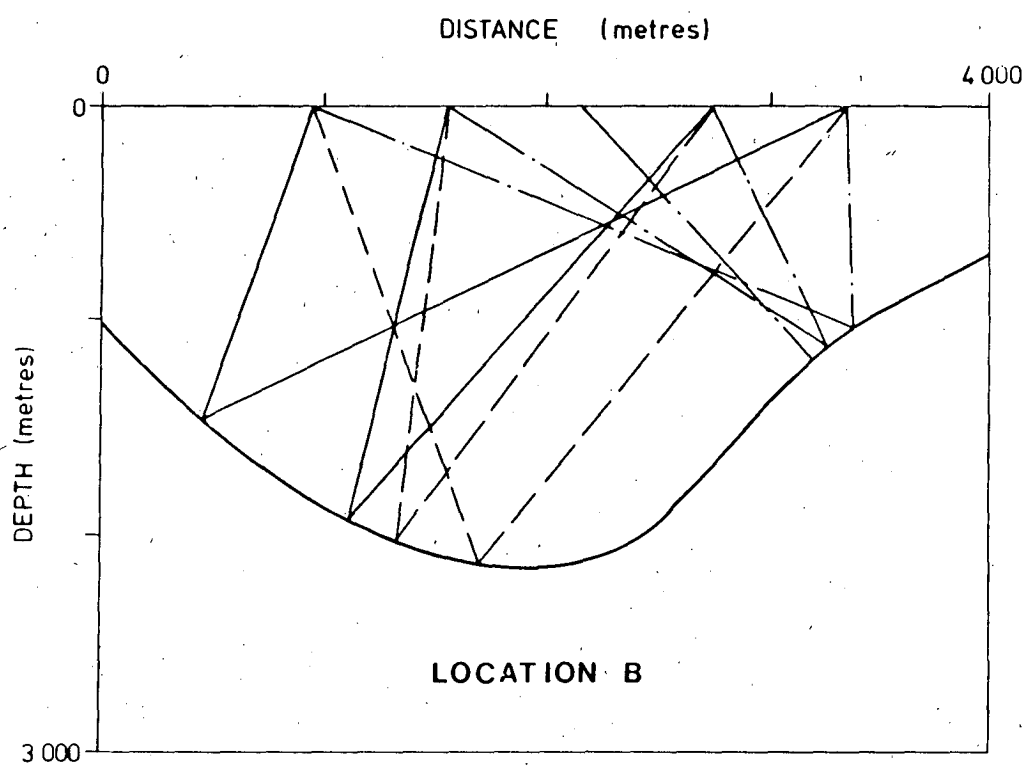


Fig. 4.7 Near middle and far traces for the synthetic gathers generated at location B (Figure 4.4). Note inner trace rays only occur for the leftmost and central common reflector points.

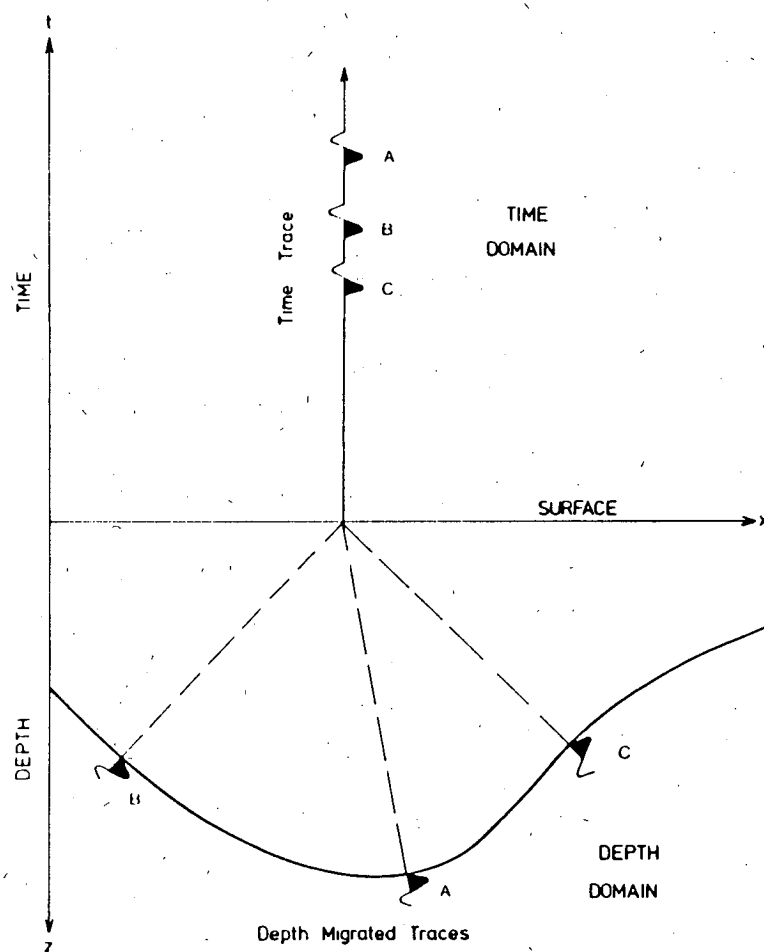


Fig. 4. 8 The seismic problem - Given a time trace can reflection events A, B, and C be placed in their correct spatial position?

given a time trace, can the reflection events A, B and C be placed in their correct spatial position?

The above formulae are applied to the gather at location A (Figure 4.4). Time gradients are determined assuming a one millisecond sampling interval and using neighbouring traces in both the x and l direction. The results shown in Table 4.1 illustrate that the time trace could be separated about the three common reflector points. Six traces for each gather are shown in the table and standard deviation in the velocities about the leftmost reflector point is 21 m/sec, 62 m/sec about the central CRP, and 42 m/sec for the rightmost CRP. Velocity errors are greater for small offsets due to the inaccuracies in determining the A time gradient. Migration of the time traces shows the changes in reflector position and reflector dip about a CRP and standard deviations from the correct position for the horizontal migration distance are 28 m, 10 m, and 74 m, while depth deviations are 11 m, 67 m, and 27 m respectively for the leftmost, central, and rightmost CRP positions.

These deviations are small, especially compared to the large migration distances and considering the steep dips. The formulae remain applicable for strongly curved surfaces, except that the depth below the origin (Z_0) will be in error since it is based on projecting a planar surface at the reflection point back to the origin. This accounts for the large Z_0 values about the leftmost and rightmost CRP's.

2. THREE-DIMENSIONAL PLANE DIPPING LAYER

Consider a plane dipping layer (Figure 4.9) with dip angle θ and a depth Z_0 below the origin (0), overlain by material having a constant velocity V . The distance SG between the source S and receiver G is ℓ while x and y denote the abscissa of the midpoint (M) of the baseline ℓ . The reflection point P is located on the boundary and SP and PG correspond to the incident and reflected rays. PN is the normal from the reflection point P (g, h, i) and α is the angle between the perpendicular to the plane and the profile line. D is the distance QM measured along the perpendicular to the reflecting plane from a point midway between the source and the detector.

It can be shown that the traveltime t is given by

$$t = \frac{1}{V} (4D^2 + \ell^2 \sin^2 \alpha)^{\frac{1}{2}} \quad \dots(14)$$

If ϕ is the angle between the profile and dip direction (Figure 4.10) then equation (14), expressed in terms of ϕ and θ becomes

$$t = \frac{1}{V} \left(4(x \sin \theta \cos \phi + y \sin \theta \sin \phi - d)^2 + \ell^2 (1 - \sin^2 \theta \cos^2 \phi) \right)^{\frac{1}{2}} \quad \dots(15)$$

The time gradients $dt/d\ell$, dt/dx , dt/dy , have the form

$$A = \frac{dt}{d\ell} = \frac{1}{V} \left[\frac{\ell(1 - \sin^2 \theta \cos^2 \phi)}{4(x \sin \theta \cos \phi + y \sin \theta \sin \phi - d)^2 + \ell^2 (1 - \sin^2 \theta \cos^2 \phi)} \right]^{\frac{1}{2}} \quad \dots(16)$$

$$B = \frac{dt}{dx} = \frac{1}{V} \left[\frac{4(x \sin \theta \cos \phi + y \sin \theta \sin \phi - d) \sin \theta \cos \phi}{4(x \sin \theta \cos \phi + y \sin \theta \sin \phi - d)^2 + \ell^2 (1 - \sin^2 \theta \cos^2 \phi)} \right]^{\frac{1}{2}} \quad \dots(17)$$

$$C = \frac{dt}{dy} = \frac{1}{V} \left[\frac{4(x \sin \theta \cos \phi + y \sin \theta \sin \phi - d) \sin \theta \sin \phi}{4(x \sin \theta \cos \phi + y \sin \theta \sin \phi - d)^2 + \ell^2 (1 - \sin^2 \theta \cos^2 \phi)} \right]^{\frac{1}{2}} \quad \dots(18)$$

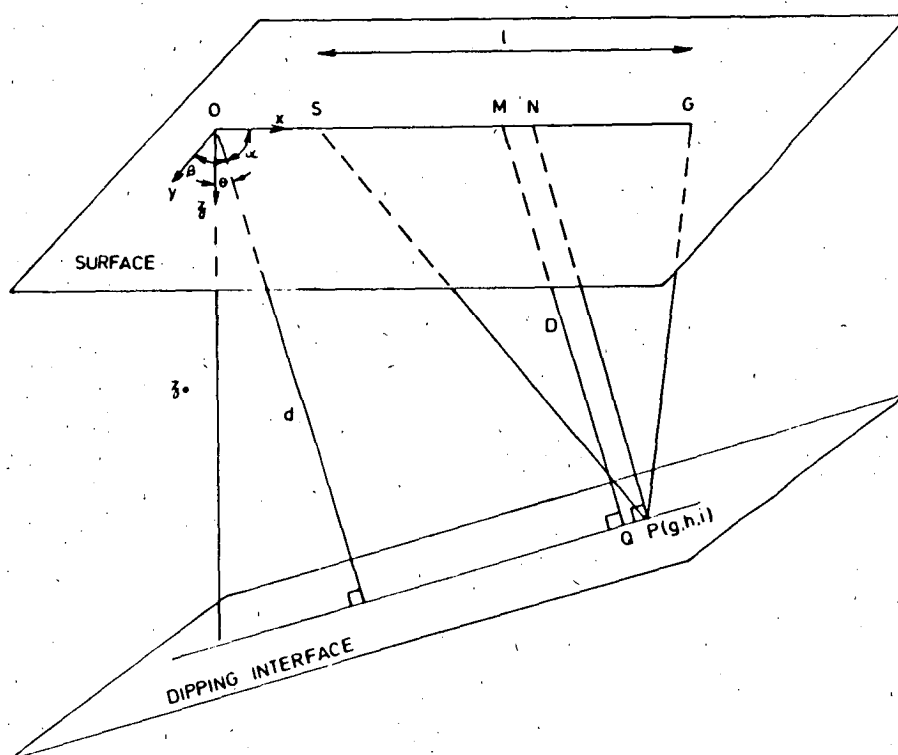


Fig. 4. 9 Three dimensional plane dipping model. The segment represents a ray from source (S) to geophone (G) reflected from a plane dipping at an angle (θ).

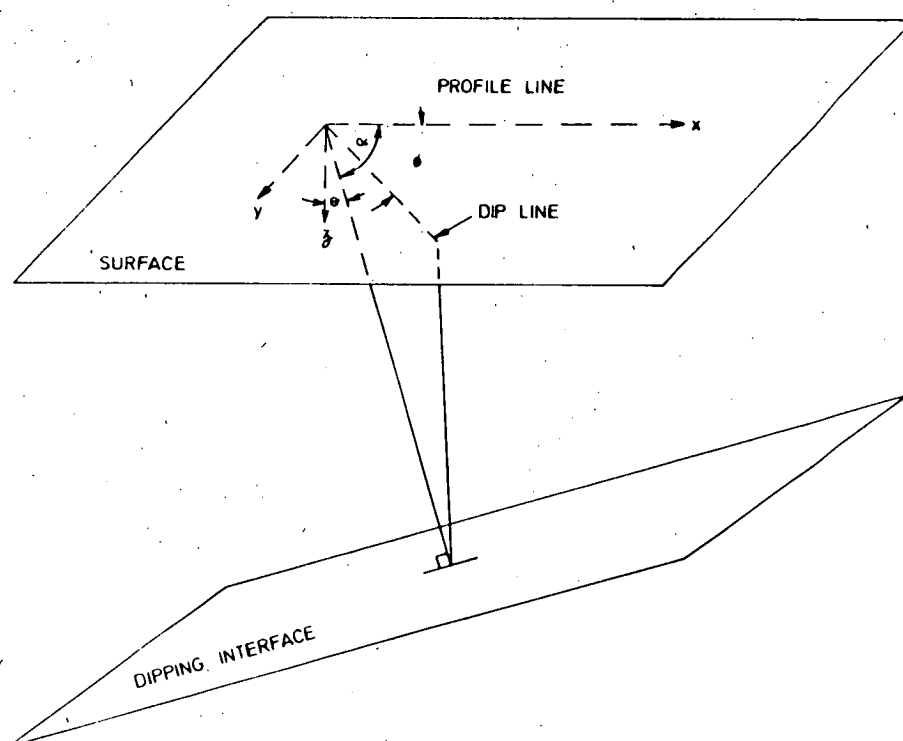


FIG. 4. 10 Relationship between the perpendicular to a plane and the profile line to the dip of the interface (θ) and the directional angle between profile and the dip lines.

Solving equations (15) to (18) and taking the origin about the midpoint M it can be shown that

$$V = \left(\frac{4\ell(t - A\ell)}{4At(t - A\ell) + B^2\ell t} \right)^{\frac{1}{2}} \quad \dots(19)$$

$$Z_0 = \frac{\ell^{\frac{1}{2}}(t - A\ell)}{[4A(t - A\ell) - \ell C^2]^{\frac{1}{2}}} \quad \dots(20)$$

and

$$\theta = \pm \arctan \left(\frac{\ell(B^2 + C^2)}{4A(t - A\ell) - \ell C^2} \right)^{\frac{1}{2}} \quad \dots(21)$$

Note that when $C = 0$ formulae (19) to (21) reduce to the two-dimensional case. The velocity formula is independent of the cross dip time gradient and is the same as the two-dimensional case. Thus for a simple dipping layer model accurate velocity determinations can be determined using single line profiles. Levin (1971) showed that the ratio of the stacking velocity to the layer velocity for this model is given by

$$\frac{V_{\text{stack}}}{V} = \frac{1}{(1 - \sin^2\theta \cos^2\phi)^{\frac{1}{2}}} \quad \dots(22)$$

These ratios have been plotted for varying dip and declination directions (Figure 4.11) and show the difference between the velocities becomes greater with increasing dip direction and dip angle. It is therefore somewhat surprising that formula (19) provides such a simple solution to the problem.

The distance (c_{dip}) from the midpoint to the surface expression of the normal from the reflecting point is

$$c_{\text{dip}} = \frac{\ell^2(B^2 + C^2)^{\frac{1}{2}}}{4(t - A\ell)} \quad \dots(23)$$

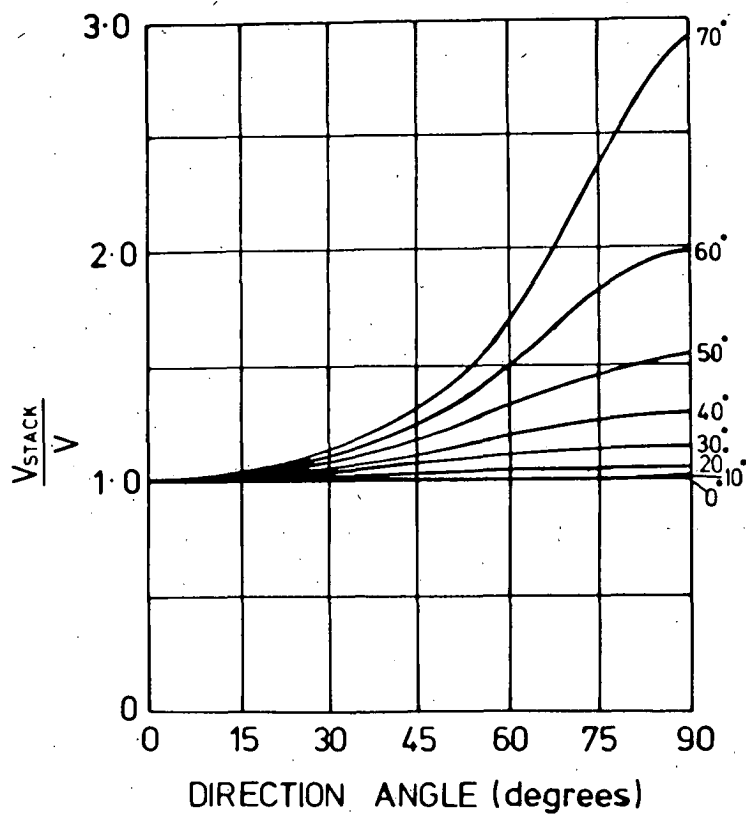


Fig. 4. 11 Ratio of the stacking velocity to the overburden velocity for the varying directional and dip angles.

This distance has two components orientated along the x and y axes.

$$c_x = \frac{B\ell^2}{4(t - A\ell)} \quad \dots(24)$$

$$c_y = \frac{C\ell^2}{4(t - A\ell)} \quad \dots(25)$$

The horizontal distance (b_{dip}) between the reflecting point (P) and the midpoint (M) is given by

$$b_{\text{dip}} = \frac{\ell(B^2 + C^2)^{\frac{1}{2}}(4t(t - A\ell) - \ell^2 C^2)}{4(t - A\ell)(4A(t - A\ell) + \ell^2 B)} \quad \dots(26)$$

which can be separated into the two components

$$b_x = \frac{\ell B(4t(t - A\ell) - \ell^2 C^2)}{4(t - A\ell)(4A(t - A\ell) + \ell^2 B)} \quad \dots(27)$$

and

$$b_y = \frac{\ell C(4t(t - A\ell) - \ell^2 C^2)}{4(t - A\ell)(4A(t - A\ell) + \ell^2 B)} \quad \dots(28)$$

Both b_{dip} and c_{dip} are offset from the midpoint of the shot receiver locations in the up-dip direction. Note that when $C = 0$ formulae (23) to (28) reduce to the two-layered case.

The depth to the reflecting point P can be obtained from

$$Z = Z_0 + b_{\text{dip}} \tan \theta \quad \dots(29)$$

3. DIFFRACTIONS

The travelttime to a diffraction point P (x_0, z_0) (Figure 4.12) is given by

$$t = \frac{1}{V} \left\{ [(x - x_0 - \frac{\ell}{2})^2 + Z_0^2]^{\frac{1}{2}} + [(x - x_0 + \frac{\ell}{2})^2 + Z_0^2]^{\frac{1}{2}} \right\} \quad \dots(30)$$

The time gradients dt/dl and dt/dx have the form

$$A = \frac{dt}{d\ell} = \frac{1}{V} \left\{ \frac{-(x - x_0 - \frac{\ell}{2})}{2[(x - x_0 - \frac{\ell}{2})^2 + Z_0^2]^{\frac{1}{2}}} + \frac{(x - x_0 + \frac{\ell}{2})}{2[(x - x_0 + \frac{\ell}{2})^2 + Z_0^2]^{\frac{1}{2}}} \right\} \quad \dots(31)$$

and

$$B = \frac{dt}{dx} = \frac{1}{V} \left\{ \frac{(x - x_0 - \frac{\ell}{2})}{[(x - x_0 - \frac{\ell}{2})^2 + Z_0^2]^{\frac{1}{2}}} + \frac{(x - x_0 + \frac{\ell}{2})}{[(x - x_0 + \frac{\ell}{2})^2 + Z_0^2]^{\frac{1}{2}}} \right\} \quad \dots(32)$$

By solving equations (30) to (32) and taking the origin about the midpoint (M) it can be shown that

$$V = \left(\frac{4\ell(t - A\ell)}{4At(t - A\ell) + B^2\ell t} \right)^{\frac{1}{2}} \quad \dots(33)$$

$$X_0 = \frac{B\ell t}{4A(t - A\ell) + B^2\ell} \quad \dots(34)$$

$$Z_0 = 2 \left(\frac{\ell A}{(t - A\ell)} \right)^{\frac{1}{2}} \frac{[(t - A\ell)^2 - (\ell B/2)^2]}{4A(t - A\ell) + B^2\ell} \quad \dots(35)$$

Note that despite the difference in the normal moveout curves between diffracting and reflecting points their two-dimensional velocity formulae derived from time gradient information are the same. The expression for x_0 corresponds to

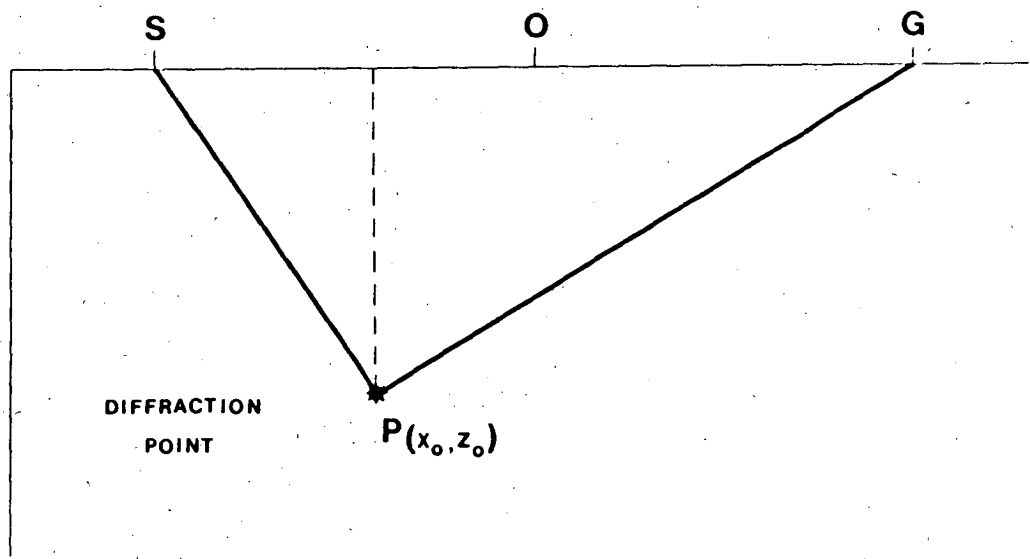


Fig. 4. 12 Raypath geometry for a diffracting point.

formula (11) in the two-dimensional plane layered case.

Attempts by the author to simplify the expression for z_0 have proved fruitless and the result bears little resemblance to equation (9).

4. MULTIPLES

The traveltime for multiple reflections is given by

$$t = \frac{1}{V} \left[[\ell \cos(n+1)\theta]^2 + 4[x \sin\theta + Z_0 \cos\theta \sin(n+1)\theta/\sin\theta]^2 \right]^{\frac{1}{2}} \quad \dots(36)$$

where n is the order of the multiple, $n = 0$ being the primary reflection, and the geometry is the same as for the two-dimensional dipping plane example. For the first-order multiple the traveltime is given by

$$t = \frac{1}{V} \left[[\ell \cos 2\theta]^2 + 4[x \sin 2\theta + 2Z_0 \cos^2 \theta]^2 \right]^{\frac{1}{2}} \quad \dots(37)$$

and the time gradients are

$$A = \frac{dt}{d\ell} = \frac{1}{V} \frac{\ell \cos^2 2\theta}{[(\ell \cos 2\theta)^2 + 4(x \sin 2\theta + 2Z_0 \cos^2 \theta)^2]^{\frac{1}{2}}} \quad \dots(38)$$

$$B = \frac{dt}{dx} = \frac{1}{V} \frac{4[x \sin \theta + 2Z_0 \cos^2 \theta] \sin 2\theta}{[(\ell \cos 2\theta)^2 + 4(x \sin 2\theta + 2Z_0 \cos^2 \theta)^2]^{\frac{1}{2}}} \quad \dots(39)$$

Solving equations (37) to (39) and taking the origin about the midpoint M , it can be shown that

$$V = \left(\frac{4\ell(t - A\ell)}{4At(t - A\ell) + B^2\ell t} \right)^{\frac{1}{2}} \quad \dots(40)$$

$$Z_0 = \frac{1}{2} \left(\frac{\ell(t - A\ell)}{4A} \right)^{\frac{1}{2}} \quad \dots(41)$$

and

$$\theta = \frac{1}{2} \arctan \left(\frac{B^2\ell}{4A(t - A\ell)} \right)^{\frac{1}{2}} \quad \dots(42)$$

Comparing the solutions (40) to (42) with those for primary reflections confirms the well known properties of multiples that their dip and depth is twice that of the primary, while their velocities are identical.

III. THE RAYPATH DISTORTION PROBLEM

The complex structure and dip of the overlying strata has significant effects on wave propagation and hence on velocity and reflector point determination and can be illustrated using a simple model composed of an irregular water-bottom layer overlying a horizontal interface (Figure 4.13). CDP gathers consisting of 48 traces with a geophone separation of 50 m and a shot-first receiver offset of 330 m are traced every 50 m and the stacking velocities, taken to equal the square root of the reciprocal of the slope of a least square straight line through points on a $t^2 - X^2$ graph derived from the gather information are calculated. The stacking velocities for the inner 24 traces and for all 48 traces at each gather location are plotted (Figure 4.13) and can be compared to the true vertical velocity. The large discrepancies highlight the raypath distortion problem. Selected traces for the gather at location A in Figure 4.13 illustrate the large lateral shifts in the reflector point position (Figure 4.14).

Complex overburden problems can be solved in a similar manner to the migration problem using the following steps —

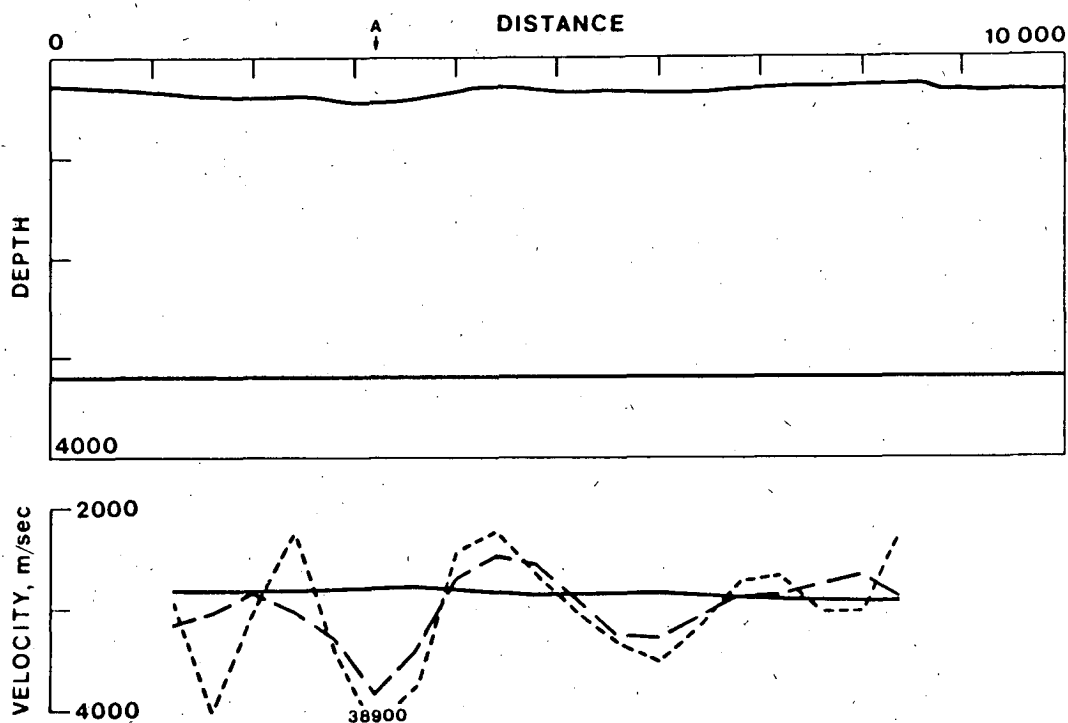


Fig. 4. 13 Irregular water-bottom layer overlying a horizontal interface and the resulting velocity profile as determined by ray-tracing.

- | | |
|-----------|--|
| ————— | True vertical velocity profile. |
| - - - - - | Stacking velocity profile using all 48 traces. |
| | Stacking velocity profile using inner 24 traces. |

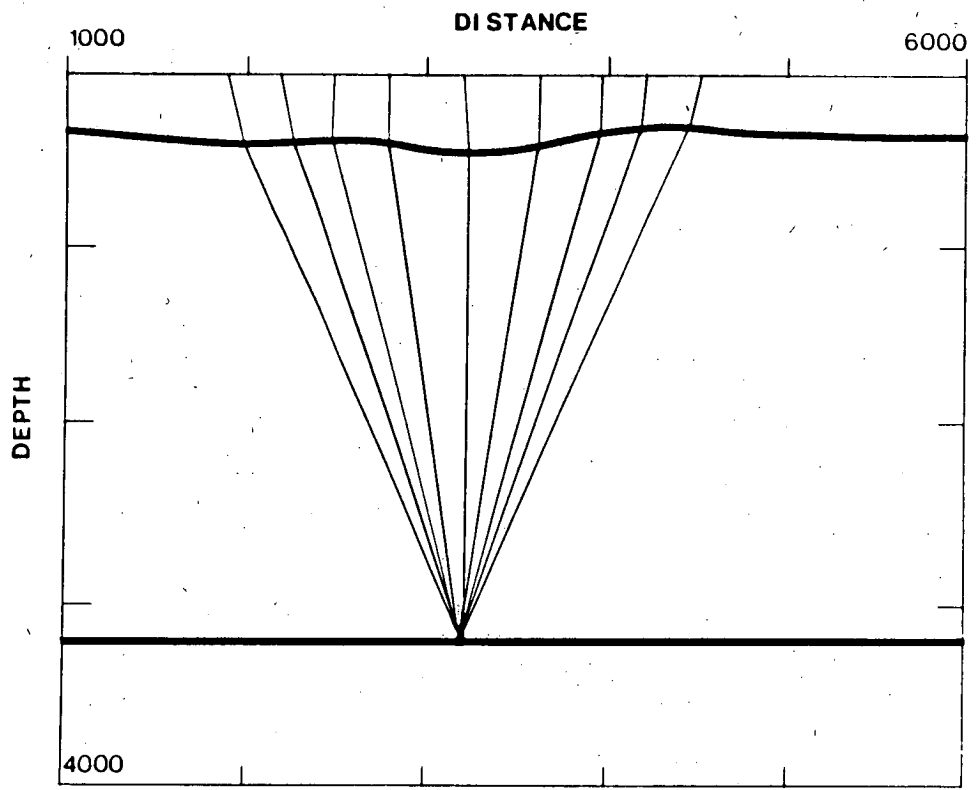


Fig. 4. 14 Selected traces for the gather location A (Figure 4.13)

1. Determination of the first layer topography

The techniques described for the migration problem can be used to determine the first layer shape and velocity.

2. Determination of derivatives of the time surfaces for the reflector

In processing seismic data it is necessary to transform the data from a continuous profile co-ordinate system to give CDP data (see Figure 4.15). The co-ordinates of the source (s) and detector (g) are measured along X axis, which represents the direction of the seismic shooting. Also along the X axis are the shot to geophone offset co-ordinate ($\ell = g - s$), and the midpoint co-ordinate ($y = (g + s)/2$) between the shot and the geophone. Let the function $t(s, g)$ and $t(\ell, y)$ represent continuous lines passing through the measured values of the reflection time (t) corresponding to any one reflector.

Let $t_g = dt/dg$, $t_s = dt/ds$, and $t_y = dt/dy$, and $t_\ell = dt/d\ell$ be the derivatives of these lines. Then t_g is the tangent to the time distance curve (t versus g) seen on a profile corresponding to a fixed shotpoint (S_i); t_s is the tangent to the time distance curve (t versus s) seen on a profile corresponding to a fixed receiver (g_i); t_y is the gradient along the seismic section plane for a given offset; while t_ℓ is the gradient along a CRP gather for a particular midpoint co-ordinate.

The derivatives of the time surfaces in the two co-ordinate systems (Shah, 1973) are

$$t_g = t_y/2 + t_\ell \quad \dots(43)$$

$$t_s = t_y/2 - t_\ell \quad \dots(44)$$

The parameters t_y and t_ℓ are easily determined from CDP data, so that t_g and t_s are readily calculated.

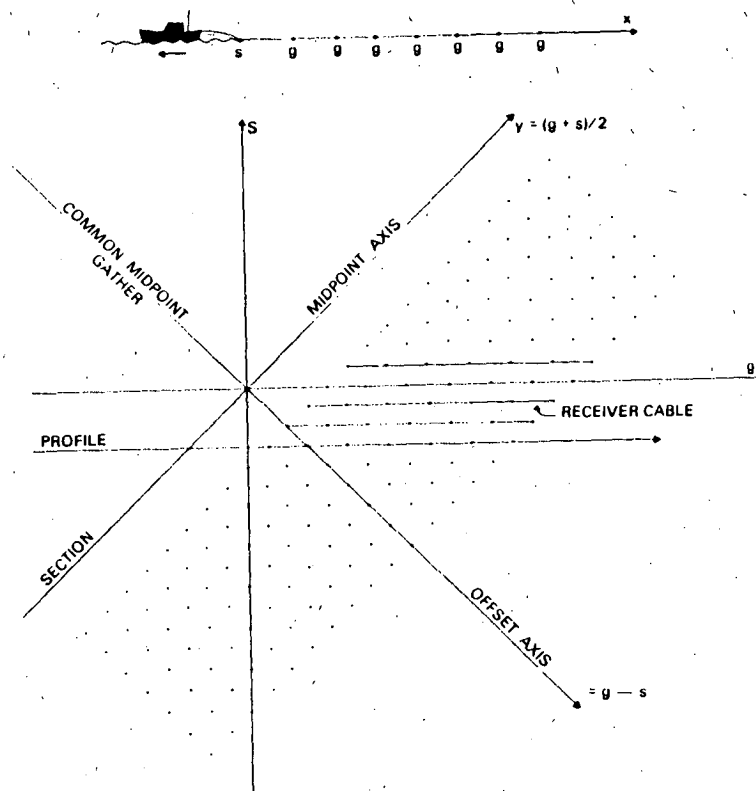


Fig 4. 15 The relationship among source co-ordinate s , geophone receiver co-ordinate g , offset co-ordinate $l = g - s$, and midpoint co-ordinate $y = (g + s)/2$ (after Claerbout 1976).

3. Determination of the emergence angle from the source and incidence angle at the detector.

Consider two rays from a fixed source emerging at two neighbouring receivers A and B. (Figure 4.16) a distance Δg apart on the surface, after reflection from some interface. Let the emergence angles (with the vertical) of the raypaths at A and B be β_g and $\beta_g + \Delta\beta_g$ respectively. AC is a tangent to the wavefront at A and if V_1 is the seismic velocity of the material near the receivers, and the infinitesimal distance BC is equal to $V_1\Delta t$ then

$$\frac{V_1\Delta t}{g} = \sin \beta_g \quad \dots(45)$$

In the limiting case, as $\Delta g \rightarrow 0$ this equation becomes

$$V_1 t_g = \sin \beta_g \quad \dots(46)$$

By means of the law of reciprocity for shots and receivers, the emergence angle for rays from various shots to a fixed receiver can also be determined. If β_s is the departure angle from the shot, then

$$V_1 t_s = \sin \beta_s \quad \dots(47)$$

Using equations (46) and (47) it is possible to determine the incident angle at all receivers and emergence angles at all shots, for data in CDP format.

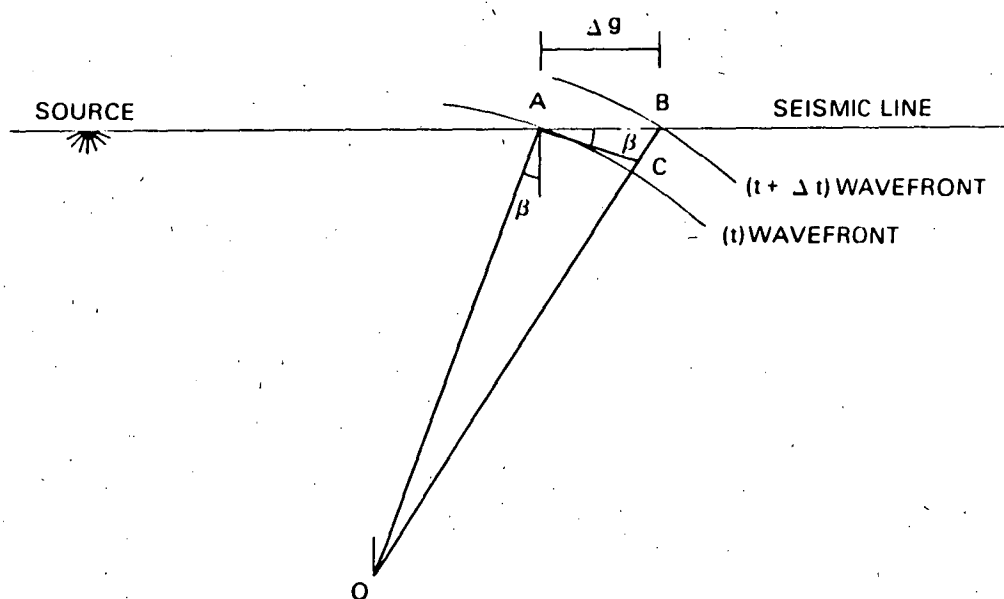


Fig. 4. 16 Geometry of a wavefront approaching receivers (after Shah 1973).

4. Downward continuation to the first layer or to the layer immediately above the reflector interface.

Using the incident angles at the receivers and emergence angles at the shots the rays are traced to the layer immediately above the reflector interface. The co-ordinates of the incident and emergent rays at this interface and the reduced traveltime (taken as the difference in total time to the traveltime of the incident rays to the intermediate interface) are determined.

5. Calculation of time derivatives and reflector point co-ordinates.

The time derivatives with respect to offset and shot distance are calculated for the bottom layer using the reduced traveltimes and co-ordinates. Layer velocity and dip, and the co-ordinates of the reflection point are calculated as for the migration problem. Since the datum is taken as the plane between the incident and emergent rays on the intermediate interface rotation of the co-ordinate system is necessary to give the true reflection point and dip information.

Application of the above method for the gather at location A (Figure 4.14) resulted in a standard deviation of 51 m/sec for the true interval velocity of the second layer.

IV. CONCLUSIONS

Simple formulae, based on reflection time and its derivatives have been derived in order to solve the reflection layer parameters for both the migration and raypath distortion problems. Synthetic models have been used to show how a single time trace can be migrated into its true depth position. While the formulae have not been applied to real data their application should be simple. Time derivatives could be calculated by correlation techniques with neighbouring traces although more traces may be required in order to provide better statistical reliability. Multiple data could be removed by migrating only the reflector which has velocities and layer dips lying within selected windows.

Chapter 5

REFLECTIVITY, TRANSMISSIVITY AND MODE CONVERSION FOR THIN LAYERS

	page
I. INTRODUCTION	5.1
II. CDP STACKING AND WAVELET PRESERVATION	5.3
III. INTERFERENCE	5.7
IV. REFLECTIVITY AND THE THOMPSON-HASKELL METHOD	5.8
V. DETERMINATION OF LAYER PARAMETERS FROM THE SPECTRA	5.12
VI. AMPLITUDE AND PHASE CHARACTERISTICS FOR VARIOUS THIN HOMOGENEOUS LAYERS	5.15
1. Layers with a High Velocity	5.17
2. Layers with a Low Velocity	5.20
3. Layers with Intermediate Velocity Increasing with Depth	5.23
4. Layers with Intermediate Velocity Decreasing with Depth	5.23
5. Summary	5.23
VII. THICKNESS OF THE LAYER AND THE FREQUENCY RANGE	5.24
VIII. VELOCITY CONTRASTS AND THE FREQUENCY RANGE	5.31
IX. DENSITY CONTRASTS AND THE FREQUENCY RANGE	5.34
X. THICKNESS-VELOCITY RELATIONSHIPS	5.40
XI. SHOT, INSTRUMENT AND PROCESSING DISTORTIONS	5.43
XII. SEISMIC NOISE	5.43
XIII. VELOCITY DISPERSION	5.48
XIV. VELOCITY DETERMINATION	5.50
XV. MULTILAYERED MEDIA	5.57
XVI. DIRECT HYDROCARBON INDICATORS (DHI)	5.62
1. One Layer Models	5.62
2. Multilayered Hydrocarbon Models	5.77
XVII. MIXED PHASE SPECTRA AND INTRABED MULTIPLES	5.83
XVIII. INVERSION METHOD FOR PRIMARY REFLECTIONS FROM THIN LAYERS	5.88
XIX. MODE CONVERSION	5.90
XX. TRANSMISSION IN THIN LAYERS	5.94
XXI. PRINCIPLE OF RECIPROCITY	5.95
XXII. CONCLUSIONS	5.96

I. INTRODUCTION

In future, oil reserves are likely to be found in subtle traps of stratigraphic, unconformity or palaeogeomorphic types (Halbouty, 1972). Most sedimentary basins contain facies changes, unconformities with resulting truncated beds, and buried erosional or constrictive surface such as reefs, hills, barrier sand bars, channels and other related geological phenomena. Vail & Mitcham (1977) stated that the unique properties of seismic reflections allow the direct application of geological concepts based on physical stratigraphy since primary reflections are parallel to stratal surfaces and unconformities. They also noted that as seismic reflections follow chronostratigraphic correlations, the following interpretations can be made from the geometry of seismic reflection correlation patterns:

1. Interpretation of post-depositional structural deformation,
2. Geologic time correlations,
3. Definition of genetic depositional units, and
4. Thickness and depositional environment of genetic units.

Lithofacies and rock type cannot be determined directly from the geometry of reflection correlation patterns.

A depositional sequence ranges from a few millimetres to hundreds of metres thick but seismic sequences can at best be correlated to the nearest reflection cycle which frequently represents a minimum thickness of several tens of metres (Mitchum, Vail & Thompson, 1977).

Lithofacies determinations such as stratigraphic variations, sand-shale ratios, reef identification, porosity and hydrocarbon information can be derived from interval velocities (Schneider, 1971; Marr, 1971) which are computed from stacking velocities using the formulae of Dix (1955). Large errors in estimated interval velocities may occur for small intervals because of the difficulty in measuring transit times for thin layers.

The ability to determine the properties of thin geological sequences is limited. Sheriff (1977) noted that in general vertical resolution is about one-eighth to one-quarter wavelength. This conclusion stems largely from the work of Widess (1973), who studied reflections from a thinning bed with a velocity twice that of the medium above and below. Wavelengths for conventional seismic exploration vary from 30 m (for shallow reflectors) to 200 m (for deeper reflectors). The wavelength increases with depth, since velocity normally increases with depth and the higher frequencies are attenuated, with increasing reflection time, due to absorption. Thus the resolution of deep features is much diminished compared to the same feature at a shallower depth. If the resolution of the seismic method is to be increased a radical change of thinking may be necessary. This chapter presents information included within the seismic data that may increase the resolution of the seismic method.

II. CDP STACKING AND WAVELET PRESERVATION

Phase, amplitude, arrival time and frequency are the basic parameters of seismic energy (Fitton & Dobrin, 1967). The use of CDP methods is detrimental in preserving these essential parameters. Dunkin & Levin (1973) studied the effect of NMO on a seismic pulse and showed that stretching of the traces produced an increase in low frequencies in a summed pulse from a CDP stack. They showed that

$$g_0(f) = a g_0(af) \quad \dots (1)$$

where $g_0(f)$ is the Fourier transform of the uncorrected pulse and $g_0(af)$ the Fourier transform of the NMO corrected pulse. Thus the spectrum of the NMO corrected pulse is compressed and multiplied by a factor a , where a depends on the zero-offset time, the source-receiver separation, the stacking velocity and the rate at which the stacking velocity varies with zero-offset time.

Buchholtz (1972) noted that reconstruction of the true zero-offset reflectivity function by application of dynamic corrections can only be an approximate process. Where intersections of hyperbolae occur accurate reconstruction is impossible. This problem may be overcome by (1) isolating the individual reflection pulses and moving them intact, or (2) by applying a time varying contraction filter to the NMO corrected traces. Since the distortion factor a depends on quantities that vary with record time such a filter could be designed. The reduction of the high frequency content of the far trace wavelets is illustrated in a typical moveout corrected CDP gather (Figure 5.1). Stacking such NMO corrected data must

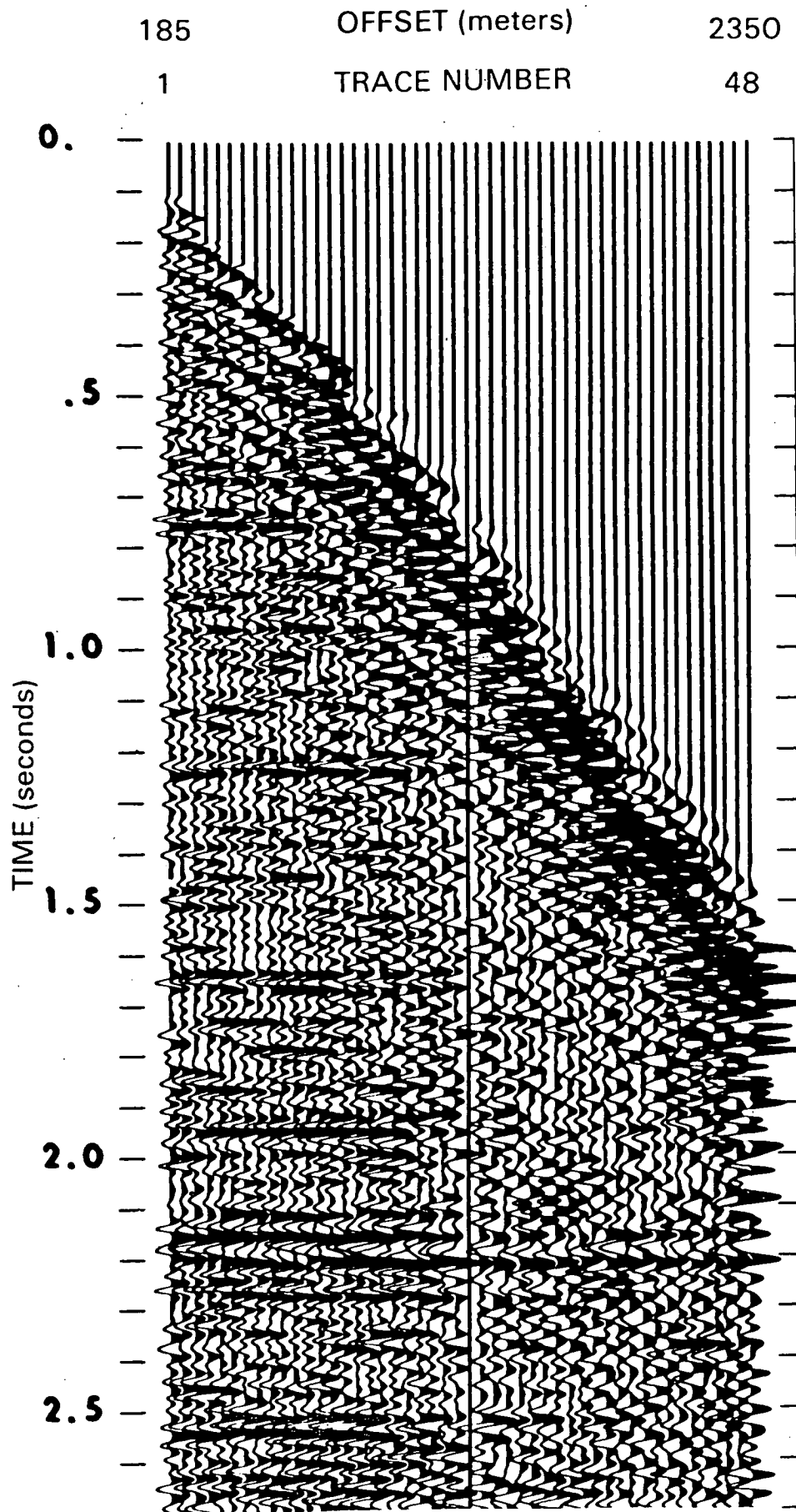


Fig. 5.1 Destruction of the frequency content of the far trace wavelets due to NMO correction of a CDP gather.

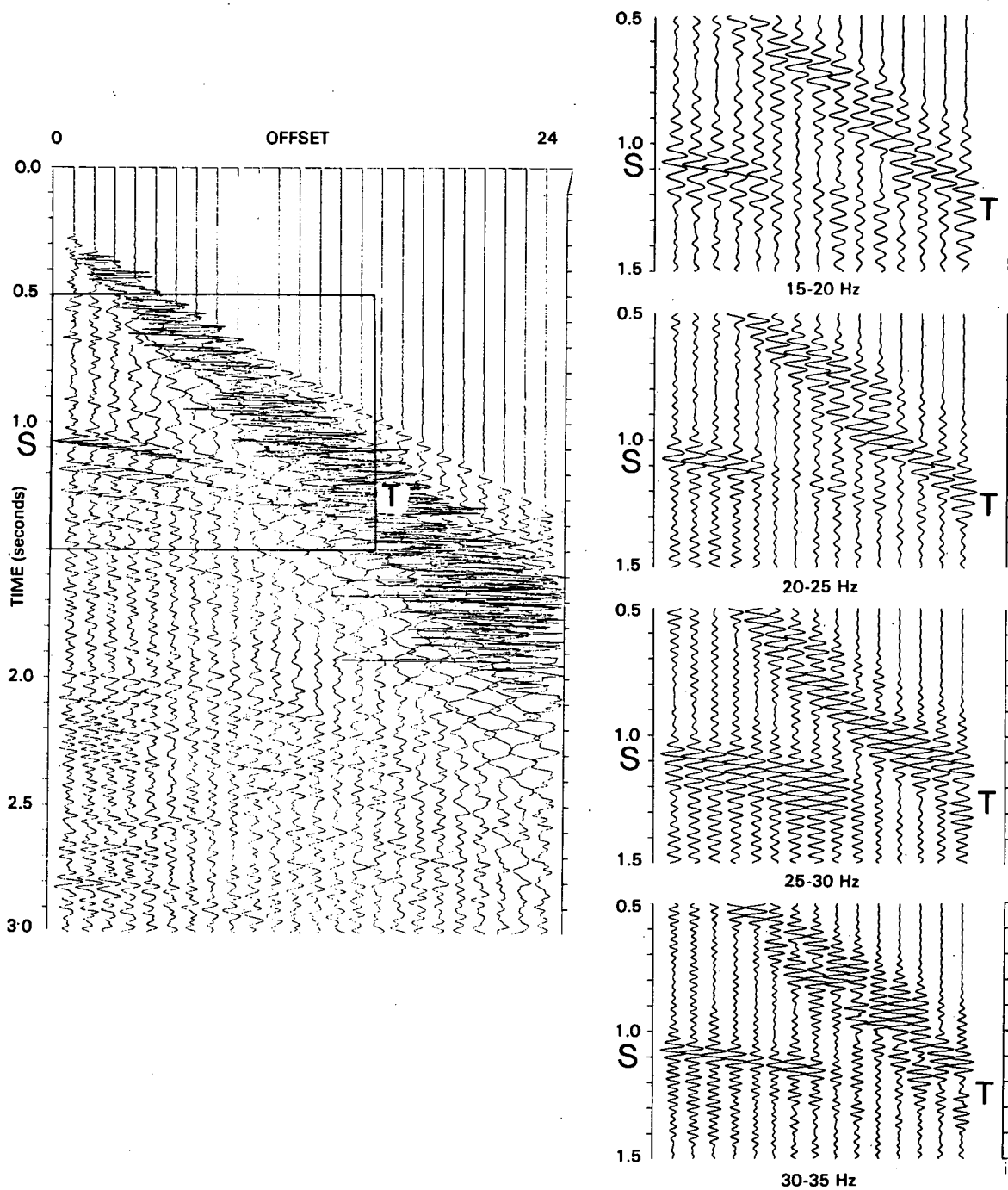


Fig. 5.2 Uncorrected CDP gather illustrating that amplitude variations are frequency as well as offset dependent.

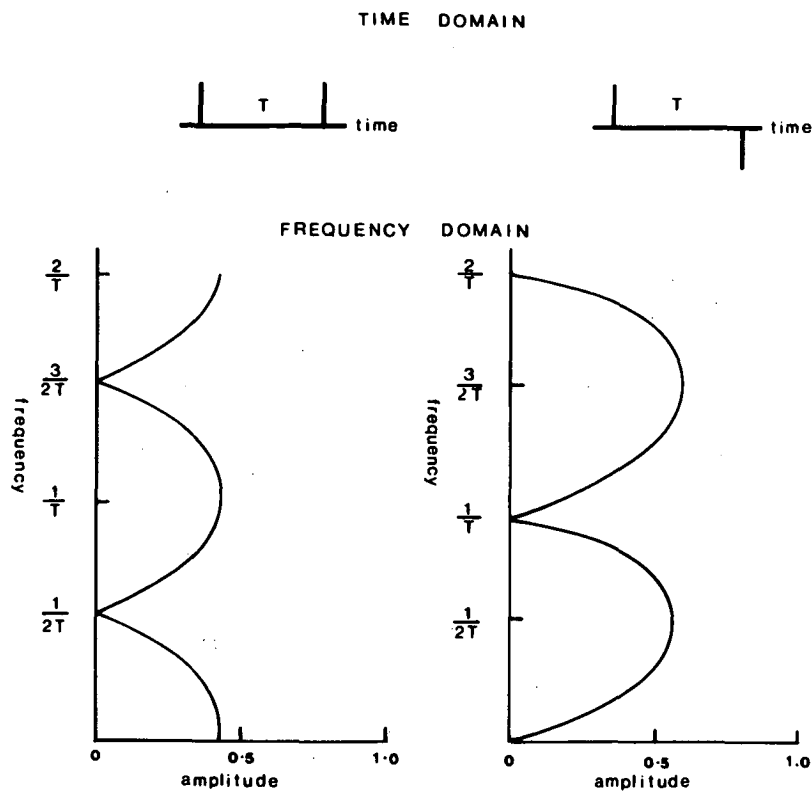


Fig. 5.3 Interference effects in frequency domain due to two reflectors having the same polarity and opposite polarity.

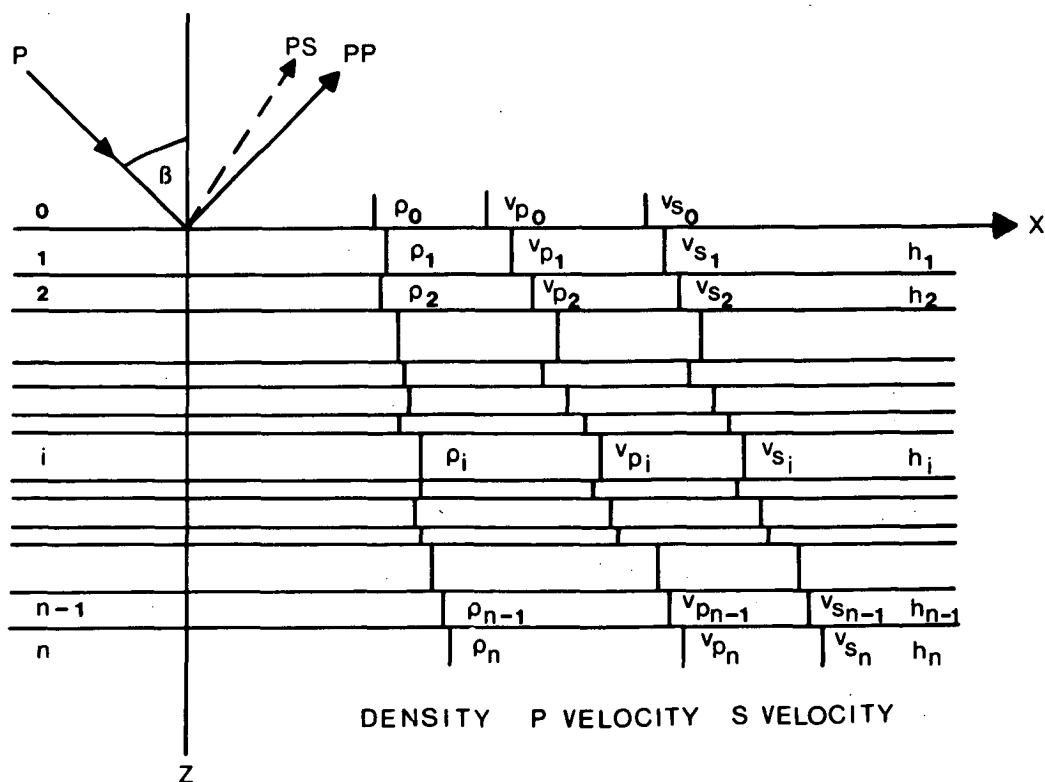


Fig. 5.4 Sequence composed of a number of thin layers.

result in a wavelet vastly different to the zero-offset wavelet. The wavelet differences among members of the CDP gather also degrade high frequencies (Larner *et al.*, 1973). Errors in stacking velocities or inadequacies in the assumption of hyperbolic moveout will cause degradation of the higher frequencies (Larner *et al.*, 1973).

III. INTERFERENCE

Band-pass filtering of an uncorrected CDP gather (Figure 5.2) shows large amplitude variations within a pass-band at differing offsets. Event S-T clearly demonstrates that these amplitude variations are frequency as well as offset dependent. Traces 6 and 7 in the passband 20 to 25 hz have greatly reduced amplitudes; the fact that the traces are not dead is illustrated by their large amplitudes in the 25 to 30 hz passband. Many authors (Sheriff, 1973; Lindsey, 1973; Fitton & Dobrin, 1967) have reported constructive and destructive interference effects due to layered earth models. Anstey (1977) noted that two reflectors of any polarity combination generated a system of peaks and notches in the frequency spectrum. Reflectors with the same polarity peak at 0 hz while opposite polarities notch at 0 hz (Figure 5.3). The notches are of zero amplitude only if the two reflection coefficients are equal in magnitude. The position of the notch or peak is directly related to the two-way time between the interfering interfaces and this would explain the amplitude variations depicted in Figure 5.2.

Anstey (1977) stated that the use of interference in the frequency domain is of little or no benefit in improving the resolution of thin beds, a not surprising result after one has destroyed the frequency content of the traced in NMO correction and then summed the amplitude and phase variations in stacking.

IV. REFLECTIVITY AND THE THOMPSON-HASKELL METHOD

Since the wavelengths involved in conventional seismic exploration are within the range 30-300 m it is necessary to consider the effect of the sequence of reflecting interfaces through which the pulse is travelling at any particular time instant (Figure 5.4) rather than the effect of the travelling pulse on a particular interface.

For normal incidence the reflectivity can be expressed in terms of the density (ρ) and P wave velocity (V) of the media on opposite sides of the interface:

$$\begin{aligned} \text{reflection coefficient} &= \frac{\text{amplitude of reflected wave}}{\text{amplitude of incident wave}} \\ &= \frac{\rho_2 V_2 - \rho_1 V_1}{\rho_2 V_2 + \rho_1 V_1} \quad \dots (2) \end{aligned}$$

As noted in Chapter 4 the reflection coefficient is dependent on incident angle, independent of frequency and involves no phase changes up to the critical angle. Sheriff (1977) stated that if the incident angle is small (up to 20°), the departure from equation (2) is small. However the reflectivity of a small zone composed of many thin layers is dependent on the

layer parameters (P and S velocities, density and thickness), and on the frequency and angle of incidence of the incident plane wave (Appendix 3). In addition the reflectivity is complex, so both amplitude and phase changes occur for different input parameters.

Figure 5.5 illustrates a typical synthetic seismogram in which the input Ricker pulse, with a spectrum peaked at 30 hz, and the subsurface which produced the seismogram, are simple. The synthetic seismogram differs from field data in that it is noiseless and all the pulses are identical. Such a gather would occur only for a subsurface model in which the layers are thick, so that no interference occurs. This can be compared to the NMO corrected field data shown in Figure 5.6. Events A to E show large variations in amplitude while events 1 to 3 have unusual phase changes with increasing offset. Such changes can only be due to complex reflectivities in the zone of interest. Consequently the writer has made an analysis of the contribution of interference and complex reflectivities and their impact on seismic resolution and interpretation using the Thompson-Haskell method (Appendix 3).

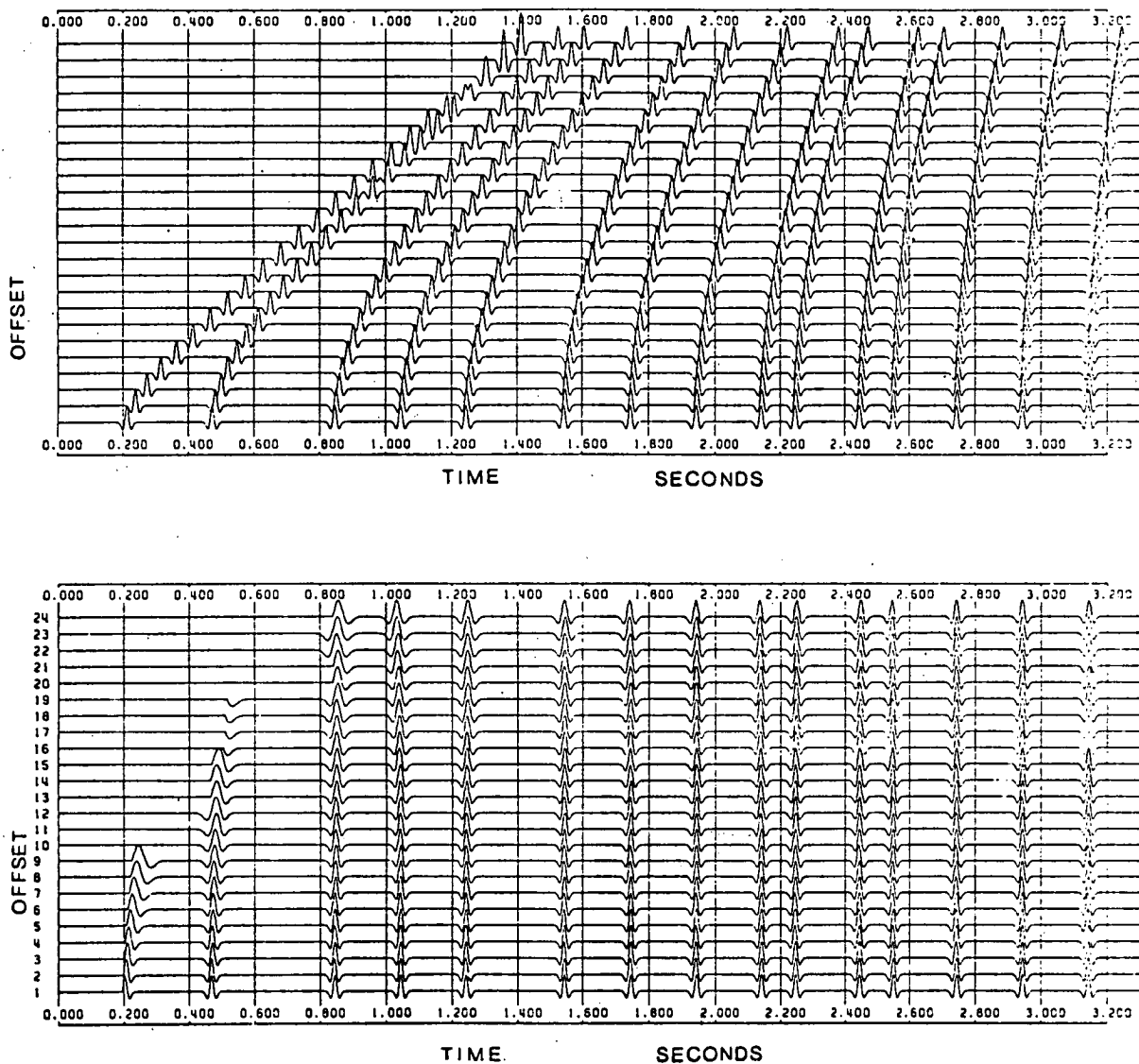


Fig. 5.5 Typical synthetic seismogram exhibiting no interference effects (after Dunkin & Levin, 1973).

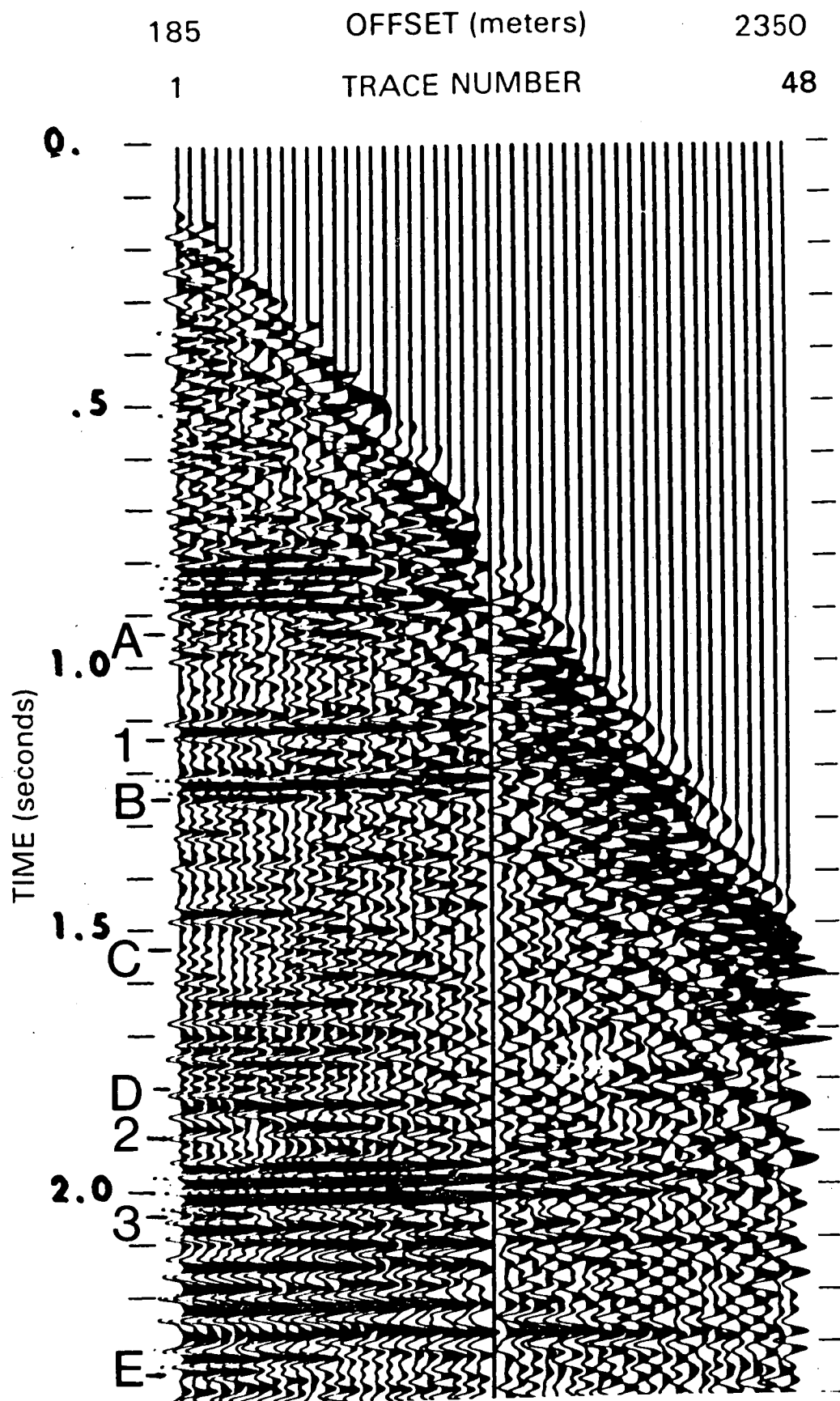


Fig. 5.6 NMO corrected gather. Events A to E show amplitude variations while events 1 to 3 illustrate phase variations with offset.

V. DETERMINATION OF LAYER PARAMETERS FROM THE SPECTRA

If two waves with similar amplitude and phase spectra interfere, the position of the spectral minima of the resultant wave is determined by the differences between the arrival time of these waves and their relative polarity. The time lag (T) of the wave reflected from the underside of the layer (Figure 5.7), relative to the wave reflection from its roof, depends on the thickness of the layer (h), the wave propagation velocity (v_2), and the angle of incidence (i), and is given by:

$$T = \frac{2h \cos i}{v_2} \quad \dots (3)$$

The polarity of the waves is determined by the ratio of the velocities in the layer and the enclosing half-spaces. All possible distributions of velocities in the layers $v_1 < v_2 < v_3$, $v_1 < v_2 > v_3$, $v_1 > v_2 < v_3$ and $v_1 > v_2 > v_3$ can be reduced to two cases.

For models in which the layer velocity is greater or less than the velocities in the enclosing half-spaces the frequency positions of the minimum amplitudes are given by

$$F_{\min}(n) = \frac{n - \frac{1}{2}}{T} \quad \dots (4)$$

and the distance between neighbouring minima is given by

$$\Delta F_{\min}(n) = \frac{1}{T} \quad \dots (5)$$

where n is the order of the minimum.

For models in which the layer velocity has an intermediate value

$$F_{\min}(n) = \frac{n}{T} \quad \dots (6)$$

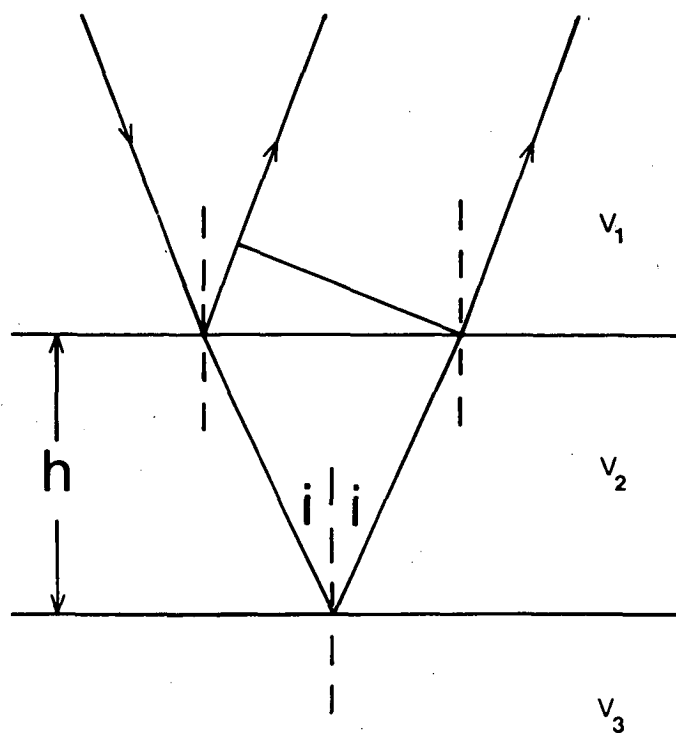
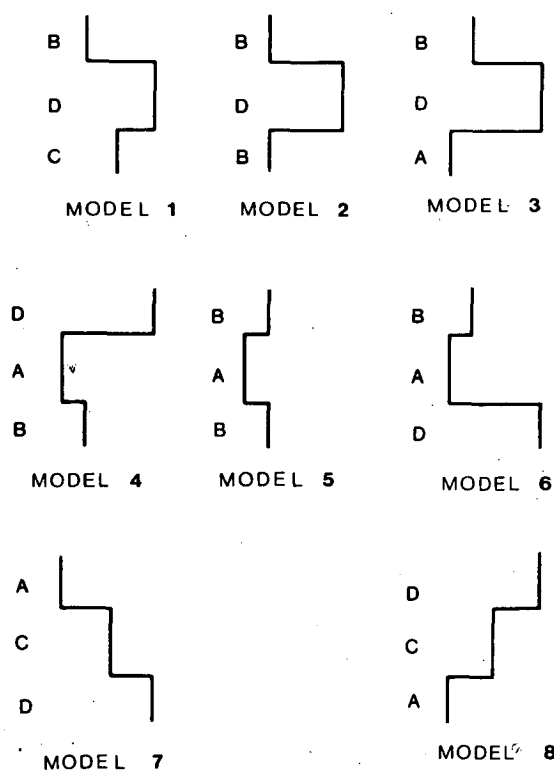
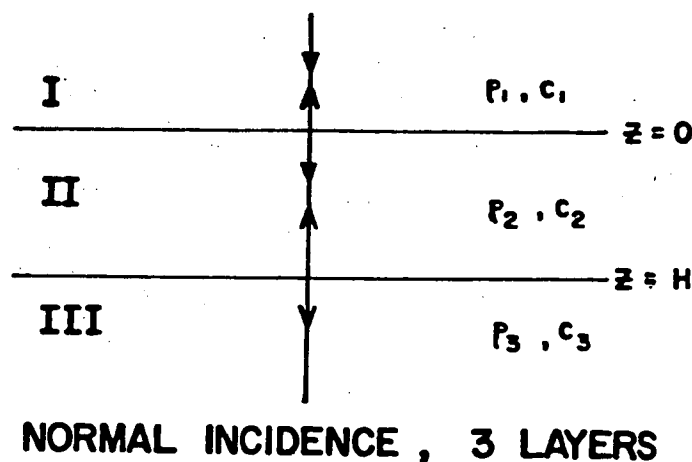
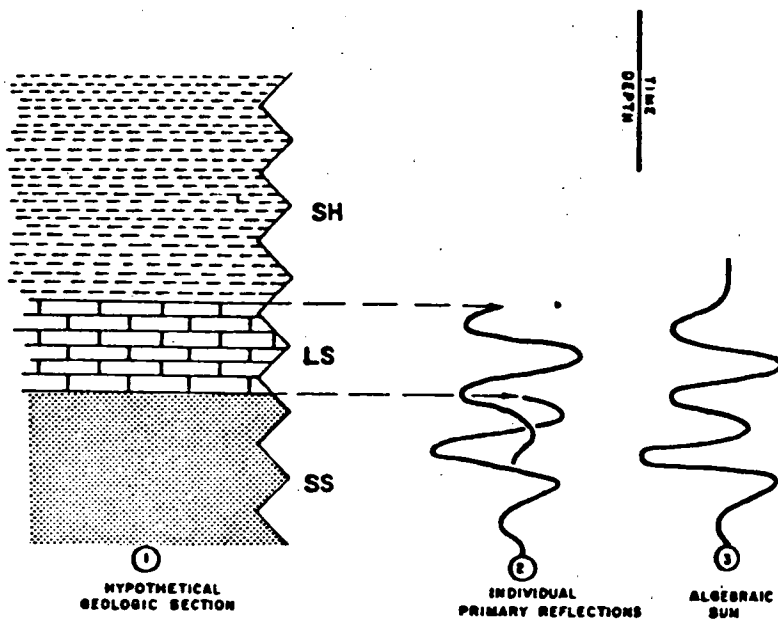


Fig. 5.7 Raypath geometries for a thin layer.



	V_P m/sec	V_S m/sec	DENSITY t/m^3
A	2210	896	2.065
B	2393	1097	2.083
C	2652	1356	2.104
D	3231	1859	2.189

Fig. 5.8 Models of thinly laminated media and their corresponding layer parameters.



$$|R| \equiv \left| \frac{A_2}{A_1} \right| = \sqrt{\frac{(e_1 + e_2)^2 \cos^2\left(\frac{WH}{C_2}\right) + (e_1 - e_2)^2 \sin^2\left(\frac{WH}{C_2}\right)}{(e_3 + e_4)^2 \cos^2\left(\frac{WH}{C_2}\right) + (e_3 - e_4)^2 \sin^2\left(\frac{WH}{C_2}\right)}}$$

$$e_1 = (P_1 C_1 - P_2 C_2)(-P_2 C_2 - P_3 C_3)$$

$$e_2 = (P_1 C_1 + P_2 C_2)(-P_2 C_2 + P_3 C_3)$$

$$e_3 = (-P_1 C_1 - P_2 C_2)(-P_2 C_2 - P_3 C_3)$$

$$e_4 = (-P_1 C_1 + P_2 C_2)(-P_2 C_2 + P_3 C_3)$$

W = circular frequency (radians)

REFLECTION COEFFICIENT

Fig. 5.9 Reflection coefficients for direct normal incidence waves for three layered media (after Paige, 1973).

and
$$\Delta F_{\min}(n) = \frac{1}{T} \quad \dots (7)$$

The phase shift between spectral components of the interfering waves is determined by the time lag in the layer and the mutual polarity of the waves as determined by the velocities in the layer and within the enclosing strata. For antiphase components the spectral amplitudes are subtracted and in the case of equality of the components they cancel out.

The phase shift between the two interfering waves is given by

$$\Delta P = 2\pi fT = 4\pi f \frac{h \cos i}{V} \quad \dots (8)$$

It should be noted that these calculations do not take into account intrabed multiples.

VI. AMPLITUDE AND PHASE CHARACTERISTICS FOR VARIOUS THIN HOMOGENEOUS LAYER MODELS

The models of a thin layer (20 m) and the layer parameters used are shown in Figure 5.8. The layer parameters are from data compiled by Gregory (1977, p.34). Paige (1973, p.202) studied the effect of travel path and wave shaping which resulted from the interaction between reflections coming from individual lithologic interfaces (Figure 5.9) and showed the reflection coefficient for normal incidence rays on a single layer to be

$$|R| \equiv \left| \frac{A_2}{A_1} \right| = \sqrt{\frac{(e_1+e_2)^2 \cos^2(\omega H/C_2) + (e_1-e_2)^2 \sin^2(\omega H/C_2)}{(e_3+e_4)^2 \cos^2(\omega H/C_2) + (e_3-e_4)^2 \sin^2(\omega H/C_2)}} \quad \dots (9)$$

where $e_1 = (\rho_1 C_1 - \rho_2 C_2)(-\rho_2 C_2 - \rho_3 C_3)$

$e_2 = (\rho_1 C_1 + \rho_2 C_2)(-\rho_2 C_2 + \rho_3 C_3)$

$e_3 = (-\rho_1 C_1 - \rho_2 C_2)(-\rho_2 C_2 - \rho_3 C_3)$

$e_4 = (-\rho_1 C_1 + \rho_2 C_2)(-\rho_2 C_2 + \rho_3 C_3)$

ω = circular frequency (radians)

H = the layer thickness

$(\rho_i, C_i, i = 1, 3)$ are densities and P wave velocities
in each of the media.

This equation excludes the effect of intrabed multiples.

Rearranging equation (9), it can be shown that for layers with a velocity lower or higher than the velocities in the surrounding media that the combined boundary impedance ratios for the top and bottom surfaces of the layer and the adjacent half spaces is

$$a_{12} = \frac{\rho_1 C_1}{\rho_2 C_2} = \sqrt{\frac{(1 \mp R_{\max})(1 \mp R_{\min})}{(1 \pm R_{\max})(1 \pm R_{\min})}} \quad \dots (10)$$

$$\text{and } a_{32} = \frac{\rho_3 C_3}{\rho_2 C_2} = \sqrt{\frac{(1 \pm R_{\min})(1 \pm R_{\max})}{(1 \mp R_{\min})(1 \mp R_{\max})}} \quad \dots (11)$$

where R_{\min} and R_{\max} are the minimum and maximum reflection coefficients calculated from equation (9). The upper signs in the numerators and denominators of equations (10) and (11) apply for model 1 and the lower signs for model 4. For models 2 and 5, equation (10) gives the value of a_{32} and equation (11) gives a_{12} ; the upper signs for model 2 and the lower signs for model 5.

For layers with an intermediate velocity (models 7 and 8) formula (10) gives a_{12} , and

$$a_{32} = \sqrt{\frac{(1 \mp R_{\min})(1 \pm R_{\max})}{(1 \pm R_{\min})(1 \mp R_{\max})}} \quad \dots (12)$$

The upper signs are used for model 7. For model 8, equation (10) gives a_{32} , and equation (12) gives a_{12} using the lower signs.

Amplitude and phase spectra determined by the writer using the Thompson-Haskell formalization for various angles of incidence ($5-90^\circ$) and frequencies (5-160 hz) in these models have been contoured (Figures 5.10 and 5.11). For convenience, and on the basis of the results, the eight models have been classified into four different groups.

1. LAYERS WITH A HIGH VELOCITY

This group is represented by models 1 to 3 of Figure 5.8. The amplitude and phase spectra for models 1 and 3 (Figures 5.10 and 5.11) are similar indicating the small effect that the ratio of the layer velocity to the underlying velocity has. At small angles of incidence distinctive amplitude maxima and minima occur at an interval of 80 hz. This corresponds to a layer thickness of 20 m when equation (3) is used with a layer velocity of 3231 m/sec.

The phase spectra decrease monotonically as the frequency increases and have discontinuities of 360° . At small angles of incidence, these discontinuities correspond to the minima of the amplitude spectra, while the zero phase areas coincide

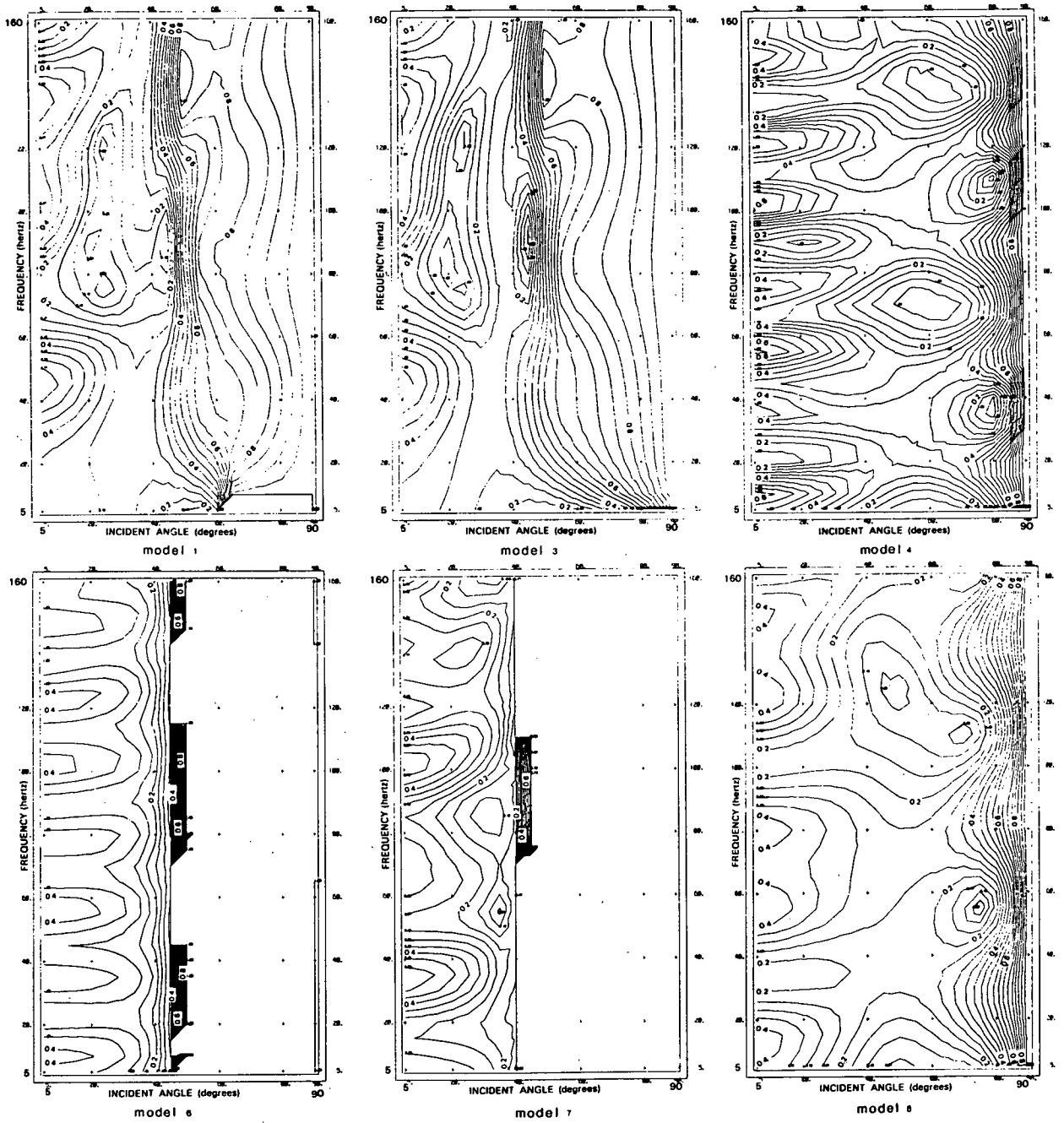


Fig. 5.10 Amplitude reflectivities for models 1, 3, 4, 6, 7 and 8.

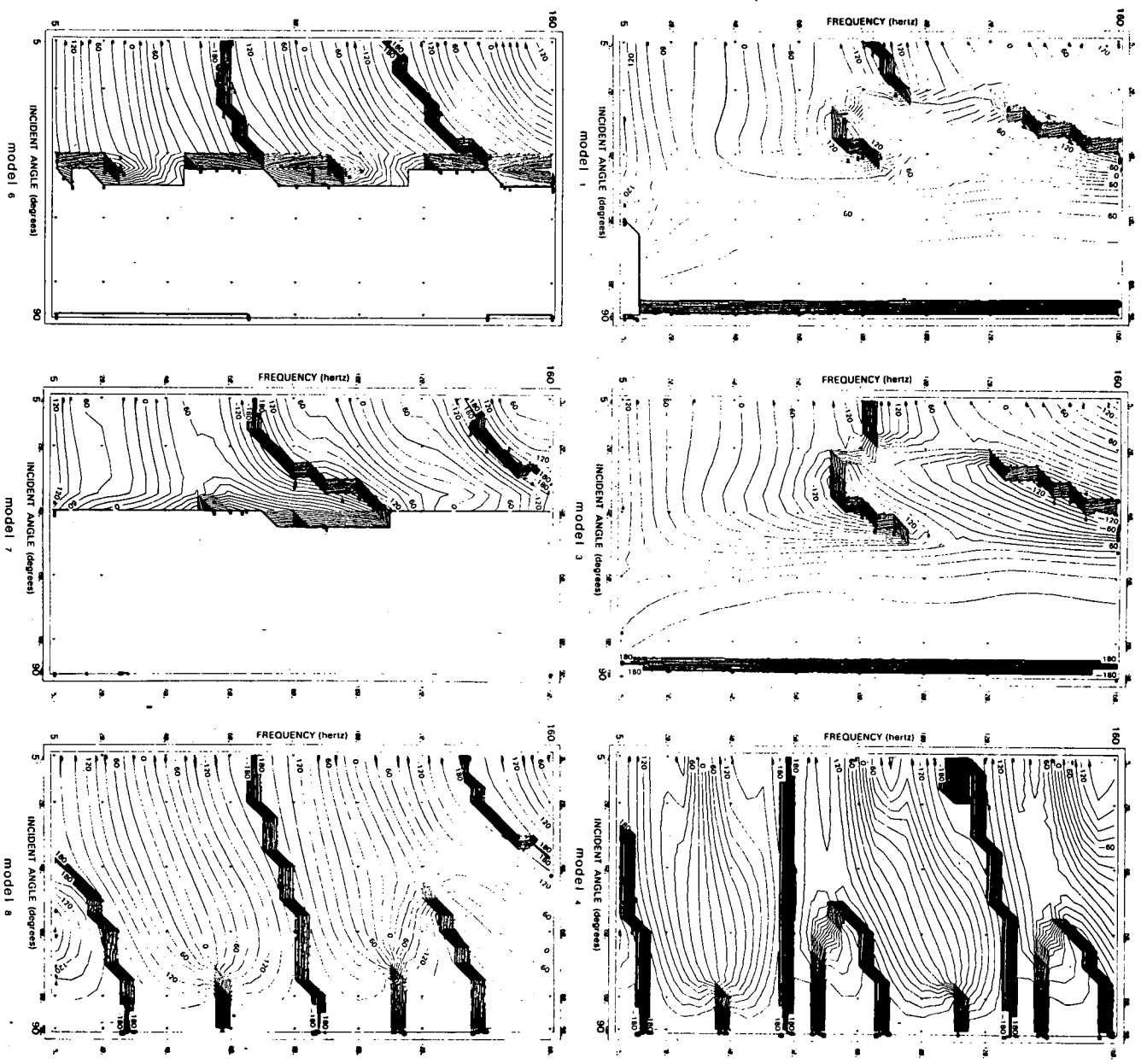


Fig. 5.11 Phase reflectivities for models 1, 3, 4, 6, 7 and 8.

with the amplitude maxima. Amplitude minima occur when $hf/v = 0.5, 1.0$ etc. while maxima occur when $hf/v = 0.25, 0.75$ etc. For small incident angles the phase characteristics are almost linear functions of frequency which leads to uniform retardation of the reflected waves with little phase distortion.

The reflectivities for near-normal incidence have far larger amplitudes than would be predicted from equation (9). Impedance ratios calculated using equations (10) and (11) are also in error. Reflectivities calculated using the Thompson-Haskell method, which includes intrabed multiple energy, are almost twice as large as those for a direct wave calculated using equation (9) (Figure 5.12). The difference is due entirely to intrabed multiple energy (Figure 5.13). Because the layer velocity is large, the lag time is small and the multiple events enhance the primary events. Consequently low transmission and large multiple energies occur for such zones. These features are characteristic of the high amplitude carbonate events found on seismic sections.

2. LAYERS WITH A LOW VELOCITY

Models 4 to 6 represent layers with lower velocities than the surrounding half-spaces (Figure 5.8). The amplitude and phase spectra (Figures 5.10 and 5.11) are similar in style and are characterised by amplitude peaks and notches that vary little for the range of incident angles commonly used in CDP shooting. However rapid changes in amplitude occur for small changes in frequency. The amplitude spectra differ greatly

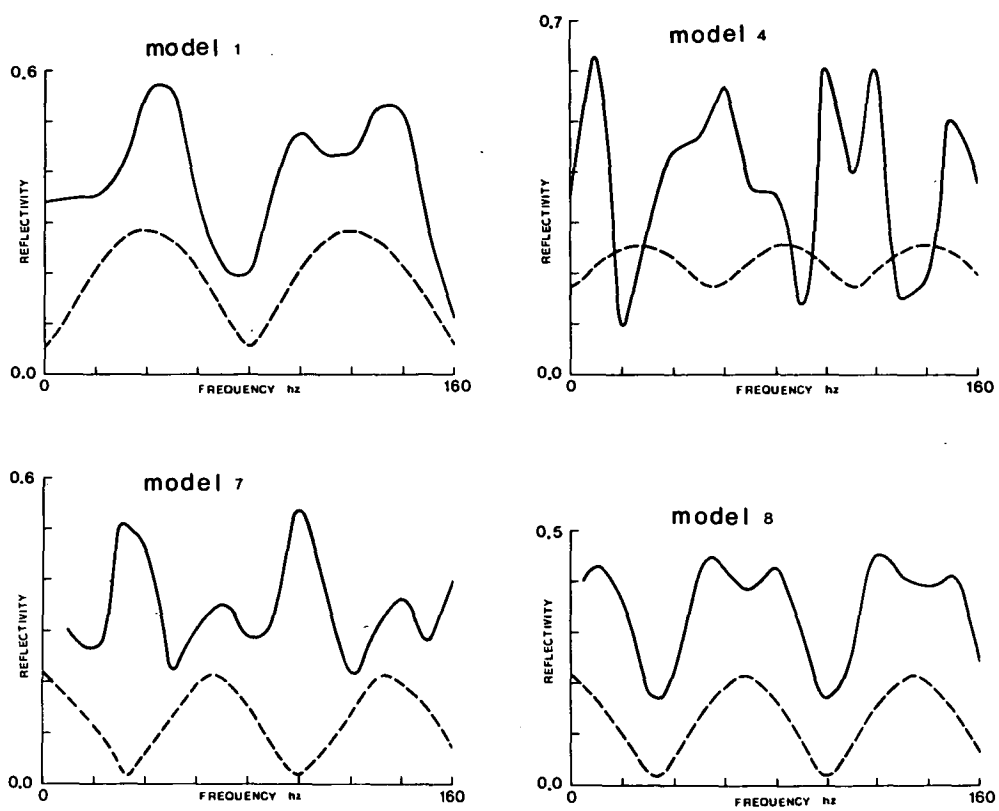


Fig. 5.12 Amplitude variations for both the total and direct waves for models 1, 4, 7 and 8. Solid line - total wave, dashed line - direct wave.

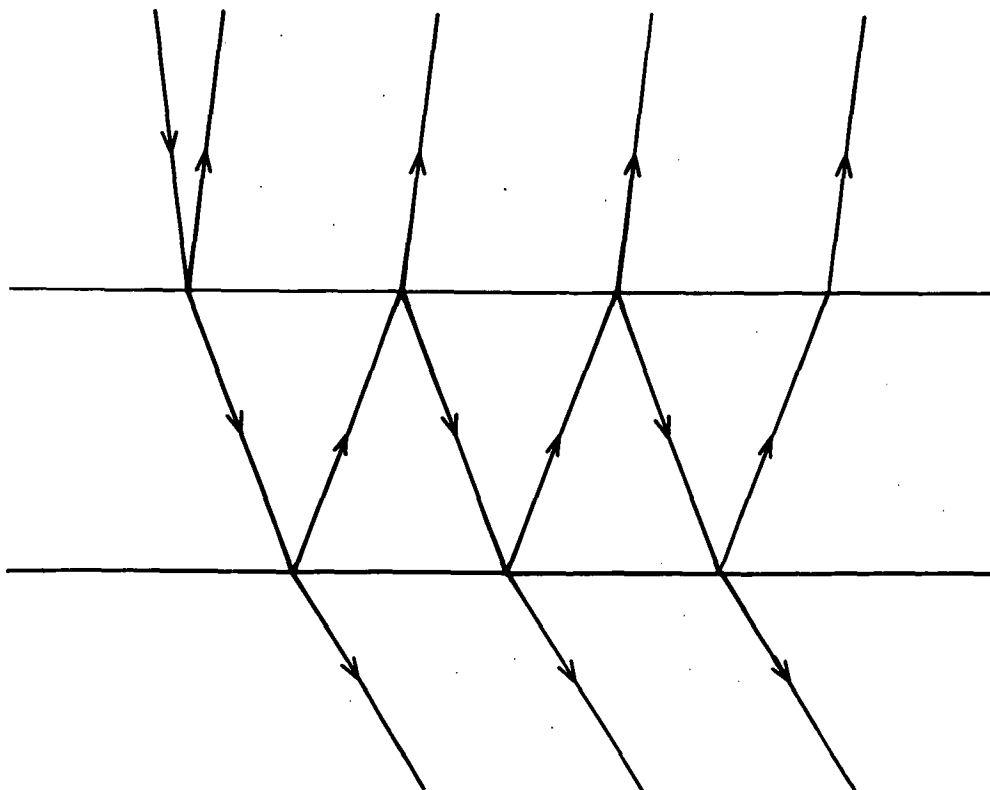


Fig. 5.13 Intrabed multiple raypaths.

from those for the high velocity layer models (models 1, 2 and 3), whose spectra have slowly varying amplitudes at high incident angles.

The break in amplitudes at 45° for model 6 corresponds to the critical reflection at which reflection amplitudes rise rapidly and then fall slowly at increasing angles. The phase spectrum is a monotonically decreasing function of frequency and has discontinuities at a spacing of 55 hz, corresponding to a layer thickness of 20 m if a layer velocity of 2210 m/sec is assumed. For the normal range of incident angles model 6 illustrates a general linear dependence of phase with frequency, while model 4 shows large departures from linearity.

A comparison of the reflectivity spectra for direct waves and composite waves for model 4 (Figure 5.12) shows the strong influence of intrabed multiples on amplitude reflectance. Amplitudes up to three times those of the direct waves and deep notches, coinciding with the predicted direct wave maxima, are characteristic. Transmitted energies are low and tend to be band limited. Such situations occur in ringing coal sections. The effect of intrabed multiples is most pronounced in model 4 due to the large impedance contrast at the upper boundary.

Since layers with lower velocities have a greater time lag than equivalent layers with higher velocities, more pronounced interference effects will produce greater character changes in the amplitude and phase spectra. Thus reflected wavelets from low velocity layers will have greater variations in wavelet shapes than wavelets from high velocity layers.

3. LAYERS WITH INTERMEDIATE VELOCITY INCREASING WITH DEPTH

Reflections for model 7 (Figure 5.8) clearly show the critical angle of 40° (Figure 5.10). The phase spectra (Figure 5.11) is similar to previous models and has discontinuities every 66 hz, corresponding to a layer thickness of 20 m if the layer velocity is 2652 m/sec. These discontinuities and the zero phase curve, coincide with amplitude maxima at small incident angles. Intrabed multiples (Figure 5.12) significantly alter the reflectivity spectrum.

4. LAYERS WITH INTERMEDIATE VELOCITY DECREASING WITH DEPTH

This case is represented by model 8 (Figure 5.8). Once again the frequency interval between the discontinuities in the phase spectrum (Figure 5.11) is characteristic of the thickness of the layer. The reflectivity spectrum has the same form as the reflectivity for the direct wave (Figure 5.12), however there is an approximately two-fold increase in reflectivity resulting from intrabed multiples. Minima occur when $hf/v = 0.5, 1.0$ etc.

5. SUMMARY

Large variations occur in the amplitude and phase of plane waves reflected from thinly-layered media for various frequencies and incident angles. The amplitudes are characterised by a sequence of maxima and minima at regular frequency intervals at the low incident angles commonly used in conventional seismic recording. The maxima and minima are partly related to the parameters of the thin beds, but

intrabed multiples significantly alter the spectrum as well as increase the reflectivity (decrease the transmitted energy). The phase spectra are all approximately linear functions of frequency at low incident angles. Although the maxima and minima in the amplitude spectra are not definitive in defining bed parameters, the frequency interval between phase discontinuities is.

Since the amplitude and phase spectra are dependent on the acoustic properties of the layers, it is necessary to study the effect of (i) the thickness of the layer and the range of frequencies excited and recorded, (ii) the ratios of the velocity in the layer to those in the overlying and underlying strata, (iii) the ratios of the densities in the layer and substratum, and (iv) the spectrum of the shot and the frequency characteristics of the instruments, before conclusions with regard to resolution and the determination of layer parameters can be drawn.

VII. THICKNESS OF THE LAYER AND THE FREQUENCY RANGE

The determination of layer parameters requires the frequency range of the spectrum of the reflected direct wave to encompass at least two peak or minimum values. The layer thickness for model 1 (Figure 5.8) has been varied from 5 m to 100 m, and frequency-thickness plots for the amplitude spectra of waves incident at 1, 10, 20 and 30 degrees have been contoured (Figures 5.14). All curves show a hyperbolic distribution of maxima and minima;

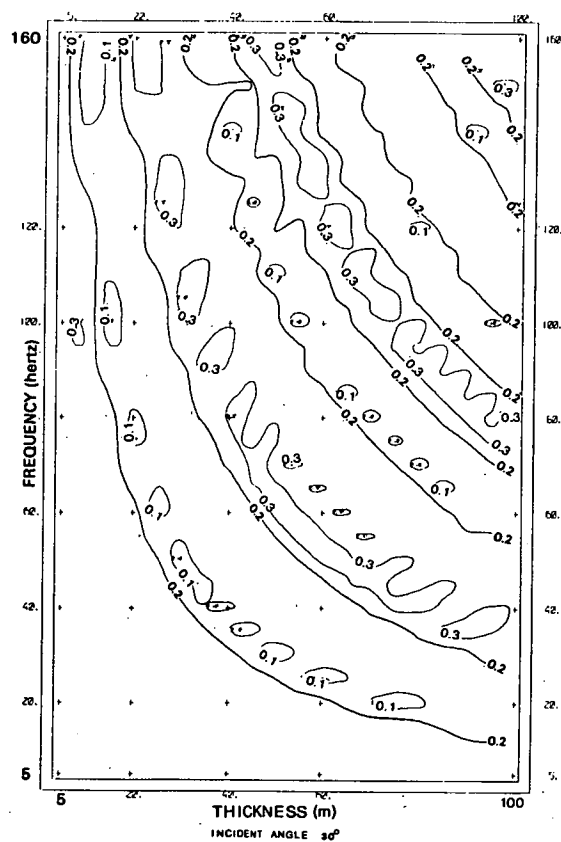
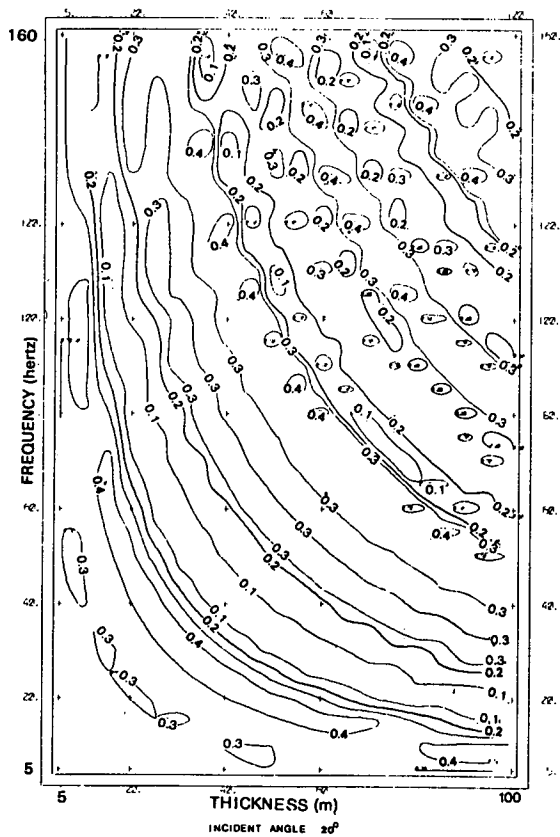
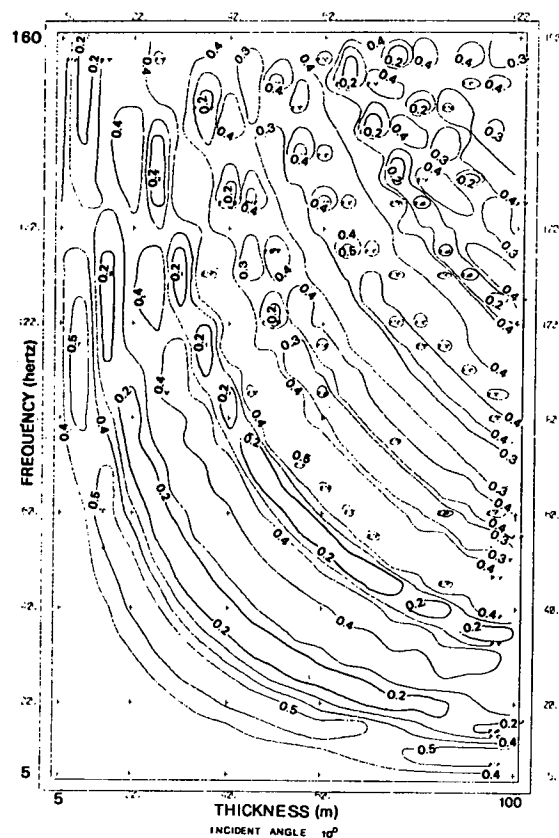
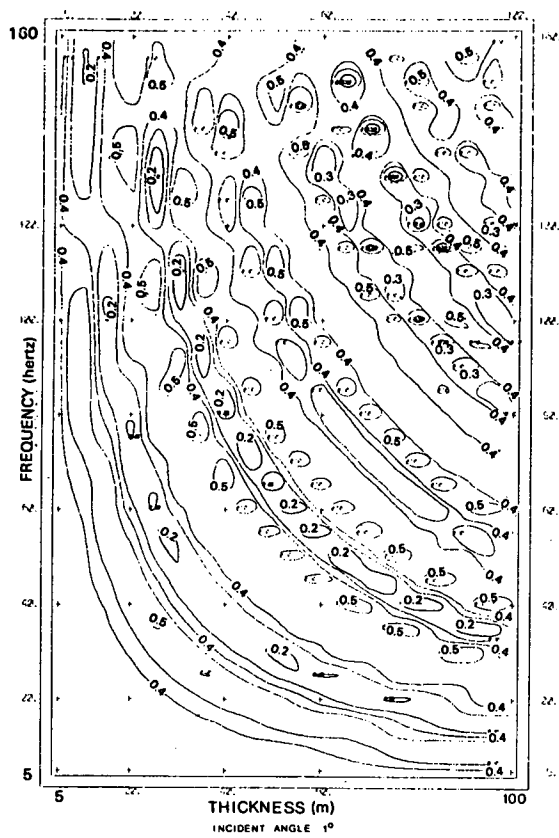


Fig. 5.14 Frequency-thickness amplitude reflectivity variations for various incident angles - model 1.

the hyperbolae become more closely spaced with increasing thickness and frequency. The effect of the incident angle and frequency on amplitude of the reflected signal can be seen by considering a bed thickness of 40 m when excited by a 60 hz plane wave. The reflectivity at low angles of incidence is approximately 0.49 but it decreases to 0.39 at 10° incident angles and to 0.18 for waves impinging at 30° . Waves at 80 hz, however, have an almost consistent reflection amplitude (0.2, 0.2, 0.29 and 0.30 for incident angles 1, 10, 20 and 30° respectively), while a 40 hz wave would be almost undetectable (relative to the 60 hz wave) as it has reflectivities of 0.22, 0.18, 0.07 and 0.10 for incident angles of 1, 10, 20 and 30° respectively. Near-vertical-incidence broad-band seismic shooting for the 40 m thick layer produces dominant amplitude events when the incident waves have frequencies of 25, 65, 95 or 140 hz. For frequency bands centred around 35, 80 or 120 hz the signal strength would be comparatively small.

The amplitude spectra illustrate that the signal strength for any particular frequency is very sensitive to bed thickness. An 80 hz normally incident wave for a bed thickness of 40 m has a reflectivity of 0.2, whereas a change in thickness of ± 5 m increases the signal strength by a factor of 2.5 (the reflectivity is 0.5).

The phase spectrum for an incident angle of 1° (Figure 5.15) shows hyperbolic discontinuities which coincide with amplitude lows. Rapid phase changes occur for high frequencies and large bed thicknesses. As the phase discontinuities coincide with amplitude minima, the frequency interval between discontinuities along a constant thickness

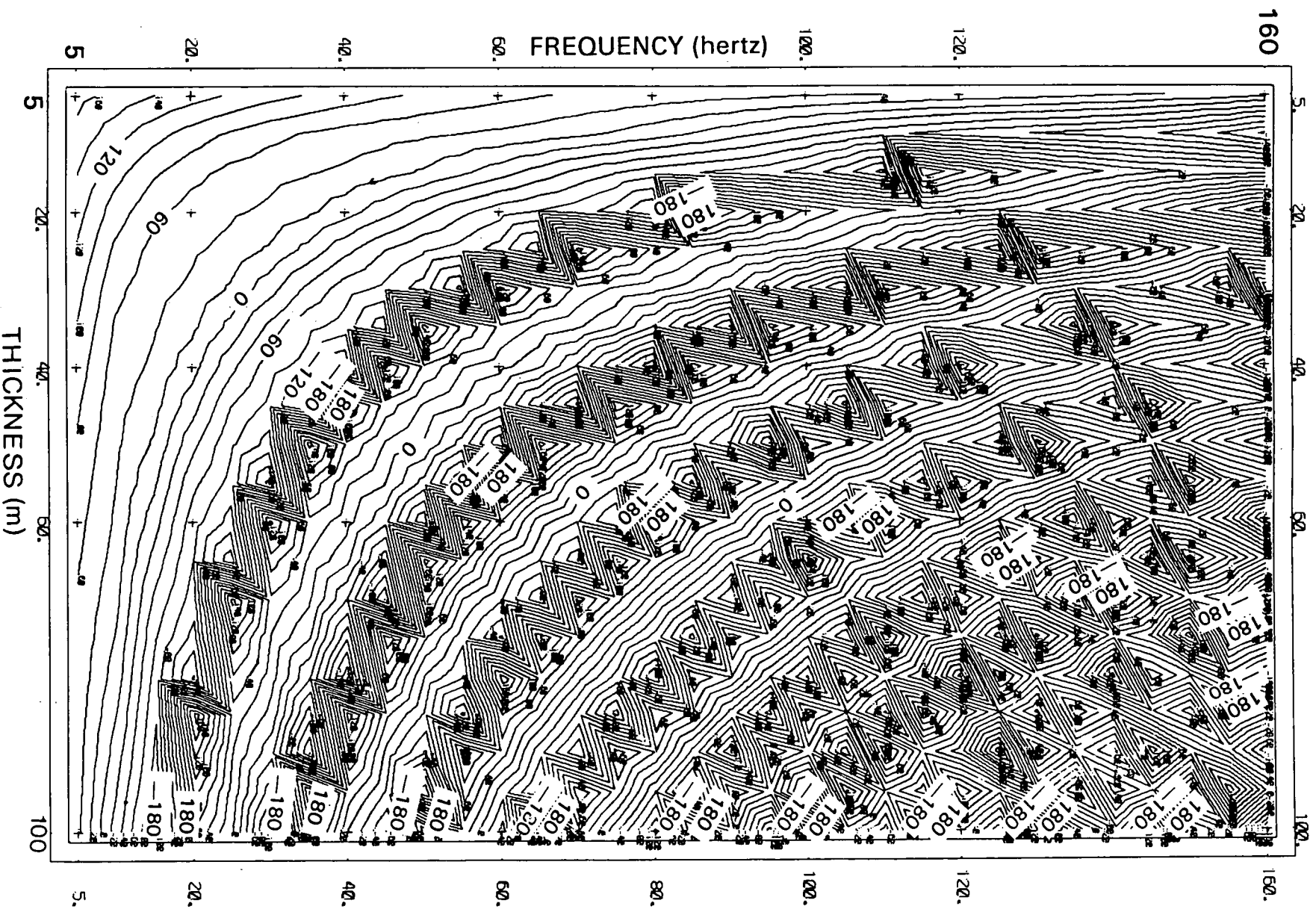


Fig. 5.15 Frequency-thickness phase reflectivity variations for an incident angle of 1 degree - model 1.

line is directly related to the transit time within the layer. Rays normally incident on a 40 m thick bed would have a frequency interval of 40 hz. Substitution in equations (3) and (5) yields a thickness of 40 m for a bed velocity of 3231 m/sec. For broad-band seismic shooting, in this case with a frequency range of 5 to 160 hz, four such frequency intervals are discernible. Such a bed could be resolvable even if the high frequency cutoff was 80 hz. Thus the resolution which is the minimum separation between reflectors needed to detect separate interfaces would be 20 m for this model and the frequency range used. From equations (3) and (5) it can be seen that smaller frequency intervals between discontinuities and hence increased bed thickness resolution would be obtained for a lower bed velocity. Gregory (1977, p.34) studied the properties of average Gulf Coast sands and noted that lower bed velocities would be obtained for sand sequences down to a depth of 2.5 km. With increased incident angle the frequency interval between discontinuities increases. This results from the $\cos i$ term in equation (3).

Transforming the reflectivity function from the frequency domain to the time domain gives the plane wave impulse response of the layered medium (Fertig & Muller, 1978). The following properties relate to the inverse amplitude transform for a zero phase spectrum:

- (1) line or undulating amplitude spectra have repetitive waveforms; continuous spectra have transient waveforms,
- (2) the fine structure of a continuous amplitude spectrum defines the waveform at longer times,

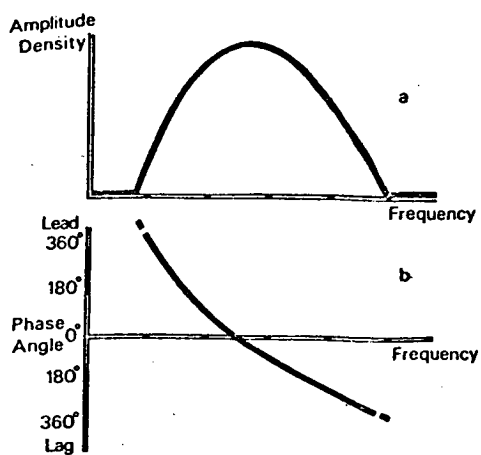
- (3) well rounded amplitude spectra have pulses that decay quickly to zero, and
- (4) short pulses have a large bandwidth - the pulse duration cannot be smaller than the reciprocal of the bandwidth.

A phase spectrum which is a straight line passing through the phase axis at the origin or an integral multiple of 2π maintains the pulse shape given by zero phase, but imposes a uniform propagation delay proportional to the slope of the line. Any other phase spectrum changes the wave shape by altering the peak amplitude, making it unsymmetric and dispersing it to occupy a greater time. Figure 5.16

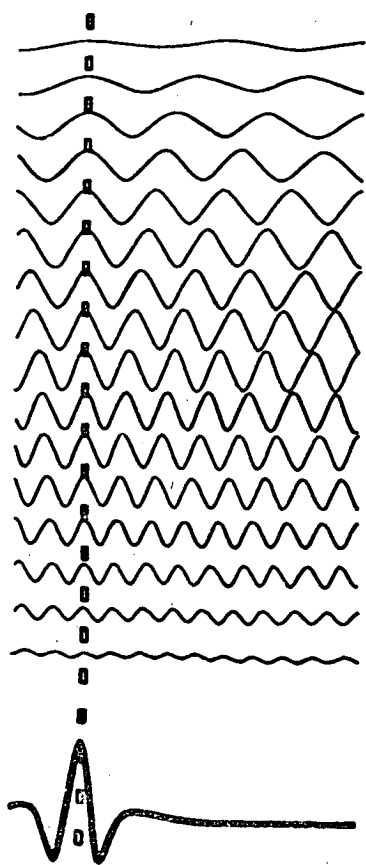
shows the time shifting of the individual frequency components due to a non-linear phase spectrum, thereby producing a somewhat distorted wavelet. The degree of distortion is directly related to the slope of the phase spectrum.

Transforming the reflectivity function for a constant layer thickness yields the impulse response. Thus a 5 m thick bed which has a broad, almost flat spectrum with an amplitude of about 0.4 corresponds to a very large amplitude impulse while a 100 m bed with its regular spectral maxima and minima would yield a time trace showing the separation of the two primary reflecting waves. As a generalization for broadband seismic recording, the arrival amplitude of a thin bed sequence increases and the pulse shape becomes narrower as the bed thins.

Three important conclusions can be drawn from the amplitude and phase spectra. Firstly, the reflectivities and amplitude differences between maximum and minimum hyperbolae decrease with increasing incident angle. Secondly, the ability



ZERO PHASE WAVELET



NON-ZERO PHASE WAVELET

using phase spectrum b

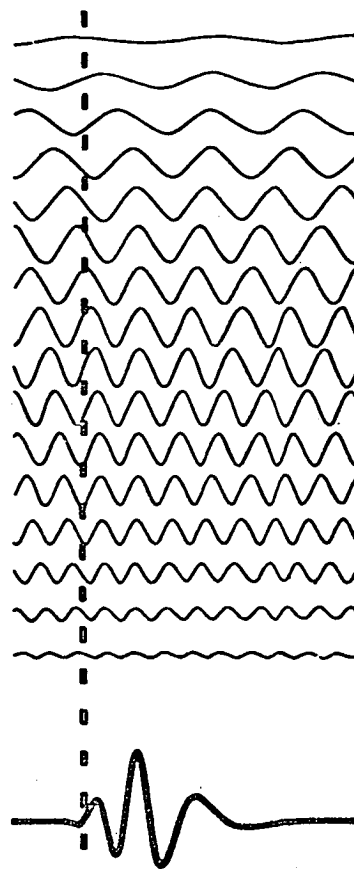


Fig. 5.16 Zero-phase and non-zero-phase wavelets (after Anstey, 1977).

to detect slight variations in thickness for very thin sequences is small compared to the resolution for thicker sequences and this resolution increases with increasing frequency. Thirdly, for a particular bed thickness amplitude variations which must be expected for varying incident angles and frequencies provide vital bed parameter information.

VIII. VELOCITY CONTRASTS AND THE FREQUENCY RANGE

Vertical resolution is determined in part by the velocity contrasts between the layer and the surrounding strata. Figure 5.17 illustrates the range of compressional velocities for various rock types. The phase and amplitude spectra for frequencies in the range 5 hz to 160 hz with various velocity contrasts between the overlying stratum and a layer are plotted in Figure 5.18. The velocity ratios for model A and B are in the range 0.5 to 1.5 which corresponds to layer velocities between 1196 and 3590 m/sec. Model A corresponds to a velocity ratio between the overlying and underlying half-spaces of 0.90, while for model B the ratio is 1.08. Incident angles of 1° are used throughout. The velocity ranges of the four type models are also illustrated.

The similarity of the amplitude spectra for both models indicates the small effect of the underlying half-space velocities on reflectivities. The spectra show distributions of maxima and minima that are almost linearly dependent on the layer velocity; the peaks become more closely spaced for low layer velocities and high frequencies. Deviations from

DOLOMITE
SALT
GRANITE
LIMESTONE
SANDSTONE
SHALE
COAL
OIL
GAS

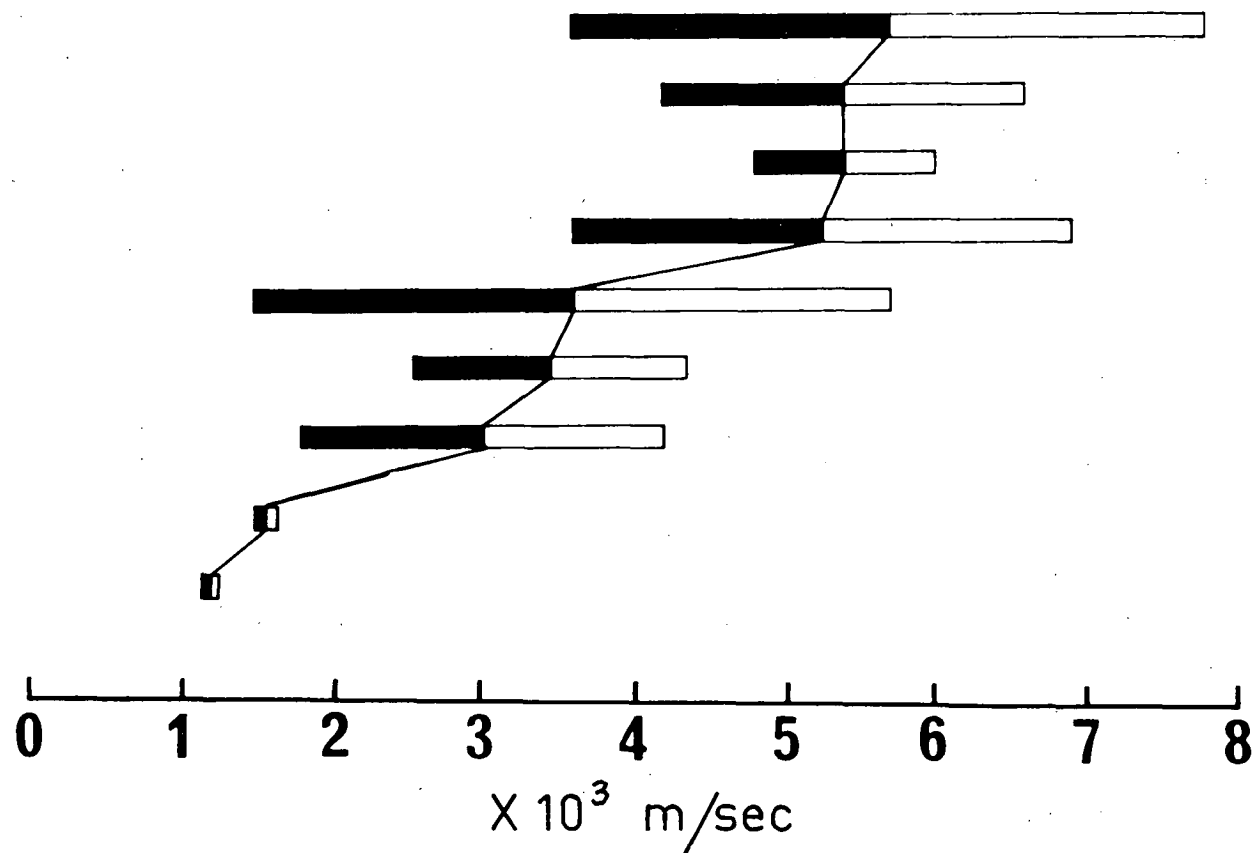
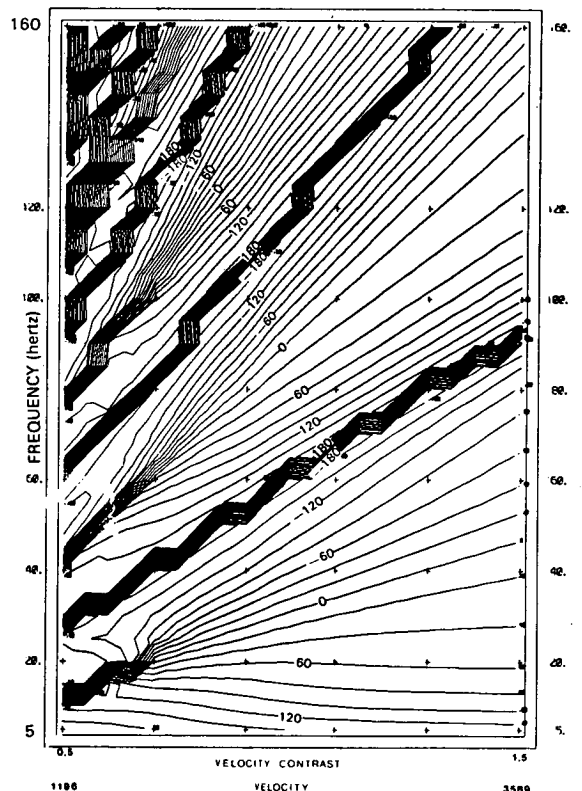
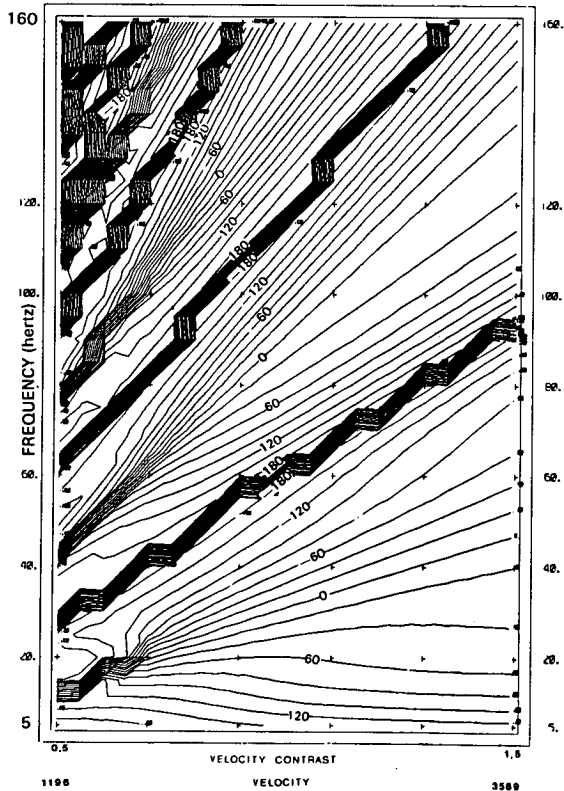
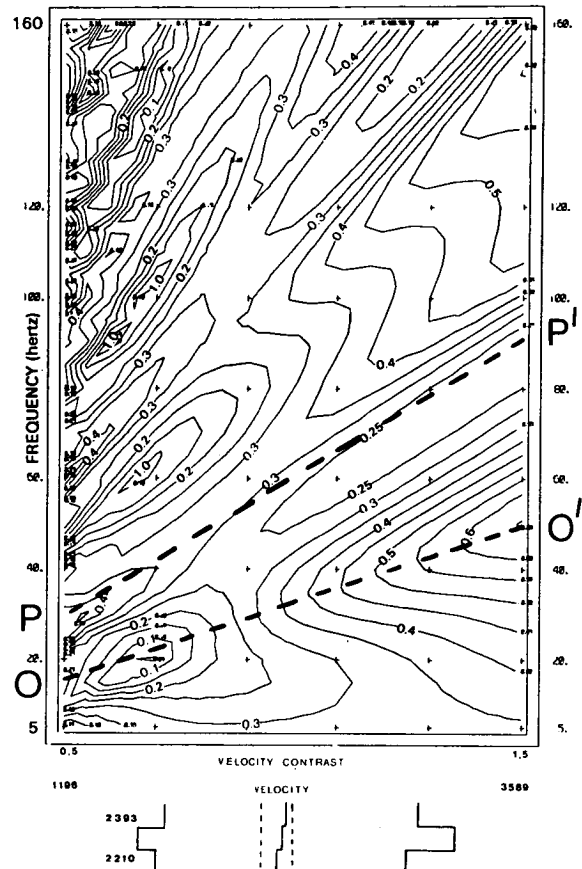
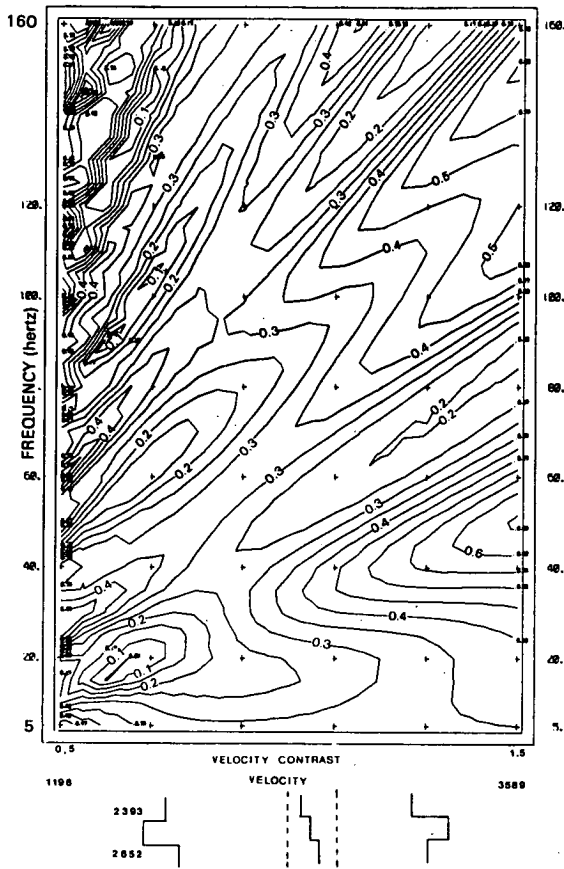


Fig. 5.17 Compressional velocity ranges for various geological rock types.



A

B

Fig. 5.18 Amplitude and phase reflectivities for varying bed velocities. O-O' represents the line for $hf/v = 0.25$, P-P' represents the line for $hf/v = 0.50$.

linearity occur for low velocity contrasts. Phase discontinuities correspond to amplitude minima for type 1 models and maxima for type 2 models. The converse is true for the zero phase curve. Amplitude signal strengths are not very sensitive to bed velocity variations, except at high frequencies and low bed velocities.

The plane wave impulse responses vary greatly with velocity ratio. High bed velocities result in relatively impulsive wavelets due to the broad rounded amplitude spectrum at low frequencies, whereas for low bed velocities the pulse is diminished in amplitude, of long duration and has a complex character.

The effect of intrabed multiples is illustrated in Figure 5.19 which compares the reflectivity amplitudes with those for the direct waves where hf/v is taken to be 0.25 and 0.50. Curves for hf/v equal to 0.25 show that intrabed multiples increase the reflectivities for velocity ratios greater than 0.8, but destructively interfere for low contrasts, thereby decreasing reflectivities. Intrabed multiples produce four- to eight-fold increases in reflectivity when hf/v is 0.5.

IX. DENSITY CONTRASTS AND THE FREQUENCY RANGE

Densities for typical environments and rock types range from 1.4 t/m^3 for peaty coals up to 2.8 t/m^3 for old deeply buried sandstones (Figure 5.20). Although sedimentary rocks have a wide range of velocities, they have a small range of densities (Figure 5.21) and have a velocity-density relation-

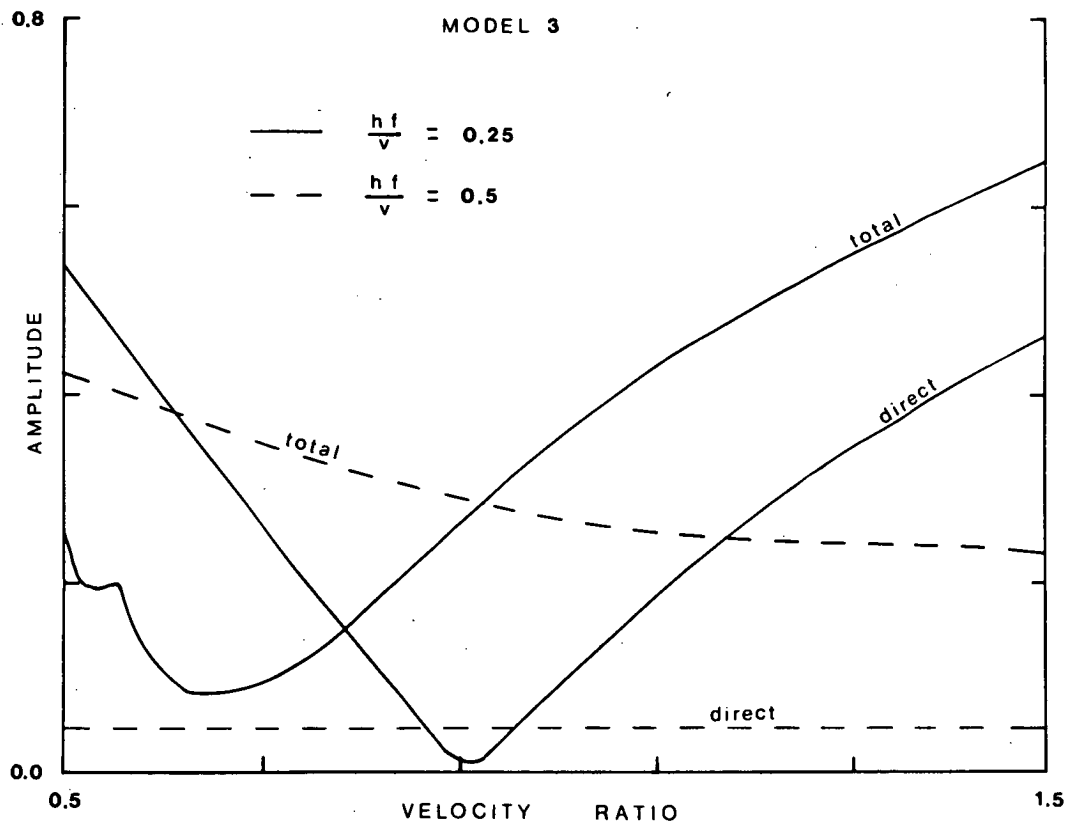


Fig. 5.19 Amplitude reflectivities for direct and total waves for varying bed velocity ratios.

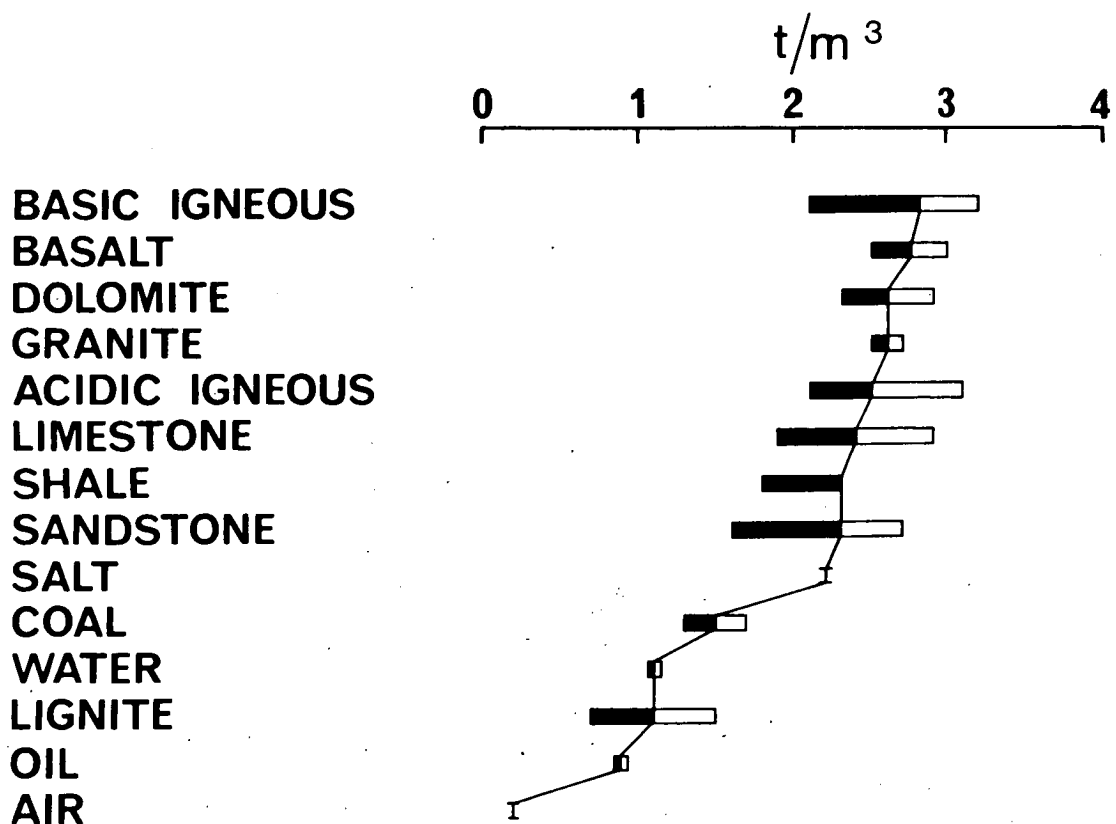


Fig. 5.20 Typical density ranges for various geological rock types.

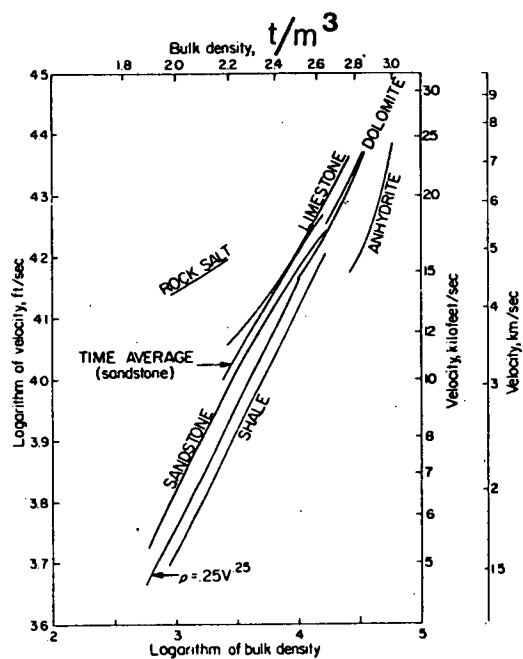


Fig. 5.21 Velocity-density relationships for common sedimentary rocks (after Gardner *et al.*, 1974).

ship that can be approximated by

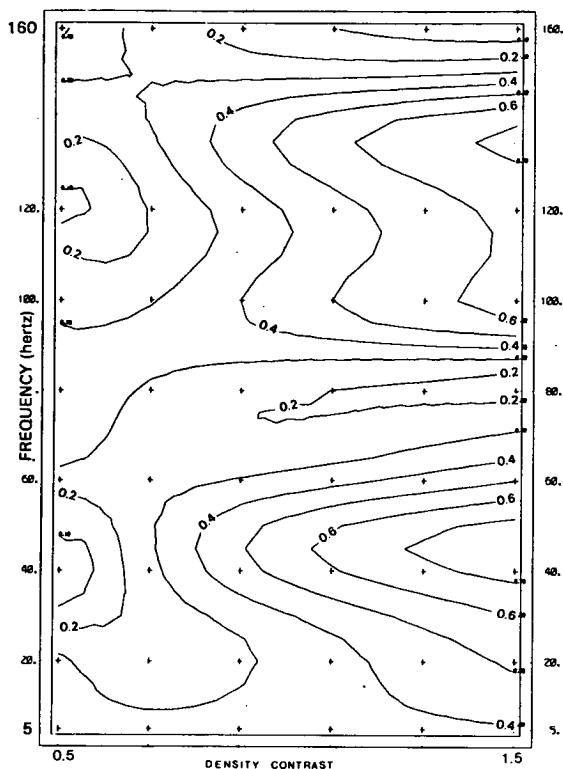
$$\rho = 0.310 V^{0.25} \quad \dots (13)$$

where V is in m/sec and ρ is in t/m^3 .

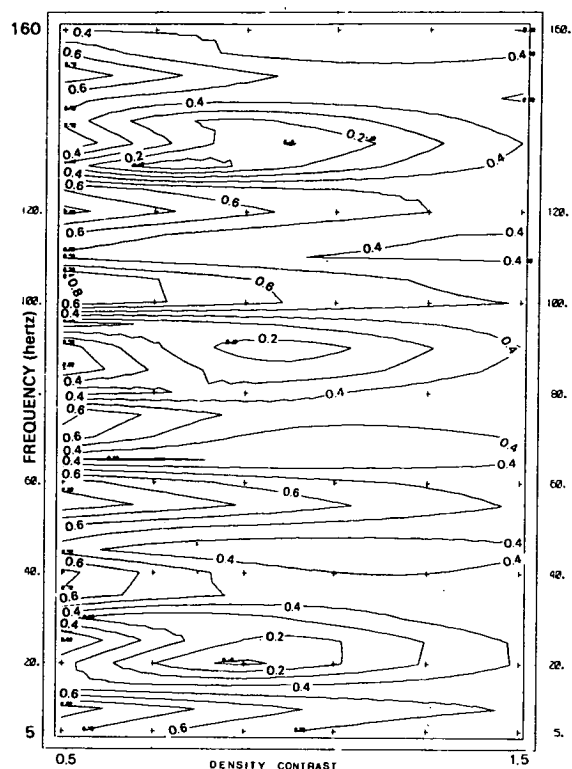
Such a relationship limits the possible range of densities likely to be associated with a particular velocity distribution. Coal, rock salt and gas-filled sands are obvious deviations from this rule.

When varying density contrasts are used the reflectivity amplitude and phase spectra of models 1, 4, 7 and 8 (Figure 5.8) are dominated by sub-horizontal trends except at very small bed densities (Figures 5.22 and 5.23) which are outside the range of normal rock densities and can thus be ignored. The phase spectra show only small phase deviations with varying density ratio. Frequency intervals between phase discontinuities for models 1, 4, 7 and 8 are 80, 55, 66 and 66 hz respectively, and correspond to the layer transit times and hence bed parameters. For models 1 and 7 the discontinuities correspond to amplitude minima and the zero phase curve corresponds to amplitude maxima, while for models 4 and 8 the amplitude maxima correspond to the phase discontinuities. The zero phase curve for model 7 corresponds to reflectivity highs, however, due to the effect of intrabed multiples there is an alternating correspondence for model 4 which may be diagnostic of high amplitude multiples.

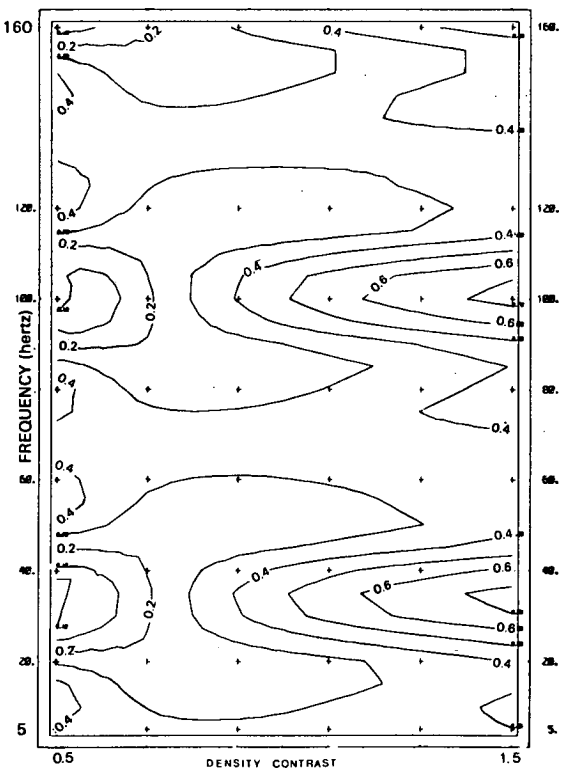
At a particular frequency the amplitude spectra are relatively insensitive to density contrast changes, but the greatest variation occurs at frequencies corresponding to amplitude maxima. Greater resolution can be achieved by



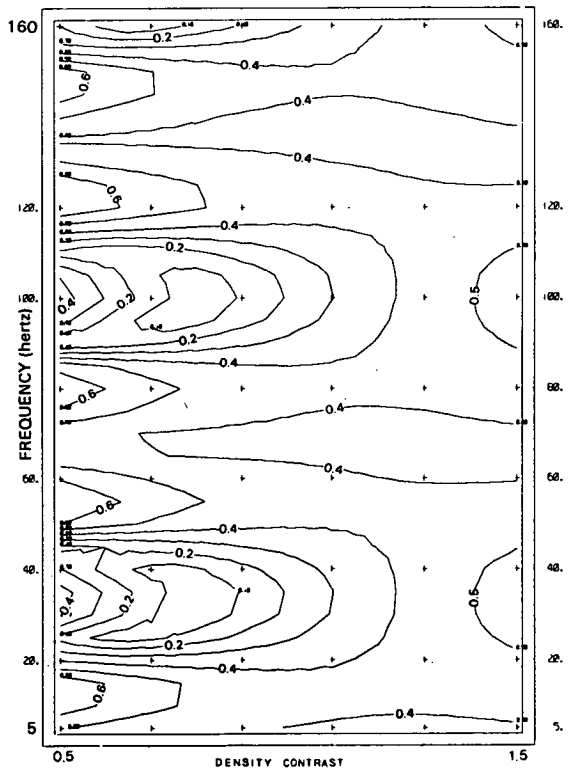
model 1



model 4

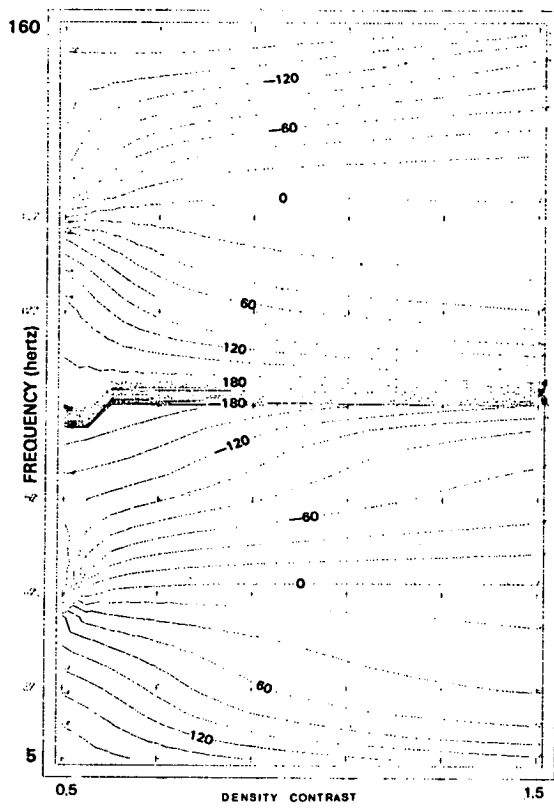


model 7

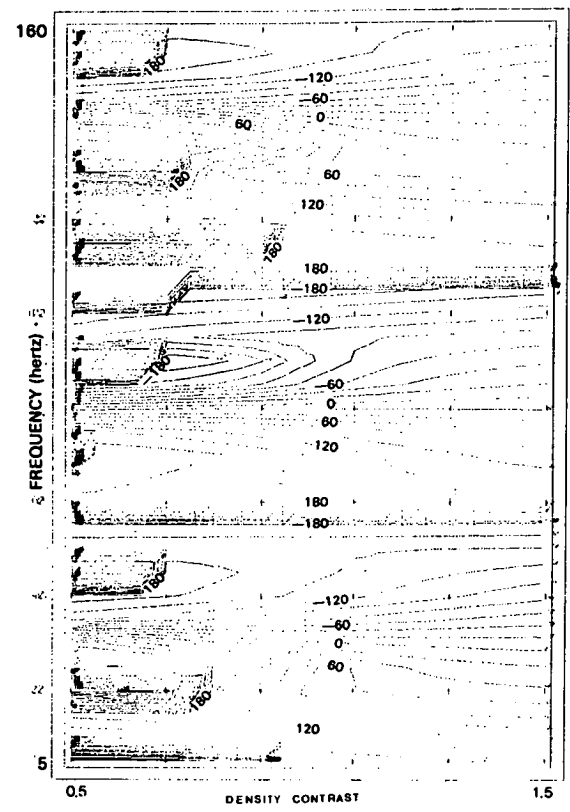


model 8

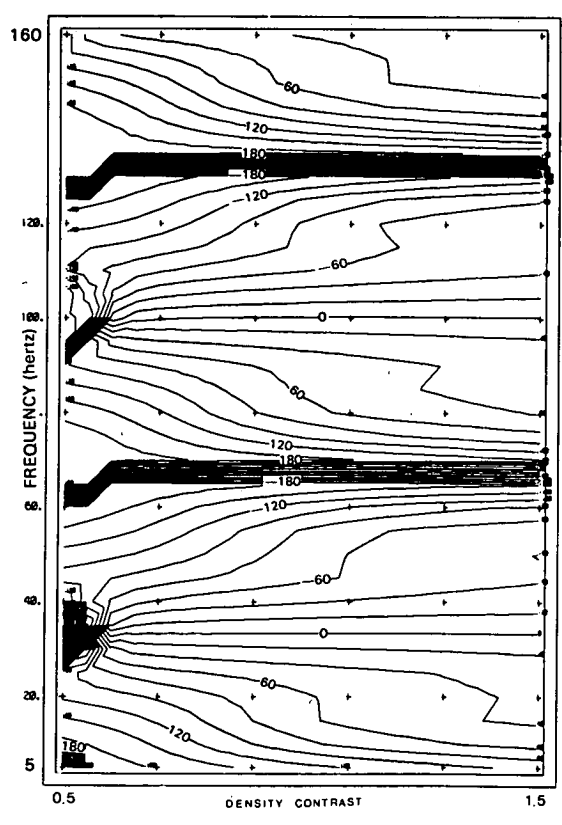
Fig. 5.22 Amplitude reflectivities for varying density contrasts for models 1, 4, 7 and 8.



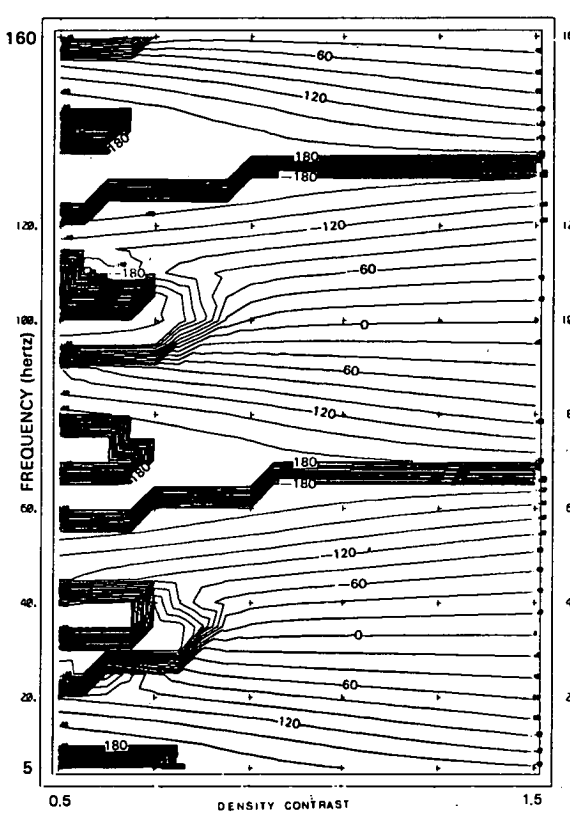
model 1



model 4



model 7



model 8

Fig. 5.23 Phase reflectivities for varying density contrasts for models 1, 4, 7 and 8.

noting the variation in the differences between maximum and minimum amplitudes with density contrast.

Layer density variations influence the reflectivity of the zone and the contribution of intrabed multiples is shown in Figures 5.24 and 5.25 which illustrate the reflectivities for the total and direct waves when hf/v is equal to 0.25 and 0.50. Large reflectivities occur when hf/v is equal to 0.25 for models 1 and 7, but these are much reduced when hf/v is equal to 0.5. The converse is true for models 4 and 8. The influence of intrabed multiples is obvious.

In summary, density variations further enhance the amplitude variations from a thin layer but the positions of the peaks and notches are related only to the layer thickness and velocity.

X. THICKNESS-VELOCITY RELATIONSHIP

Since the amplitude spectra are closely related to the layer velocity and thickness it is necessary to study the inter-relationships of these two parameters. Figure 5.26 illustrates the reflectivity variations for thicknesses ranging from 5 to 100 m and velocities from 1615 to 4847 m/sec at frequencies of 30, 50 and 80 hz using model 1 type parameters (Figure 5.8). These variations show that for a constant frequency, changes in velocity introduce greater amplitude and phase changes at large thicknesses than small thicknesses. Similarly, thickness variations produce the greatest changes in amplitude and phase at low velocities.

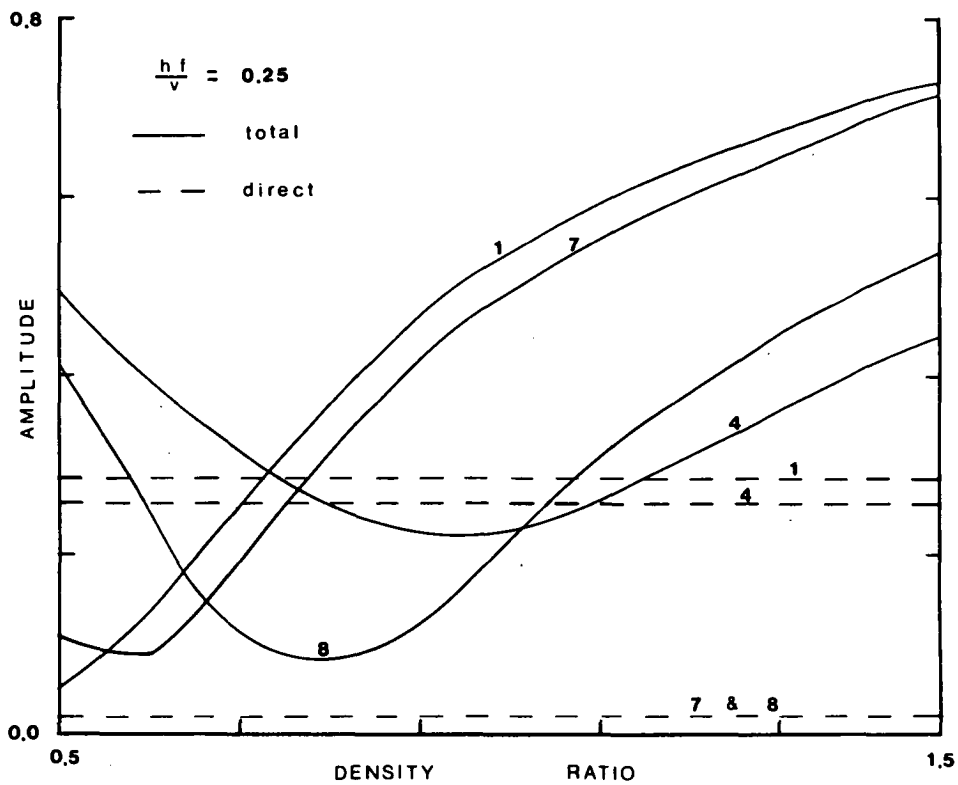


Fig. 5.24 Amplitude variations for both the total and direct waves due to varying bed density ratios for models 1, 4, 7 and 8.

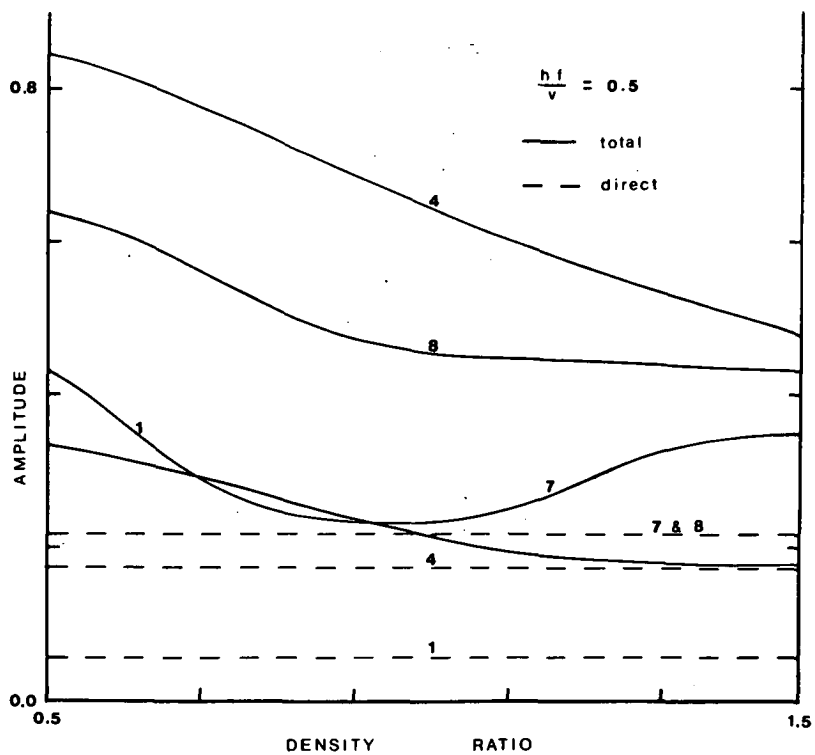
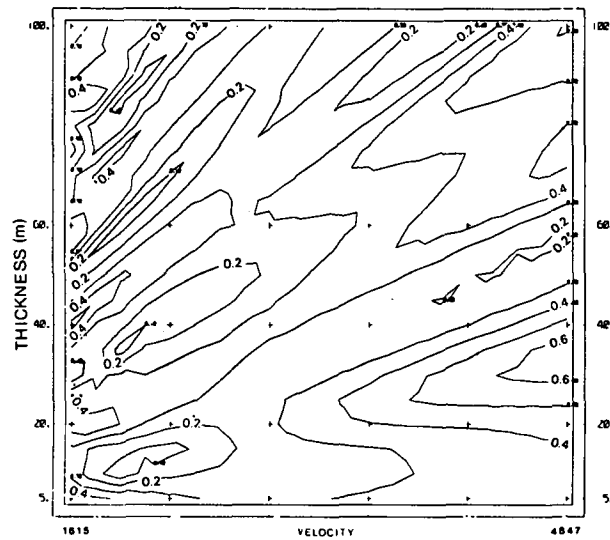
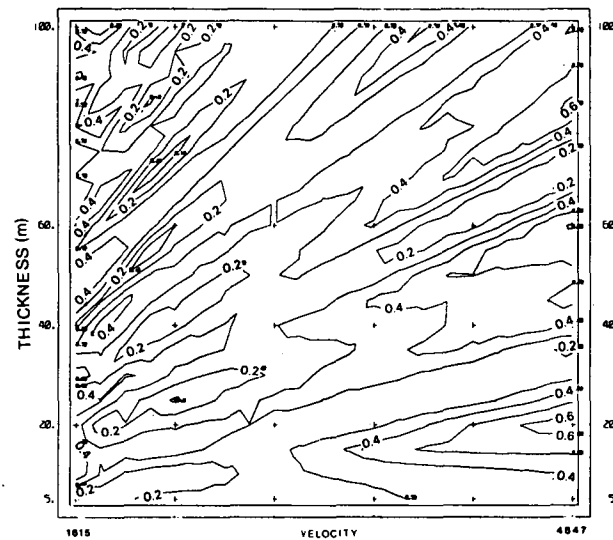


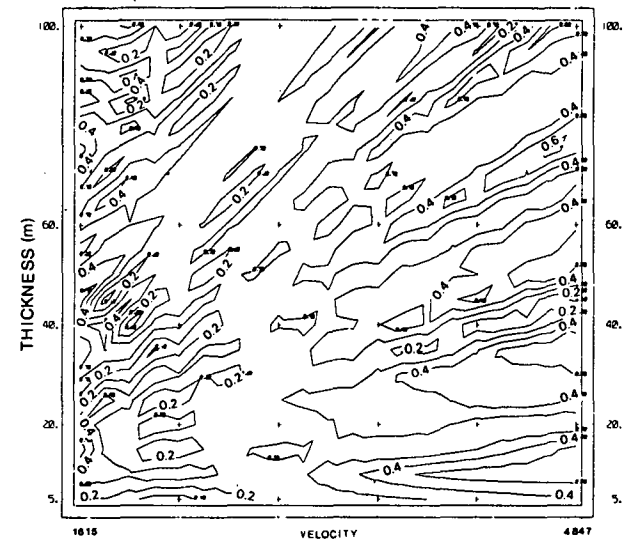
Fig. 5.25 Amplitude variations for both the total and direct waves due to varying bed density ratios for models 1, 4, 7 and 8.



FREQUENCY 30 (hertz)



FREQUENCY 50 (hertz)



FREQUENCY 80 (hertz)

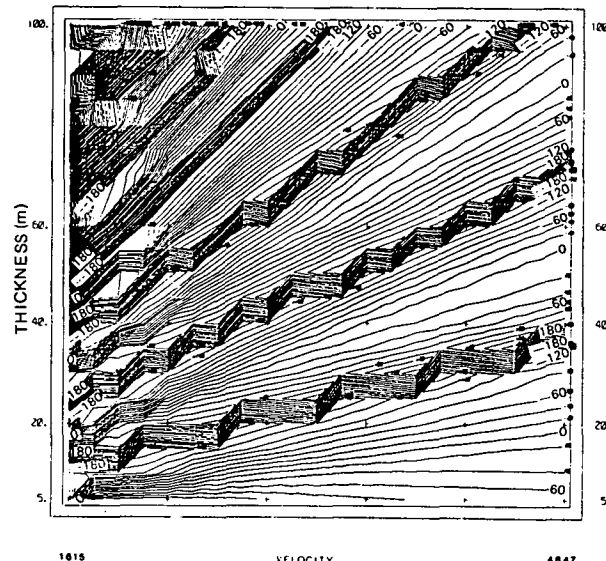
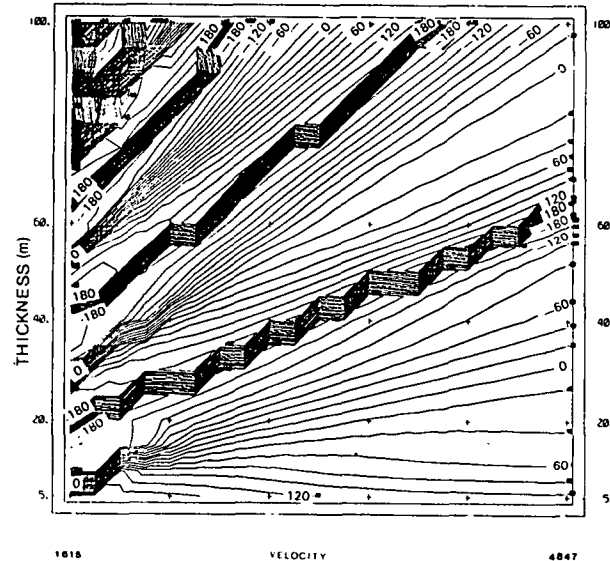


Fig. 5.26 Amplitude and phase reflectivities for various thickness-bed velocity combinations using model 1 type parameters.

Hence resolution is greatest for thick beds with low velocity contrasts and high frequencies.

XI. SHOT, INSTRUMENT AND PROCESSING DISTORTIONS

Reflectivity distortions may be introduced by the shot spectrum and by phase changes introduced by the recording instruments. Differences in the shot and geophone environment may also induce waveshape changes. Seismic processing such as deconvolution to remove near-surface reverberations and wavelet shaping to broaden the frequency spectrum further distort the wavelets. CDP stacking continues the degradation of the wavelet information.

XII. SEISMIC NOISE

Sheriff (1977) noted that data must be essentially noise-free before proceeding with stratigraphic interpretation so that the variations in waveshape represent variations in the subsurface and not changes in noise. Noise problems vary due to different amplitude decay rates in different areas requiring charges varying from large quantities of explosives to a single cap (O'Doherty & Anstey, 1971).

Conventional seismic processing generally includes time variant filtering of the broadband stacked trace (Figure 5.27). Some of the principal markers on the conventional section are insignificant on the broadband section, while others appear to be displaced in time. The filtering process partly removes

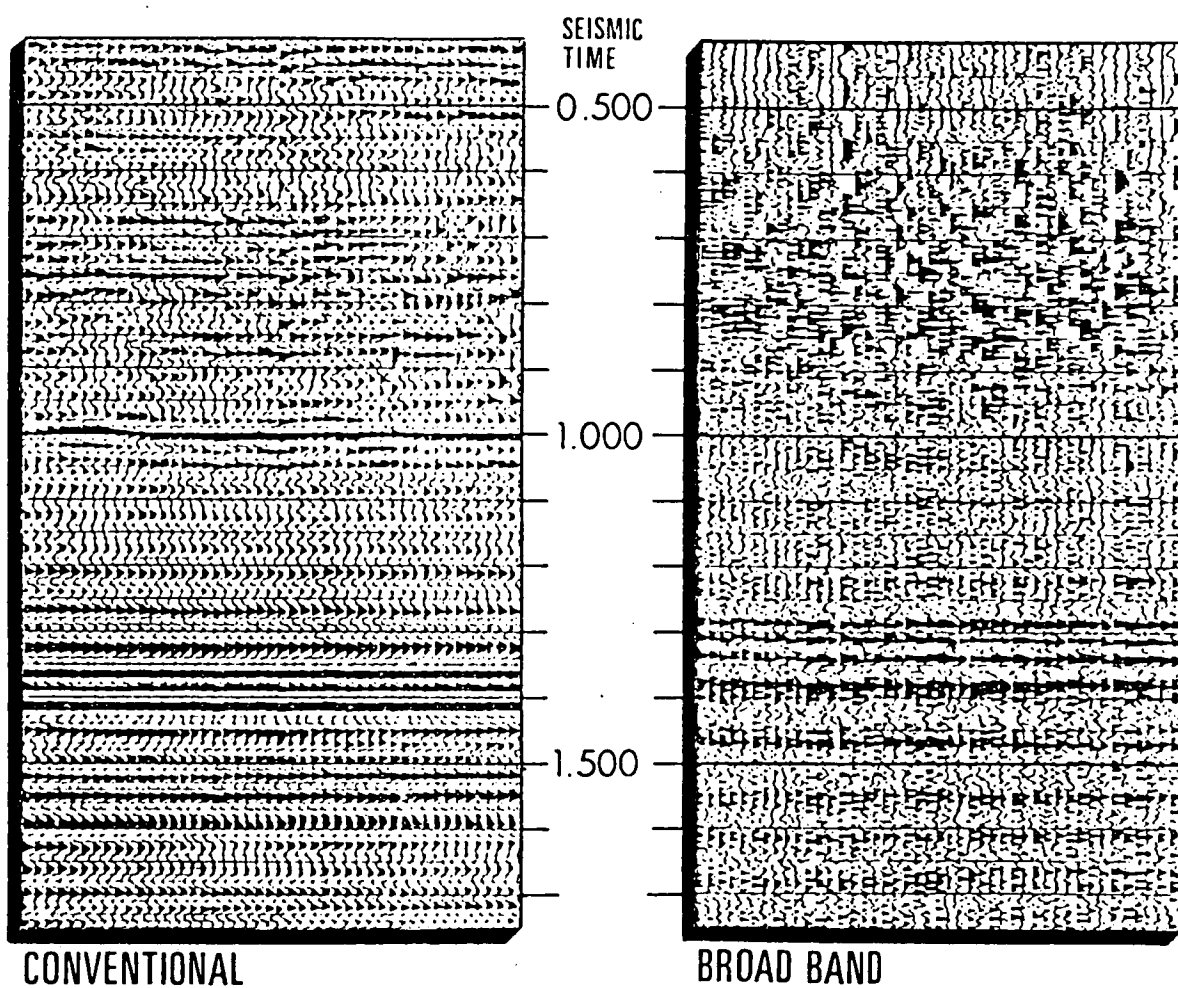


Fig. 5.27 Comparison of conventional and broadband seismic data.

high frequency noise and enhances reflectors by choosing frequency bands that yield maximum trace-to-trace correlation. The occurrence of high frequency uncorrelated noise is a natural result of the reflectivity of the geological sequence. High frequency signals are subject to rapid variations in amplitude due to changes in the angle of incidence so the wavelet character varies across a CDP gather. Such signals may depend on only minor changes in bed thickness or velocity, thereby making stacked trace-to-trace correlation difficult.

Of greater consequence are the phase changes that occur at high frequencies. Consider the phase spectrum (Figure 5.28) for model 1 (Figure 5.8) at frequencies of 20 and 120 hz for incident angles less than 25° . Virtually no phase shift occurs for the 20 hz signal whereas a 50° phase shift results at the higher frequency. Figure 5.29 illustrates synthetic seismograms constructed with arrivals uniformly phase-shifted by 0, 45, 90, 135 and 180° . Thus phase-shifted arrivals at 120 hz introduce systematic traveltimes errors as the incident angle varies due to the relative changes in the peak and trough positions of the gather arrival wavelets. There is a 230° phase shift between the wavelets of both frequencies for near normal angles of incidence. This continuous variation of phase with frequency accounts for the principal markers on the conventional section being displaced in time on the broadband section. The time variant filter is in part an attempt to define frequency bands where the phase shifts are minimal, thereby allowing easier correlation by making the amplitudes more uniform.

In regions composed of thin units or where the beds have high velocities relative to the surrounding strata, large

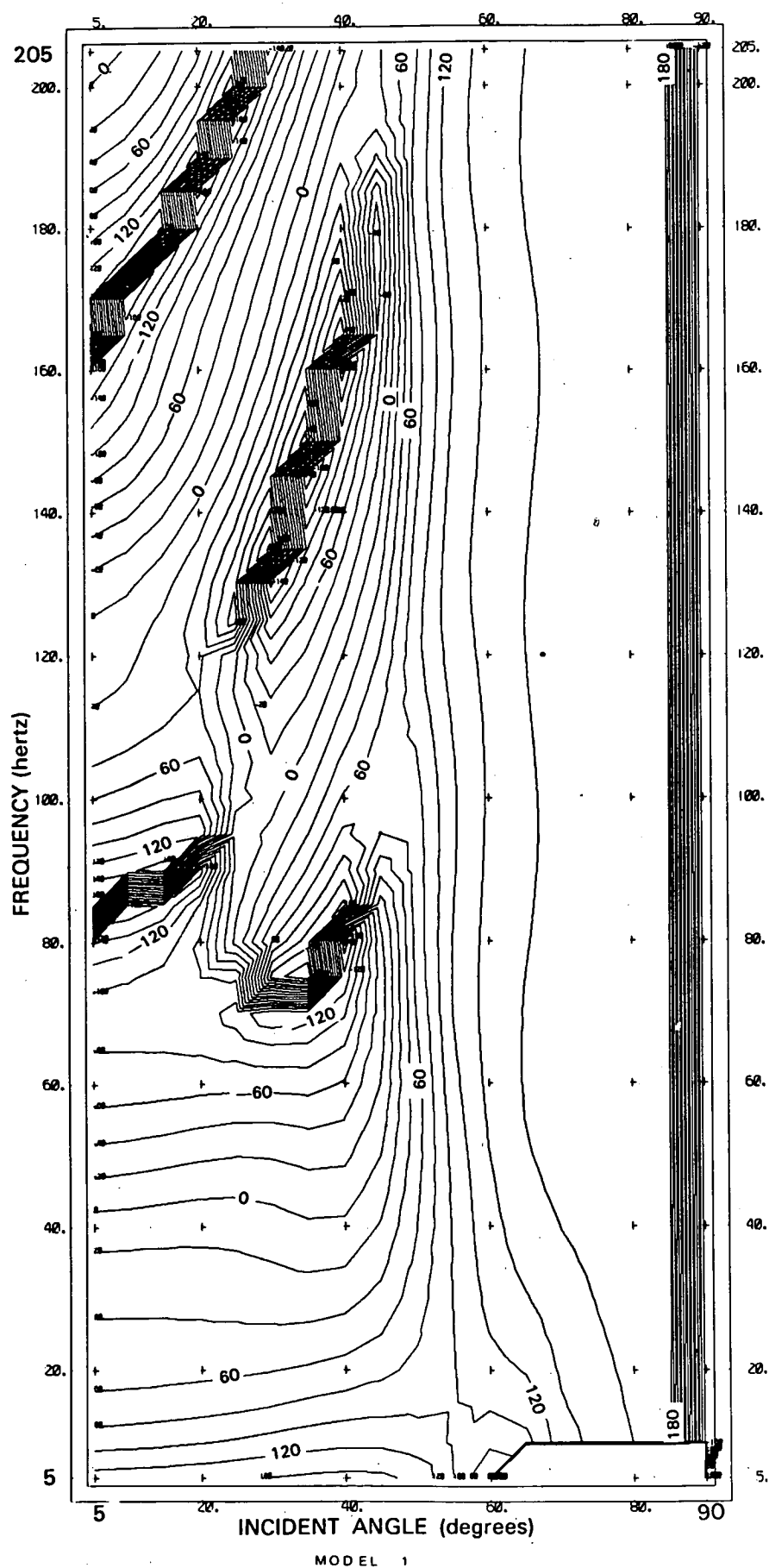
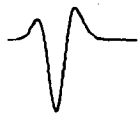


Fig. 5.28 Phase spectrum for model 1.

pulse



PHASE SHIFTS:

0° 45° 90° 135° 180°

SYNTHETIC SEISMOGRAM

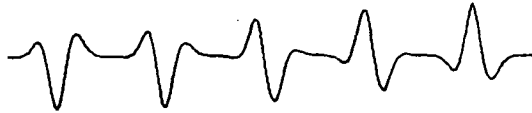


Fig. 5.29 Synthetic seismograms for various phase shifted pulses.

reflectivities are obtained for low frequencies, thereby reducing the transmitted energy. However at the gaps in the reflectivity spectrum the higher frequencies will be transmitted. For thick sequences or where beds have low velocity contrasts notching of the reflectivity increases thereby allowing a greater number of frequencies to be transmitted. Alternating sequences of thin beds having large velocity contrasts would transmit only small frequency ranges. Transmitted energy is therefore frequency dependent and determined by the path geometry.

XIII. VELOCITY DISPERSION

The form of an elastic wave travelling in an homogeneous isotropic ideally elastic medium does not change with distance travelled. In an inelastic medium amplitude distortions result from attenuation and phase distortion is produced by dispersion. O'Brien (1961) considered that the phase distortions are small, while Wuenschel (1965) showed that body wave dispersion may be predicted from the attenuation coefficient and that there is an increase in phase velocity with frequency. Gupta (1966) stated that dispersion effects due to inhomogeneities may occur even if absorption were completely absent.

The phase curves for the layered models discussed earlier show that the phase shifts are dependent on the layer parameters, frequency and angle of incidence of the wave. The time delay associated with a monochromatic wave passing through a medium is given by

$$T = [\Phi(\omega) \pm 2n\pi]/\omega \quad \dots (14)$$

where n is an integer, ω is the angular frequency and Φ is the phase shift (Bath, 1974, p.239). The phase velocity between two points separated by a distance (ℓ) is given in the general case by

$$v_p = \frac{\omega \ell}{\Phi(\omega) \pm 2n\pi} \quad \dots (15)$$

Rayleigh (1896, p.87) showed that for a plane wave normally incident on an homogeneous thin layer between two homogeneous half-spaces with identical properties

$$\tan \Phi = \frac{1}{2}(\alpha + \alpha^{-1}) \tan \left(\frac{\omega h}{V_2} \right) \quad \dots (16)$$

where $\alpha = V_1 \rho_1 / V_2 \rho_2$; V_1 , ρ_1 , V_2 and ρ_2 being the velocities and densities in the half-spaces and layered medium of thickness (h), respectively. The phase shift increases continuously as $\omega h / V_2$ rises and fluctuates around the straight line

$$\Phi = \omega h / V_2 \quad \dots (17)$$

From equations (16) and (17) the relative phase velocity (v_p / V_2) is given by

$$\frac{v_p}{V_2} = \frac{\omega \ell / V_2}{\arctan[\frac{1}{2}(\alpha + \alpha^{-1}) \tan(\omega h / V_2)]} \quad \dots (18)$$

Thus phase velocity dispersion results from heterogeneity and is most marked when $\omega h / V_2$ is small ($\omega h / V_2 < \pi/2$). For large values of $\omega h / V_2$ the phase velocity (v_p) is similar to the true layer velocity (V_2). Dispersion is abnormal when $\omega h / V_2$ is

small, especially for thin layers where the acoustic impedance contrasts are large. The phase velocity is the same as the layer velocity (V_2) when $\omega h/V_2 = n/4$. Although this theory applies to direct waves it is apparent that dispersion in thin layers may be significant.

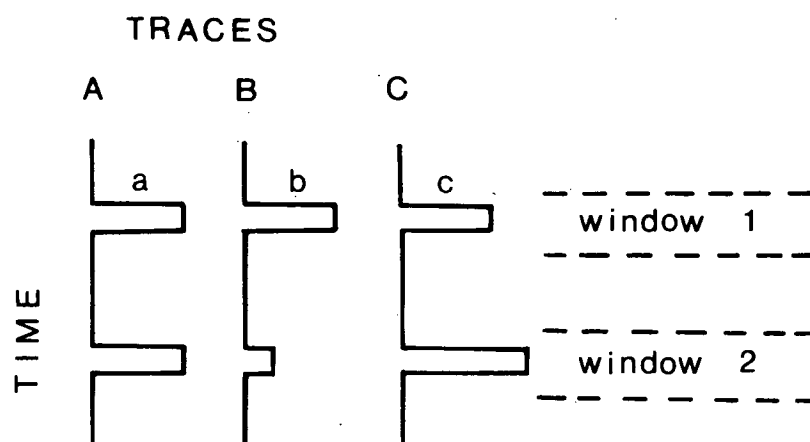
XIV. VELOCITY DETERMINATION

Multifold ground coverage using CDP techniques allows direct determination of the rms velocities associated with a reflector by performing hyperbolic searches for maximum correlation among appropriate gathered traces using the relation

$$\Delta T = \sqrt{T_0^2 + \frac{X^2}{V^2}} - T_0 \quad \dots (19)$$

where ΔT is the NMO associated with each trace for a particular input velocity (V).

Taner & Koehler (1969) used normalised cross-correlation functions to measure the signal strength of the NMO corrected traces. Other coherence measurements include cross correlation, semblance, absolute sum and normalised sum (Figure 5.30). Such measurements are obtained by relating the times of either the amplitude peaks or valleys of the event on each trace. The variation of amplitude and phase with incident angle has been clearly demonstrated and must affect the accuracy of the velocity determination techniques which assume there are no phase changes. Previous discussion has shown that phase changes are virtually negligible at low frequencies. Wardell (1973) stated that time varying filtering before



coherence coefficient	$\frac{1}{2} \frac{(a+b+c) - (a^2 + b^2 + c^2)}{(a^2 + b^2 + c^2)}$
cross correlation	$(a \times b) + (a \times c) + (b \times c)$
normalized cross correlation	$\frac{(a \times b) + (a \times c) + (b \times c)}{\sqrt{(a^2) (b^2) (c^2)}}$
semblance	$\frac{(a \times b) + (a \times c) + (b \times c)}{(a^2 + b^2 + c^2)}$
absolute sum	$ a + b + c $

Fig. 5.30 Coherence measurements used in NMO velocity determination.

velocity determination is necessary to provide a good signal-to-noise ratio. Such filtering invariably selects a low frequency band where the phase amplitude effects are minimal. Since phase shifts correspond to time delays it is necessary to ascertain the errors resulting from velocity determinations at different frequencies.

Let t_m , the measured time, be the sum of the true travel-time (t) plus a delay (Δt), which can be positive or negative. On the assumption that the reflector is horizontal, t is given by:

$$t^2 = t_o^2 + \frac{X^2}{V_{rms}^2} \quad \dots (20)$$

$$\text{so that } t_m^2 = t_o^2 + \frac{X^2}{V_{rms}^2} + 2\Delta t \sqrt{t_o^2 + \frac{X^2}{V_{rms}^2}} + \Delta t^2 \quad \dots (21)$$

For small spreads and deep reflectors $t_o \gg X/V_{rms}$. Expanding the square root and neglecting higher order terms

$$t_m^2 = t_o^2 + X^2 \left(\frac{1}{V_{rms}^2} + \frac{\Delta t}{t_o V_{rms}^2} \right) + \dots + 2t_o \Delta t + \Delta t^2 \quad \dots (22)$$

$$= \left(t_o + \Delta t \right)^2 + \frac{X^2}{V_{rms_app}^2} \quad \dots (23)$$

$$\text{where } V_{rms_app} = \frac{V_{rms}}{\sqrt{1 + \Delta t/t_o}} \quad \dots (24)$$

Thus for positive delays the effect of Δt is to give an apparent velocity less than the true velocity. At the other extreme, when $X/V_{rms} \gg t_o$, consider two points, one at $X = 0$ and the other at large X and pass a hyperbola through them.

For $X = 0$,

$$t_m^2 = t_O^2 + 2t_O\Delta t + \Delta t^2 = A \quad \dots (25)$$

and for X large,

$$t_O^2 + \frac{X^2}{V_{rms}^2} + \Delta t \sqrt{t_O^2 + \frac{X^2}{V_{rms}^2}} + (\Delta t)^2 = A + BX^2 \quad \dots (26)$$

Letting $B = 1/V_{rms_app}^2$ and solving

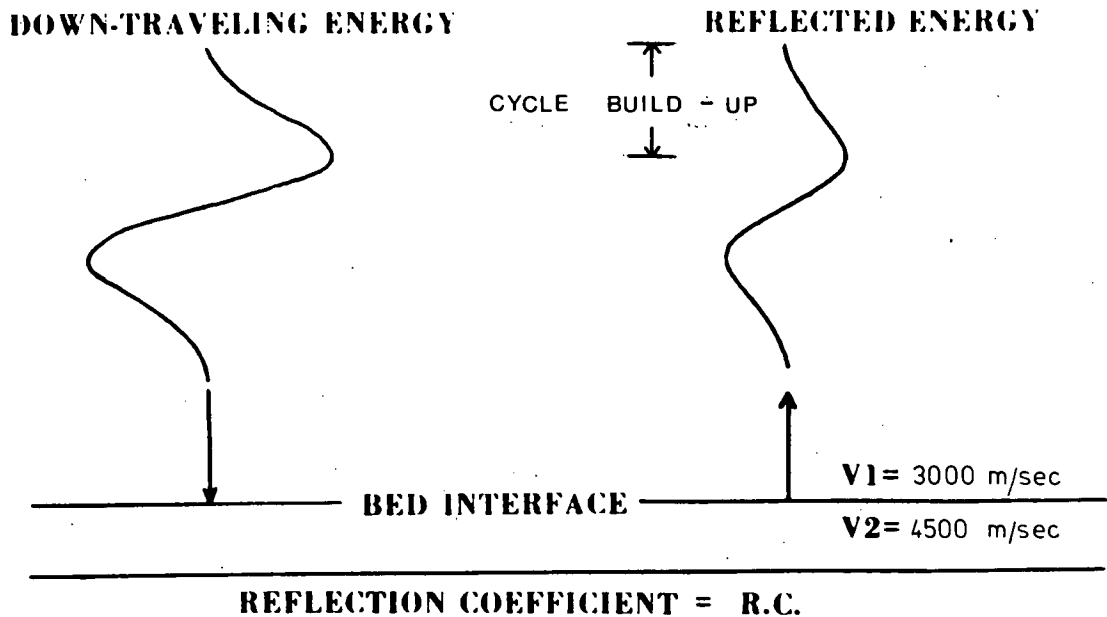
$$V_{rms_app} = \frac{V_{rms}}{\sqrt{1 + (2V_{rms}\Delta t)/X}} \quad \dots (27)$$

Once again positive delays result in apparent rms velocities less than true rms velocities.

The delays may result from onset time buildup (Figure 5.31) or phase dispersion effects. As seismic velocities are a function of frequency it is generally assumed that the part of the pulse travelling through an absorptive medium with an almost constant velocity is the high amplitude part, so coherence measurements are measured relative to the peak or valley events on the trace. Figure 5.32 shows the delays in onset time produced by absorption while the distorting effect of interference due to single and multiple layers is shown in Figure 5.33. The synthetic seismogram in Figure 5.34 was constructed using a modified version of the Fortran program developed by Rudman & Blakely (1976) and shows the dominance of arrivals from high velocity contrast reflectors. Onset time corrections are related to the frequency band used for velocity determination and as the corrections are always positive velocities determined are always less than the true rms velocities.

REFLECTION PROCESS

ONE INTERFACE; LOW TO HIGH VELOCITY



$$R.C. = \frac{V_2 - V_1}{V_1 + V_2} = \frac{4500 - 3000}{7500} = .20$$

Fig. 5.31 Cyclic buildup due to reflection from a single interface.

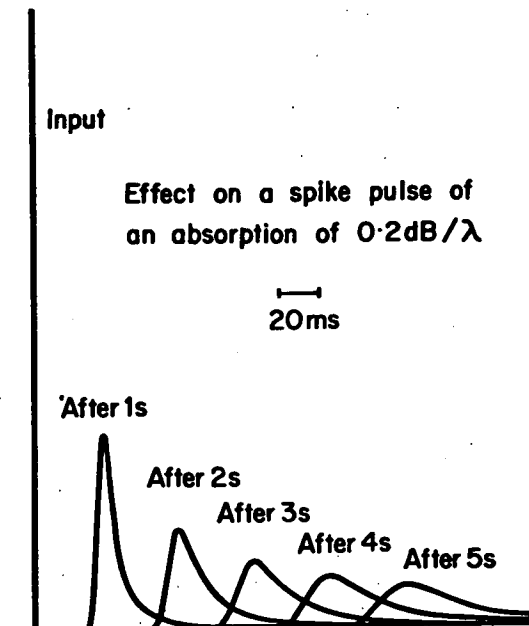
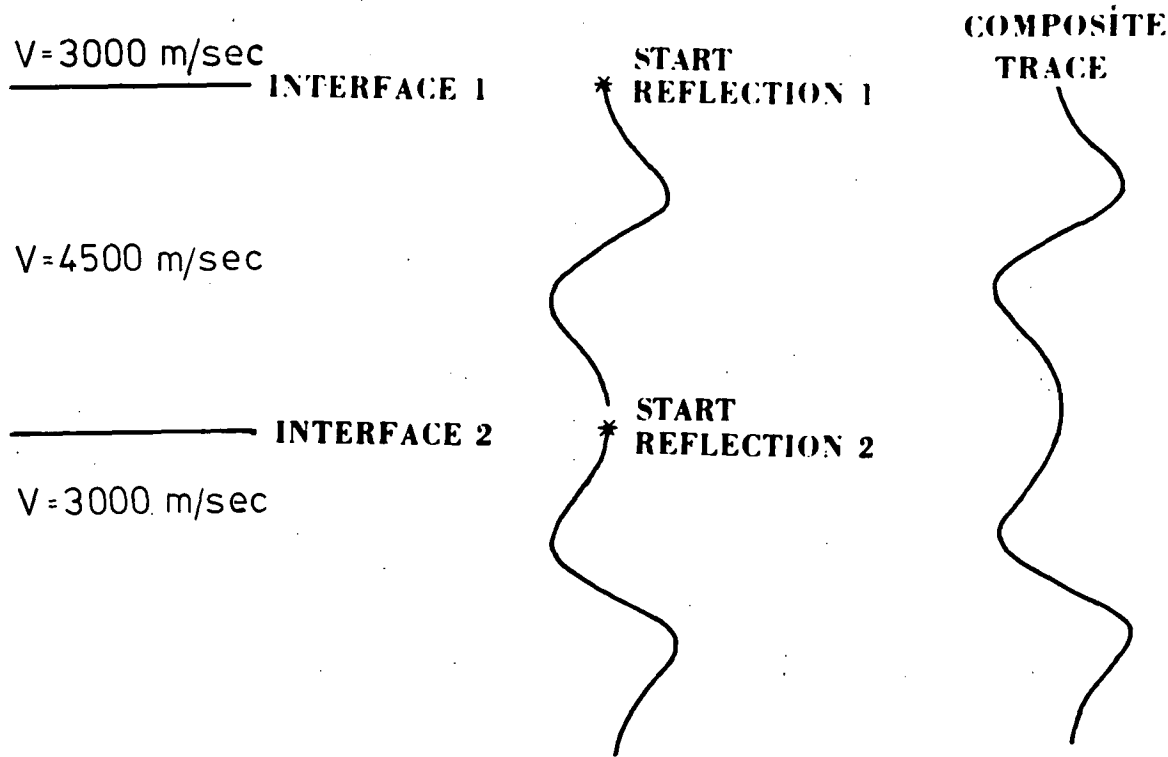


Fig. 5.32 Onset time variations due to absorption (after Anstey, 1977).

REFLECTION PROCESS — TWO INTERFACES

NO INTERFERENCE



WITH INTERFERENCE

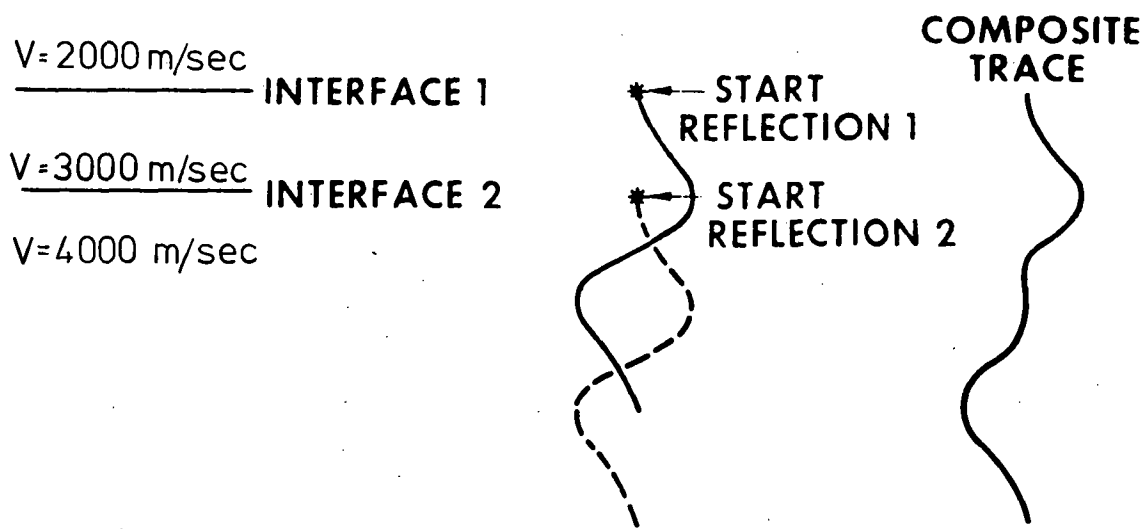


Fig. 5.33 Reflection process for two interfaces illustrating their interference effect.

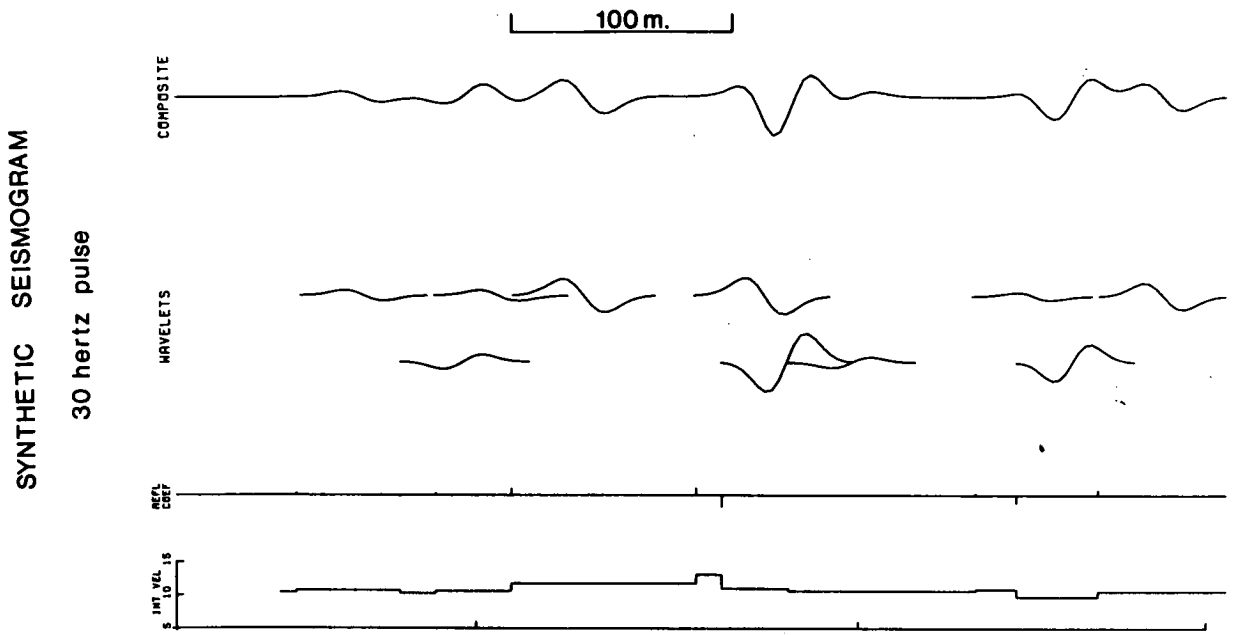


Fig. 5.34 Synthetic seismogram showing complex interference effects and consequent onset time delay problems.

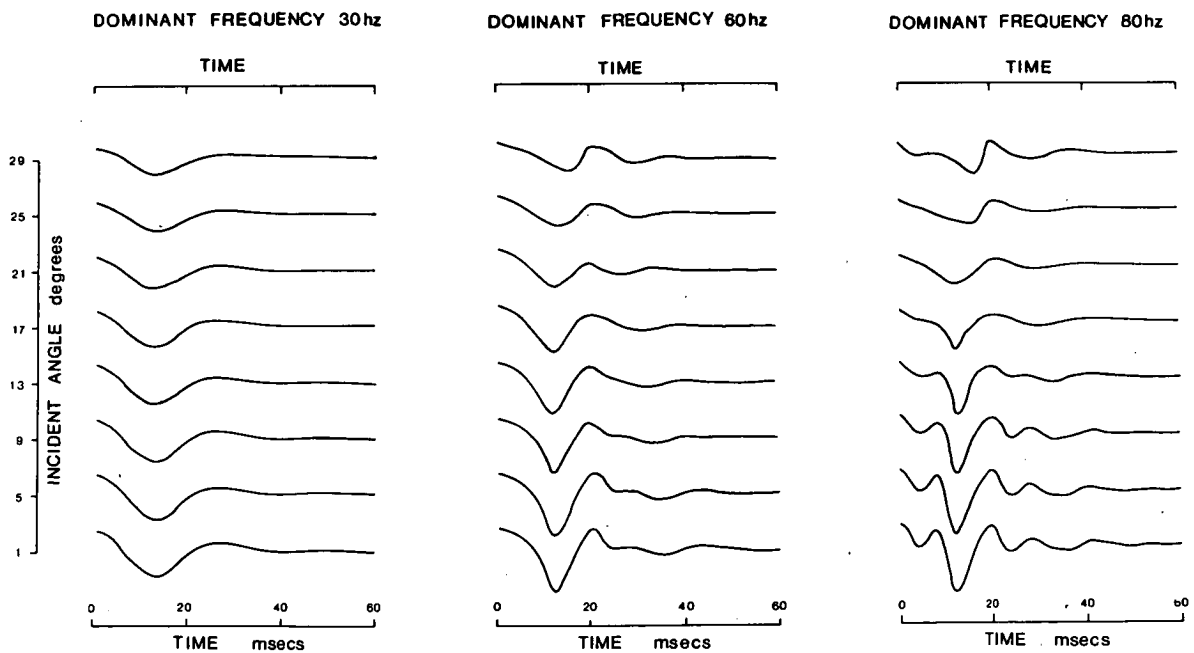


Fig. 5.35 Time pulses for various incident angles showing the difficulties in trace correlation due to amplitude and phase variations.

Phase changes due to interference effects introduce time shifts into the wavelet for any frequency thereby altering the onset time. Traces obtained by multiplying Ricker wavelet frequency spectra with the reflectivity function and inverse transforming, using dominant frequencies of 30, 60 and 80 hz and various angles of incidence (Figure 5.35), illustrate the difficulties of correlation due to trace-to-trace amplitude and phase variations. Difficulties are especially pronounced at high frequencies due to rapid changes in the shape of the signal wavelet.

XV. MULTILAYERED MEDIA

The previous results may be extended to wave propagation in layered structures where the bed parameters vary discontinuously from layer to layer. As well as direct and intrabed multiply reflected events, interbed multiples occur (Figure 5.36). Due to the large number of possibilities the discussion will be restricted to two examples which are represented geologically by a braided stream and a shoreface environment. Density, sonic and gamma-ray logs for both these environments are illustrated in Figures 5.37 and 5.38, while their corresponding models (Figure 5.39), which have an overall thickness of 15 m, have been derived from the log information. The phase spectra (Figure 5.40) for both models are similar for low incident angles and if the average velocity for each sequence is determined (3467 and 3409 m/sec for the braided stream and shoreface sequences respectively), the frequency interval of approximately 110 hz yields a thickness for both of 15 m.

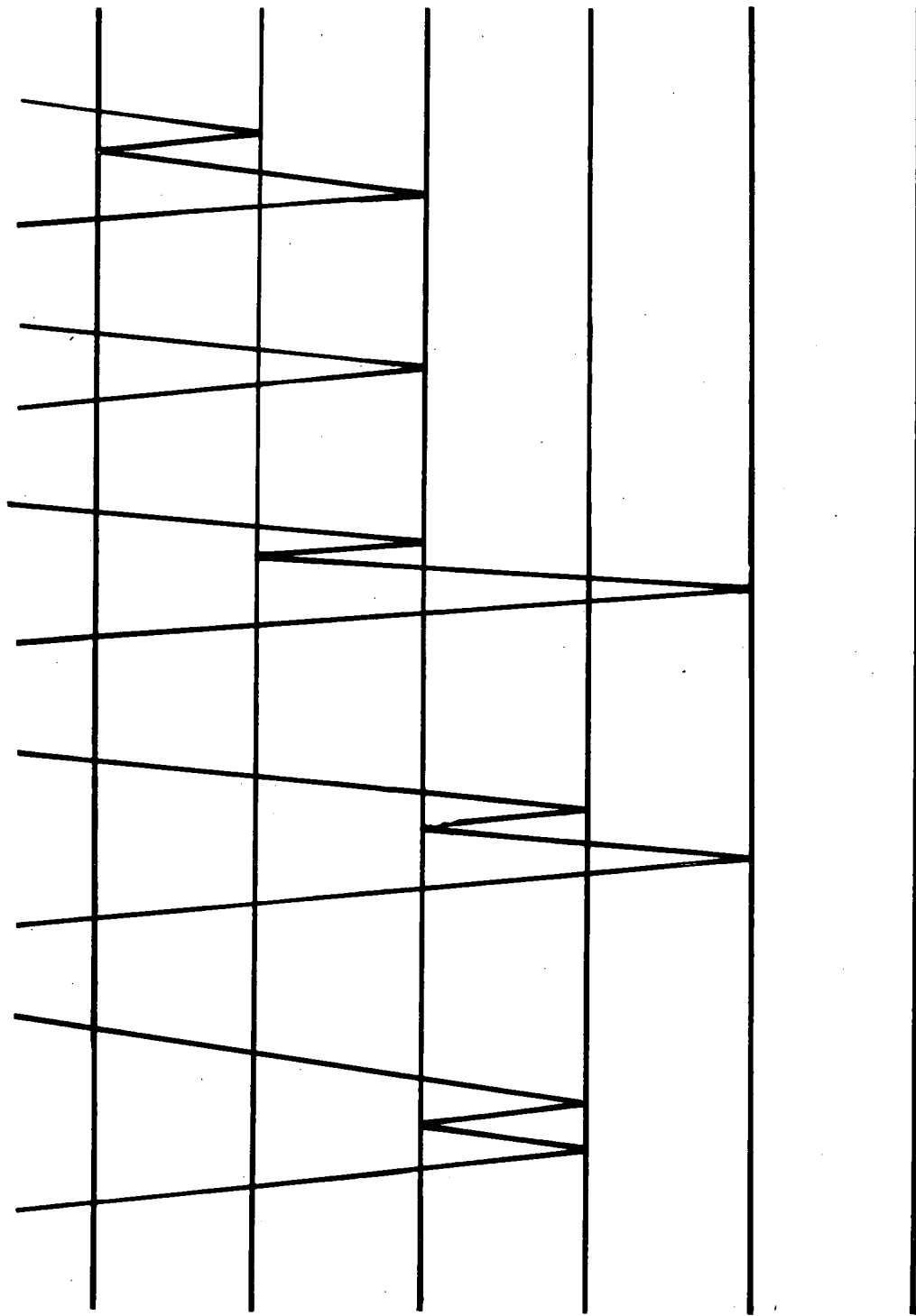


Fig. 5.36 Intrabed and interbed multiples.

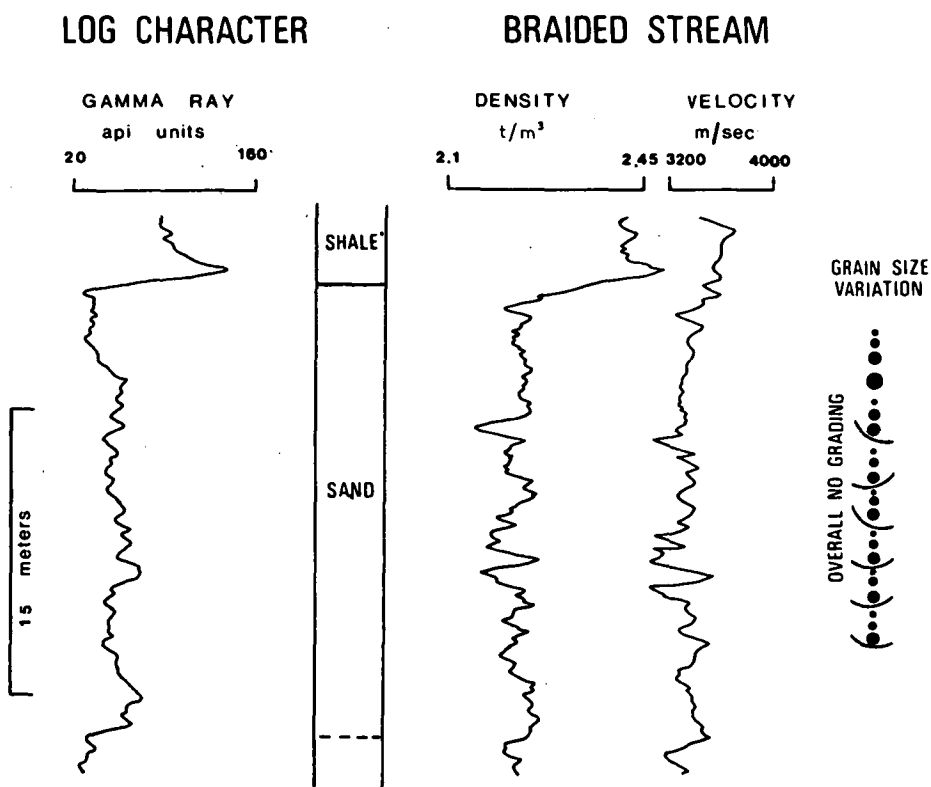


Fig. 5.37 Log characteristics of a braided stream sequence.

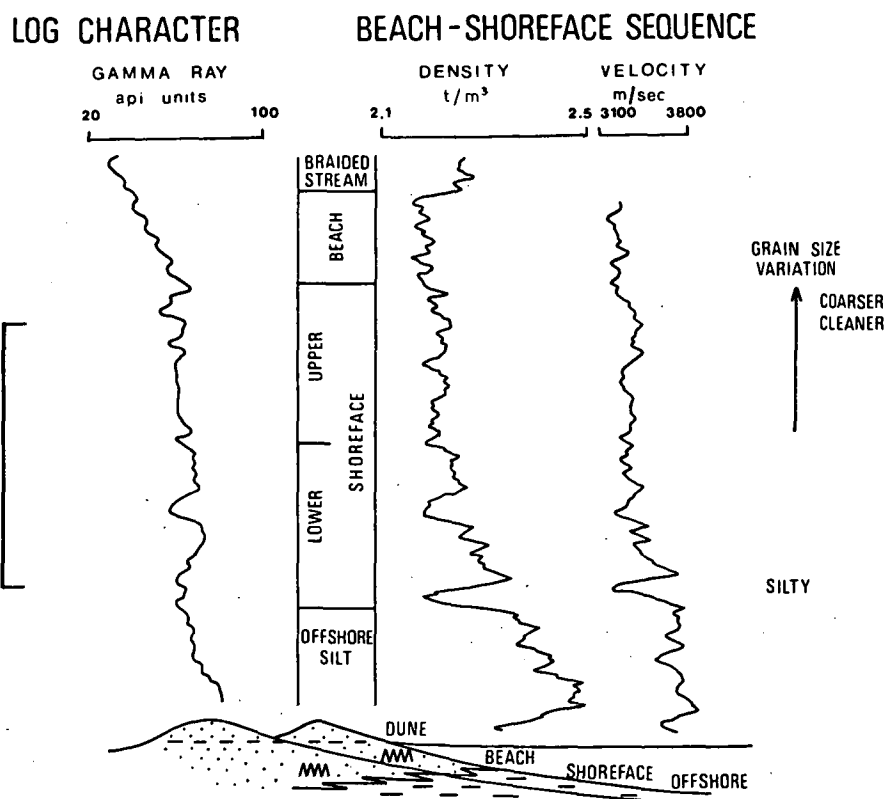


Fig. 5.38 Log characteristics of a beach-shoreface sequence.

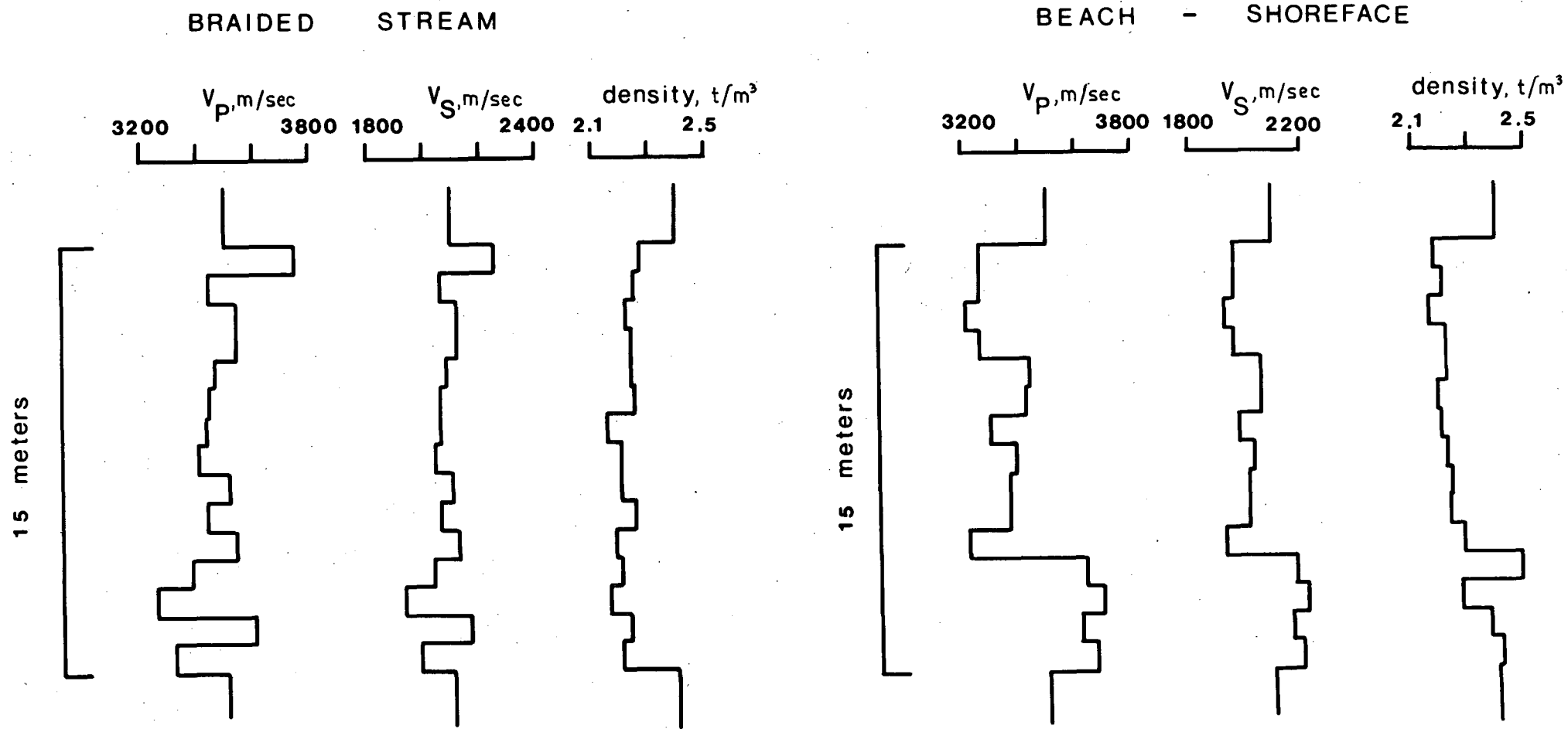


Fig. 5.39 Braided stream and beach-shoreface models.

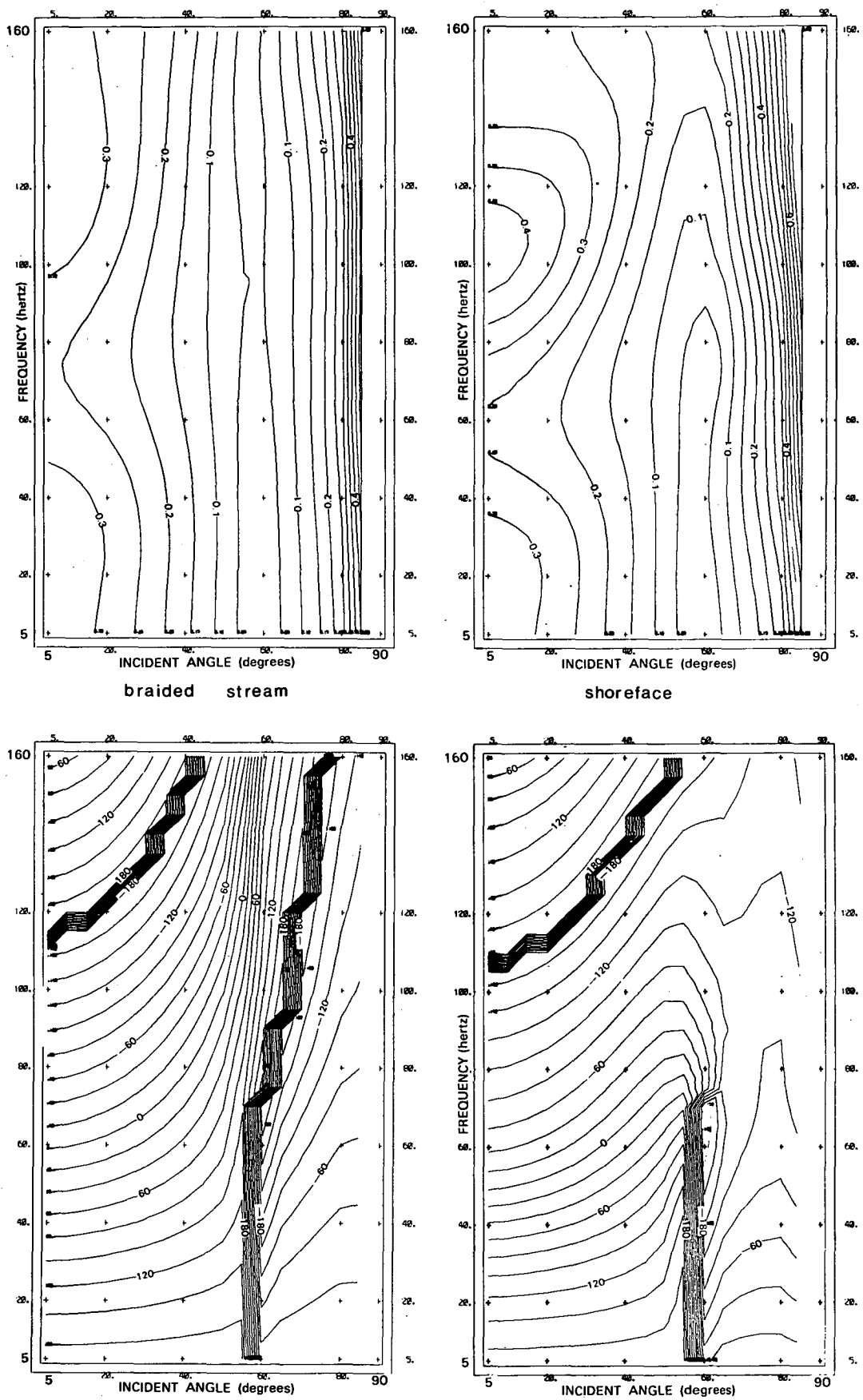


Fig. 5.40 Amplitude and phase spectra for the braided stream and shoreface models.

The large differences in the amplitude spectra especially at high frequencies and small angles of incidence show how differences in wavelet shape occur for very thin sequences. Since the phase spectrum yields the velocity thickness relationship and there are large differences in amplitude character, discriminatory analysis techniques such as those used by Mathieu & Rice (1969) could be used to statistically predict lithology, especially if all CDP traces are used.

XIV. DIRECT HYDROCARBON INDICATORS (DHI's)

1. ONE LAYER MODELS

Direct hydrocarbon detection methods have been extensively discussed and can be classed as one of the following types:

- (i) flat spot or the detection of the gas-liquid interface,
- (ii) anomalous amplitudes or reflection coefficients,
- (iii) anomalous low velocities,
- (iv) inversion of polarity,
- (v) shadows or loss of amplitudes below bright spots, or
- (vi) diffractions.

Each method is used in conjunction with CDP stacked data with the exception of (iii) which is determined during the stacking procedure. All the methods rely on an acoustic contrast associated with the presence of hydrocarbons. Information presented by Gregory (1977) showed the greatest variation in acoustic properties occurred if the hydrocarbon is gas.

Reflectivities affect indicator methods (ii), (iii), (iv) and (v).

Reflectivities for three models consisting of brine, gas and oil saturated sands (Figure 5.41), having thicknesses of 5, 15 and 25 m and contained within a half-space composed of brine saturated shale, have been modelled for frequencies in the range 5 hz to 160 hz and angles of incidence of 5 to 90° (Figures 5.42 and 5.43). All acoustic properties are taken from Gregory (1977) and represent typical values of average Gulf Coast sands (or sandstones) and shales at a depth of 3000 m. The phase and amplitude curves for the brine and oil saturated sands are similar. The gas saturated sands have distinctive amplitude spectra for thicknesses as small as 5 m. The phase spectra for a 25 m thickness are characterised by discontinuities at frequency intervals of 40 hz. The discontinuities and the zero phase curve correspond to the amplitude minima. The large reflectivities of the gas zone at certain frequencies accounts for the frequency selective loss of amplitudes below the hydrocarbon zone.

Amplitude time traces obtained by Hilbert transforming the reflectivity function, which has been multiplied by the shaped source spectrum - in this case Ricker wavelets having dominant frequencies of 30 and 60 hz and zero phase, are illustrated in Figure 5.44 for incident angles of 1 and 30° . The brine and oil saturated sand traces for the 25 m bed are similar, whereas phase changes have distorted the gas saturated bed sequence. The diminished amplitude of the gas saturated sequence, especially for the 60 hz dominant signal, is due to the existence of neighbouring frequency minima. A narrower spectrum would enhance the trace wavelet. In general trace amplitudes for the gas saturated beds are smaller than for the oil saturated

density t/m ³	V _p m/sec	V _s m/sec		
2360	3170	1865		
2210	3292	1908	BRINE SATURATED SAND	
2360	3170	1865		
2360	3170	1865		
2150	3249	1932	OIL SATURATED SAND	
2360	3170	1865		
2360	3170	1865		
1920	3069	2045	GAS SATURATED SAND	
2360	3170	1865		

Fig. 5.41 Acoustic properties of the brine, oil and gas models.

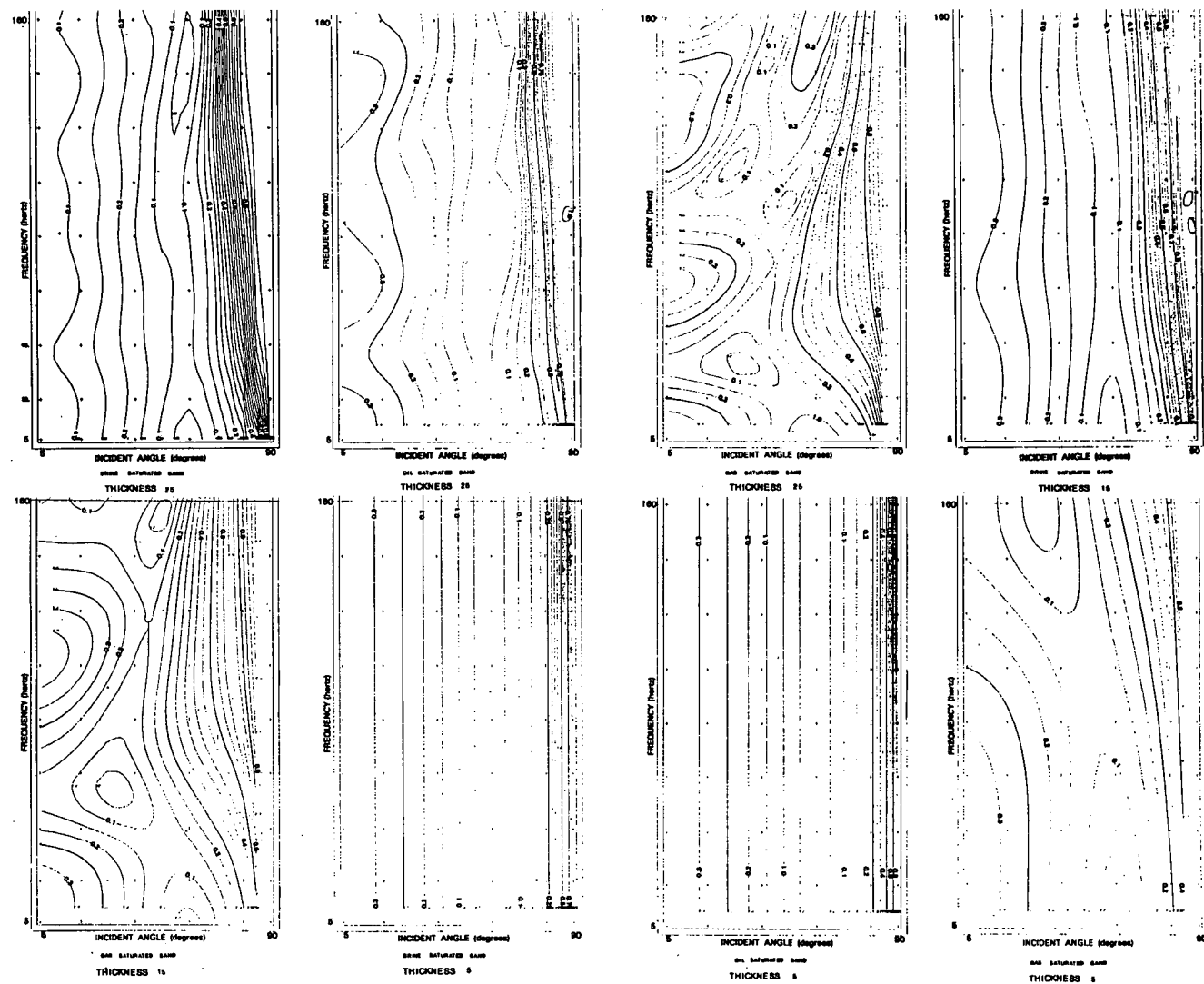


Fig. 5.42 Amplitude reflectivities for PP waves due to brine, oil and gas saturated sands of varying thickness.

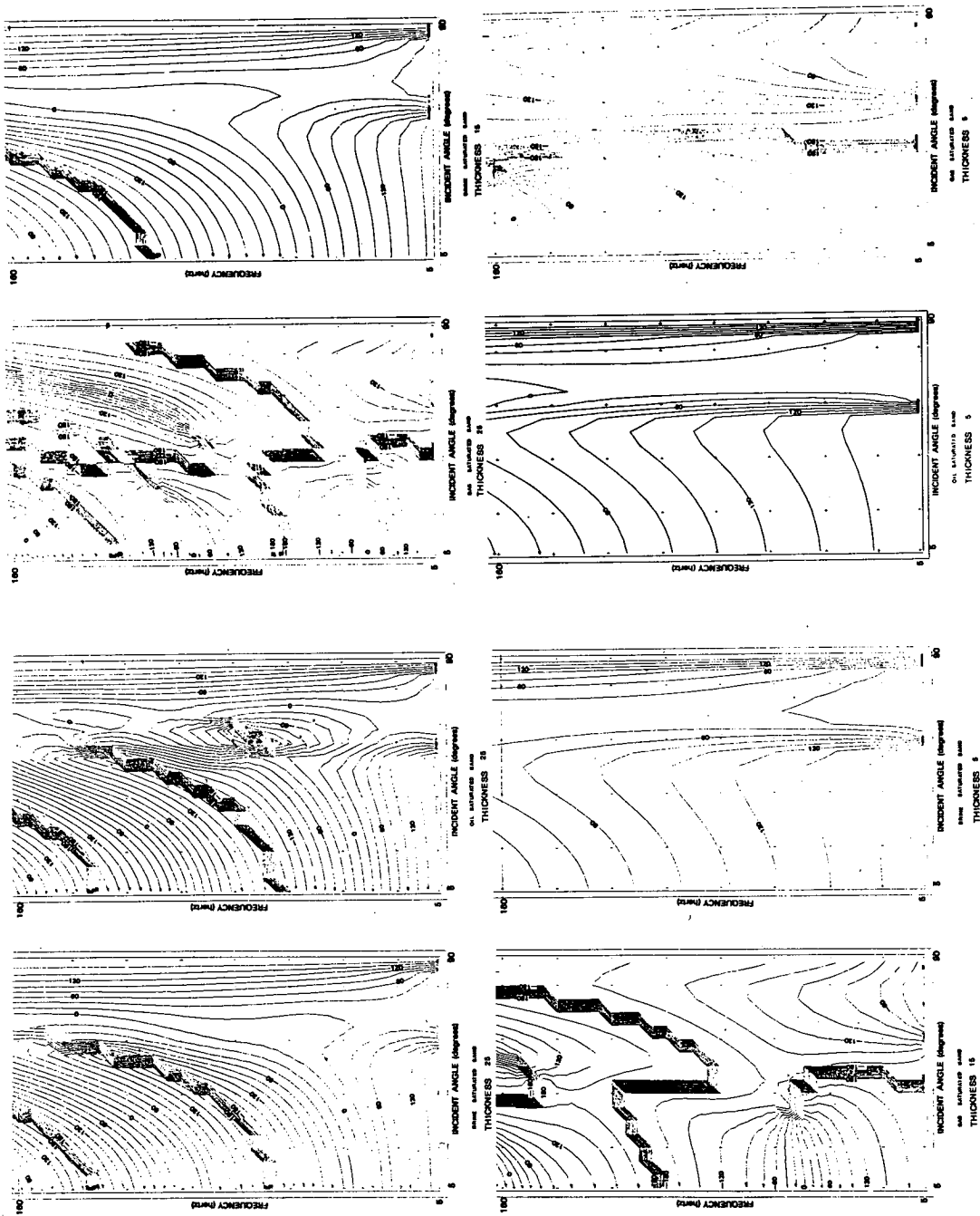


Fig. 5.43 Phase reflectivities for PP waves due to brine, oil and gas saturated sands of varying thicknesses.

THICKNESS 25 m

INCIDENT ANGLE 1 degree

INCIDENT ANGLE 30 degrees

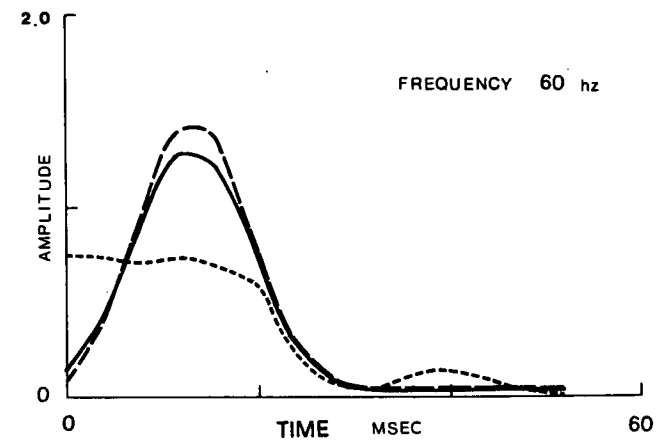
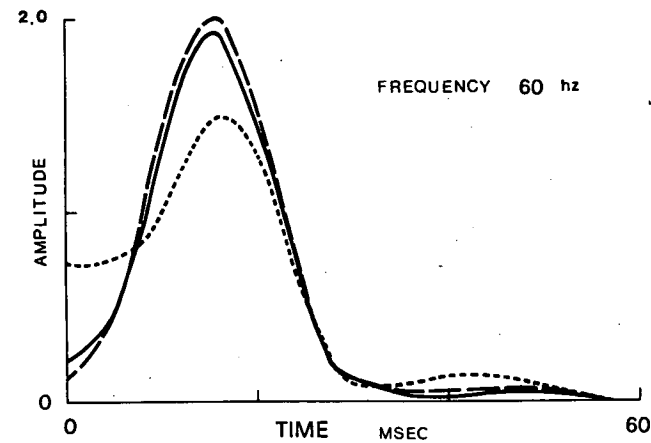
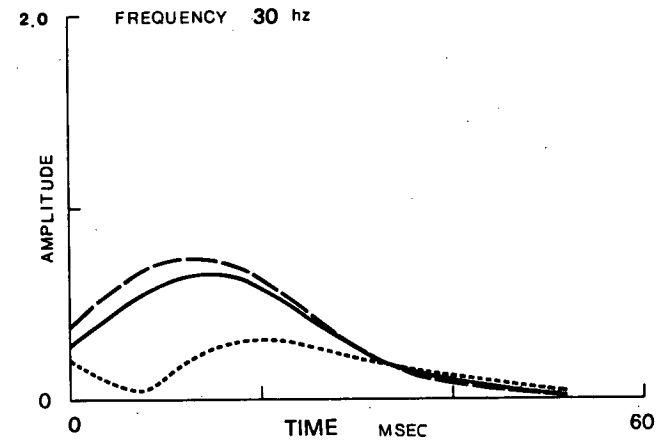
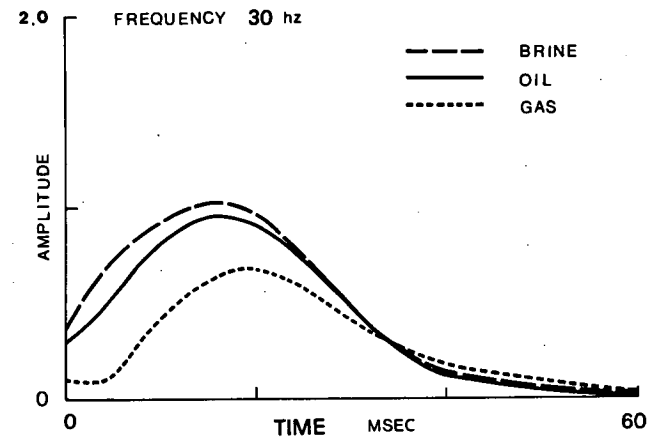


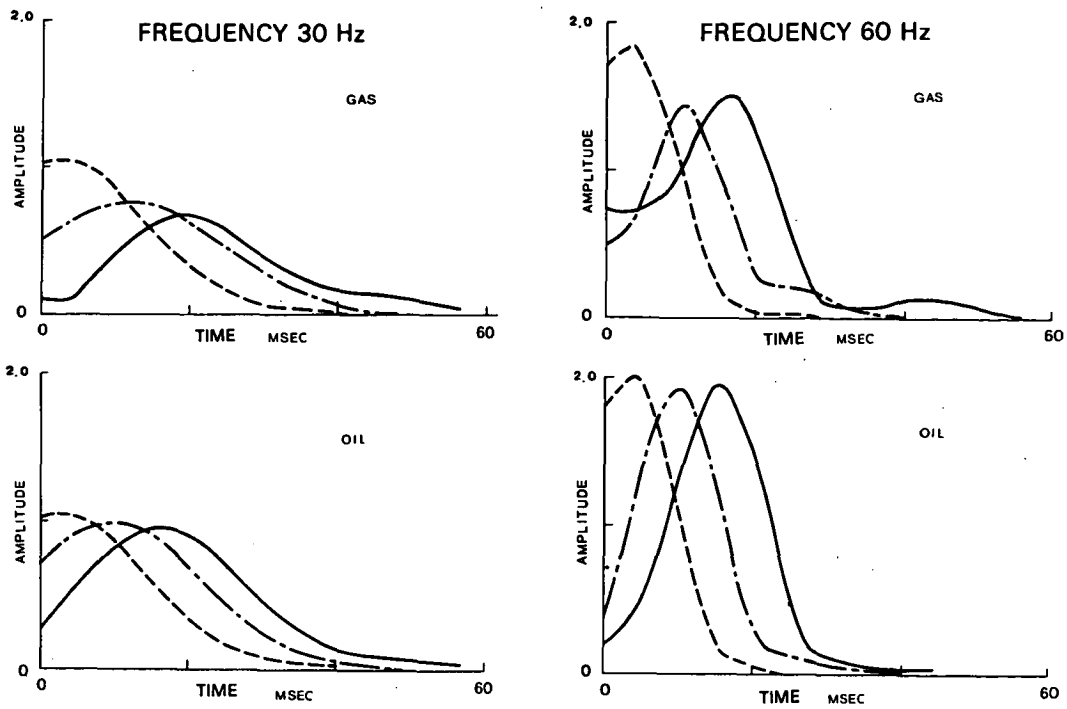
Fig. 5.44 Comparison of wave trace shapes for the oil, gas and brine saturated sand models at different incident angles.

beds (Figure 5.45). Local anomalies in reflection amplitude can be due to interference effects so that although small acoustic impedances occur the amplitudes may be large, whereas the gas filled sand with a large impedance contrast produces smaller amplitudes. Thus gas filled zones encased in shale are not necessarily typified by large reflection amplitudes. Due to the greater reflection contrasts of the gas sands, they will always have a greater amplitude where maximum interference occurs. At other frequencies oil saturated sands may be dominant. The effect of phase changes can be seen by the later arrival of the amplitude maximum with increasing thickness (Figure 5.45).

Time traces obtained by modelling Ricker wavelets normally incident on a layer of gas or oil saturated sand are shown in Figure 5.46. Although the impedance contrasts at the boundaries of the gas saturated sand are larger than for the oil saturated sand trace amplitudes are greater for the oil saturated sands. This results from constructive interference at small oil sand thicknesses because the high interval velocity produces small transit times. As the frequency and layer thickness increase a second pulse on the time trace, corresponding to an intra-bed multiple, becomes increasingly separated from the primary pulse. The time position of the large negative part of the primary pulse is constant for a constant layer thickness. The position is a function of the layer transit time and corresponds to the linear slope of the phase spectrum (e.g. Figure 5.47).

Multiple energy is greater for the gas saturated sands and becomes particularly prominent at high frequencies and large bed thicknesses. This steady increase is reflected by

INCIDENT ANGLE 1 degree



INCIDENT ANGLE 30 degrees

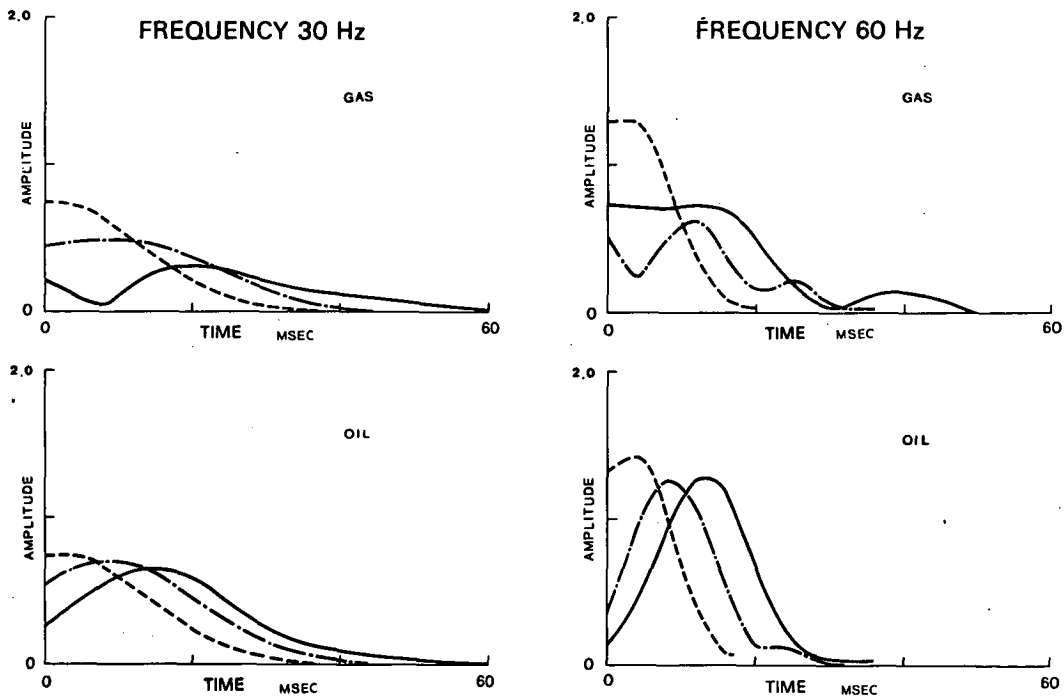


Fig. 5.45 Comparison of wave trace shapes for oil and gas saturated sands of varying thicknesses. ---- 5 m thickness, -.-.- 15 m thickness, — 25 m thickness.

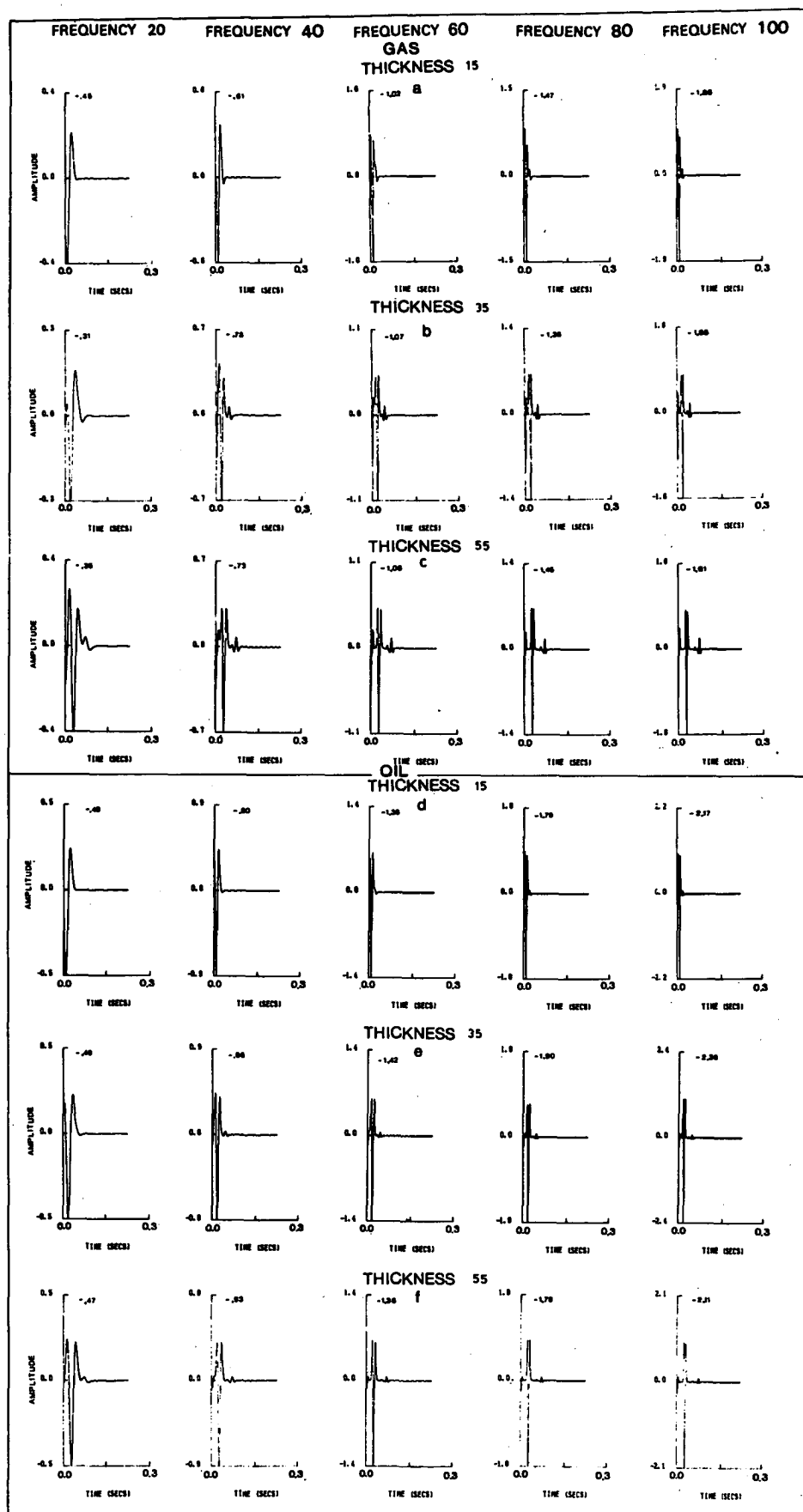


Fig. 5.46 Time traces for Ricker wavelets having dominant frequencies of 20, 40, 60, 80 and 100 hz and thicknesses of 15, 35 and 55 m. a, b, c - the gas model; d, e, f - the oil model. Maximum or minimum trace values are given.

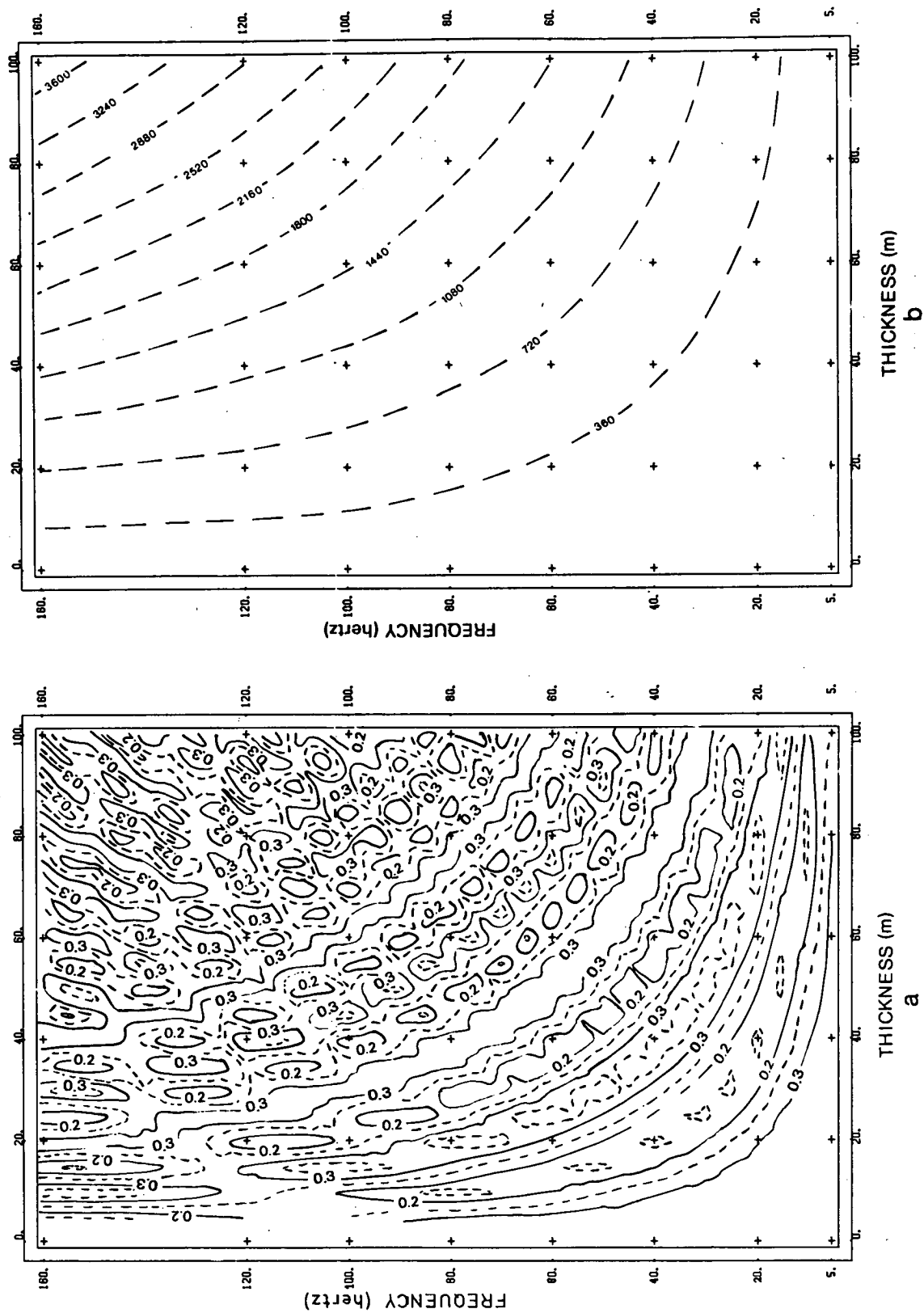


Fig. 5.47 Frequency-thickness amplitude (a) and phase (b) reflectivity variations for normally incident plane waves.

rapidly changing reflectivity amplitude and phase spectra (Figure 5.47). These spectra also indicate the variation of trace amplitude with frequency observed in the time traces of Figure 5.46.

Time traces corresponding to different velocity contrasts between the gas saturated sand and the surrounding strata (Figure 5.48) show less interference of events and larger multiple energy for the low velocity contrasts. Once again this is a result of increased transit time within the sands. The amplitude characteristics of the time traces can readily be predicted from the amplitude and phase spectra for differing velocity contrasts (Figure 5.49).

Tatham & Stoffa (1976) noted that P and S velocity ratios for zones of undersaturation or gas saturation produce observable anomalies as shear waves are less sensitive to fluid saturants than compressional waves. They suggest that an indirect source of shear waves could be generated in marine areas by mode conversion of P to S waves at sharp refracting boundaries such as the water bottom in regions of relatively high velocity sediments. Reflectivity plots for mode converted P-S waves due to brine, oil and gas saturated sands are shown in Figures 5.50 and 5.51. Plots for the same thickness are similar, with the maximum amplitudes occurring for incident angles in the range of 35 to 60° and these correspond to discontinuities in the phase spectra. Because the S wave velocity is lower than the P wave velocity, the frequency interval between the phase discontinuities is smaller than for PP reflections, thereby increasing the resolution of bed thickness-velocity determination.

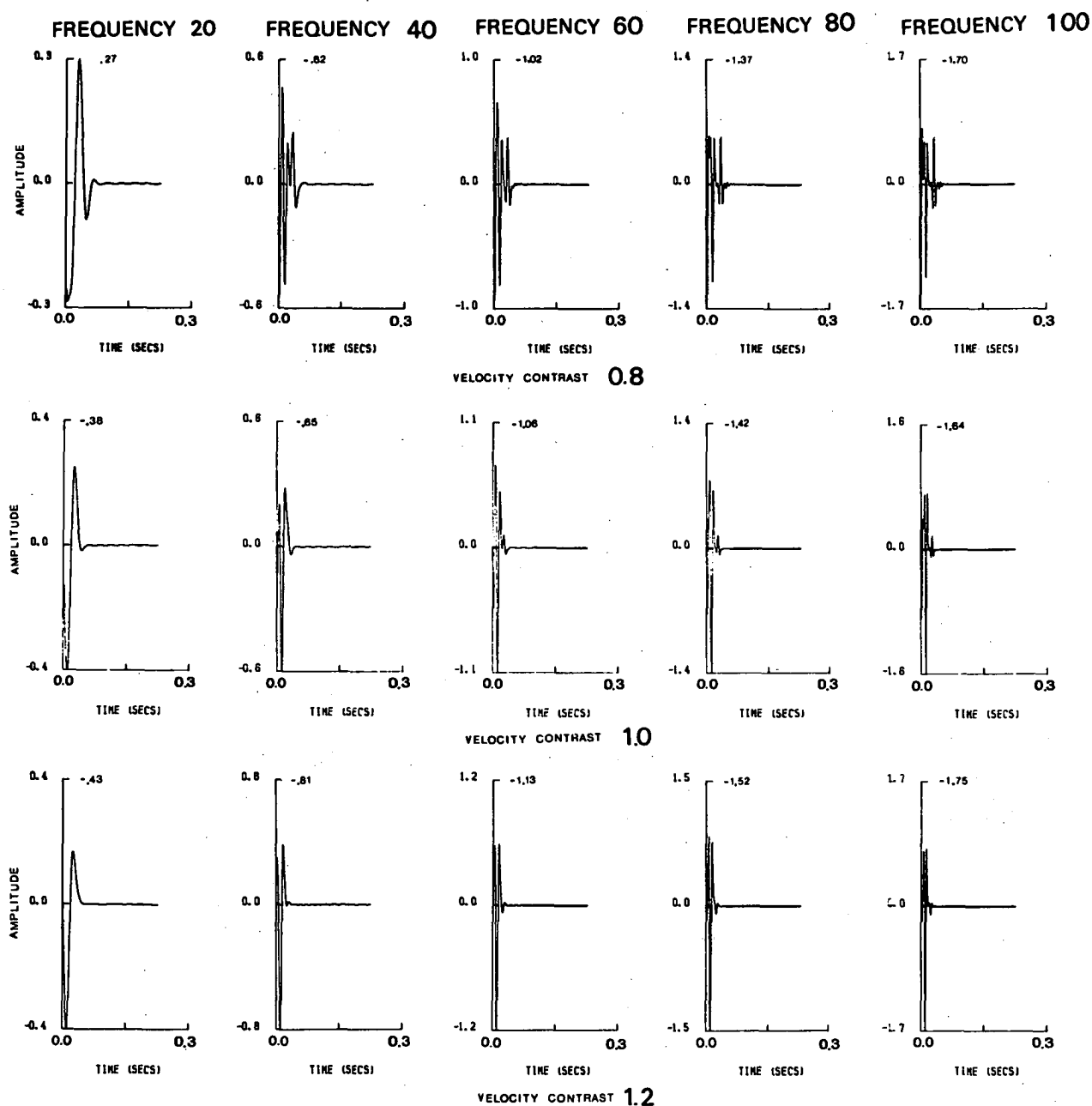


Fig. 5.48 Time traces for Ricker wavelets having dominant frequencies of 20, 40, 60, 80 and 100 hz and velocity contrasts of 0.8, 1.0 and 1.2 (corresponds to bed velocities of 2536, 3170 and 3804 m/sec). Maximum or minimum trace values are given.

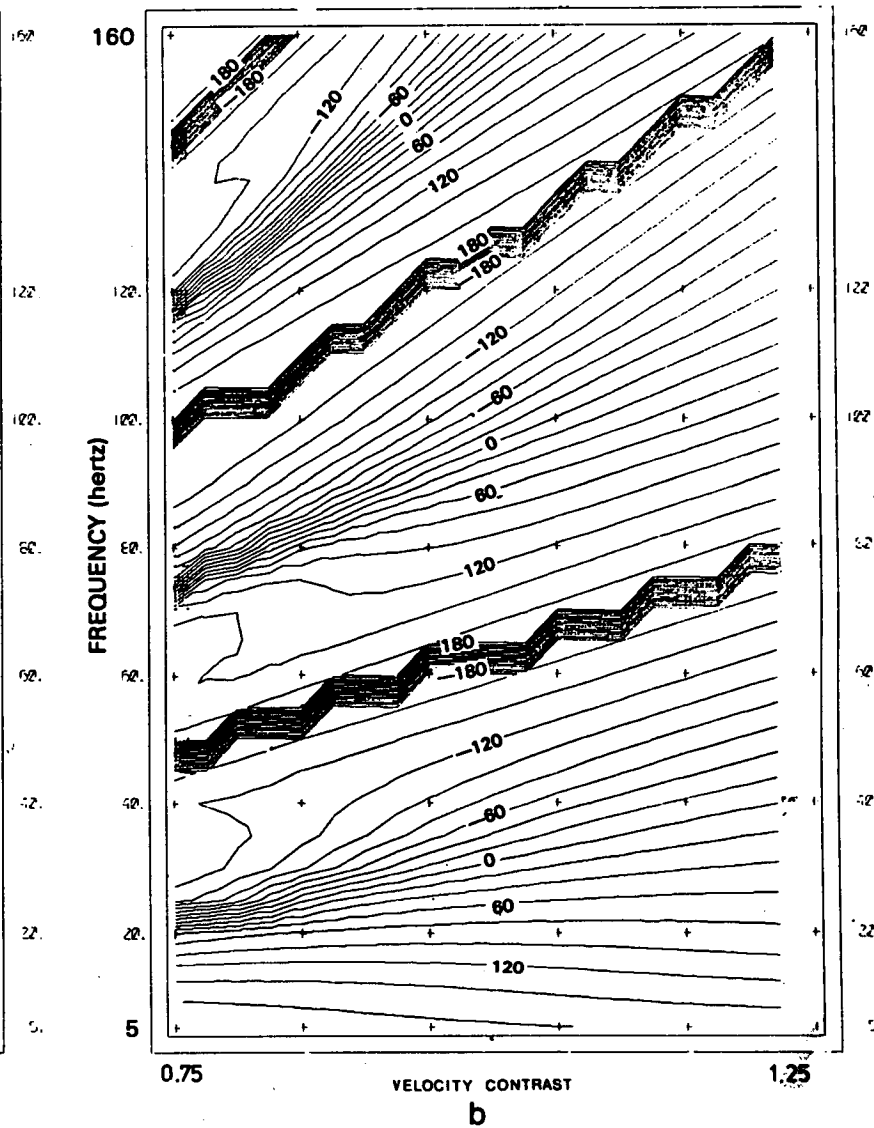
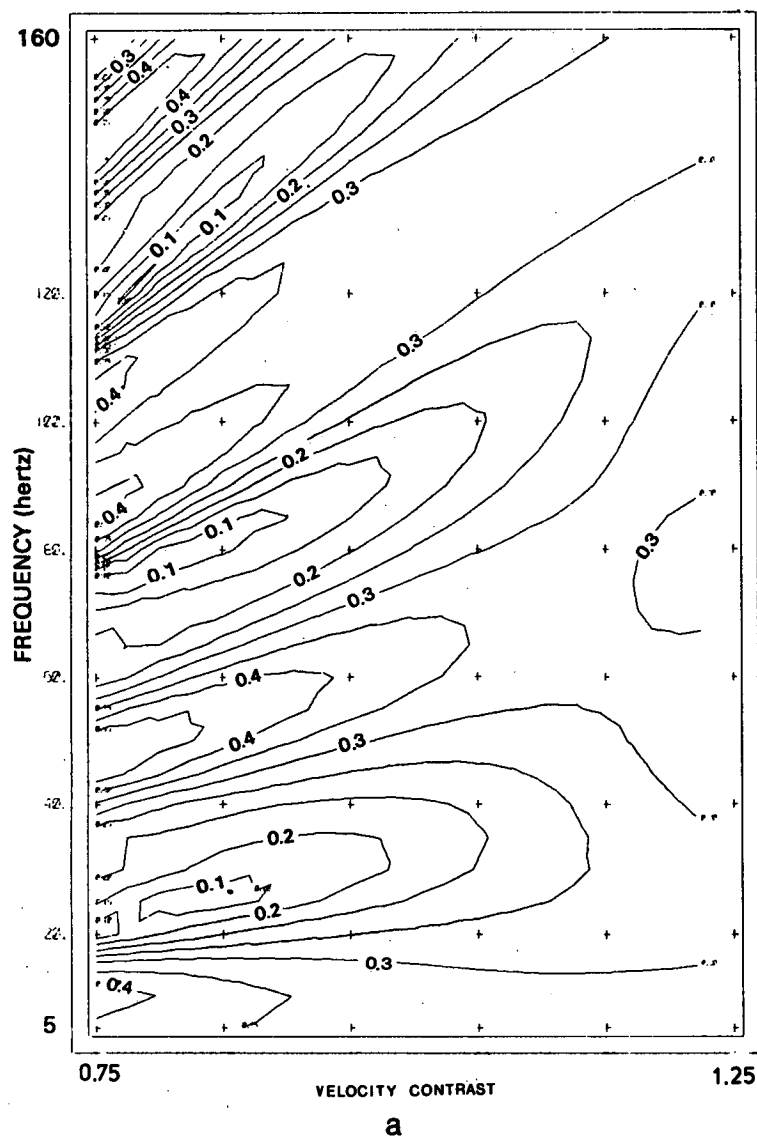


Fig. 5.49 Normal incident amplitude (a) and phase (b) reflectivities for varying velocity contrasts.

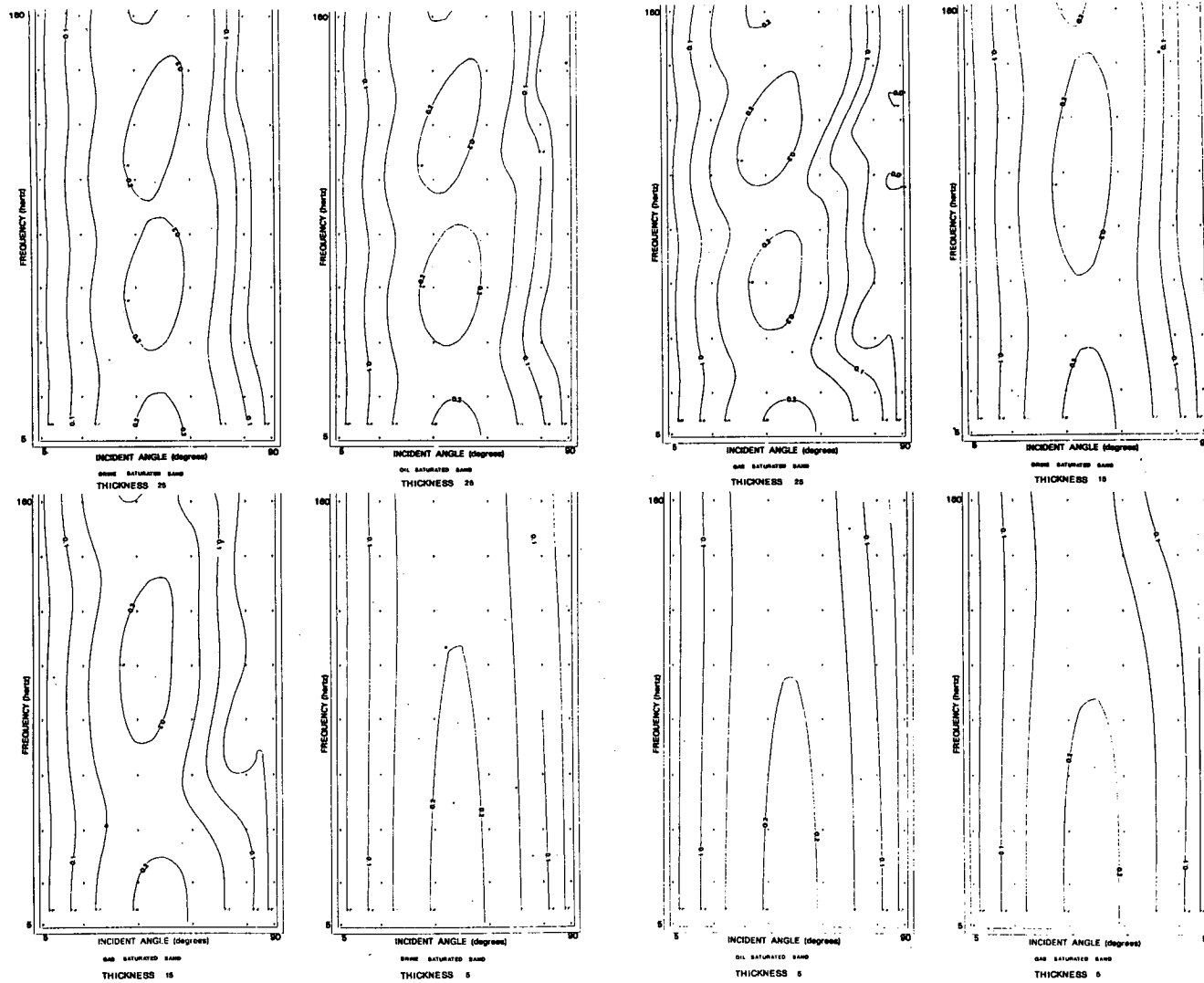


Fig. 5.50 Amplitude reflectivities for mode-converted PS waves due to brine, oil and gas saturated sands of varying thicknesses.

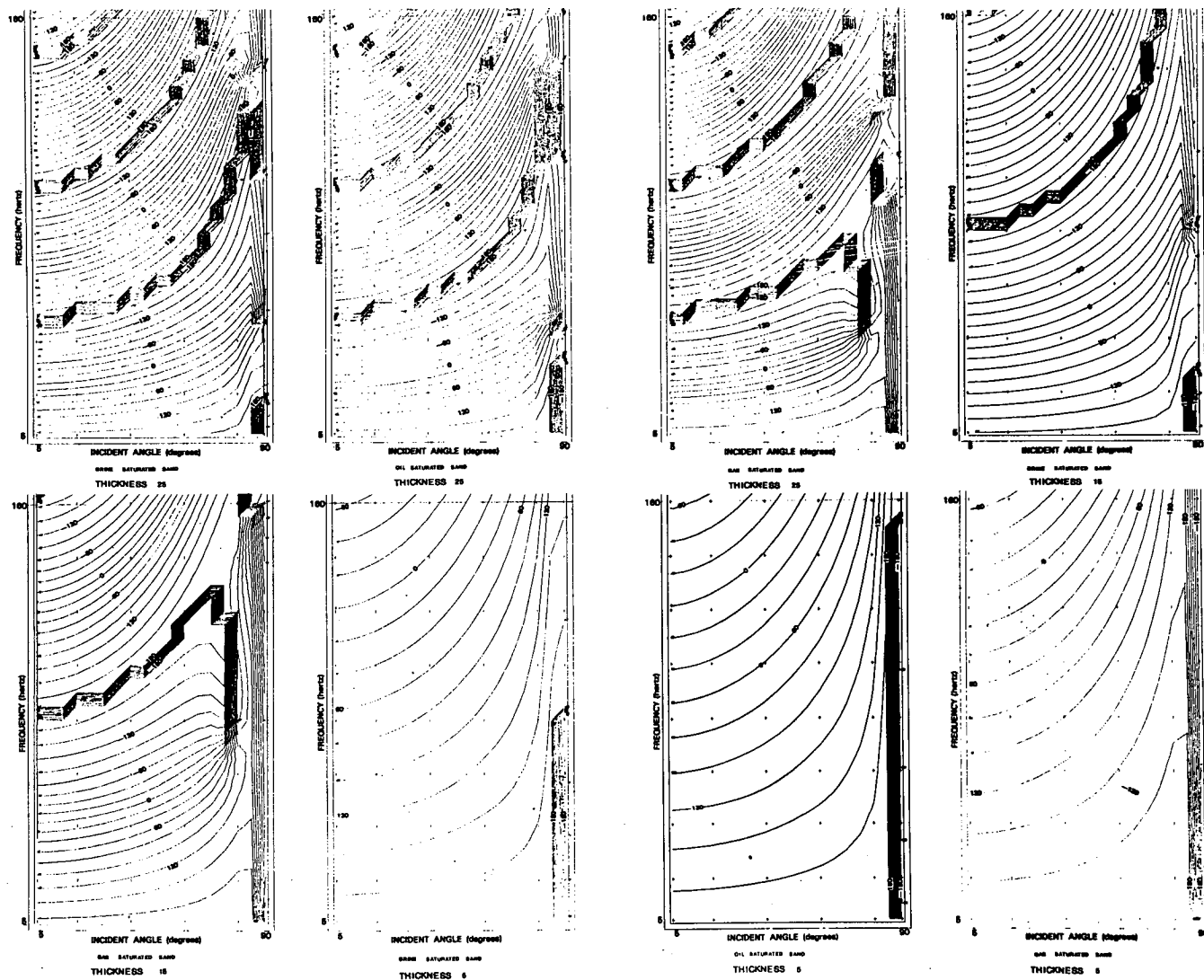


Fig. 5.51 Phase reflectivities for mode-converted PS waves due to brine, oil and gas saturated sands of varying thicknesses.

2. MULTILAYERED HYDROCARBON MODELS

Four density and sonic logs representing varying gross oil columns (Figure 5.52) were represented by density and velocity models consisting of 40 layers each 3 m thick (Figure 5.53). The reflectivity spectra (Figure 5.52) show large variations in amplitude as the frequency and incident angle change and exhibit amplitude maxima and minima similar to those described earlier in this chapter. To enable comparison with the logs only normal incidence amplitude and phase spectra (Figures 5.54a and b) will be considered.

Reflectivities $[R(\omega)]$ are complex functions and can be represented by the following two forms:

- (1) the sum of the real and complex parts

$$R(\omega) = a(\omega) - ib(\omega) \quad \dots (28)$$

where ω is the angular frequency

- (2) the product of the real and complex parts

$$R(\omega) = |R(\omega)| e^{i\Phi(\omega)} \quad \dots (29)$$

The amplitude $[|R(\omega)|]$ and phase $[\Phi(\omega)]$ spectra are then given by

$$|R(\omega)| = [a^2(\omega) + b^2(\omega)]^{\frac{1}{2}} \quad \dots (30)$$

$$\Phi(\omega) = \tan^{-1} \left(\frac{-b(\omega)}{a(\omega)} \right) + 2n\pi \quad \dots (31)$$

$n = 0, \pm 1, \pm 2, \dots$ respectively.

The principal value (I) of the phase spectrum is defined as $\tan^{-1} \left(\frac{-b(\omega)}{a(\omega)} \right)$ where I has a value in the range

$$-\pi \leq I \leq \pi. \quad \dots (32)$$

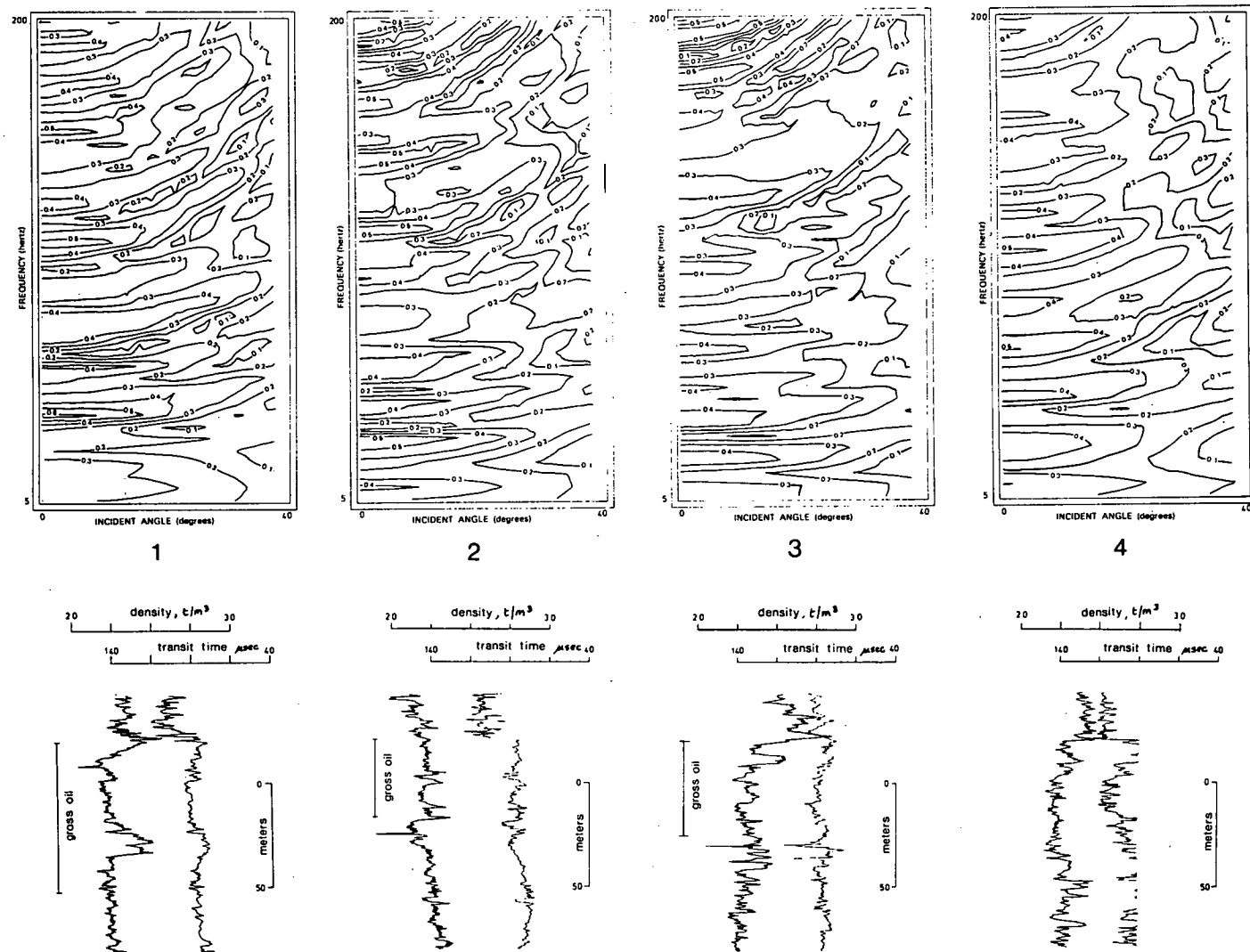


Fig. 5.52 Four density and sonic logs over a 120 m interval representing varying gross oil columns and their incident angle dependent amplitude reflectivity spectra.

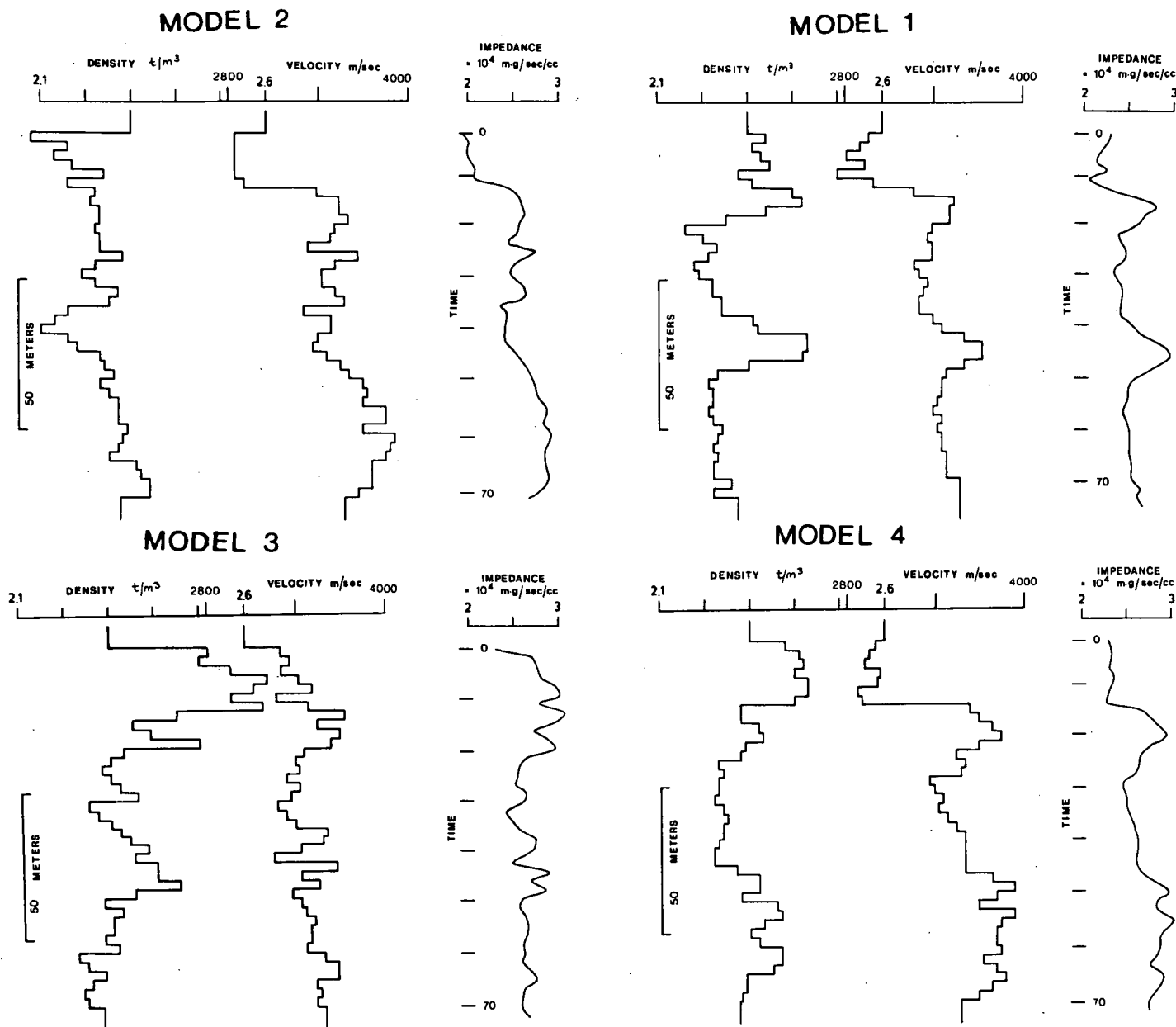


Fig. 5.53 Density and velocity models for 120 m intervals and their acoustic impedance logs.

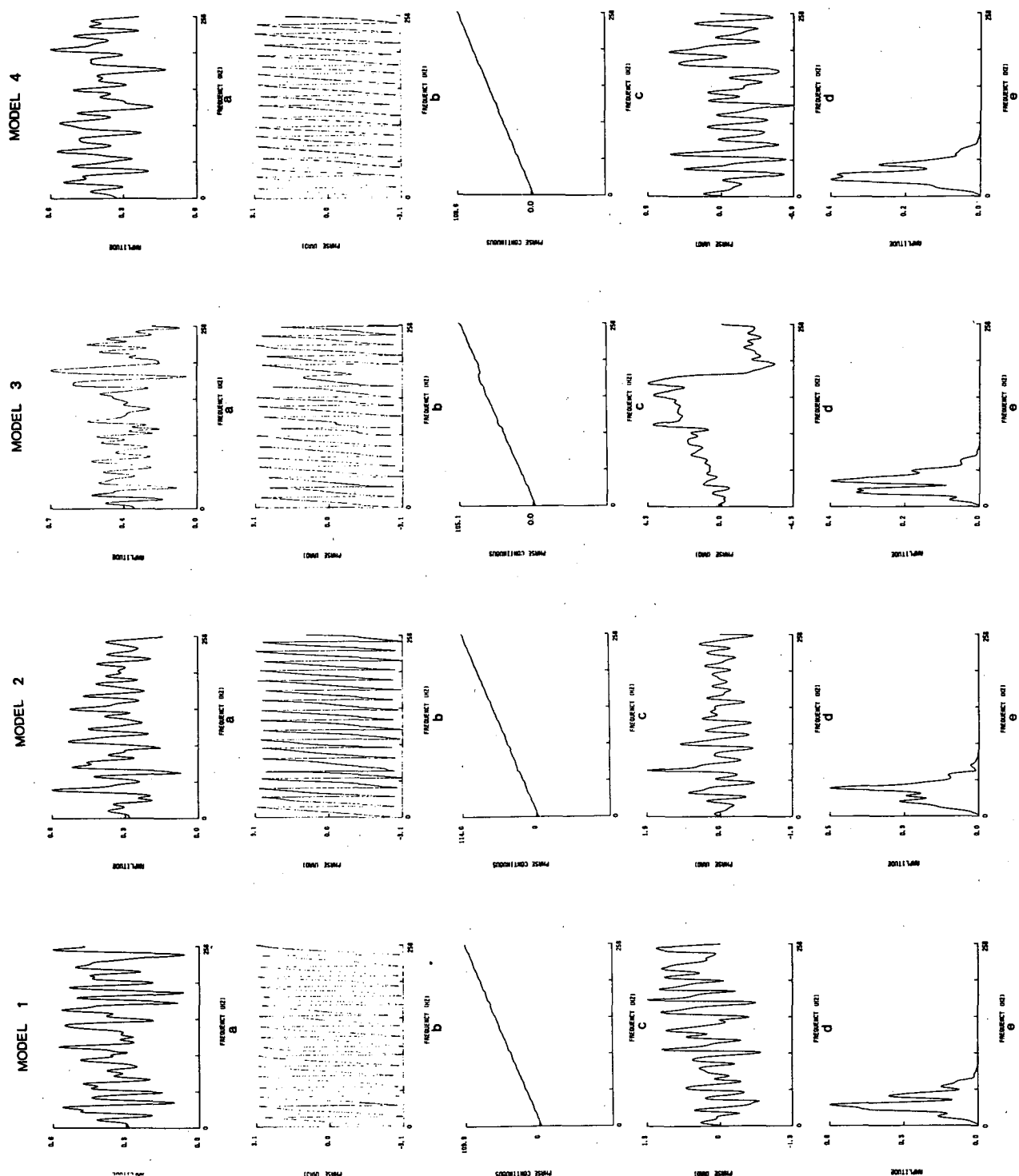


Fig. 5.54 Normal incident reflectivities for models 1 to 4.
a - amplitude spectra; b - principal value phase spectra;
c - unwrapped phase spectra; d - unwrapped phase spectra with
the linear trend removed; e - amplitude spectra shaped with
a 30 hz Ricker pulse.

The principal value is a function of angular frequency with discontinuities when

$$I = n\pi \quad \dots(33)$$

$$n = 1, 3, 5 \dots$$

These discontinuities may be removed by unwrapping the principal value phase spectrum using the method outlined by Schafer (1969). This method was applied to the phase spectra for models 1 to 4 (Figure 5.54c). The almost linear trend approximates minimum phase conditions in which the frequency components are uniformly delayed according to the slope of the spectrum. An approximately zero phase situation may be produced by removing the linear trend (Figure 5.54d). The spectra were shaped by multiplying the reflectivity amplitude spectrum by the spectrum of a 30 hz Ricker pulse (Figure 5.54e).

Spectral components taken from the shaped spectrum of model 1 at 5 hz intervals have been plotted for both the minimum phase and zero phase spectrum (Figure 5.55). By summing these components an approximate time trace was produced. The minimum phase time trace shows a distinct negative pulse at 73 msec and this corresponds to both the two-way traveltime of the model and the slope of the unwrapped phase curve. After removing the linear trend on the phase curve to produce a zero-phase spectrum the corresponding time trace is compressed.

The logarithm of the power spectrum of a signal containing an echo should have a periodic component whose repetition rate is related to the echo delay (Bogert *et al.*, 1963). Thus the power spectrum of the logarithm of the power spectrum, the cepstrum, should exhibit a peak at the echo delay time.

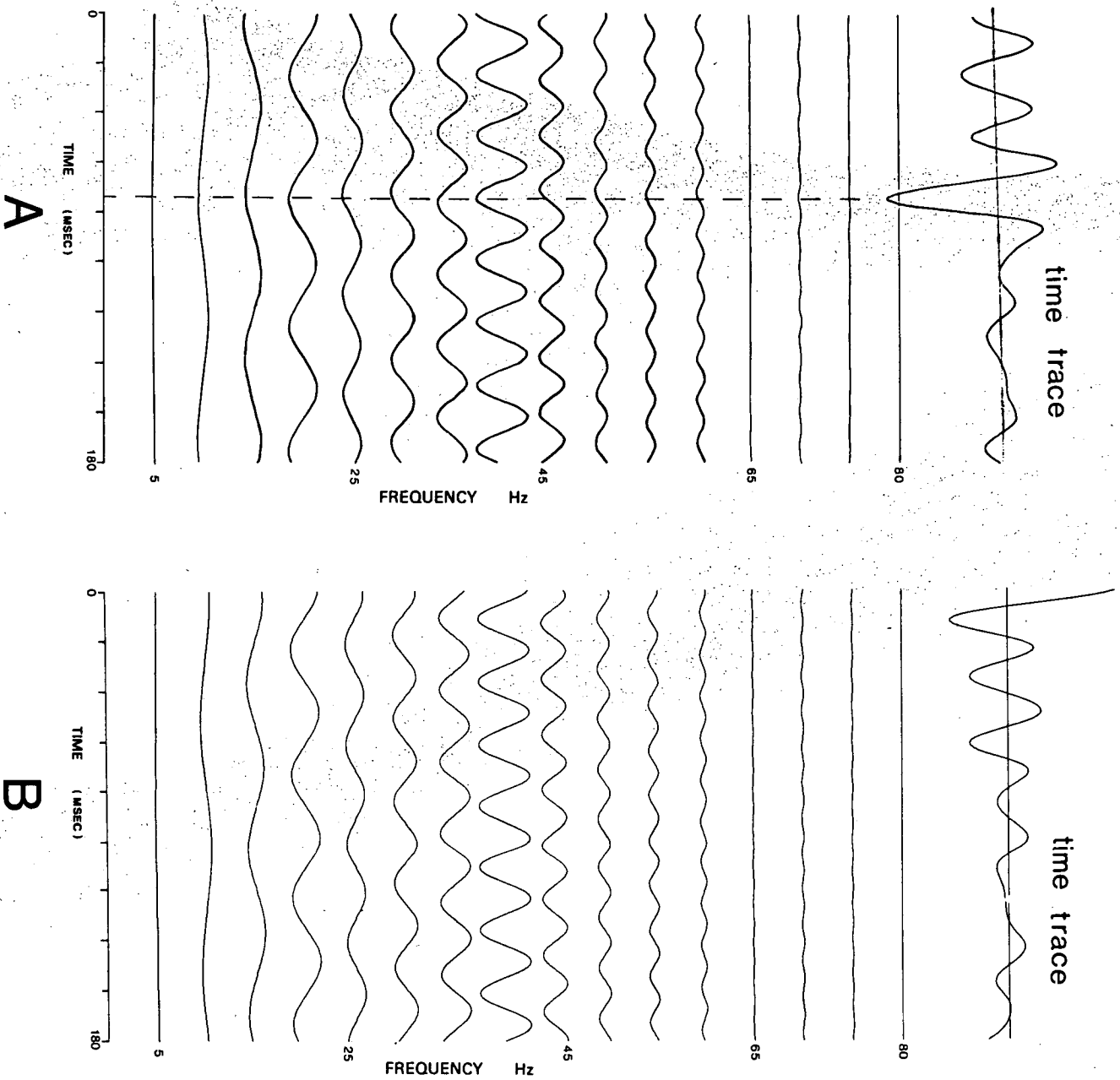


Fig. 5.55 Fourier frequency components at 5 hz intervals for the model 1 shaped spectrum using the approximate minimum phase (A) and zero-phase (B) spectra.

The complex cepstrum is obtained by taking the Fourier transform (magnitude and phase) of the amplitude and phase spectrum rather than the power spectrum and is used for signal recovery rather than the detection of echoes (Schafer, 1969). Cepstra and complex cepstra for the shaped spectra of models 1 to 4 are shown in Figure 5.56. Times for prominent cepstral peaks are labelled. The cepstrum for model 3 has dominant peaks of 36, 28 and 16 msec (Figure 5.56) which corresponds to the time delay between the peaks and troughs on the impedance curve (Figure 5.53). The correlation between the complex cepstrum and the impedance curve for model 3 (Figure 5.57) shows that cepstrum analysis may provide a direct indication of the impedance sequence and hence the thin layer properties.

XVII. MIXED PHASE SPECTRA AND INTRABED MULTIPLES

Consider a wave incident on an earth section composed of two reflecting layers, with complex reflection coefficients given by

$$R_1(\omega) = |R_1(\omega)|e^{-i\phi_1(\omega)} \quad \dots(34)$$

and

$$R_2(\omega) = |R_2(\omega)|e^{-i\phi_2(\omega)} \quad \dots(35)$$

i.e. at reflection both amplitude and phase are altered. The reflection is equivalent to a filtering action on the signal, and as such is expressed as convolution in the time domain and multiplication in frequency domain. In addition the reflected signal is delayed by time intervals τ_1 and τ_2 .

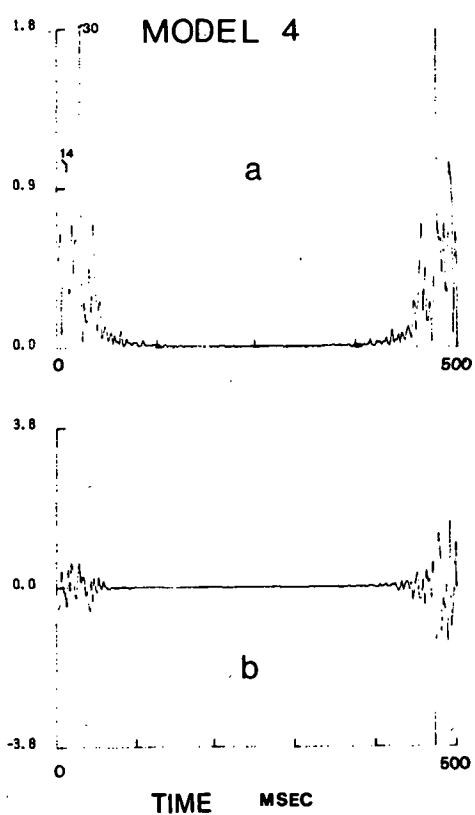
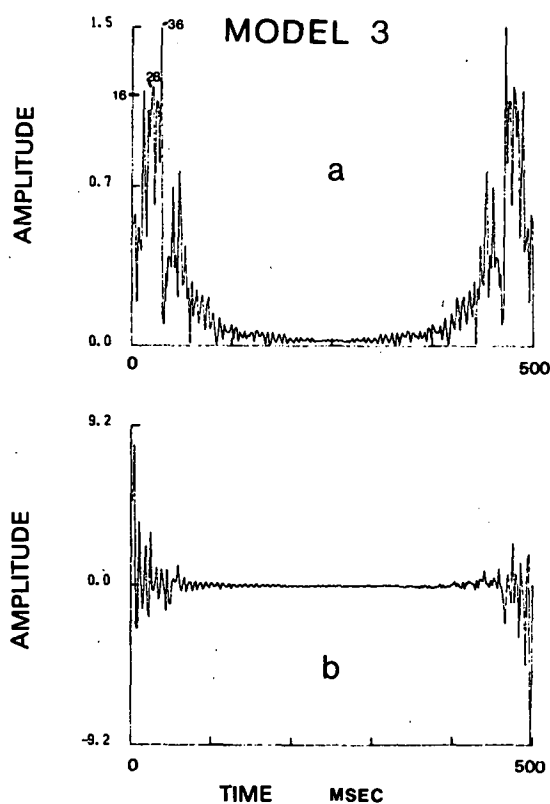
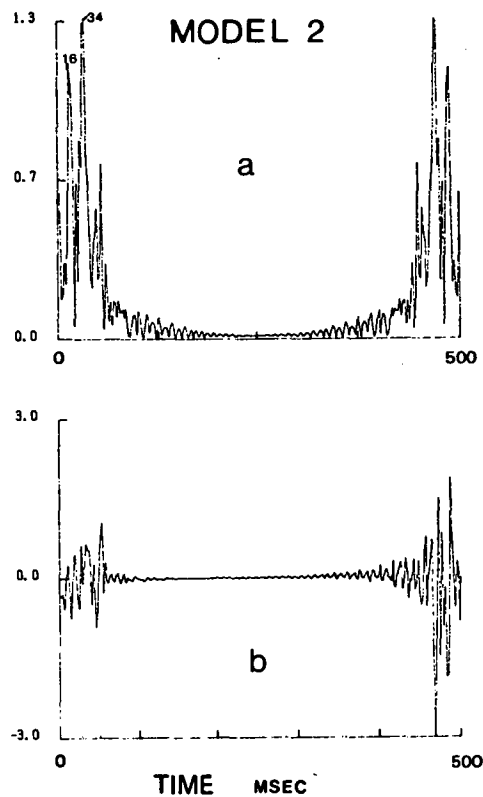
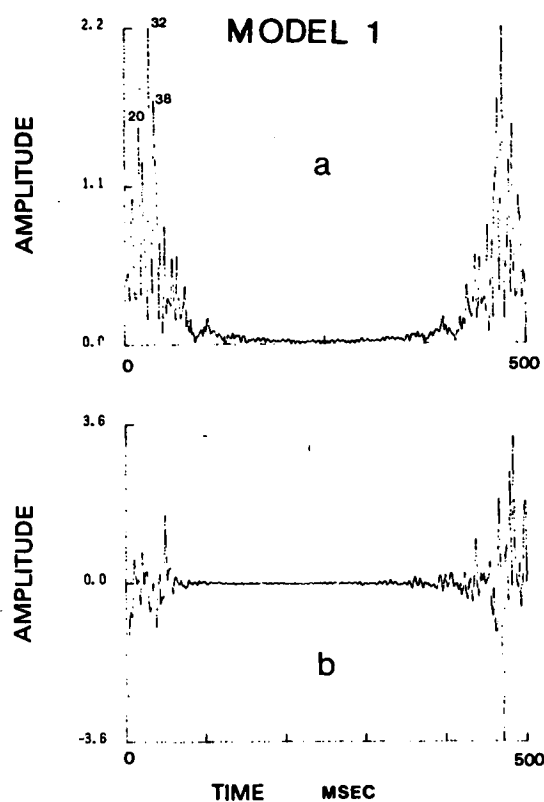


Fig. 5.56 Cepstra (a) and complex cepstra (b) for models 1 to 4.

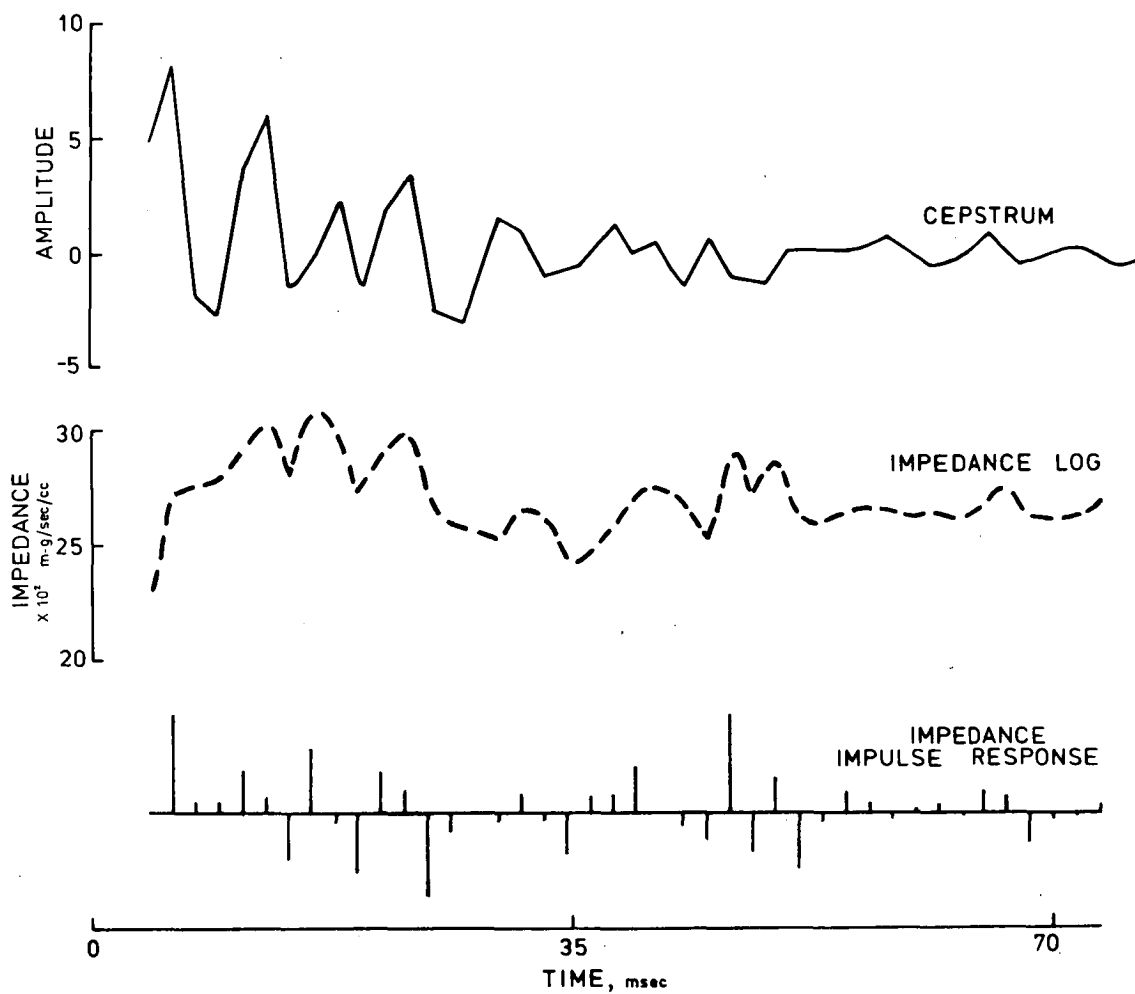


Fig. 5.57 Comparison of the complex cepstrum and impedance log for model 3.

Suppose $f(t)$ is the initial input signal, then the following transforms from time (t) to frequency (ω) domain are:

Input signal

$$f(t) \leftrightarrow F(\omega) \quad \dots(36)$$

Reflection coefficients

$$r_1(t) \leftrightarrow R_1(\omega) \quad \dots(37)$$

$$r_2(t) \leftrightarrow R_2(\omega) \quad \dots(38)$$

Time delayed signal

$$f(t-\tau_1) \leftrightarrow F(\omega)e^{-i\omega\tau_1} \quad \dots(39)$$

$$f(t-\tau_2) \leftrightarrow F(\omega)e^{-i\omega\tau_2} \quad \dots(40)$$

and reflected signal

$$g_1(t) = r_1(t)*f(t-\tau_1) \leftrightarrow R_1(\omega) \cdot F(\omega)e^{-i\omega\tau_1} \quad \dots(41)$$

$$g_2(t) = r_2(t)*f(t-\tau_2) \leftrightarrow R_2(\omega) \cdot F(\omega)e^{-i\omega\tau_2} \quad \dots(42)$$

The signal recieved is the sum of the direct and the two reflected signals:

$$F(\omega) \left\{ 1 + |R_1(\omega)|e^{-i(\omega\tau_1+\phi_1)} + |R_2(\omega)|e^{-i(\omega\tau_2+\phi_2)} \right\} \quad \dots(43)$$

Bath (1974, p.398) showed that the logarithmic power expression can be approximated by

$$\begin{aligned} \ln |F(\omega)|^2 &+ 2|R_1(\omega)|\cos(\omega\tau_1+\phi_1) + 2|R_2(\omega)|\cos(\omega\tau_2+\phi_2) \\ &- |R_1(\omega)|^2\cos 2(\omega\tau_1+\phi_1) - |R_2(\omega)|^2\cos 2(\omega\tau_2+\phi_2) \\ &- 2|R_1(\omega)||R_2(\omega)|\cos\{(\omega\tau_1+\phi_1) + (\omega\tau_2+\phi_2)\} \end{aligned} \quad \dots(44)$$

If R is independent of ω and R_1 and R_2 are positive for $\phi_1 = \phi_2 = 0$ and negative for $\phi_1 = \phi_2 = \pi$ expression (44) reduces to

$$\begin{aligned} \ln |F(\omega)|^2 &+ 2R_1 \cos\omega\tau_1 + 2R_2 \cos\omega\tau_2 - R_1^2 \cos 2\omega\tau_1 \\ &- R_2^2 \cos 2\omega\tau_2 - 2R_1R_2 \cos\omega(\tau_1+\tau_2) \end{aligned} \quad \dots(45)$$

Thus the spectrum will have "ripples" with periods of $2\pi/\tau_1$, $2\pi/\tau_2$, $2\pi/2\tau_1$, $2\pi/2\tau_2$, and $2\pi/(\tau_1+\tau_2)$. The transit times τ_1 and τ_2 correspond to the delay times to the reflector, times $2\tau_1$ and $2\tau_2$ to the first multiples to both reflectors, while the time $\tau_1+\tau_2$ represents a composite multiple.

Earlier it was shown (equation 14) that the time delay associated with a monochromatic wave passing through a medium was related to the gradient of the phase spectra. The linear gradient associated with the phase spectra for the 25 m brine-saturated sand model depicted in Figure 5.43 corresponds to the two-way traveltime through the sand layer. As the impedance contrasts between the sandstone layer and the under- and overlying shale half spaces are small, intrabed multiple energy can be expected to be minimal, however intrabed multiple energy will be significant for the 25 m gas-saturated sand model. This is reflected in the two distinct linear gradient trends in the phase spectra (Figure 5.43) for small incident angles. The steep gradients between 17 and 37 hz and 110 hz coincides with the traveltime for the first intrabed multiple while the linear trend elsewhere reflects the two-way traveltime in the gas-saturated sand layer. Thus the multiple energy is frequency selective and has a ripple frequency corresponding to the two-way time through the layer. Thus mixed phase spectra must result in layered sequences with large impedance contrasts.

XVIII. INVERSION METHOD FOR PRIMARY REFLECTIONS
FROM THIN LAYERS

Consider a medium consisting of n ideally elastic homogeneous and isotropic layers with plane parallel boundaries located between an upper half-space (0) and lower half-space ($n+1$) (Figure 5.4). The transition zone is placed at a depth h below the surface. The parameters of each layer are known: the velocity of the longitudinal velocity (V_{p_i}), the density (ρ_i), the thickness (h_i), and the incident angle (θ_i).

The impulse response for such a model can be determined from the reflection coefficients and delay times. Transmission losses will be ignored. The reflection coefficient between layer i and $i+1$ is given by

$$r_i = \frac{Z_{i+1} - Z_i}{Z_{i+1} + Z_i} \quad \dots(46)$$

where Z_i is the acoustic impedance, which for any layer is given by

$$Z_i = \rho_i V_{p_i} \quad \dots(47)$$

There is no time delay associated with the first interface as this is the time reference. Thus the impulse response from the first interface would be

$$R_1(t) = r_1 \delta(t-0) \quad \dots(48)$$

where $\delta(t-\tau) = 1$ for $t = \tau$

$$= 0 \text{ for } t \neq \tau \quad \dots(49)$$

The time delay associated with layer i is the two-way travelttime (τ_i) to the interface

$$\tau_i = 2 \sum_{k=1}^{i-1} \frac{d_k}{V_{p_k}} \cos \theta_k \quad \dots(50)$$

and the impulse response is

$$R_i(t) = r_i \delta(t - \tau_j) \quad \dots(51)$$

while the total response would be the sum of the individual responses

$$R(t) = \sum_{i=1}^{n-1} R_i(t) \quad \dots(52)$$

The frequency response of $R(t)$ can be found by replacing all $\delta(t - \tau)$ by $e^{i\omega\tau}$ in equation (52),

$$R(\omega) = \sum_{i=1}^{n-1} R_i(\omega) = \sum_{i=1}^{n-1} E_i r_i \quad \dots(53)$$

where

$$E_i = e^{j\omega\tau_i} \quad \dots(54)$$

and

$$j = \sqrt{-1} \quad \dots(55)$$

Partial derivatives of the impulse response with respect to the model parameters are required for nonlinear regression analysis. The partials can be computed from $R(\omega)$ and are given by

$$\frac{\partial R(\omega)}{\partial \tau_j} = j\omega \sum_{k=1}^{n-1} R_k(\omega) \quad \dots(56)$$

$$\frac{\partial R(\omega)}{\partial z_i} = E_{i-1} \left(\frac{1}{2z_i} \right) + E_i \left(\frac{-2z_{i+1}}{(z_i + z_{i+1})^2} \right) \quad \dots(57)$$

$$\frac{\partial R(\omega)}{\partial h_i} = \frac{\partial R}{\partial \tau_i} \frac{2 \cos \theta_i}{V_{p_i}} \quad \dots(58)$$

$$\frac{\partial R(\omega)}{\partial v_{p_i}} = \frac{\partial R}{\partial \tau_i} = \left(\frac{-2d_i \cos \theta_i}{v_{p_i}} \right) + \frac{\partial R}{\partial z_i} \rho_i \quad \dots(59)$$

$$\frac{\partial R(\omega)}{\partial \rho_i} = \frac{\partial R}{\partial z_i} v_{p_i} \quad \dots(60)$$

Nonlinear regression schemes can be used to iteratively solve the layer parameters using all the CDP gather traces given some initial strata model. This procedure will not be further described since the technique has not been tested on field data.

XIX. MODE CONVERSION

Solution of the Zoeppritz equations shows that mode conversion occurs only when the angle of incidence is non-vertical and is more efficient as the incident wavefront becomes more oblique due to increased shearing stresses at the boundary. Thus the transmitted and reflected waves contain both P and S components. Tatham & Stoffa (1976) suggested that the mode converted arrivals would be observed on the far traces of multifold CDP data. Figure 5.58 shows the reflection and refraction of an incident plane compression wave at a boundary. For a geologic section in which the velocity increases with depth the reflection angle of the mode converted P wave is smaller than that for the reflected P wave,

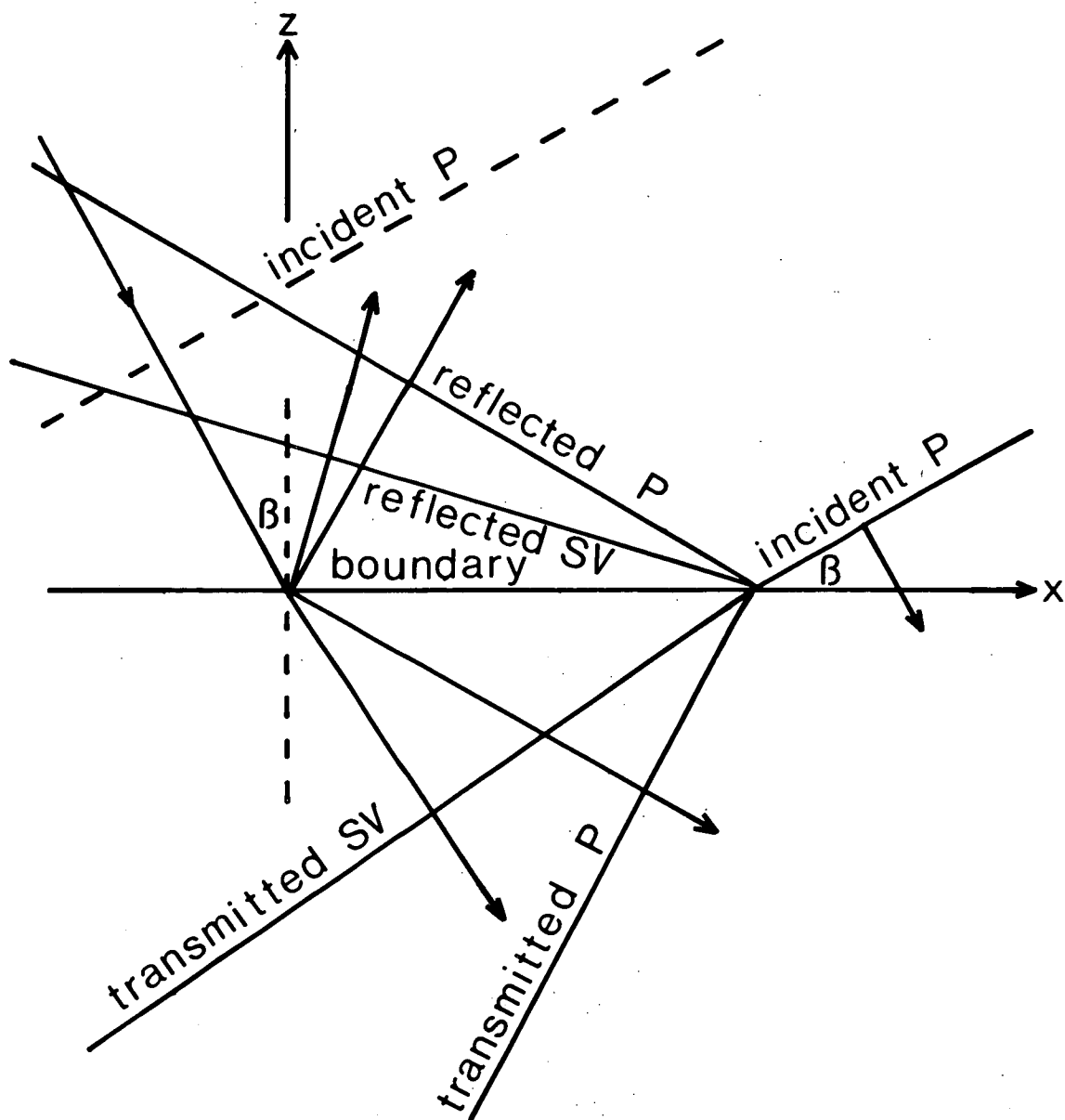


Fig. 5.58 Reflection and refraction of an incident plane compressional wave at a boundary.

thereby reducing the offset required for PS reflection detection. To ascertain the significance of the mode conversion process plots of the ratio of the PS amplitude to that of the PP (Figure 5.59) are contoured for models 1, 4, 7 and 8 of Figure 5.8. The plots show that mode conversion can be significant and that amplitude ratios greater than one can be obtained, although these tend to occur at incident angles greater than 30° . For high frequencies and small incident angles, large ratios are obtained for model 1. The amplitude ratios in part reflect the fact that the amplitude maxima and minima for the PP and PS cases do not coincide directly at any particular frequency.

XX. TRANSMISSION IN THIN LAYERS

Mode conversion has been shown to be significant, so that transmission determinations must take into account the reflectivity of the PS waves. By applying the principle of conservation of energy the transmissivity of thin layers (models 1, 4, 7 and 8 of Figure 5.8) has been determined (Figure 5.60). These transmissivities represent both the transmitted P and S waves. The inclusion of the mode conversion component diminishes the influence of the maxima and minima that are present for PP reflectivities.

Significant points are:

1. Little energy is transmitted for layers with large bed velocities at low frequencies for incident angles conventionally used in CDP techniques. However large transmissivities occur at high frequencies (model 1).

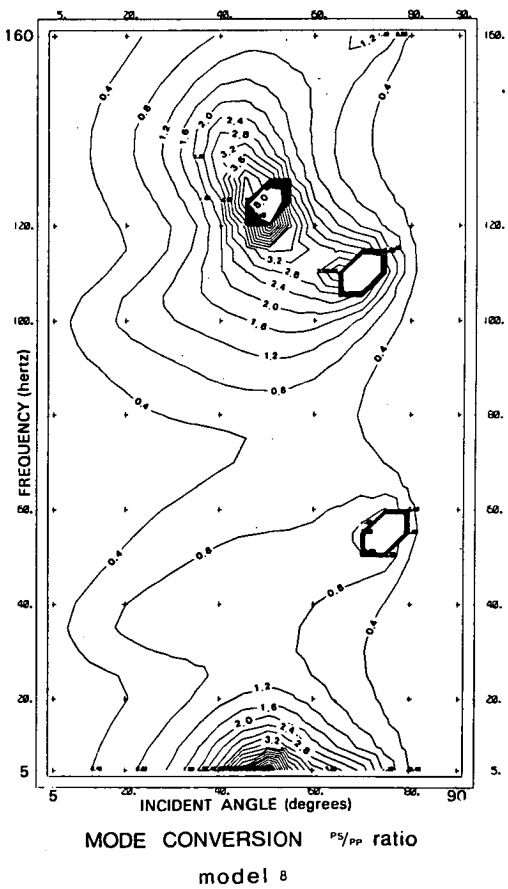
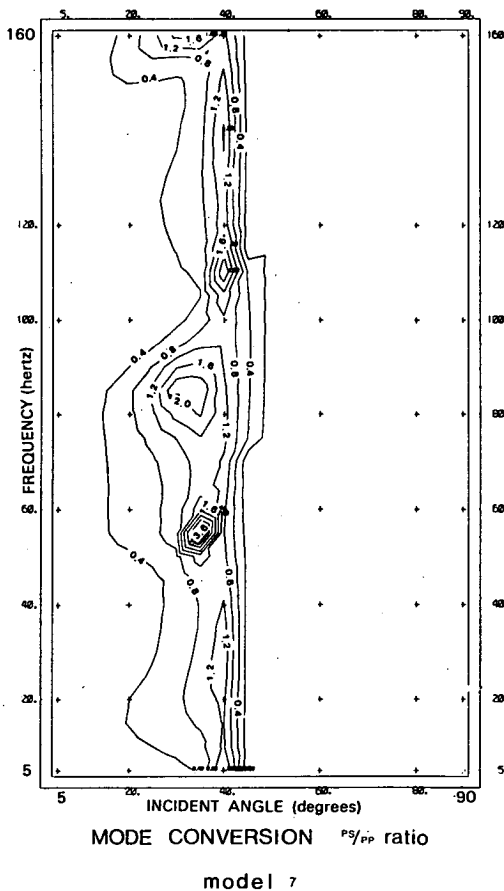
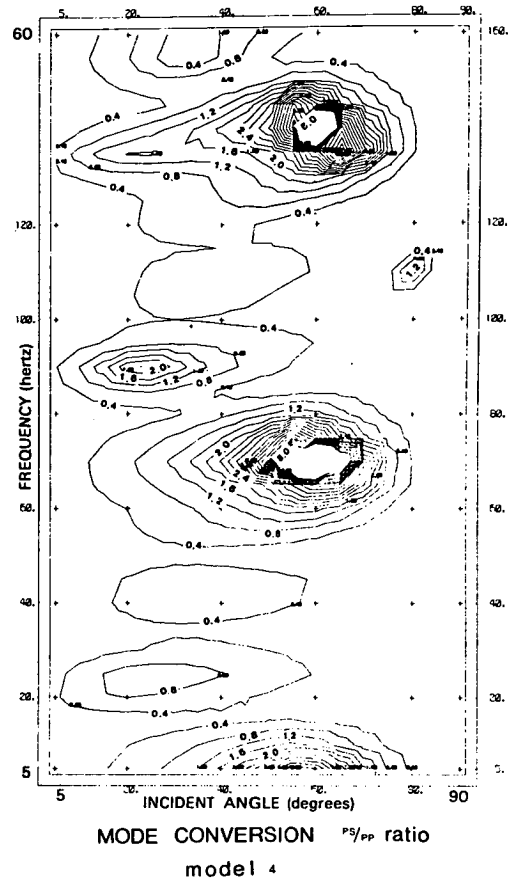
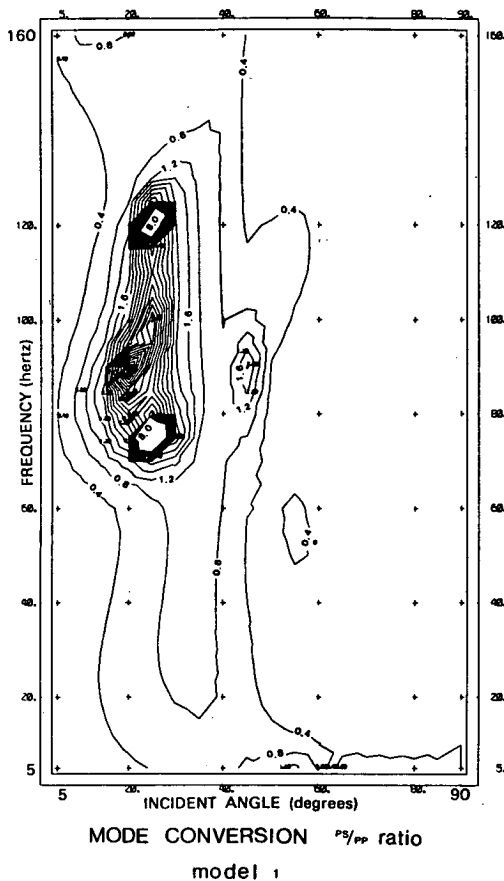


Fig. 5.59 PS:PP amplitude ratios for models 1, 4, 7 and 8.

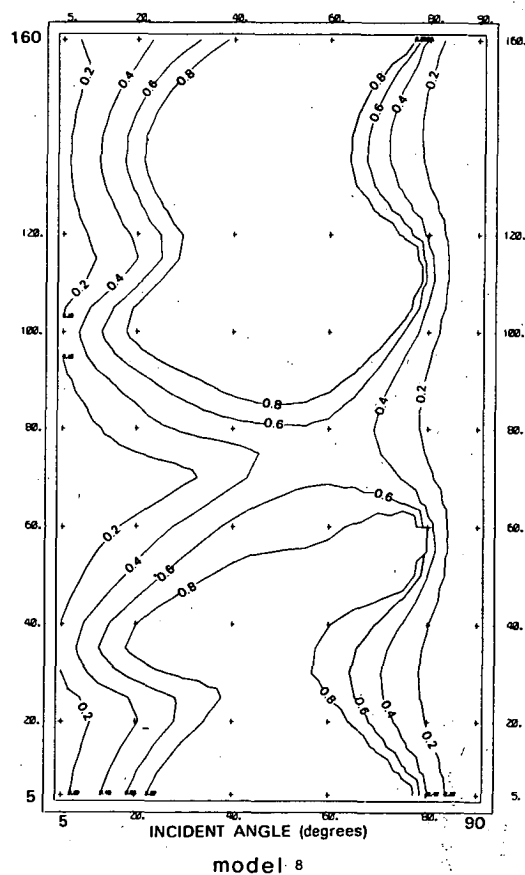
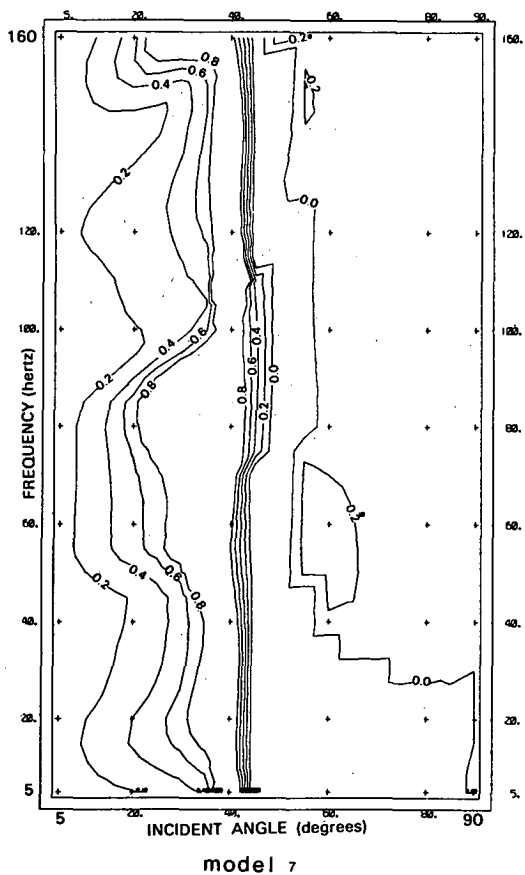
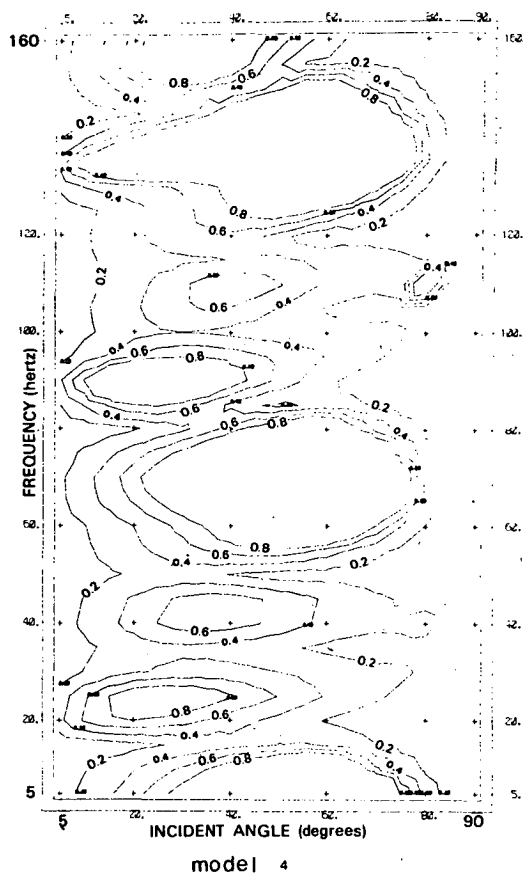
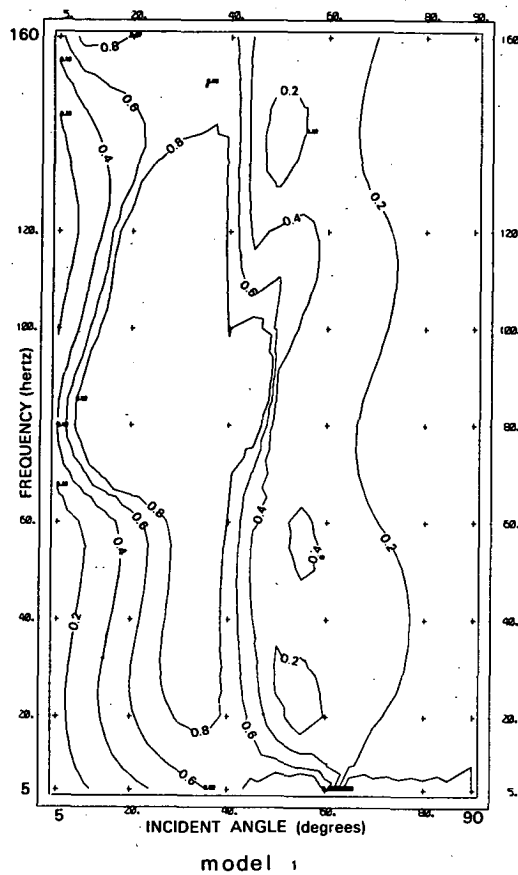


Fig. 5.60 Transmissivity for models 1, 4, 7 and 8.

- An increased bed thickness would allow greater transmission at low frequencies as would lower bed velocities.
2. A closely spaced gapped transmitted energy spectrum occurs for low velocity layers and conventional incident angles (model 4). Little transmitted energy occurs for most frequencies at small incident angles. This accounts for the diminished amplitudes of events beneath reflections from coal or gas saturated sand sequences.
 3. Increasing and decreasing velocity profiles have gapped transmissivities for conventional incident angles (models 7 and 8). The position of the maximum transmissivity is determined by the bed thickness and velocity.

XXI. PRINCIPLE OF RECIPROCITY

The principle of reciprocity states that a source and receiver may be interchanged and the same waveform will be observed. On the basis of controlled field experiments

Bulachandran (1974) noted that interchangeability of the source and receiver cannot be assumed when the near surface layers are heterogeneous. Discussion of reflectivities and and transmissivities has illustrated that wave propagation is frequency-selective so that the principle of reciprocity cannot apply for transmission through heterogeneous thin layers.

CONCLUSIONS

Phase, amplitude, arrival time and frequency are the basic parameters of seismic energy. The use of CDP methods is detrimental to these essential parameters. Stacking NMO corrected data results in a wavelet vastly different from that for the zero-offset wavelet. Studies of the reflectivity, transmissivity and mode conversion of thin layers illustrates that variations in wavelet shape are a function of the layering properties, incident angles and frequency of the incident plane wave. CDP stacking destroys this amplitude and phase information. Offset-dependent phase changes are most pronounced at high frequencies, and introduce time shifts into the wavelet with increasing offset. Trace-to-trace correlations become difficult, so that stacking reduces signal quality, and time shifts result in errors in seismic velocity determination. A study of multilayered media shows that the layering properties can be related to the complex cepstrum.

Mode conversion of P waves to S waves at a reflecting sequence can be shown to be a significant process at certain frequencies and large offsets. DHI studies show that for small thicknesses oil saturated sands may produce larger amplitude events than gas saturated sands.

Chapter 6

CONCLUSIONS

CONCLUSIONS

Raypath modelling of primary P waves over a suite of simple non-horizontally layered two-dimensional models has shown that data processed using conventional CDP techniques may contain velocity conversion errors of up to 50 percent and timing errors of up to 120 msec. The resultant depth errors, which involve the interplay of both velocity and timing errors, may be so significant as to impede the detection of subtle hydrocarbon traps. It has been shown that conventional CDP techniques may fail because:

1. The customary assumption that stacking velocities approximate rms velocities is invalid in areas of non-horizontal structures;
2. Rapid lateral changes in stacking velocities due to geological factors may confuse velocity information from horizons overlain by irregularities. Slight timing shifts and these lateral changes may cause diminishment of wavelets during CDP stacking and, in extreme cases, pulse splitting;
3. Standard fitting of hyperbolic curves to produce NMO traces is not valid in geologically difficult areas;
4. Stacking velocities may not be consistent for seismic lines shot over the same area using different field configurations.
5. Replacement static corrections are time variant and not surface consistent in irregular water-bottom environments. Provided the weathered layer velocity and profile are known wavefront statics may be used to overcome this problem.

6. Stacking velocities can vary greatly for the same spread length with different shot-first receiver offsets.
7. Three-dimensional structures further increase conversion errors.

Information about the characteristics of a reflecting surface is contained within the reflected wavelet but may be lost as a result of wavelet modification introduced by CDP stacking or the amplitude and phase responses of the overlying geology. Variations in wavelet shape with incident angle, normally a function of offset, may cause diminution of the reflected wavelet when stacked.

The shape of wavelets reflected from thin layers is a function of the layer properties, incident angle and frequency of the incident plane wave. Offset-dependent phase changes are most pronounced at high frequencies and the resultant time shifts produce errors in velocity determinations and difficulty in trace-to-trace correlation. Provided that this fundamental amplitude and phase information has not been distorted or destroyed by CDP stacking some of the layer properties may be determined from the reflected arrivals. For example, in the single layer models, arrivals from oil saturated sand layers were larger than those from gas-bearing sands only for thin layers, but intra-layer multiples were more pronounced for the gas-bearing sands at all layer thicknesses studied. An extension of the model study to multi-layer sequences showed that the reflectivity function of the sequence was closely approximated by the complex cepstrum of the reflected wavelet. Mode conversion of P waves to S waves in multi-layered sequences is more significant than

in single layers, and hence sufficient S arrivals may be received to allow increased resolution of the thin beds using PS and SS waves.

The extension of the simple geological structures discussed in this thesis, to the complex real earth must further downgrade the accuracies and resolution of seismic reflection techniques.

REFERENCES

- Al-Chalabi, M., 1973. Series approximation in velocity and travel time computations. *Geophys. Prosp.*, 21, 785-795.
- Al-Chalabi, M., 1974. An analysis of stacking, rms, average, and interval velocities over a horizontally layered ground. *Geophys. Prosp.*, 22, 458-475.
- Alford, R.M., Kelly, K.R., and Boore, D.M., 1974. Accuracy of finite difference modelling of the acoustic wave equation. *Geophysics*, 39, 834-842.
- Anstey, N.A., 1977. *Seismic interpretation: the physical aspects*. Boston, I.H.R.D.C.
- Arnold, M.E., 1977. Beam forming with vibrator arrays. *Geophysics*, 42, 1321-1338.
- Balachandran, K., 1974. Non interchangeability of sources and receivers in a heterogeneous medium. *Geophysics*, 39, 73-80.
- Bath, M., 1974. *Spectral analysis in geophysics: Developments in Solid Earth Physics 7*. Elsevier, Amsterdam.
- Benderskii, V.Ya., Vasil'ev, Yu.A., Raikher, L.D., and Kharaz, I.I., 1965. Elements of a theory of variable control of seismic wavefronts. *Bull. (Izvestiya) Acad. Sci. USSR, Geophysics Series*, 6, 368-374.
- Blackburn, G.J., 1980. Errors in stacking velocity-true velocity over complex geologic situations. *Geophysics*, 45, 1465-1488.
- Bogert, B.P., Healy, M.J.R., and Tukey, J.W., 1963. The Que frequency analysis of time series for echoes: cepstrum, pseudo-autocovariance, cross-cepstrum and saphe cracking. in *Proceedings of the Symposium on Time Series Analysis*. John Wiley and Sons, Inc., New York.
- Booker, A.H., Linville, A.F., and Wason, C.B., 1976. Long wavelength static estimation. *Geophysics*, 41, 939-959.

- Brown, R.J.S., 1969. Normal moveout and velocity relations for flat and dipping beds and for long offsets. *Geophysics*, 34, 180-195.
- Buchholtz, H., 1972. A note on signal distortion due to dynamic (NMO) corrections. *Geophys. Prosp.*, 20, 395-402.
- Chandler, R., 1977. On tracing seismic rays with specified end points in layers of constant velocity and plane interfaces. *Geophys. Prosp.*, 25, 120-124.
- Claerbout, J.F., 1970. Course grid calculations of waves in inhomogeneous media with applications to delineation of complicated seismic structure. *Geophysics*, 35, 407-418.
- Claerbout, J.F., 1971. Toward a unified theory of reflector mapping. *Geophysics*, 36, 467-481.
- Claerbout, J.F., 1976. *Fundamentals of Geophysical Data Processing with Applications to Petroleum Prospecting*. McGraw-Hill, New York.
- Claerbout, J.F., and Doherty, S.M., 1972. Downward continuation of moveout corrected seismograms. *Geophysics*, 37, 741-768.
- Claerbout, J.F., and Johnson, A.G., 1971. Extrapolation of time dependent waveforms along their path of propagation. *Geophys. Jour. R. Astr. Soc.*, 26, 285-293.
- Dix, C.H., 1955. Seismic velocities from surface measurements. *Geophysics*, 20, 68-86.
- Dobecki, T.L., 1973. Three-dimensional seismic modelling for arbitrary velocity distributions. *Geophys. Prosp.*, 21, 330-339.
- Dobrin, M.B., 1976. *Introduction to Geophysical Prospecting*. McGraw-Hill, New York.

- Doherty, S.M., and Claerbout, J.F., 1976. Structure independent seismic velocity estimation. *Geophysics*, 41, 850-881.
- Dunkin, J.W., 1965. Computation of modal solutions in layered, elastic media at high frequencies. *Bull. Seis. Soc. Am.*, 55, 335-358.
- Dunkin, J.W., and Levin, F.K., 1971. Isochrons for a 3-D seismic system. *Geophysics*, 36, 1099-1137.
- Dunkin, J.W., and Levin, F.K., 1973. Effect of normal moveout on a seismic pulse. *Geophysics*, 38, 635-642.
- Fertig, J., and Muller, G., 1978. Computations of synthetic seismograms for coal seams with the reflectivity method. *Geophys. Prosp.*, 26, 868-883.
- Fitton, J.C., and Dobrin, M.B., 1967. Optical processing and interpretation. *Geophysics*, 32, 801-818.
- French, W.S., 1974. Two-dimensional and three-dimensional migration of model-experiment reflection profiles. *Geophysics*, 39, 265-277.
- Fuchs, K., 1968. Das Reflexions - und transmissionsvermogen eines geschichteten mediums mit beliebiger tiefenverteilung der elastischen modulum and der dichte fur schragen einfall ebener wellen. *Zeits. Geophys.*, 34, 389-413.
- Fuchs, K., 1970. The method of stationary phase applied to the reflection of spherical waves from transition zones with arbitrary depth-dependent elastic moduli and density. *Zeits. Geophys.*, 37, 89-117.
- Gardner, G.H.F., French, W.S., and Matzuk, T., 1974. Elements of migration and velocity analysis. *Geophysics*, 39, 811-825.

Gardner, G.H.F., Gardner, L.W., and Gregory, A.R., 1974.

Formation velocity and density - the diagnostic basics of stratigraphic traps. *Geophysics*, 39, 770-780.

Green, C.H., 1938. Velocity determinations by means of reflection profiles. *Geophysics*, 3, 295-305.

Gregory, A.R., 1977. Aspects of rock physics from laboratory and log data that are important to seismic interpretation, in *Seismic Stratigraphy - applications to hydrocarbon exploration*. A.A.P.G. Memoir 26, Oklahoma, U.S.A.

Greville, T.N.E., 1967. Spline functions, interpolation and numerical quadrature, in *Mathematical Methods for Digital Computers*, 2. John Wiley and Sons, New York.

Gupta, I.N., 1966. Dispersion of body waves in layered media. *Geophysics*, 31, 821-823.

Hagedoorn, J.G., 1954. A process of seismic reflection interpretation. *Geophys. Prosp.*, 21, 85-127.

Halbouty, M.T., 1972. Rationale for deliberate pursuit of stratigraphic, unconformity and paleogeomorphic traps, in *Stratigraphic Oil and Gas Fields - classification, exploration methods and case histories*. A.A.P.G. Memoir 16, Oklahoma, U.S.A.

Harkrider, D.G., 1964. Surface waves in multilayered elastic media 1. Rayleigh and Love waves from buried sources in a multilayered elastic half space. *Bull. Seis. Soc. Am.*, 54, 627-679.

Harkrider, D.G., 1970. Surface waves in multilayered elastic media 2. Higher mode spectra and spectral ratios from point sources in plane layered earth models. *Bull. Seis. Soc. Am.*, 60, 1937-1987.

- Haskell, N.A., 1953. The dispersion of surface waves on multilayered media. *Bull. Seis. Soc. Am.*, 43, 17-34.
- Hazebroek, P., 1966. Elastic waves from a finite line source. *Proc. Roy. Soc. Lond., Series A*, 294, 38-65.
- Hileman, J.A., Embree, P., and Pflueger, J.C., 1968. Automated static corrections. *Geophys. Prosp.*, 16, 326-358.
- Hilterman, F.J., 1970. Three-dimensional seismic modelling. *Geophysics*, 35, 1020-1037.
- Hubral, P., and Krey, T., 1980. Interval velocities from reflection time measurements. *SEG Monograph Series*, Tulsa.
- Knott, C.G., 1899. Reflection and refraction of elastic waves, with seismological applications. *Phil. Mag. (London)*, 48, 567-569.
- Knopoff, L., 1964. A matrix method for elastic wave problems. *Bull. Seis. Soc. Am.*, 54, 431-438.
- Larner, K.L., Mateker, E.J., and Wu, C., 1973. Amplitude: its information content, in *Lithology and Direct Detection of Hydrocarbons Using Geophysical Methods*. Geophysical Society of Houston.
- Levin, F.K., 1971. Apparent velocity from dipping interface reflections. *Geophysics*, 36, 510-516.
- Levin, F.K., 1979. Seismic velocities in transversely isotropic media. *Geophysics*, 44, 918-936.
- Lindsey, J.P., 1973. Modelling for lithology, in *Lithology and Direct Detection of Hydrocarbons Using Geophysical Methods*. Geophysical Society of Houston.
- Lowenthal, D., Lu, L., Robinson, R., and Sherwood, J., 1976. The wave equation applied to migration. *Geophys. Prosp.*, 24, 380-399.
- Marr, J.D., 1971. Seismic stratigraphic exploration - part III. *Geophysics*, 36, 676-689.

- Mathieu, P.G., and Rice, G.W., 1969. Multivariate analysis used in the detection of stratigraphic anomalies from seismic data. *Geophysics*, 34, 507-515.
- May, B.T., and Hron, F., 1978. Synthetic seismic sections of typical petroleum traps. *Geophysics*, 43, 1119-1147.
- McCamy, K., Meyer, R.P., and Smith, T.J., 1962. Generally applicable solutions of Zoeppritz' amplitude equations. *Bull. Seis. Soc. Am.*, 52, 923-955.
- Meckel, L.D., and Nath, A.K., 1977. Geologic considerations for stratigraphic modelling and interpretation, in *Seismic Stratigraphy - Applications to Hydrocarbon Exploration*. A.A.P.G. Memoir 26, Oklahoma, U.S.A.
- Miller, M.K., 1974. Stacking of reflections from complex structures. *Geophysics*, 39, 427-440.
- Mitcham, P.R., Vail, P.R., and Thompson, S., 1977. Seismic stratigraphy and global changes of sea level, part 2. The depositional sequences as a basic unit for stratigraphic analysis, in *Seismic Stratigraphy - Applications to Hydrocarbon Exploration*. A.A.P.G. Memoir 26, Oklahoma, U.S.A.
- Neidel, N.S., and Poggiagliolmi, E., 1977. Stratigraphic modelling and interpretation - Geophysical principles and techniques, in *Seismic Stratigraphy - Applications to Hydrocarbon Exploration*. A.A.P.G. Memoir 26, Oklahoma, U.S.A.
- Newman, P., 1973. Divergence effects in a layered earth. *Geophysics*, 38, 481-488.
- O'Brien, P.N.S., 1961. A discussion on the nature and magnitude of elastic absorption in seismic prospecting. *Geophys. Prosp.*, 9, 261-275.

- O'Doherty, R.F., and Anstey, N.A., 1971. Reflections on amplitudes. *Geophys. Prosp.*, 19, 430-458.
- Paige, D.S., 1973. The dark side of the bright spot, in *Lithology and Direct Detection of Hydrocarbons Using Geophysical Methods*. Geophysical Society of Houston.
- Phinney, R.A., and Jurdy, D.M., 1979. Seismic imaging of deep crust. *Geophysics*, 44, 1637-1660.
- Rayleigh, Lord, 1896. *The Theory of Sound*. MacMillan and Co. Ltd., London.
- Richards, T.C., 1961. Motion of the ground on arrival of reflected longitudinal and transverse waves at wide-angle reflection distances. *Geophysics*, 26, 277-297.
- Ricker, N.H., 1977. Transient waves in visco-elastic media, in *Developments in Solid Earth Geophysics*, 10. Elsevier, Amsterdam.
- Rudman, A.J., and Blakely, R.F., 1976. Fortran program for generation of synthetic seismograms. *Dept. Natural Resources Geol. Surv. Occ. Paper 13*, Bloomington, Indiana, U.S.A.
- Sattlegger, J.W., and Stiller, P.K., 1974. Section migration, before stack, after stack, or in between. *Geophys. Prosp.*, 22, 297-314.
- Schafer, R.W., 1969. Echo removal by discrete generalised linear filtering. *Mass. Inst. Tech. Res. Lab. of Electronics, Tech. Rept. 466*.
- Schneider, W.A., 1971. Developments in seismic data processing and analysis (1968-1970). *Geophysics*, 36, 1043-1073.
- Schneider, W.A., and Backus, M., 1968. Dynamic correlation analysis. *Geophysics*, 33, 105-126.

- Schoenberger, M., and Levin, F.K., 1974. Apparent attenuation due to intrabed multiples. *Geophysics*, 39, 278-291.
- Schultz, P.S., and Claerbout, J.F., 1978. Velocity estimation and downward continuation by wavefront synthesis. *Geophysics*, 43, 691-714.
- Schwab, F.A., and Knopoff, L., 1972. Fast surface wave and free mode computations, in *Methods in Computational Physics*, II. Academic Press, New York.
- Shah, P.M., 1973a. Use of wavefront curvature to relate seismic data with subsurface parameters. *Geophysics*, 38, 812-825.
- Shah, P.M., 1973b. Ray tracing in three dimensions. *Geophysics*, 38, 600-604.
- Shah, P.M., and Levin, F.K., 1973. Gross properties of time distance curves. *Geophysics*, 38, 643-656.
- Sheriff, R.E., 1973. Factors affecting amplitudes - a review of physical principles, in *Lithology and Direct Detection of Hydrocarbons Using Geophysical Methods*. Geophysical Society of Houston.
- Sheriff, R.E., 1977. Limitations on resolution of seismic reflections and geologic detail derivable from them, in *Seismic Stratigraphy - Applications to Hydrocarbon Exploration*. A.A.P.G. Memoir 26, Oklahoma, U.S.A.
- Sheriff, R.E., 1980. Nomogram for Fresnel-zone calculation. *Geophysics*, 45, 968-972.
- Sherwood, J., Adams, H., Blum, C., Judson, D., Lin, J., and Meadours, B., 1976. Developments in filtering seismic data. Paper presented at the 46th Annual Int. Meeting of SEG, Houston, U.S.A.

- Smith, S.G., 1977. A reflection profile modelling system. *Geophys. Jour.*, 49, 723-738.
- Taner, M.T., Cook, E.E., and Neidell, N.S., 1970. Limitations of the reflection seismic system: lessons from computer simulations. *Geophysics*, 35, 551-573.
- Taner, M.T., and Koehler, F., 1969. Velocity spectra-digital computer derivation and applications of velocity functions. *Geophysics*, 34, 859-881.
- Taner, M.T., Koehler, F., and Alhilali, K.A., 1974. Estimation and correction of near surface time anomalies. *Geophysics*, 39, 441-463.
- Tatham, R.H., and Stoffa, P.L., 1976. V_p - V_s - a potential hydrocarbon indicator. *Geophysics*, 41, 837-849.
- Thompson, W.T., 1950. Transmission of elastic waves through a stratified solid medium. *J. Appl. Phys.*, 21, 89-93.
- Thrower, E.N., 1965. The computation of the dispersion of elastic waves in layered media. *J. Sound Vib.*, 2, 210-226.
- Vail, P.R., and Mitcham, P.R., 1977. Seismic stratigraphy and global changes of sea level, part 1: overview, in *Seismic Stratigraphy - Application to Hydrocarbon Exploration*. A.A.P.G. Memoir 26, Oklahoma, U.S.A.
- Vasil'ev, Yu.A., Raikher, L.D., and Sagalova, E.I., 1964. Conditions for formation of a total wave excited by a linear arrangement of explosion points. *Bull. (Izvestiya) Acad. Sci. USSR, Geophysics Series*, 8, 725-729.
- Wardell, J., 1973. A method of continuous velocity analysis. *A.P.E.A. Jour.*, 13, 97-103.

- Watson, T.H., 1970. A note on fast computation of Rayleigh wave dispersion in the multilayered elastic half-space. *Bull. Seis. Soc. Am.*, 60, 161-166.
- Widess, M.B., 1973. How thin is a thin bed? *Geophysics*, 38, 1176-1180.
- Wiggins, R.A., Larner, K.L., and Wisecup, R.D., 1976. Residual statics analysis as a general linear inverse problem. *Geophysics*, 41, 922-938.
- Will, M., 1976. Calculations of traveltimes and raypaths for lateral inhomogeneous media, in *Explosion Seismology in Central Europe*. Springer-Verlag, Berlin.
- Wolff, I., and Malter, L., 1930. Directional radiation of sound. *J. Acoust. Soc. Am.*, 2, 232-233.
- Wuenschel, P.C., 1965. Dispersive body waves - an experimental study. *Geophysics*, 30, 539-551.
- Young, G.B., and Braile, L.W., 1976. A computer program for the application of Zoeppritz's amplitude equations and Knott's energy equations. *Bull. Seis. Soc. Am.*, 66, 1881-1885.
- Zoeppritz, K., 1919. Erdbebenwellen VIIIB, Über Reflexion und Durchgang seismischer Wellen durch Unstetigkeitsflächen. *Göttingen Nachr.*, 1, 66-84.

Appendix 1

RAY TRACING SYSTEM - TWO DIMENSIONS

	page
I. INTRODUCTION	A1.1
II. REFLECTION PROFILE MODELLING SYSTEM	A1.1
1. Program Input	A1.2
a. Model description	A1.2
b. Shooting parameters	A1.2
c. Control parameters	A1.2
2. Generating the Model	A1.2
3. Zero-Offset Ray Tracing	A1.3
4. Non-Zero-Offset Ray Tracing	A1.3
5. Determination of Stacking Velocities and Zero-Offset Times	A1.4
6. Limitations of the Modelling System	A1.4

I. INTRODUCTION

Modelling systems for reflection profiling have been developed by numerous authors, but all systems have some limitations. *Taner et al.* (1970) produced a ray tracing system and traveltimes calculations; *Hilterman* (1970) and *Dunkin & Levin* (1971) produced three-dimensional (3D) reflection profile modelling systems for one layer only - a constant velocity section down to a single reflector; *Dobecki* (1973) produced 3D models for arbitrary velocity distributions but limited to plane reflectors. *Smith* (1977) described a modelling system for normal incidence reflection for two-dimensional (2D) models. *Shah* (1973) gives an algorithm to trace rays through a 3D model consisting of plane or curved surfaces.

II. REFLECTION PROFILE MODELLING SYSTEM

This computer program was designed to trace rays through 2D earth models and to compute traveltimes and NMO velocities for primary events and is described below.

1. PROGRAM INPUT

Input is in three stages:

a. Model description

The geological model is represented by L laterally inhomogeneous but vertically homogeneous layers separated by L+1 continuous curves which are mathematically represented as cubic spline functions. These layers are defined by inputting sufficient coordinates of points on the surface to define the curve. Interval velocities are specified at each of these digitised points and lateral interval velocities between these points are defined by linear interpolation.

b. Shooting parameters

The line geometry (first and last shot point and shot point interval) together with CDP gather information (gather locations, shot-first receiver distance, geophone spacing and the fold of the synthetic data) are input. All shot and receiver locations are assumed to be at the uppermost horizontal surface of the model.

c. Control parameters

The control parameters specify the type of output options, plotting parameters as well as specifying the reflector to be used for ray tracing.

2. GENERATING THE MODEL

The program then constructs a model according to the input specifications and a number of checks are performed to detect possible errors. Cubic spline functions, using the method of Greville (1967, p.156), are determined for the set

of data points for each surface and the second derivative coefficients are stored. A cross section of the model is then plotted.

3. ZERO-OFFSET RAY TRACING

This involves the use of the normal incidence technique in which one-way raypaths emanate at right angles from the reflecting surface at depth, propagating upward to the surface of the earth. The point of contact at depth is iteratively adjusted so that the raypath is within a specified tolerance of the shot-geophone location. In homogeneous layers, straight line ray tracing, similar to that of Smith (1977), is used within the layer but where lateral velocity changes are significant, curved raypaths are traced using the method of Will (1976). Arrival times, amplitudes and the point of contact at depth for each shot point are listed. Zero-offset raypaths are plotted.

Since it is possible for the rays reaching a given gather location to have varying subsurface CRP's it is imperative to sort the data according to gather location, and also according to subsurface CRP.

4. NON-ZERO-OFFSET RAY TRACING

This uses the point of contact of a zero-offset raypath as the initial condition and iteratively adjusts the reflection angle and the point of contact to produce non-zero-offset raypaths which arrive within a specified tolerance of the designated shot and receiver locations. Raypath plots for

each gather location are produced as well as listings of arrival times.

5. DETERMINATION OF STACKING VELOCITIES AND ZERO-OFFSET TIMES

The stacking velocity is taken to equal the square root of the reciprocal of the slope of a least squares straight line through points on the T^2-X^2 graph derived from the gather information. The zero-offset time (T_0) is taken to be the square root of the intercept at $X^2 = 0$. These values are compared to the true vertical velocity and true vertical time at the gather location.

6. LIMITATIONS OF THE MODELLING SYSTEM

The following limitations apply to the modelling system:

- (1) only two-dimensional geological situations can be modelled,
- (2) the reflecting surfaces must be represented by smooth curves and be continuous across the model. No surface can be represented by more than one depth value at any location,
- (3) the layer velocity must be vertically invariant but can vary laterally,
- (4) the change of pulse shape due to absorption or to phase changes at the interfaces is not taken into account,
- (5) the source and geophone are taken to be on the surface, and
- (6) shear waves are not traced. However energy losses due to mode conversion at the interfaces are included.

Appendix 2

RAY TRACING USING FERMAT'S PRINCIPLE

	page
I. INTRODUCTION	A2.1
II. TWO-DIMENSIONAL RAY TRACING	A2.1
1. Statement of Problem	A2.1
2. Solution	A2.3
III. THREE-DIMENSIONAL RAY TRACING	A2.7
1. Statement of Problem	A2.7
2. Solution	A2.11
IV. CONCLUSIONS	A2.14

I. INTRODUCTION

Ray tracing for constant velocity layers is treated as a variational problem of Fermat's principle and is solved using the Newton Raphson iteration procedure. The method is an extension to Chandler's (1977) treatment except that curved rather than plane interfaces are used.

II. TWO-DIMENSIONAL RAY TRACING

1. STATEMENT OF THE PROBLEM

Let (x_0, z_0) and (x_{n+1}, z_{n+1}) be the coordinates for the source and receiver respectively (Figure A2.1). The geological model is represented by (n) constant velocity layers with continuous curved boundaries which are mathematically represented by third-order polynomials of the form

$$z = A_i x^3 + B_i x^2 + C_i x + D_i \quad \text{for } i = 1, \dots, n \quad \dots(1)$$

with $(A_i, B_i, C_i$ and $D_i, i = 1, \dots, n)$ known for each interface. The constant velocity v_i for $i=1, \dots, n+1$ between surfaces $i-1$ and i is known. v_1 is the constant velocity between the source and the first layer while v_{n+1} is the velocity between the last layer and the detector. Seismic ray paths are to be traced through these layers and may include critical refraction or multiple reflections along the path (Figure A2.1). The source and detector can be both at the surface or both buried at the same or unequal elevation with respect to the datum. Let P_0 to P_{n+1} (Figure A2.1) be the consecutive vertices of the intersections of the polygonal seismic rays with the curved interfaces, with P_0 representing the source and P_{n+1} the detector. Let $(x_i, z_i), i = 0, \dots, n+1$ be the coordinates of these vertices respectively. The problem is to trace the ray by determining the

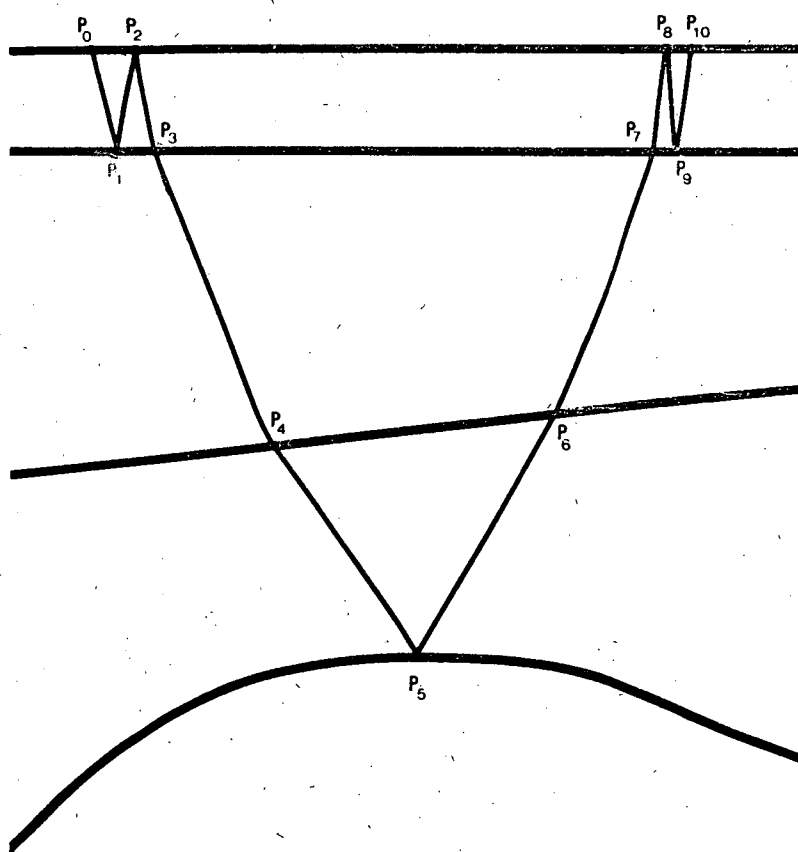


Fig. A2.1 Two Dimensional Geological Model with Curved Surfaces.

coordinates (x_i, z_i) , $i=1 \dots n$ of the vertices P_1 to P_n such that Fermat's principle is satisfied along the ray path.

2. SOLUTION

The travelttime t along the ray P_0-P_{n+1} is given by the sum

$$t = \sum_{i=1}^{n+1} [(x_i - x_{i-1})^2 + (z_i - z_{i-1})^2]^{\frac{1}{2}} v_i^{-1} \quad \dots(2)$$

Also the coordinates of vertices P_1 to P_n must satisfy the equations of the respective interfaces in which they lie. Therefore

$$z_i = A_i x_i^3 + B_i x_i^2 + C_i x_i + D_i \quad i=1, \dots, n \quad \dots(3)$$

Since z_1 to z_n can be expressed in terms of x_i , for $i=1, \dots, n$ the travelttime t is a function of the x coordinates of the vertices P_1 to P_n . Fermat's principle, that the travelttime be stationary for small variations in ray paths, will be satisfied if the following n equations hold simultaneously

$$\begin{aligned} \frac{\partial t}{\partial x_i} &= \frac{[(x_i - x_{i-1}) + (z_i - z_{i-1})(3A_i x_i^2 + 2B_i x_i + C_i)]}{[(x_i - x_{i-1})^2 + (z_i - z_{i-1})^2]^{\frac{1}{2}} v_i} \\ &\quad - \frac{(x_{i+1} - x_i) + (z_{i+1} - z_i)(3A_i x_i^2 + 2B_i x_i + C_i)}{[(x_{i+1} - x_i)^2 + (z_{i+1} - z_i)^2]^{\frac{1}{2}} v_{i+1}} \\ &= 0 \quad i = 1, \dots, n \quad \dots(4) \end{aligned}$$

These equations can be solved using the Newton-Raphson iteration procedure for nonlinear equations. We first define

$$f_i(x_i) = \partial t / \partial x_i \quad \text{for } i=1, \dots, n \quad \dots(5)$$

$$X = [x_1, x_2 \dots x_n]^t \quad \dots(6)$$

and

$$f_{ij}(X) = \frac{\partial f_i(X)}{\partial x_j} \quad \dots(7)$$

Next define the matrix $\phi(X)$ as

$$\phi(X) = [f_{ij}(X)] \quad \text{for } i=1, \dots, n \text{ and } j=1, \dots, n \quad \dots(8)$$

Thus $\det[\phi(X)]$ is the Jacobian of the system evaluated for the vector

$X = [x_1, x_2, \dots, x_n]^t$. Now define the vector $F(X)$ as

$$F(X) = [f_1(x), f_2(x), \dots, f_n(x)]^t \quad \dots(9)$$

With these definitions in mind, and with the starting vector

$X_0 = [x_{10}, x_{20}, \dots, x_{n0}]^t$ let

$$X_{k+1} = X_k + \delta_k \quad \dots(10)$$

where δ_k is the solution vector for the set of simultaneous linear equations

$$\phi(X_k)\delta_k = -F(X_k) \quad \dots(11)$$

Let $A = [\phi(X_k) - F(X_k)] = 0$ be the augmented matrix.

If the components of $\phi(X)$ are continuous in a neighbourhood of a point such that $F(\alpha) = 0$, if $\det \phi(\alpha) \neq 0$ and if X_0 is "near" α then $\lim_{k \rightarrow \infty} X_k = \alpha$.

The Newton-Raphson method may be summarized as follows:-

(1) Choose a starting vector $X_k = X_0 = [x_{10}, x_{20}, \dots, x_{n0}]$ where X_0 is hopefully near a solution α . $[x_{10}, x_{20}, \dots, x_{n-1,0}]$ are the initial guesses for the horizontal coordinates of the vertices P_1 to P_n .

(2) Solve the system of linear equations

$$\phi(X_k)\delta_k = -F(X_k) \quad \dots(12)$$

where

$$\phi_{ij}(X_k) = \frac{\partial f_i}{\partial x_j}(X_k) \quad \begin{matrix} i=1, \dots, n \\ j=1, \dots, n \end{matrix} \quad \dots(13)$$

and

$$F(X_k) = \left(\frac{\partial t}{\partial x_1}, \frac{\partial t}{\partial x_2}, \dots, \frac{\partial t}{\partial x_n} \right)^t \quad \dots(14)$$

and the increment vector

$$\delta_k = [\delta_{1k}, \delta_{2k}, \dots, \delta_{nk}]^t \quad \dots(15)$$

(3) Update the approximation to the root for the next iteration

$$x_{k+1} = x_k + \delta_k \quad \dots(16)$$

(4) Check for possible convergence to a root α . Test to see if

$$|\delta_{ik}| < \epsilon_2 \quad i=1, \dots, n \quad \dots(17)$$

If (17) is true for all i then x_{k+1} is taken to be the root. If expression (17) is failed for any i , then the process is repeated starting with Step 2. The iterative process is continued until expression (17) is passed for some k or when k exceeds some specified upper limit.

It is necessary to set up the augmented matrix of partial derivatives required for the solution of the non-linear equations as derived from Fermat's principle. This matrix is simplified by noting

$$\phi_{ij}(x_k) = \frac{\partial f_i}{\partial x_j}(x_k) = 0 \quad \text{for } j \neq i-1, i, i+1 \quad i, j=1, \dots, n \quad \dots(18)$$

The non-zero components of the augmented matrix are readily determined by using the following procedure for $i=1, \dots, n$.

$$XDIS1(i) = x_i - x_{i-1}$$

$$XDIS2(i) = x_{i+1} - x_i$$

$$ZIM1(i) = A_{i-1}x_{i-1}^3 + B_{i-1}x_{i-1}^2 + C_{i-1}x_{i-1} + D_{i-1} \quad \text{for } i=2, \dots, n \quad \dots(19)$$

$$= z_0 \quad \text{for } i=1 \quad \dots(20)$$

$$ZI(i) = A_i x_i^3 + B_i x_i^2 + C_i x_i + D_i \quad \text{for } i=1, \dots, n \quad \dots(21)$$

$$ZIP1(i) = A_{i+1}x_{i+1}^3 + B_{i+1}x_{i+1}^2 + C_{i+1}x_{i+1} + D_{i+1} \quad \text{for } i=1, \dots, n-1 \quad \dots(22)$$

$$= z_{n+1} \quad \text{for } i=n \quad \dots(23)$$

$$DZIM1(i) = 3A_{i-1}x_{i-1}^2 + 2B_{i-1}x_{i-1} + C_{i-1} \quad \text{for } i=2, \dots, n \quad \dots(24)$$

$$= 0 \quad \text{for } i=1 \quad \dots(25)$$

$$DZI(i) = 3A_i x_i^2 + 2B_i x_i + C_i \quad \text{for } i=1, \dots, n \quad \dots(26)$$

$$DZIP1(i) = 3A_{i+1}x_{i+1}^2 + 2B_{i+1}x_{i+1} + C_{i+1} \quad \text{for } i=1, \dots, n-1 \quad \dots(27)$$

$$= 0 \quad \text{for } i=n \quad \dots(28)$$

$$DDZI(i) = 6A_i x_i + 2B_i \quad \text{for } i=2, \dots, n-1 \quad \dots(29)$$

$$= 0 \quad \text{for } i=1 \text{ or } i=n \quad \dots(30)$$

$$W(i) = \text{SQRT}[XDIS1(i)^2 + (ZI(i) - ZIM1(i))^2] \quad \dots(31)$$

$$X(i) = 1 + DZI(i)^2 + (ZI(i) - ZIM1(i)) * DDZI(i) \quad \dots(32)$$

$$Y1(i) = XDIS1(i) + (ZI(i) - ZIM1(i)) * DZIM1(i) \quad \dots(33)$$

$$Y2(i) = XDIS1(i) + (ZI(i) - ZIM1(i)) * DZI(i) \quad \dots(34)$$

$$E12(i) = 1 + DZIM1(i) * DZI(i) \quad \dots(35)$$

$$WW(i) = \text{SQRT}[XDIS2(i)^2 + (ZIP1(i) - ZI(i))^2] \quad \dots(36)$$

$$XX(i) = -[1 - DZI(i)^2 + (ZI(i) - ZIP1(i)) * DDZI(i)] \quad \dots(37)$$

$$YY2(i) = XDIS2(i) + (ZIP1(i) - ZI(i)) * DZI(i) \quad \dots(38)$$

$$YY3(i) = XDIS2(i) + (ZIP1(i) - ZI(i)) * DZIP1(i) \quad \dots(39)$$

$$E23(i) = 1 + DZI(i) * DZIP1(i) \quad \dots(40)$$

Then

$$\emptyset(i, i-1) = \frac{[-W(i) * E12(i) + (Y2(i) - Y1(i)) / W(i)]}{W(i) * W(i) * v(i)} \quad \dots(41)$$

$$\begin{aligned} \emptyset(i, i) = & \frac{[W(i) * X(i) - (Y2(i) * Y2(i)) / W(i)]}{W(i) * W(i) * v(i)} \\ & - \frac{WW(i) * XX(i) + (YY2(i) * YY2(i)) / WW(i)}{WW(i) * WW(i) * v(i+1)} \quad \dots(42) \end{aligned}$$

$$\emptyset(i, i+1) = - \frac{WW(i) * E23(i) - (YY3(i) * YY2(i)) / WW(i)}{WW(i) * WW(i) * v(i+1)} \quad \dots(43)$$

and

$$F(x_i) = \frac{-Y2(i)}{W(i) * v(i)} + \frac{YY2(i)}{WW(i) * v(i+1)} \quad \dots(44)$$

In the programs that follow, the elements of the augmented matrix

$$A = [\emptyset(X_k) - F(X_k)] \quad \dots(45)$$

are evaluated by the subroutine CALCN3. The system of linear equations (11)

is solved by calling the function SIMUL which utilizes the Gauss-Jordan

method.

The main program reads data values for itmax, iprint, n, ϵ , ϵ_2 and x_1, x_2, \dots, x_n . Here, itmax is the maximum number of Newton-Raphson iterations, iprint is a variable that controls printing of the intermediate output, n is the number of nonlinear solutions, ϵ is the minimum pivot magnitude allowed in the Gauss-Jordan reduction algorithm, ϵ_2 is a small positive number used to test condition (17), and x_1, x_2, \dots, x_n are the initial estimates $x_{10}, x_{20}, \dots, x_{n0}$, that is the elements of X_0 . The coefficients representing the mathematical surfaces and interval velocities are also given. Flow diagrams for the main program and the function routine SIMUL are shown in Figures A2.2 and A2.3.

III. THREE-DIMENSIONAL RAY TRACING

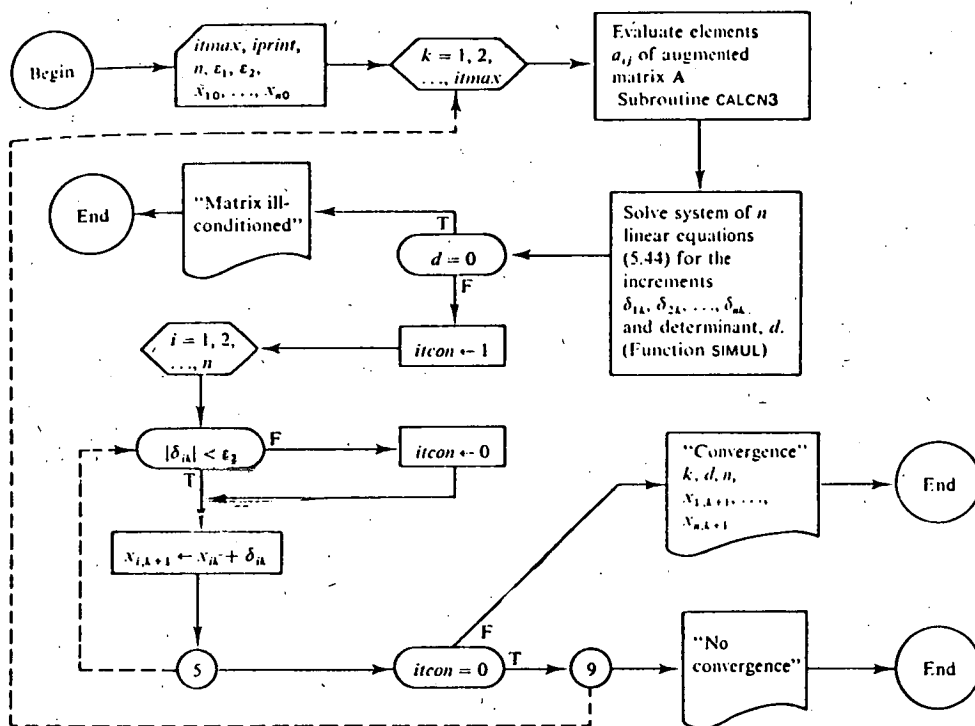
1. STATEMENT OF THE PROBLEM

Let (x_0, y_0, z_0) and $(x_{n+1}, y_{n+1}, z_{n+1})$ be the coordinates for the source and receiver respectively (Figure A2.4). The geological model is represented by n constant velocity layers with continuous curved boundaries which are mathematically represented by polynomials of the form

$$z_i = A_i + B_i x_i + C_i y_i + D_i x_i^2 + E_i y_i^2 + F_i x_i y_i \quad \dots (46)$$

with $(A_i, B_i, C_i, D_i, E_i$ and $F_i, i=1, \dots, n)$ known for each interface. The constant velocity v_i for $i=1, \dots, n+1$ between surfaces $i-1$ and i is known.

Once again let P_0 to P_{n+1} (Figure A2.4) be the consecutive vertices of the intersections of the rays with the curved interfaces, with P_0 representing the source and P_{n+1} the detector. If $(x_i, y_i, z_i) i=0, \dots, n+1$ are the coordinates of these vertices then the problem is to determine the vertices of P_1 to P_n .



Subroutine CALCN3 Arguments: x_k, A, N

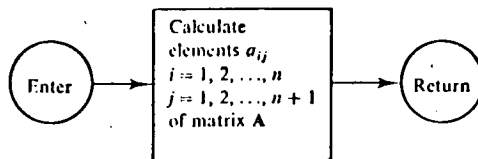


Fig. A 2.2 Flow Diagram for Computer Program FERMAT.

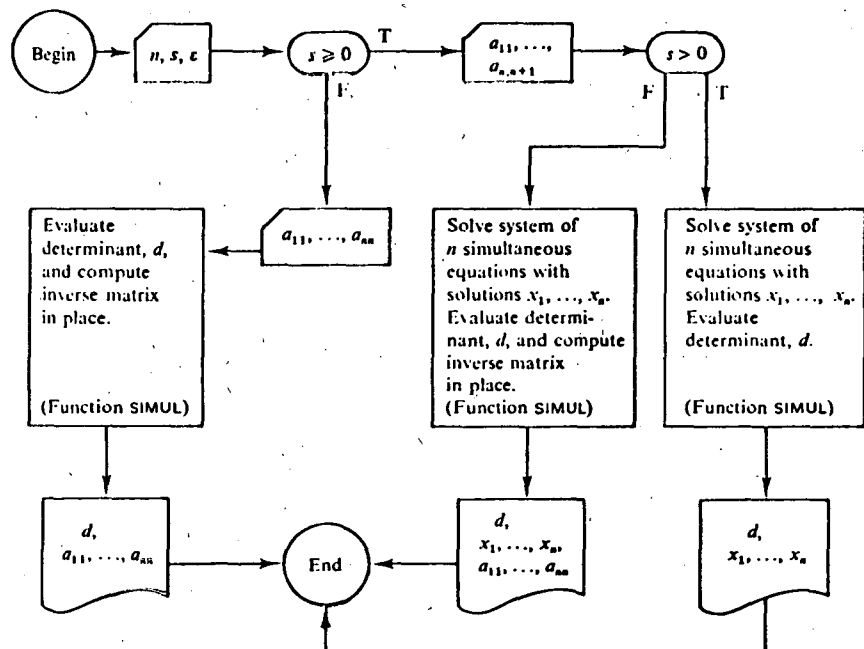


Fig. A 2.3 Flow Diagram for Function Routine SIMUL

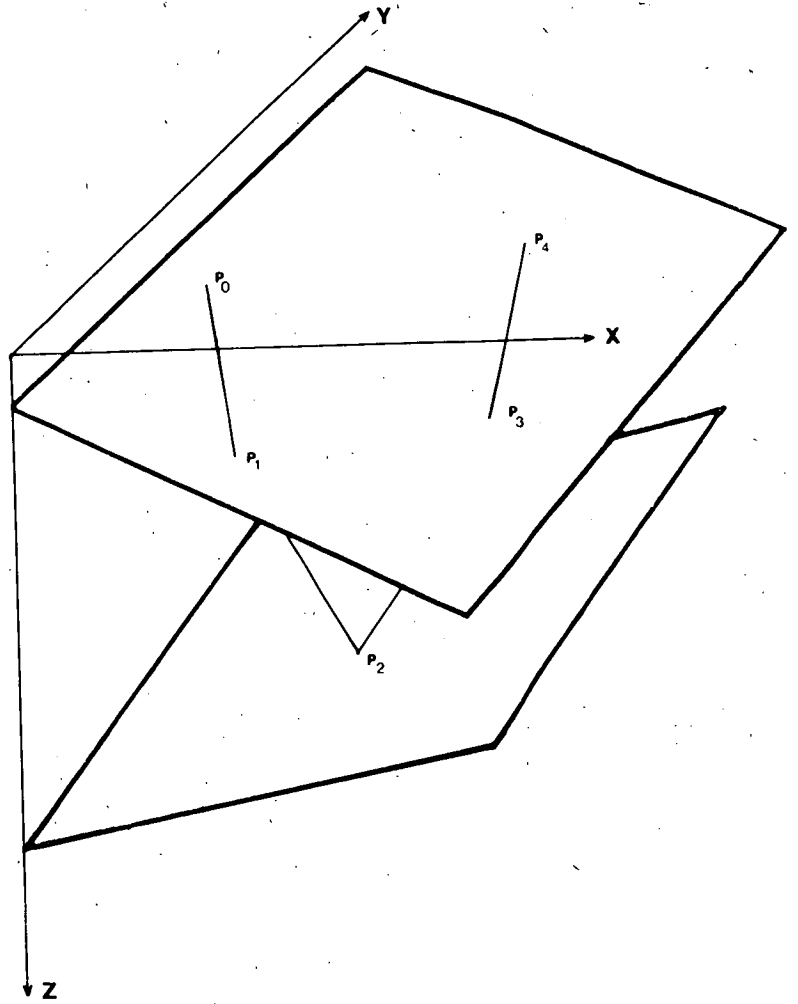


Fig. A2.4 Three dimensional geological model.

2. SOLUTION

The method of solution is similar to the two-dimensional case. The traveltime t along the ray P_0-P_{n+1} is given by the sum

$$t = \sum_{i=1}^{n+1} \left[(x_i - x_{i-1})^2 + (y_i - y_{i-1})^2 + (z_i - z_{i-1})^2 \right]^{1/2} v_i \quad \dots(47)$$

The problem reduces to solving the following $2n$ equations simultaneously.

$$\begin{aligned} \frac{\partial t}{\partial x_i} &= \frac{[(x_i - x_{i-1}) + (z_i - z_{i-1})(B_i + 2D_i x_i + F_i y_i)]}{[(x_i - x_{i-1})^2 + (y_i - y_{i-1})^2 + (z_i - z_{i-1})^2]^{1/2} v_i} \\ &\quad - \frac{[(x_{i+1} - x_i) + (z_{i+1} - z_i)(B_i + 2D_i x_i + F_i y_i)]}{[(x_{i+1} - x_i)^2 + (y_{i+1} - y_i)^2 + (z_{i+1} - z_i)^2]^{1/2} v_{i+1}} \\ &= 0 \quad i=1, \dots, n \end{aligned} \quad \dots(48)$$

and

$$\begin{aligned} \frac{\partial t}{\partial y_i} &= \frac{[(y_i - y_{i-1}) + (z_i - z_{i-1})(C_i + 2E_i y_i + F_i x_i)]}{[(x_i - x_{i-1})^2 + (y_i - y_{i-1})^2 + (z_i - z_{i-1})^2]^{1/2} v_i} \\ &\quad - \frac{[(y_{i+1} - y_i) + (z_{i+1} - z_i)(C_i + 2E_i y_i + F_i x_i)]}{[(x_{i+1} - x_i)^2 + (y_{i+1} - y_i)^2 + (z_{i+1} - z_i)^2]^{1/2} v_{i+1}} \\ &= 0 \quad i=1, \dots, n \end{aligned} \quad \dots(49)$$

The non-zero components of the augmented matrix are readily determined using the following procedure for $i=1$ to n .

$$XDIS1(i) = x_i - x_{i-1} \quad \dots(50)$$

$$YDIS1(i) = y_i - y_{i-1} \quad \dots(51)$$

$$XDIS2(i) = x_{i+1} - x_i \quad \dots(52)$$

$$YDIS2(i) = y_{i+1} - y_i \quad \dots(53)$$

$$\begin{aligned} ZIM1(i) &= A_{i-1} + B_{i-1}x_{i-1} + C_{i-1}y_{i-1} + D_{i-1}x_{i-1}^2 + E_{i-1}y_{i-1}^2 + F_{i-1}x_{i-1}y_{i-1} \\ &\quad \text{for } i=2, \dots, n \end{aligned} \quad \dots(54)$$

$$= z_0 \quad \text{for } i=1 \quad \dots(55)$$

$$ZI(i) = A_i + B_i x_i + C_i y_i + D_i x_i^2 + E_i y_i^2 + F_i x_i y_i \quad \text{for } i=1, \dots, n \quad \dots(56)$$

$$\text{ZIP1}(i) = A_{i+1} + B_{i+1}x_{i+1} + C_{i+1}y_{i+1} + D_{i+1}x_{i+1}^2 + E_{i+1}y_{i+1}^2 + F_{i+1}x_{i+1}y_{i+1} \quad \text{for } i=1, \dots, n-1 \quad \dots(57)$$

$$= z_n \quad \text{for } i=n \quad \dots(58)$$

$$\text{DXZIM1}(i) = B_{i-1} + 2D_{i-1}x_{i-1} + F_{i-1}y_{i-1} \quad \text{for } i=2, \dots, n \quad \dots(59)$$

$$= 0 \quad \text{for } i=1 \quad \dots(60)$$

$$\text{DYZIM1}(i) = C_{i-1} + 2E_{i-1}y_{i-1} + F_{i-1}x_{i-1} \quad \text{for } i=2, \dots, n \quad \dots(61)$$

$$= 0 \quad \text{for } i=1 \quad \dots(62)$$

$$\text{DXZI}(i) = B_i + 2D_ix_i + F_iy_i \quad \dots(63)$$

$$\text{DYZI}(i) = C_i + 2E_iy_i + F_ix_i \quad \dots(64)$$

$$\text{DXZIP1}(i) = B_{i+1} + 2D_{i+1}x_{i+1} + F_{i+1}y_{i+1} \quad \text{for } i=1, \dots, n-1 \quad \dots(65)$$

$$= 0 \quad \text{for } i=n \quad \dots(66)$$

$$\text{WXY}(i) = \text{SQRT}[\text{XDIS1}(i)^2 + \text{YDIS1}(i)^2 + \{ \text{ZI}(i) - \text{ZIM1}(i) \}^2] \quad \dots(67)$$

$$\text{RX}(i) = 1 + \text{DXZI}(i)^2 + 2D_i \{ \text{ZI}(i) - \text{ZIM1}(i) \} \quad \dots(68)$$

$$\text{RY}(i) = 1 + \text{DYZI}(i)^2 + 2E_i \{ \text{ZI}(i) - \text{ZIM1}(i) \} \quad \dots(69)$$

$$\text{SX1}(i) = \text{XDIS1}(i) + \{ \text{ZI}(i) - \text{ZIM1}(i) \} \text{DXZIM1}(i) \quad \dots(70)$$

$$\text{SY1}(i) = \text{YDIS1}(i) + \{ \text{ZI}(i) - \text{ZIM1}(i) \} \text{DYZIM1}(i) \quad \dots(71)$$

$$\text{SX2}(i) = \text{XDIS1}(i) + \{ \text{ZI}(i) - \text{ZIM1}(i) \} \text{DXZI}(i) \quad \dots(72)$$

$$\text{SY2}(i) = \text{YDIS1}(i) + \{ \text{ZI}(i) - \text{ZIM1}(i) \} \text{DYZI}(i) \quad \dots(73)$$

$$\text{EX12}(i) = 1 + \text{DXZM1}(i) * \text{DXZI}(i) \quad \dots(74)$$

$$\text{EY12}(i) = 1 + \text{DYZM1}(i) * \text{DYZI}(i) \quad \dots(75)$$

$$\text{WWXY}(i) = \text{SQRT}[\text{XDIS2}(i)^2 + \text{YDIS2}(i)^2 + \{ \text{ZIP1}(i) - \text{ZI}(i) \}^2] \quad \dots(76)$$

$$\text{RXX}(i) = -[1 - \text{DXZI}(i)^2 + 2D_i \{ \text{ZI}(i) - \text{ZIP1}(i) \}] \quad \dots(77)$$

$$\text{RYY}(i) = -[1 - \text{DYZI}(i)^2 + 2E_i \{ \text{ZI}(i) - \text{ZIP1}(i) \}] \quad \dots(78)$$

$$\text{SXX2}(i) = \text{XDIS2}(i) + \{ \text{ZIP1}(i) - \text{ZI}(i) \} \text{DXZI}(i) \quad \dots(79)$$

$$\text{SYY2}(i) = \text{YDIS2}(i) + \{ \text{ZIP1}(i) - \text{ZI}(i) \} \text{DYZI}(i) \quad \dots(80)$$

$$\text{SXX3}(i) = \text{XDIS2}(i) + \{ \text{ZIP1}(i) - \text{ZI}(i) \} \text{DXZIP1}(i) \quad \dots(81)$$

$$\text{SYY3}(i) = \text{YDIS2}(i) + \{ \text{ZIP1}(i) - \text{ZI}(i) \} \text{DYZIP1}(i) \quad \dots(82)$$

$$\text{EX23}(i) = 1 + \text{DXZI}(i) * \text{DXZIP1}(i) \quad \dots(83)$$

$$\text{EY23}(i) = 1 + \text{DYZI}(i) * \text{DYZIP1}(i) \quad \dots(84)$$

$$A(i,i-1) = \frac{[-WXY(i)*EX12(i) + (SX2(i)*SX1(i))/WXY(i)]}{WXY(i)^2 v_i} \quad \dots (85)$$

$$A(i,i) = \frac{[WXY(i)RX(i) - SX2(i)SX2(i)/WXY(i)]}{WXY(i)^2 v_i} - \frac{[WWXY(i)RXX(i) + SXX2(i)SXX2(i)/WWXY(i)]}{WWXY(i)^2 v_{i+1}} \quad \dots (86)$$

$$A(i,i+1) = \frac{[-WWXY(i)EX23(i) - SXX3(i)SXX2(i)/WWXY(i)]}{WWXY(i)^2 v_{i+1}} \quad \dots (87)$$

$$A(n+1,n+i-1) = \frac{[-WXY(i)EY12(i) + SY2(i)SY1(i)/WXY(i)]}{WXY(i)WXY(i) v_i} \quad \dots (88)$$

$$A(n+i,n+i) = \frac{[WXY(i)RY(i) - SY2(i)SY2(i)/WXY(i)]}{WXY(i)WXY(i) v_i} - \frac{[WWXY(i)RYY(i) - SYY2(i)^2/WWXY(i)]}{WWXY(i)^2 v_{i+1}} \quad \dots (89)$$

$$A(n+i,n+i+1) = \frac{[-WWXY(i)EY23(i) + SYY3(i)SYY2(i)/WWXY(i)]}{WWXY(i)^2 v_{i+1}} \quad \dots (90)$$

$$A(i,2n+1) = \frac{-SX2(i)}{WXY(i)*v_i} + \frac{SXX2(i)}{WWXY(i)v_{i+1}} \quad \dots (91)$$

$$A(n+i,2n+1) = \frac{-SY2(i)}{WXY(i)v_i} + \frac{SYY2}{WWXY(i)v_{i+1}} \quad \dots (92)$$

In the program the augmented matrix of partial derivatives required for the solution of the nonlinear equations which describe the three-dimensional ray paths is set up in the subroutine CAL3D. This can be substituted for the subroutine CALCN3 in the two-dimensional example.

Computer listings of the essential elements of the program are given in the microfilm listing at the rear of the thesis.

IV. CONCLUSIONS

A method is described for tracing reflection, refraction and multiple rays from specified source and detector locations through layers of arbitrary shape and orientation. A solution is presented which is amenable to rapid calculation using digital computers. The ray tracing is treated as a variation problem and stems from Fermat's principle. The solution can be checked by determining whether triplet of consecutive vertices P_{i-1} , P_i , and P_{i+1} lie in a plane perpendicular to the interface containing P_i as well as determining whether Snells Law is satisfied at each vertex where the ray is refracted and whether the angles of incidence and reflection are identical at each vertex where reflection occurs.

Appendix 3

THOMPSON-HASKELL METHOD

	page
I. INTRODUCTION	A3.1
II. THOMPSON-HASKELL METHOD	A3.1

I. INTRODUCTION

The reflectivity of transitional zones with arbitrary depth-dependent distributions of elastic moduli and density for plane waves at arbitrary angles of incidence has been described by Thompson (1950) who laid down the theoretical groundwork later extended by Haskell (1953). Knopoff (1964, Harkrider (1964, 1970), Dunkin (1965) and Watson (1970) used the method to study the surface wave dispersion in a multi-layered elastic half-space, while Schwab & Knopoff (1972) and Fuchs (1968) have calculated the reflections of plane body waves in a layered medium. Fuchs (1970) later studied the reflection of spherical waves from a transitional zone.

II. THOMPSON-HASKELL METHOD

Consider a medium consisting of $n-1$ ideally elastic homogeneous and isotropic layers with plane parallel boundaries located between an upper half-space (0) and lower half-space (n) (Figure A3.1). The transition zone is placed at a depth h below the surface. The parameters of each layer are known: the velocity of the longitudinal (V_{p_i}) and transverse (V_{s_i}) waves, the density (ρ_i) and the thickness (h_i). A potential vector is defined for each of the $n-1$ different media

$$\Phi_i = \begin{pmatrix} \psi_i^-, \psi_i^-, \psi_i^+, \psi_i^+ \end{pmatrix} \quad i = 1, n-1 \quad \dots (1)$$

(Dunkin, 1965)

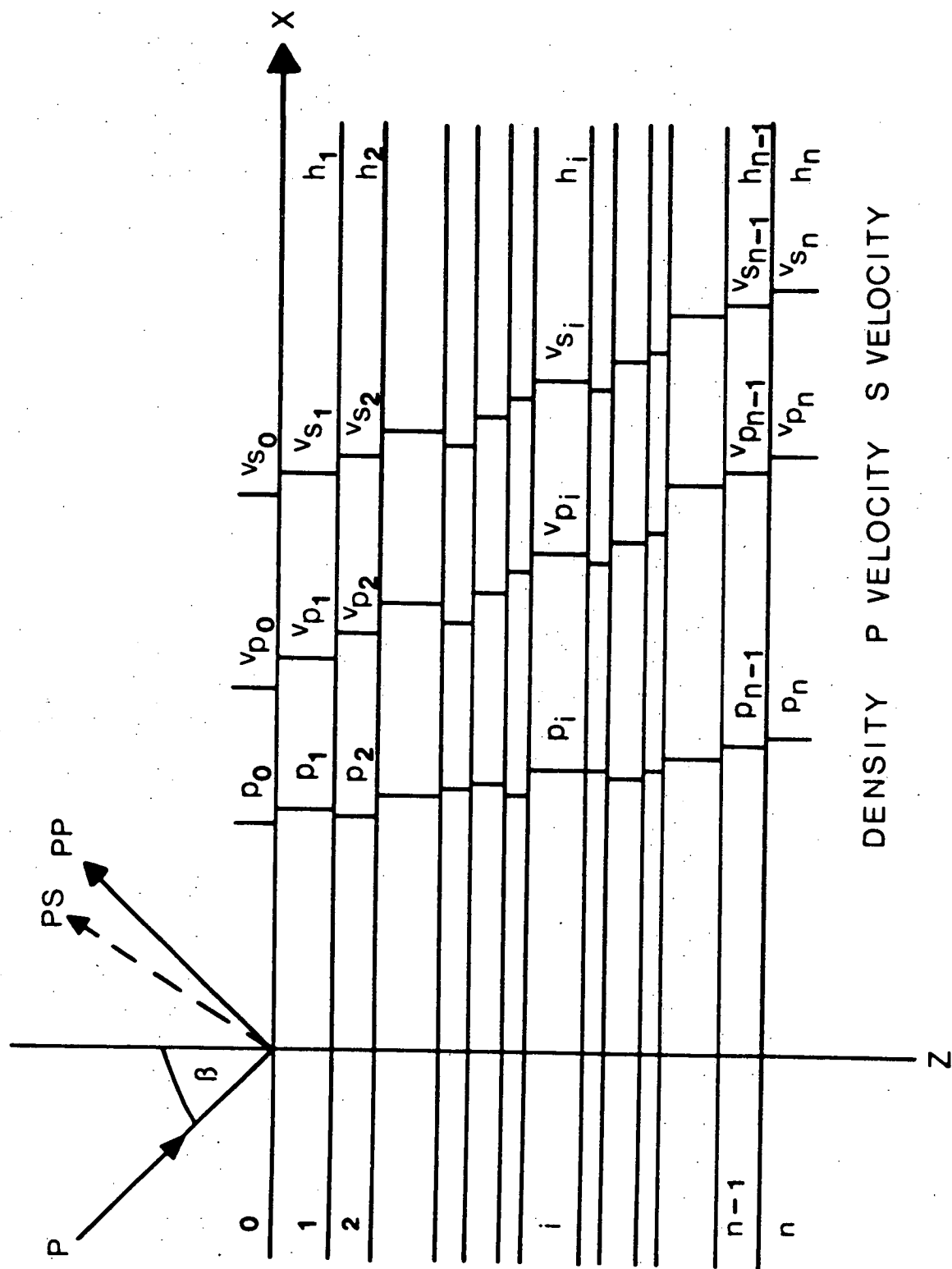


Fig. A3.1 Transition zone between two homogeneous half-spaces. Each layer is characterised by P and S wave velocities, density and thickness. P is the oblique incident P wave, PP and PS the reflected P and S waves respectively.

where ψ_i^+ , ψ_i^- and Ψ_i^+ , Ψ_i^- are the P and SV wave potentials, respectively, corresponding to waves travelling in the positive (downwards) and negative (upwards) z direction. The application of boundary conditions (Dunkin, 1965) yields a relation between the potential vectors of the lower and upper half-space:

$$\Phi_n = M\Phi_0 \quad \dots(2)$$

where M is the Haskell matrix. It is the product of the matrix of the lower half-space T_n , the $n-1$ matrices G_i , and the matrix of the upper half-space T_0 .

$$M = T_n \cdot G_{n-1} \dots G_1 T_0 \quad \dots(3)$$

Fuchs (1968) and Harkrider (1970) listed the elements of these matrices. The Haskell matrix contains exponential terms which become very large at high frequencies (Watson, 1970). Thus equation (2) cannot be solved directly due to the intrinsic loss of precision. Knopoff (1964), Dunkin (1965) and Thrower (1965) have offered alternative methods which avoid this difficulty.

By defining a new 6 x 6 delta matrix of the 4 x 4 Haskell matrix, which is obtained by computing all possible 2 x 2 sub-determinants of the 4 x 4 matrix, the offending terms are eliminated analytically. The elements in the delta matrix are given in Fuchs (1968). Watson (1970) noted that due to symmetry the 6 x 6 delta matrix can be reduced to a 5 x 5 delta matrix. Fuchs (1968) has calculated the reflection coefficients from equation (2) in terms of the elements \hat{M}_{ij} of the delta matrix \hat{M}

$$\begin{aligned}
 R_{PP} &= \hat{M}_{14} / \hat{M}_{11} \\
 R_{PS} &= -\hat{M}_{12} / \hat{M}_{11}
 \end{aligned}
 \dots(4)$$

Dunkin (1965) proved that the delta matrix of a product matrix is equal to the product of the delta matrices of the individual factor matrices. Therefore the \hat{M}_{ij} can be computed by multiplication of the delta matrices \hat{T}_n , \hat{G}_i and \hat{T}_0 of T_n , G_i and T_0 [see equation (3)].

The matrix formalization has been programmed to yield the PP and PS reflection coefficients. Theory shows that the reflection coefficients are dependent on the layer parameters (P and S velocities, density and thickness), on the frequency and angle of incidence of the incident plane wave. The coefficients are complex so that both amplitude and phase changes occur for different input parameters.